LUND UNIVERSITY

The formation and fate of planetesimals at planetary gap edges

Eriksson, Linn

2022

The formation and fate of planetesimals at planetary gap edges

LINN ERIKSSON
DEPT. OF ASTRONOMY AND THEORETICAL PHYSICS | LUND UNIVERSITY 2022

The formation and fate of planetesimals at planetary gap edges

Linn Eriksson

LUND
UNIVERSITY

Thesis for the degree of Doctor of Philosophy

Thesis advisor: Prof. Anders Johansen
Co-advisors: Dr. Thomas Ronnet, Dr. Beibei Liu, Dr. Oscar Agertz
Faculty opponent: Dr. Zhaohuan Zhu

To be presented, with the permission of the Faculty of Science of Lund University, for public criticism in the Lundmark lecture hall (Lundmarksalen) at the Department of Astronomy and Theoretical Physics on Friday, 13th of May, 2022 at 13:00.

Organization LUND UNIVERSITY Department of Astronomy and Theoretical Physics Box 43, SE-22100 Lund, Sweden	**Document name** DOCTORIAL DISSERTATION **Date of issue** 2022-04-19
Author(s) Linn Eriksson	Sponsoring organization

Title and subtitle
The formation and fate of planetesimals at planetary gap edges

Abstract

High resolution observations with ALMA have revealed that concentric rings and gaps are common features in protoplanetary disks. The favored mechanism for creating these substructures are planet-disk interactions, in which growing planets open gaps in the disk, and particles become trapped at the pressure maxima that form at the corresponding gap edges. Since the particle density in these pressure bumps can become much higher than the global value, they are likely sites for planetesimal formation via the streaming instability.

In a series of three papers, we have studied the formation and fate of such planetesimals formed at planetary gap edges. By performing global simulations of an evolving disk perturbed by multiple planets, and including a state-of-the-art dust evolution model, we find that planetesimals indeed should form at planetary gap edges, and in significant amounts. Furthermore, the described process has a dramatic impact on the evolution of solids in protoplanetary disks, and therefore also on how the disks appear in observations. We find that planets larger than the pebble isolation mass trap pebbles efficiently at the gap edges, and depending on the efficiency of planetesimal formation, the disk transforms to either a transition disk with a large inner hole devoid of dust or to a disk with narrow bright rings. When lower planetary masses are used, the result is a disk with a series of weak ring patterns.

By using gravitational N-body simulations we demonstrate that the close proximity between the planetesimals and the planets causes the planetesimals to leave their birth locations soon after formation and spread out across the disk. In the current paradigm of planet-disk interactions, planetary gaps are often invoked as a mechanism to separate the disk into an inner and outer part that do not exchange material, but our results show that scattered planetesimals can in fact carry material past these gaps. We further consider the accretion efficiency of these planetesimals onto the forming planets and show that it is very low, even in the most favorable cases. The high heavy element content of giant planets is often explained with planetesimal accretion during the gas accretion phase, but our results rather demonstrate that this is very unlikely. In conclusion, our work highlights that planetesimal formation at planetary gap edges can have huge implications for disk evolution and planet formation.

Key words
Protoplanetary disks, planet-disk interactions, planetesimal formation, planetesimal dynamics, giant planet formation

Classification system and/or index terms (if any)

Supplementary bibliographical information	**Language** English
ISSN and key title	**ISBN** ISBN: 978-91-8039-196-2 (print) ISBN: 978-91-8039-195-5 (pdf)
Recipient's notes	**Number of pages** 132 / Price
	Security classification

Signature 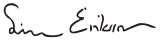 Date 2022-03-29

The formation and fate of planetesimals at planetary gap edges

Linn Eriksson

LUND
UNIVERSITY

Faculty Opponent

Dr. Zhaohuan Zhu
Department of Physics and Astronomy, University of Nevada,
Las Vegas, USA

Evaluation Committee

Dr. Nienke van der Marel
Leiden Observatory, Leiden University,
Leiden, The Netherlands

Docent Per Bjerkeli
Department of Space, Earth and Environment, Chalmers University of Technology,
Göteborg, Sweden

Docent Paul McMillan
Department of Astronomy and Theoretical Physics, Lund University,
Lund, Sweden

Cover: Artist impression of a protoplanetary disk with forming planets. Credit: ESO/L. Calcada. Edited by Eric Andersson.
Funding information: This thesis work is financially supported by the Swedish Research Council (Project Grant 2018-04867), the European Research Council (ERC Consolidator Grant 724 687-PLANETESYS) and the Royal Physiographic Society of Lund (Stiftelsen Walter Gyllenbergs fond and Märta och Erik Holmbergs donation).

Faculty of Science, Department of Astronomy and Theoretical Physics

ISBN: 978-91-8039-196-2 (print)
ISBN: 978-91-8039-195-5 (pdf)

Printed in Sweden by Media-Tryck, Lund University, Lund 2022

Media-Tryck is a Nordic Swan Ecolabel certified provider of printed material. Read more about our environmental work at www.mediatryck.lu.se

MADE IN SWEDEN

Contents

List of publications

This thesis is based on the following peer-reviewed publications:

I **Pebble drift and planetesimal formation in protoplanetary discs with embedded planets**
L.E.J. Eriksson, A. Johansen, B. Liu (2020)
Astronomy & Astrophysics, vol. 635, A110 (19 pp.)

II **The fate of planetesimals formed at planetary gap edges**
L.E.J. Eriksson, T. Ronnet, A. Johansen (2021)
Astronomy & Astrophysics, vol. 648, A112 (22 pp.)

III **A low accretion efficiency of planetesimals formed at planetary gap edges**
L.E.J. Eriksson, T. Ronnet, A. Johansen, R. Helled, C. Valletta, A.C. Petit (2022)
Astronomy & Astrophysics, in press, 10.1051/0004-6361/202142391 (13 pp.)

Work not included in the thesis

Peer-reviewed publications not included in this thesis:

I **Atmospheric signatures of giant exoplanet formation by pebble accretion**
N. Madhusudhan, B. Bitsch, A. Johansen, **L.E.J. Eriksson** (2017)
Monthly Notices of the Royal Astronomical Society, vol. 469, 4102-4115 (14 pp.)

II **Circularizing Planet Nine through dynamical friction with an extended, cold planetesimal belt**
L.E.J. Eriksson, A.J. Mustill, A. Johansen (2018)
Monthly Notices of the Royal Astronomical Society, vol. 475, 4609-4616 (8 pp.)

Popular summary

Protoplanary disks comprised of dust and gas surround newborn stars, creating nurseries for forming planets. Planet formation is a multistage process which spans several mechanisms from the collisions of tiny dust grains to the final assembly of giant planets several hundred times more massive than Earth. Our knowledge of these steps are continuously improving due to extensive observations of protoplanetary disks and other planetary systems. Additionally, clues obtained from missions within our Solar System and laboratory experiments have helped with the aims to recreate conditions for planetary formation processes. To interpret these observations and experimental results we use computer simulations and theoretical calculations. The combination of observations and simulations have consolidated our understanding of planet formation to what it is today.

This thesis covers several steps of the planet formation process, with a focus on the formation and evolution of planetesimals. Planetesimals, referred as the building blocks of planets, are asteroid-like objects formed via the gravitational collapse of small pebbles. In order for this process to work there needs to be an over-concentration of pebbles in the disk, and one location where this has been predicted to occur is at the edges of gas gaps carved by growing giant planets. In this thesis we use computer simulations to answer whether or not this is possible; and if so, what happens with these planetesimals once they have formed.

Our findings show that planetesimals do indeed form at the edges of planetary gaps, and in significant amounts. These planetesimals do not remain at their birth locations but are soon kicked away by the growing planets. If the planetesimals end up in the innermost Solar System they might lose mass due to frictional heating, resulting in the formation of new pebbles. We also investigate how often formed planetesimals collide with the nearby planets, finding that this only occurs in rare cases.

Populärvetenskaplig sammanfattning

Protoplanetära skivor bestående av gas och stoft omger nyfödda stjärnor, och det är inuti dessa skivor som planeter föds. Planetbildning är en flerstegsprocess som inkluderar allt från kollisioner mellan små stoftpartiklar till slutmonteringen av jätteplaneter med flera hundra gånger mer massa än jordens. Vår kunskap om dessa steg ökar kontinuerligt med nya observationer av protoplanetära skivor och exoplanetsystem. Utforskningen av vårt eget solsystem och nya laboratorieexperiment har ytterligare bidragit med kunskap kring förhållandena som råder under planetbildningen. För att tolka resultaten av dessa observationer och experiment använder vi oss av datorsimuleringar och teoretiska beräkningar. Kombinationen av observationer och simuleringar har lett fram till den bild av planetbildning som vi har idag.

Den här avhandlingen behandlar flera steg av planetbildningen, med fokus på födseln och utvecklingen av planetesimaler. Planetesimaler refereras ofta till som planeternas byggstenar och är asteroidliknande objekt som bildas genom gravitationell kollaps av småstenar. För att den processen ska initieras krävs en överkoncentration av småsten någonstans i skivan. Ett ställe där man förutsett att detta kan ske är vid kanten av gasgropar som karvats ut av växande jätteplaneter. I den här avhandlingen använder vi oss av datorsimuleringar för att se om det här är möjligt, och om så är fallet, vad som händer med planetesimalerna efter de har bildats.

Våra upptäckter visar på att planetesimaler kan bildas vid kanten av gropar karvade av planeter, och i betydande mängder. Dessa planetesimaler förblir inte där de bildats utan blir ivägsparkade av de växande planeterna. Om planetesimalerna hamnar i det inre solsystemet kan de förlora massa på grund av värmefriktion, vilket leder till bildandet av nya småstenar. Vi undersöker också hur ofta planetesimalerna som bildas kolliderar med de närliggande planeterna, och finner att det endast sker i sällsynta fall.

Acknowledgements

First and foremost I would like to extend my deepest gratitude to Anders Johansen, who has been my supervisor throughout my bachelor, master and PhD studies. Thank you for coming up with great projects, for sending me to conferences all around the world, and for shaping me into the researcher that I am today. I am also extremely grateful for all the time you have spent helping me apply for postdoc positions and planning for my future in academia. I have had an amazing time at Lund Observatory and a lot of that is thanks to you.

I further wish to send a big thank you to Thomas Ronnet, for being an amazing co-supervisor during the last two projects. Our debugging sessions in REBOUND were numerous, and my solutions not always super pretty (why run one simulation with 10,000 particles when you can run 1,000 simulations with 10 particles...), but without you they would have been a lot uglier. I will also take this opportunity to apologize for the occasional intense spamming on slack, for which you never complained even once. I also wish to thank my first co-supervisor Beibei Liu for always having your door open if I had any questions, and for many great ping-pong matches. My last co-supervisor Oscar Agertz also deserves a thank you, for helping me out with postdoc planning and for inviting me to multiple dinners together with the galaxy formation group. I also wish to thank Ravit Helled whom I collaborated with during my final project, for inviting me to Zurich and for writing numerous recommendation letters.

For the writing of my thesis I am indebted to Herrgårn (a.k.a. Eric Andersson), Brian Thorsbro, Bibiana Prinoth and Alexander Mustill; Herrgårn for editing the front page, Brian for providing the thesis template and for writing a great thesis himself that I used as inspiration on many occasions, Bibiana for reading it all through and providing comments as well as helping me make the SED sketch, and Alex for reading it through and helping me improve on the language and grammar.

I am extremely grateful for the many friends I have made at Lund Observatory throughout the years. For the many fun evenings I have spent together with Bibi, Madeleine, Nic, Alvaro, Herrgårn, Brian and Florent, especially during Covid. I am thankful for my great office mates, Noemi and Rebecca, who stayed despite me always putting the temperature in the office as high as possible. I wish to send an extra thanks to Brian, for being the god of server maintenance and for helping me out with my postdoc applications. I also wish to send an extra thanks to my amazing best friend Bibi, you make astro a great workplace just by being here, and its incredible how you manage to work $\gg$ 100% and at the same time organize

dinners, social events, trips...

I would like to thank my family, especially my parents Eva and Sverker, for being my biggest supporters and for all the help you have provided throughout the years. I also wish to thank my amazing extra family from Grönahög. Last but not least, a big thank you to my Herrgårn, for all the love and support you have given me over the years. Thank you for always staying and helping me with whatever problems I am struggling with, even when my patience and mood drops downwards.

Part I

Research context

Chapter 1

Protoplanetary disk structure and evolution

Protoplanetary disks surround newly formed stars and are the birthplace of planets. They are predominantly composed of gas with a small fraction of dust, the mixture and composition of which is inherited from the host molecular cloud. The disk evolves as matter is accreted onto the central star and is typically assumed to have a lifetime of a few Myr, thus putting a time constraint on the planet formation process.

Protoplanetary disk temperatures range from $\gtrsim 1000$ K near the star to a few tens of K in the outer disk (Boss, 1998). Because of this, they radiate at a wavelength range from micrometer to millimeter, allowing them to be observed with infrared telescopes and radio telescopes (see Fig. 1.1). Similar to the great variety of exoplanets, observations have found disks with largely varying sizes, masses and morphologies (see recent review by Andrews 2020).

1.1 Evolution of Young Stellar Objects (YSOs)

The evolutionary stages of YSOs are typically classified according to the shape and features of their spectral energy distribution (SED). A sketch showing how the general shape of these SEDs evolves during the four main classes is presented in Fig. 1.2. The original formalism presented three classes, I-II-III, respectively, which were defined based on the slope of the SED at mid-IR wavelengths,

$$\alpha_{\rm IR} = \frac{{\rm d}\log(\lambda F_\lambda)}{{\rm d}\log\lambda}, \tag{1.1}$$

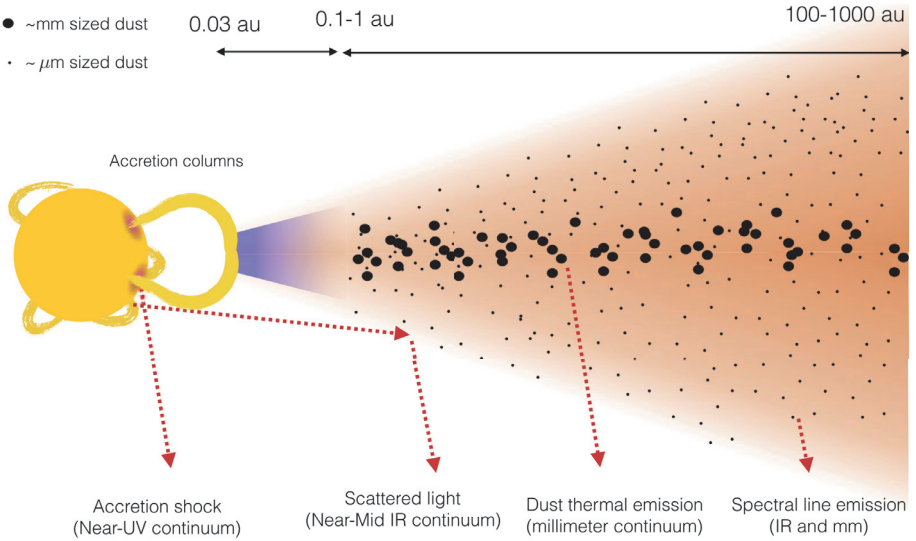

Figure 1.1: Sketch of a protoplanetary disk showing the distribution of different sized solids and the various observational diagnostics (adapted from Lesur (2020) with permission).

where $\alpha_{\rm IR}$ is termed the spectral index (Lada, 1987). About ten years later the scheme was extended by Andre et al. (1993) to also include an earlier phase, Class 0.

The Class 0 collapse phase is the earliest observed stage of star formation, recognized by having a SED which peaks in the far-IR and without any optical or near-IR emission. These very young objects are not much hotter than the molecular cloud cores from which they form, and physically have a deeply embedded central core which is surrounded by a much more massive accreting gas and dust envelope. As the collapse continues a circumstellar accretion disk develops and the mass of the system soon becomes dominated by the protostar; this is known as the Class I phase. Class I objects have a SED with a very large IR excess, and distinguish themselves from Class 0 sources by having detectable near-IR emission. This radiation is emitted by the now visible warm inner regions of the disk.

The deeply embedded Class 0 and I phases last for about $\sim 0.5\,$Myr, and towards the end of it the collapsing cloud has settled onto the star or onto the disk. Now begins the Class II phase, and for the remainder of this thesis, protoplanetary disks refer to disks around Class II YSOs. These disks are accretion disks which typically contain $\sim 1\%$ of the stellar mass. Observationally, the YSO is now for

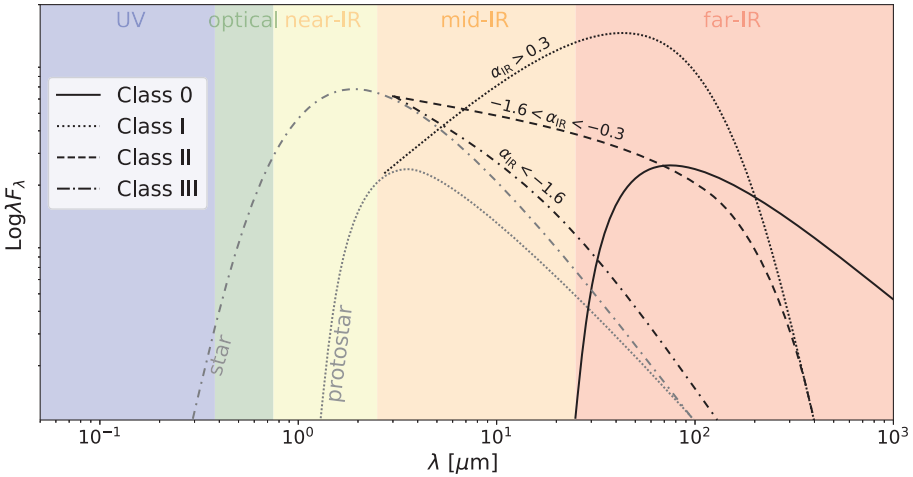

Figure 1.2: A sketch of how the general shape of SEDs vary during the four stages of protostar evolution. The SED slopes for class I-III are indicated on the plot (Greene et al., 1994).

the first time optically visible, and the SED is recognized by having an IR excess which is moderately falling in the mid-IR. The average lifetime of protoplanetary disks has been estimated by observing young clusters of varying age and counting what fraction of their YSOs that show IR excess. One such example is shown in Fig. 1.3, where it is found that 50% of YSOs have lost their disks after 3 Myr. A characteristic lifetime of 3 Myr was also found in Mamajek (2009), and is the lifetime which is most often adopted in simulations. However, a recent study by Michel et al. (2021) finds characteristic lifetimes that are 2-3 times larger than this estimate, thus challenging the standard picture of disk evolution.

The last evolutionary stage for an YSO is the Class III phase. At this point the disk is all but gone, and there is little or no accretion onto the star. The SED is now fairly stellar, but can be distinguished from that of a normal main sequence star by being more luminous (such that the star lies above the main sequence).

1.2 Disk substructures

Observations of substructures

High resolution observations performed with the Atacama Large Millimeter/submillimeter Array (ALMA) have revealed that disks exhibit a plethora of different types of sub-

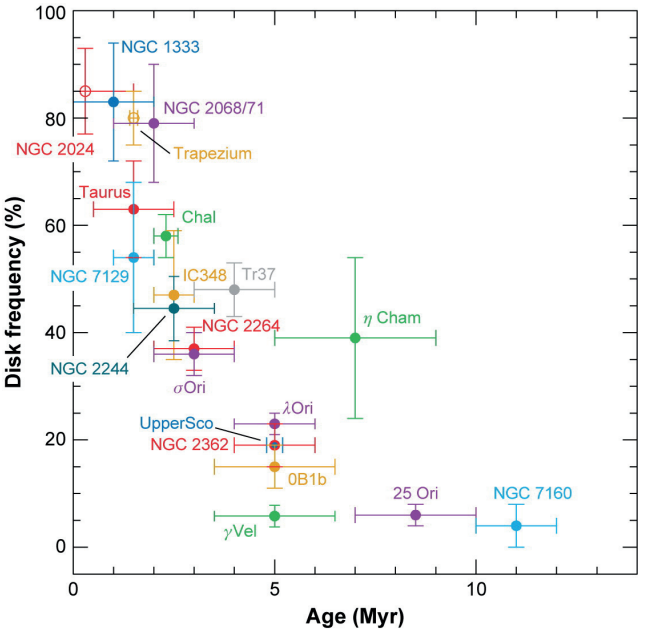

Figure 1.3: Fraction of stars with detectable near-IR excess as a function of the stellar group age. Near-IR excess indicates that there is a dust disk present at $<<$ 1 au. This plot suggests that 50% of stars lose their disks within 3 Myr (adapted from Wyatt (2008) with permission).

structures. These substructures have been detected at all spatial scales down to the current resolution limit at $\sim 1 - 5$ au, and in disks with ages ranging from < 0.5 Myr to 10 Myr (e.g. Huang et al. 2018; Segura-Cox et al. 2020). Substructures are mostly observed in the thermal continuum emission at millimeter/submillimeter wavelengths associated with pebbles, but have also been detected in scattered light emission from small dust grains, and spectral line emission from gas molecules (see Fig. 1.1).

Limited angular resolution and a bias towards observing bright disks make it hard to determine the fraction of disks that harbor substructures; however, recent studies hint that smooth disks without any large-scale features are more common than structured disks. This can be seen in Fig. 1.4, which shows a relatively unbiased sample of disks from the Taurus disk survey (Long et al., 2019). This study finds smooth disks to be generally compact with small radii, whereas substructure is primarily observed in large disks. Considering the disk dust masses, structured

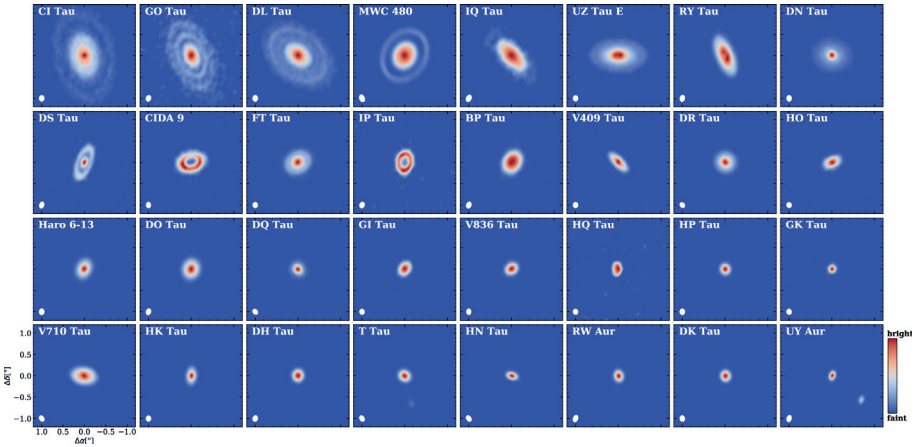

Figure 1.4: 1.3 mm images of the protoplanetary disks observed in the Taurus disk survey. These 32 disks constitute a relatively unbiased sample (the major bias being that previously observed disks at high resolution were excluded), and features 12 disks with large scale structure (adapted from Long et al. 2019). © AAS. Reproduced with permission.

disks tend to have high masses that are kept over long lifetimes, whereas smooth compact disks have smaller masses that decrease with age (van der Marel & Mulders, 2021). In general, disk dust masses, and hence also the fraction of structured disks, increase with the stellar mass (e.g. Ansdell et al. 2016; Pascucci et al. 2016; Testi et al. 2022).

Structured disks can be broadly classified into four categories based on their morphology: concentric rings and gaps; transition disks; spirals; and non-axisymmetric disks (Andrews, 2020). Examples of disks belonging to each category are shown in Fig. 1.5. Note that in some cases a disk can fit into more than one category.

- **Concentric rings and gaps** refer to an axisymmetric pattern of alternating increases and decreases in intensity, and are the most common substructure morphologies detected in the distribution of pebbles (e.g. ALMA Partnership et al. 2015) and dust (e.g. Ginski et al. 2016). Similar patterns have also been detected in the gas surface density (e.g. Favre et al. 2019). The number, width and intensity of the gaps and rings vary significantly within the category, and additional examples of such disks observed in mm continuum can be seen Fig. 1.4 (compare for example GO Tau, DL Tau and MWC 480).

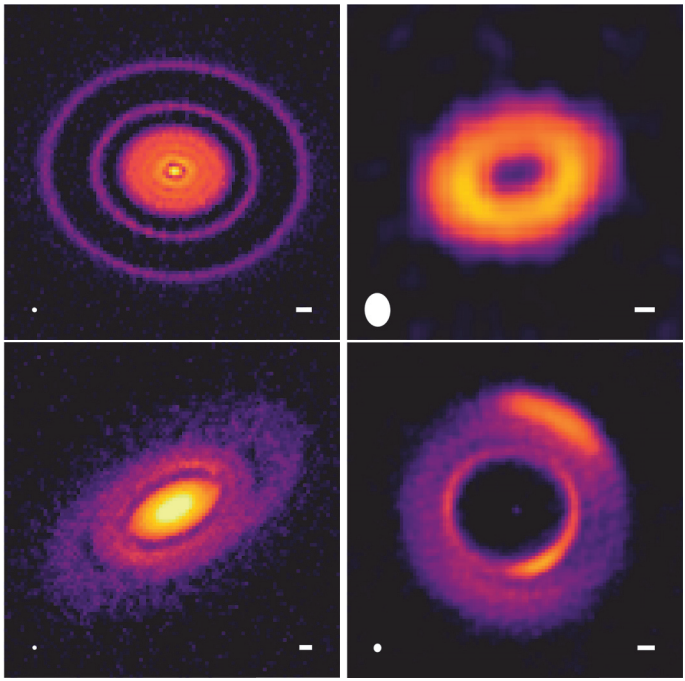

Figure 1.5: Images of disks with various substructure morphologies in mm continuum. The white ellipses in the lower left corners mark the resolution of the observations, and the white bars in the lower right corners are 10 au scalebars. *Top left:* AS 209, belonging to the category concentric rings and gaps (Andrews et al. 2018; Guzmán et al. 2018). *Top right:* CIDA 9, belonging to the category transition disks (Long et al., 2018). *Bottom left:* Elias 27, belonging to the category spirals (Andrews et al., 2018). *Bottom right:* MWC 758, belonging to the category non-axisymmetric disks (Dong et al., 2018). Note that MWC 758 also could be categorized as a transition disk following my definition (adapted from Andrews (2020) with permission).

- **Transition disks** are disks with inner cavities that are depleted of pebbles. Associated cavities are often, but not always, detected in scattered light (e.g. Villenave et al. 2019) and spectral line emission (e.g. van der Marel et al. 2016). The cavity is encircled by one or several rings with varying widths and intensities.

- **Spirals** refer to disks with large-scale spiral structures, the number and intensity of which varies significantly within the category. Spirals are mostly

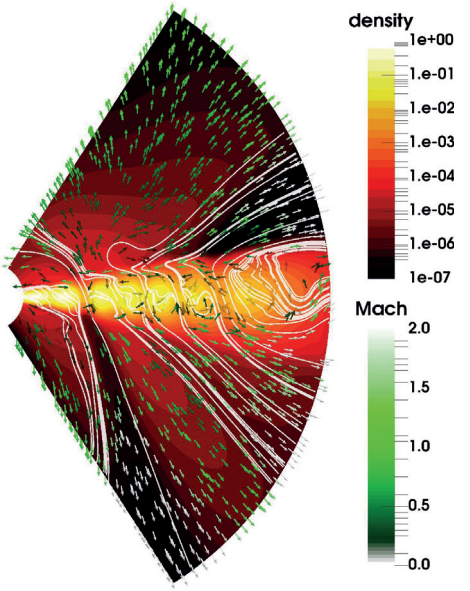

Figure 1.6: Plot showing the emergence of axisymmetric density rings due to self-organization of magnetic field lines (white lines) in a non-ideal MHD simulation. The radial domain stretches from $1 - 10\,\mathrm{au}$ and the green arrows indicate the velocity field. The density is measured in comparison to the initial midplane density (adapted from Béthune et al. 2017). Reproduced with permission © ESO.

detected in scattered light (e.g. Akiyama et al. 2016), but have also been observed in mm continuum (e.g. Huang et al. 2018) and spectral line emission (e.g. Teague et al. 2019) in a few rare cases.

- **Non-axisymmetric disks**, sometimes called arcs, are as the name suggests disks which exhibit non-axisymmetric substructures. These can manifest themselves as partial rings around a cavity (e.g. Casassus et al. 2013), or as additional substructures within rings and gaps (see Fig. 1.5).

Origins of substructures

There is a remarkable and continuously increasing number of proposed mechanisms to generate disk substructures in the literature. In fluid dynamics there is a huge variety of mechanisms that can generate perturbations in the gas pressure, which in turn acts to concentrate particles and halt or slow down their radial

drift (see Section 2.2 for a description of particle drift). A few common examples are: zonal flows arising due to MHD turbulence (Johansen et al., 2009) or self-organization of magnetic field lines (see Fig. 1.6, Béthune et al. 2017); vortices generated at the edge of dead zones (Lyra et al., 2009) or by various hydrodynamical instabilities (e.g. Klahr & Bodenheimer 2003; Richard et al. 2016; Schäfer et al. 2020); wind-driven instabilities (Riols & Lesur, 2019); global gravitational instability (GI) due to self-gravity (Toomre, 1964); and secular GI triggered by dust-gas friction (Takahashi & Inutsuka, 2014). These mechanisms are naturally occurring and produce substructures that can trap particles and promote planetesimal formation, thus creating favorable initial conditions for planet formation. The recent discovery that multiple rings have widths that are consistent with dust trapping inside pressure maxima, lends additional credibility to these kind of fluid dynamics mechanisms (although the pressure maxima might also be created by planet-disk interactions, Dullemond et al. 2018).

Another frequently suggested explanation for substructure formation is that they are related to processes occurring around condensation fronts, also called snowlines or icelines. When icy particles drift across icelines of abundant volatile species, a significant amount of solid ice is sublimated, resulting in a depletion of solids and an increase of gas interior to the icelines. This gas can be mixed back over the icelines and re-condense onto already existing particles, resulting in enhanced particle growth and solid densities (e.g. Stevenson & Lunine 1988; Ros et al. 2019). Furthermore, it has been shown that the fragmentation velocity of icy particles varies depending on the composition of the ice, and therefore changes across different icelines (Pinilla et al., 2017). As a result, particles grow to different sizes depending on which side of the icelines they are on, and since the drift velocity depends on the particle size, this results is traffic jams and increased solid densities. Icelines are naturally occurring and have been shown to be favorable locations for planetesimal formation (Drążkowska & Alibert, 2017). However, although some substructures appear to be consistent with the iceline scenario (Zhang et al., 2015), recent disk surveys show that it fails to explain the majority of ring locations (Huang et al. 2018; van der Marel et al. 2019).

The typically favored mechanism for creating disk substructures are planet-disk interactions, in which growing planets repel material from their orbits, resulting in the formation of gas gaps (Goldreich & Tremaine 1980; Papaloizou & Lin 1984). At the edge of these gas gaps a pressure maximum is formed, which traps drifting solids and results in ring formation (e.g. Zhu et al. 2012; Zhang et al. 2018; Eriksson et al. 2020). The width and depth of the gaps depend crucially on

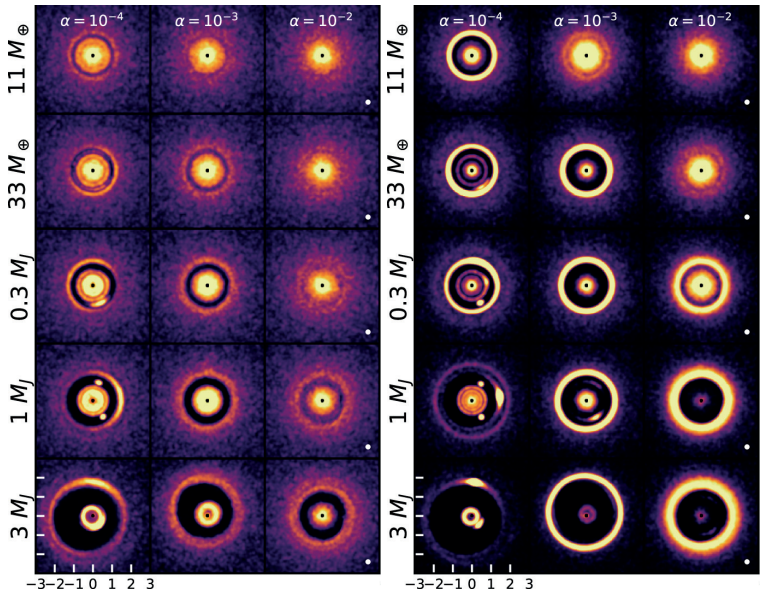

Figure 1.7: *Left*: Dust continuum emission maps based on 2D hydrodynamical simulations of a disk with one embedded planet of varying mass and three different values for the turbulent α. The maximum particle size is $100\,\mu$m, and the aspect ratio (H/r) is equal to 0.05. *Right*: Similar to the left maps but for a maximum particle size of $1\,$cm, and a different slope for the particle size distribution (adapted from Zhang et al. 2018). © AAS. Reproduced with permission.

the planetary masses, where giant planets are invoked to explain transition disks, and lower mass planets are invoked to explain ring and gap structures (see Fig. 1.7). In Eriksson et al. (2020), we simulated the evolution of a large disk containing multiple gap-opening planets and a large amount of solid particles, and found that disks with inner holes in the solid distribution is the typical outcome when the planets are larger than the pebble isolation mass ($M_{\rm iso}$, see Section 3.1 for a description). We further showed that the particle distribution depends heavily on the planetesimal formation efficiency at the gap edges, the size of the particles and the level of turbulence (see Fig. 1.8).

The direct imaging of a giant planet inside the PDS 70 disk cavity lends much credibility to the planet-disk hypothesis (Keppler et al., 2018). A recent study by van der Marel & Mulders (2021) further finds a link between the fraction of structured disks and exoplanet occurance rates. Additional clues have been obtained from observations of gas depletions within cavities (van der Marel et al.,

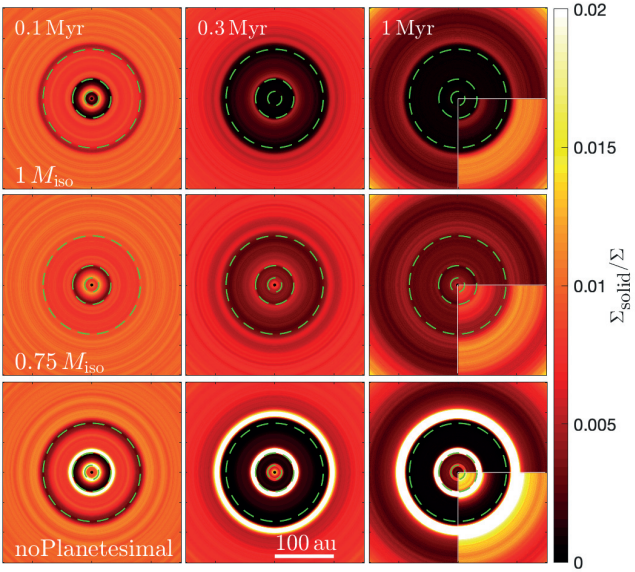

Figure 1.8: 2D symmetric disk images of the evolution of the solid-to-gas surface density ratio for a disk perturbed by three planets. The semimajor axes of the planets are marked with green dashed lines. The boxes in the bottom right corners at 1 Myr show the solid-to-gas densities in the same systems but where the maximum particle size has been limited to 100 μm (the particle size is $\sim$1 mm otherwise). When the planet mass is larger than 1 $M_{\rm iso}$ (*top*), the inner disk becomes depleted of particles. When the planet mass is lower than 1 $M_{\rm iso}$ (*middle*), there is no strong depletion but instead a series of density enhancements and depletions. When the planet mass is larger than 1 $M_{\rm iso}$ and planetesimal formation is ignored (*bottom*), the outcome is a series of bright rings and deep gaps. Decreasing the particle size results in longer drift timescales and higher solid-to-gas ratios. Data from Eriksson et al. (2020).

2015) and continuum gaps (Zhang et al., 2021), as well as kinematic detections of planets from gas dynamics (Casassus & Pérez, 2019; Pinte et al., 2019).

In conclusion, the origin of disk substructures in still under debate, and it might very well be that there are numerous mechanisms which are responsible. Typically, the planet-disk hypothesis and fluid dynamics mechanisms are viewed as more credible than the iceline scenario, and detections of planets within structured disks indicate that at least some disk substructures are caused by planet-disk interactions. Considering the implications of the planet-disk hypothesis and the

fluid dynamics mechanisms, one major difference is that the latter serves to produce favorable initial conditions for planet formation, while the former gives rise to the follow-up question: can large planets form early enough to explain the existence of structure in young disks?

1.3 Disk models

One of the most elemental components of any planet formation simulation is the underlying disk model, which describes how fundamental disk properties such as density and temperature vary with the radial distance from the star and the height above the midplane. Any such model builds upon one or several observables, one simple and well-known example being the Minimum Mass Solar Nebula (MMSN, Weidenschilling 1977). This disk model is constructed by: (1) For each Solar System planet, start with the known heavy element mass and add enough mass in hydrogen and helium to obtain Solar composition; and (2) split the Solar System into annuli such that there is one planet in each annulus, and uniformly distribute the planetary mass obtained in step (1) across the annulus. This results in a total *minimum* disk mass of $\sim 0.01\,\mathrm{M}_\odot$, and a surface density profile which can be approximated by

$$\Sigma = 1.7 \times 10^3 \left(\frac{r}{\mathrm{au}}\right)^{-3/2} \mathrm{g\,cm^{-2}}, \tag{1.2}$$

where r is the semimajor axis (Hayashi, 1981). One major issue with this disk model is that all planets are assumed to form in situ, while today it is generally accepted that planets migrate through the disk during their formation (Goldreich & Tremaine, 1980). Furthermore, the radial density slope in the MMSN differs from observational estimates based on mm continuum observations, which generally suggest a shallower profile in the inner disk and a much steeper profile in the outer disk (see Andrews 2020 and references therein).

One key property of disks which can be loosely constrained from observations is the rate at which material is falling onto the star, estimated from the accretion luminosity. The inferred accretion rates show a strong dependence with the stellar mass (Muzerolle et al., 2003) and age (Hartmann et al., 1998), and ranges from around $10^{-7} - 10^{-10}\,\mathrm{M}_\odot\mathrm{yr}^{-1}$ (Manara, 2014). In a commonly adopted model by Hartmann (2009), the disk accretion rate decreases from $10^{-7}\,\mathrm{M}_\odot\mathrm{yr}^{-1}$ to $10^{-8}\,\mathrm{M}_\odot\mathrm{yr}^{-1}$ over the course of 3 Myr.

Although it has been known for many decades that disks accrete onto their central star, the main mechanism which drives the accretion is still up for debate.

To fall onto the star, gas in the disk must lose angular momentum, and this could occur either via a transport of angular momentum radially outwards in the disk (viscous driven accretion), or via the direct removal of angular momentum vertically by a magnetized wind (wind-driven accretion). Although the former is by far the most common in the literature, partly because of its easy implementation, the lack of viable mechanisms to trigger sufficient angular momentum transport has resulted in disk winds now being viewed as the most plausible mechanism for driving disk accretion.

Viscous accretion disks

One generic feature of viscous disk evolution is that as $t \to \infty$, mass flows towards $r = 0$ and angular momentum is carried towards $r \to \infty$ by a negligible fraction of the mass. This results in the disk expanding radially outwards with time. The outwards transport of angular momentum is generally described as caused by a "viscosity"; however, the origin of this viscosity is still a matter of debate. In the original formalism, the transport of angular momentum is driven by molecular viscosity (Lynden-Bell & Pringle, 1974); however, the observed accretion rates are too large to be explainable by the small molecular viscosity of the gas. Instead, today this "viscosity" is assumed to be the outcome of some turbulent process.

In ideal magnetohydrodynamics (MHD), that is when the magnetic field is perfectly coupled to the gas, a weakly magnetized disk is unstable if the angular momentum decreases outwards, which is the case in protoplanetary disks. This is called the magnetorotational instability (MRI, Balbus & Hawley 1991), and it is a linear instability which has long been the favored driver of turbulence. The condition for ideal MHD is however only expected to be fulfilled in the inner thermally ionized region and outermost low-density region of the disk, meaning that in the major part of the disk non-ideal MHD effects have to be taken into account. These non-ideal effects have been shown to strongly affect and often suppress the MRI, resulting in little or no radial transport of angular momentum. Other possible drivers of turbulence that have been investigated are nonmagnetic entropy-driven instabilities (Klahr & Bodenheimer 2003; Dubrulle et al. 2005), and self-gravity in young massive disks.

The level of turbulence in disks has been loosely constrained from high-resolution ALMA observations. Estimates based on turbulent broadening of molecular emission lines suggest $\alpha < 10^{-4} - 10^{-3}$, which is a much lower value than what is expected from ideal MHD turbulence (Flaherty et al. 2017, 2018). Similar low estimates of turbulence are obtained from observations of the vertical dust thick-

ness in disk rings (Pinte et al., 2016). In general, most studies are consistent with a turbulent alpha of $\sim 10^{-4}$ (Lesur et al., 2022).

In the classical "α-prescription" by Shakura & Sunyaev (1973), the problem of the origin of the viscosity was circumvented by introducing a dimensionless parameter α, which describes the level of turbulence and takes on a value between 0 (no turbulence) and 1. The viscosity can then be written as

$$\nu = \alpha \Omega_K H^2, \tag{1.3}$$

where Ω_K is the Keplerian angular velocity, calculated as $\Omega_K = \sqrt{GM_*/r^3}$ where G is the gravitational constant and M_* is the stellar mass, and H is the scale height of the disk.

The evolution equation for the surface density of a thin viscous accretion disk was derived by Pringle (1981), and is written as

$$\frac{\partial \Sigma}{\partial t} = \frac{3}{r} \frac{\partial}{\partial r} \left[r^{1/2} \frac{\partial}{\partial r} \left(\nu \Sigma r^{1/2} \right) \right]. \tag{1.4}$$

If the viscosity is dependent on the surface density, this is a diffusive non-linear partial differential equation with no analytical solutions, except in the case when the viscosity can be written as a power-law in radius $\nu \propto r^{\gamma}$ (Lynden-Bell & Pringle, 1974). In this case, if the surface density profile at $t = 0$ corresponds to a steady-state solution with an exponential cut-off beyond $r = r_1$, the self-similar solution is

$$\Sigma(t) = \frac{\dot{M}(t)}{3\pi\nu_1 (r/r_1)^{\gamma}} \exp \left[-\frac{(r/r_1)^{(2-\gamma)}}{T_1} \right], \tag{1.5}$$

where

$$T_1 = \frac{t}{t_s} + 1, \tag{1.6}$$

and

$$t_s = \frac{1}{3(2-\gamma)^2} \frac{r_1^2}{\nu_1}. \tag{1.7}$$

The evolution of the disk accretion rate $\dot{M}(t)$ is then given by

$$\dot{M}(t) = \dot{M}(t=0) T_1^{-(\frac{5}{2}-\gamma)/(2-\gamma)}. \tag{1.8}$$

In Fig. 1.9, the evolution of the surface density and disk accretion rate for a thin viscous accretion disk with scale height $H = c_s/\Omega_K$, sound-speed $c_s =$

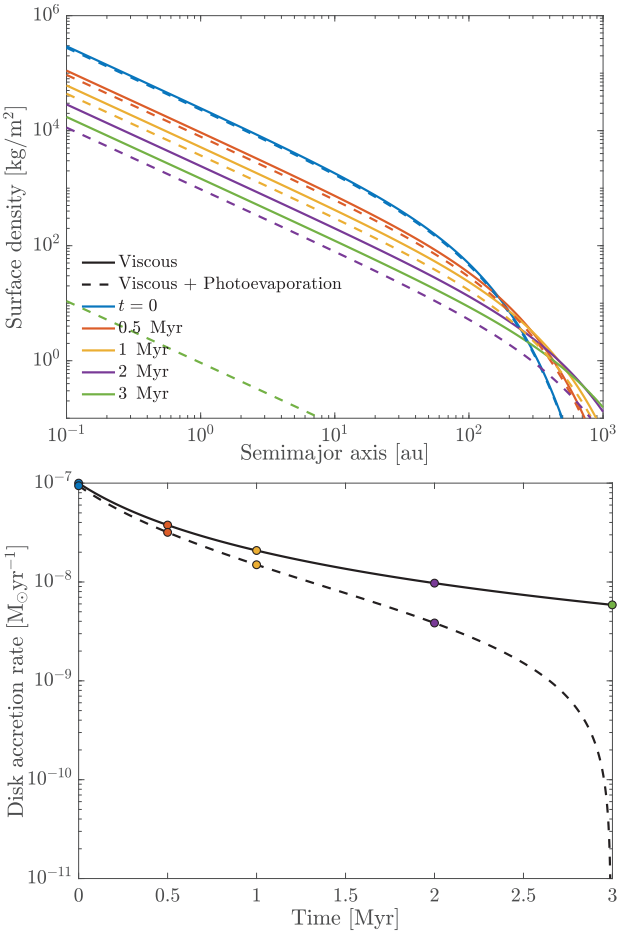

Figure 1.9: Plot showing the evolution of the surface density (*top*) and the disk accretion rate (*bottom*) for a thin viscous accretion disk. Solid lines show only the viscous evolution, and dashed lines show the evolution when a constant photoevaporation rate is included (a discussion on disk dispersal is found at the end of this chapter). The plot is for a disk with $r_1 = 75\,\mathrm{au}$, $\alpha = 10^{-2}$, $\dot{M}(t=0) = 10^{-7}\,\mathrm{M_\odot yr^{-1}}$ and $\dot{M}_{\mathrm{photo}} = 5.9 \times 10^{-9}\,\mathrm{M_\odot yr^{-1}}$.

$\sqrt{k_\mathrm{B}T/\mu m_\mathrm{H}}$ and temperature profile $T = 150\,\mathrm{K} \times (r/\mathrm{au})^{-3/7}$ are shown (Chiang & Goldreich, 1997). In the expression for the sound-speed k_B is the Bolzmann constant, m_H is the mass of the hydrogen atom and μ is the mean molecular weight, here taken to be 2.34 (Hayashi, 1981).

Wind-driven accretion

The presence of a vertical magnetic field which is threading the disk is key for wind-driven accretion models. Such fields are believed to be a natural outcome of the disk formation process, where during the collapse of a magnetized molecular cloud, a part of the magnetic field becomes trapped in the forming disk. There have been multiple attempts to deduce the strength and structure of the field from observations (e.g. Kataoka et al. 2015; Segura-Cox et al. 2015; Vlemmings et al. 2019; Teague et al. 2021); however, in general the properties and time evolution of the field remain poorly constrained.

The coupling of the field to the gas depends crucially on the ionization fraction of the gas, which is yet another highly unconstrained quantity. In most parts of the disk the gas is expected to be weakly ionized, implying that most of the disk is in the regime of non-ideal MHD. This introduces three non-ideal MHD effects to the MRI: Ohmic resistivity, the Hall effect, and ambipolar diffusion (see Lesur 2020 for a recent review on MHD in protoplanetary disks). When these effects are included, the radial transport of angular momentum is significantly reduced compared to the case of ideal MHD. Instead, angular momentum tends to be transported vertically away from the disk in MHD disk winds.

In these magnetically-driven outflows, gas is vertically accelerated along the field lines threading the disk, and by doing so increases its specific angular momentum. As a reaction, the field applies a torque on the disk that removes a corresponding amount of angular momentum, allowing for gas in the disk to flow towards the star. The resulting outflow does not only carry angular momentum away from the disk, but also carries away gas at a rate that can be comparable to the disk accretion rate. Global models of disks including non-ideal MHD effects find that disk accretion is mainly driven by magnetic outflows, and measure accretion rates comparable to observational estimates at radii of $\sim$10 au (Bai 2017; Béthune et al. 2017; Yang & Bai 2021). However, one major problem with these models is that the accretion rate onto the star can be significantly smaller (see discussion in Lesur 2021). Examples of global non-ideal MHD simulations are shown in Fig. 1.10.

Unlike viscous disk models that are very well studied and have been used by the disk community for decades, wind-driven disk models are still in the process of being developed, and there are many unknowns. The radius of the disk has traditionally been expected to shrink in wind-driven models, and expand in viscous disk models, but global non-ideal MHD simulations by (Yang & Bai, 2021) show that expansion can occur also in wind-driven models. Today, most of the

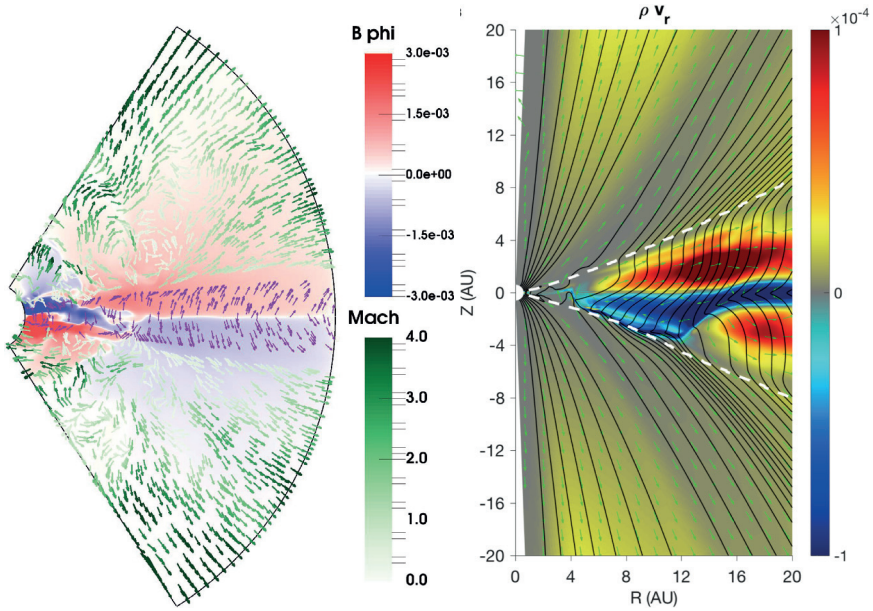

Figure 1.10: *Left*: Plot showing the orientation of the angular momentum flux (purple arrows), the poloidal velocity field (green arrows), and the toroidal magnetic field (color background) for a non-ideal MHD simulation. The direction of the angular momentum flux indicates that angular momentum is transported vertically away from the disk, rather than radially (adapted from Béthune et al. 2017). Reproduced with permission © ESO. *Right*: Plot showing the radial mass flux (color background), poloidal flux contours (black lines), and velocity vectors (green arrows) for another non-ideal MHD simulation. Mass transport occurs both radially in the midplane of the disk, and vertically away from the disk along with the wind (adapted from Bai (2017) with permission).

disk community still relies on viscous disk models, since they are well understood. However, as the research progresses, wind-driven models and models that include both viscous driven accretion and wind-driven accretion are likely to become more and more common.

Temperature profile

The disk temperature is set by a balance between heating and cooling processes. The main heating processes are the absorption of stellar radiation and viscous heating, where stellar radiation typically dominates except in the very innermost parts

of the disk. The primary cooling process is via thermal emission from dust grains, which is the cause of the IR dust continuum radiation seen in observations. Other minor heating/cooling processes are e.g. line cooling, photoelectric heating, dust thermal accommodation and cosmic ray heating.

The simplest yet still useful temperature profile is that of a passive disk, i.e. a disk whose temperature is set by only the stellar radiation. The temperature scaling of a thin, flat, passive disk that absorbs all incoming stellar radiation and re-emits it as a blackbody is $T \propto r^{-3/4}$ (see e.g. Armitage 2015). By further taking into account the flared geometry of the disk and the fact that small dust grains do not emit as a true blackbody, Chiang & Goldreich (1997) developed the commonly adopted analytical model for the midplane temperature of a passive disk,

$$T = 150\,\mathrm{K} \times (r/\mathrm{au})^{-3/7}. \tag{1.9}$$

It should be noted that the surface layer of the disk has a much higher temperature than the midplane, with one implication being that the location of icelines vary with the height above the midplane.

Vertical structure

The gas density (ρ) at some height z away from the midplane is obtained from the condition of hydrostatic equilibrium. In the case of a thin ($z << r$), vertically isothermal ($P = \rho c_s^2$, where P is the pressure), non-self-gravitating disk the equation of hydrostatic equilibrium has the solution

$$\rho(z) = \frac{\Sigma}{\sqrt{2\pi}H} \exp\left[\frac{-z^2}{2H^2}\right]. \tag{1.10}$$

The shape of the disk is described by the aspect ratio H/r. If the sound speed can be parametrized as $c_s \propto r^{-\xi}$, then the aspect ratio will depend on r as,

$$\frac{H}{r} \propto r^{-\xi+1/2}. \tag{1.11}$$

Using the temperature profile from Chiang & Goldreich (1997), this results in an aspect ratio which varies as $r^{2/7}$. Such a disk in which the aspect ratio increases with semimajor axis is called a flaring disk. Because of the flaring geometry, these disks capture a significant amount of stellar radiation at large radii where the disk is cool, thereby enhancing the emission in far-IR. This process explains the strong far-IR flux that is seen in the SED of most YSOs, and further shows that flaring disks are the norm (Kenyon & Hartmann, 1987).

Disk dispersal

Viscous disk evolution predicts a relatively slow decay of the gas disk towards late times, which should result in a population of stars with weak disks signatures. Such a disk population is not observed, which has been interpreted as a sign that some other process(es) exist(s) which lead(s) to a rapid dispersal of the disk. The most plausible mechanism for disk dispersal is photoevaporation, and there is observational evidence supporting this (see Alexander et al. 2014 and references therein), but other processes such as MHD winds could also contribute.

Photoevaporation occurs when high-energy radiation (UV and/or X-ray photons) heats the surface of the disk to high temperatures, resulting in the launching of a thermal wind from radii where the heated gas is unbound. This process typically shortens the protoplanetary disk lifetime by a significant amount compared to the pure viscous lifetime (see Fig. 1.9). Furthermore, the removal of gas from the disk has major implications for planet formation processes, such as increased planetesimal formation (Carrera et al., 2015), suppressed gas accretion and modified planetary migration. The detailed effects of photoevaporation on disk evolution have been studied in e.g. Picogna et al. (2019) and Kunitomo et al. (2021).

Chapter 2

From dust to planetesimals

Planet formation is a multistage process which spans several, distinct mechanisms, from the collisions of microscopic dust grains, to the final assembly of giant planets several hundred times more massive than the Earth. In this chapter, I review the first two steps of the planet formation process, that is the growth from $\sim\mu$m-sized dust particles to $\sim$mm-sized pebbles, and the subsequent formation of $\sim$100 km-sized planetesimals.

2.1 Dust coagulation

The solid component of the disk holds about 1% of the disk mass, initially in the form of $\sim\mu$m-sized dust and ice particles. Even though these particles are small and thus well-coupled to the gas motion, they do possess some velocity relative to the gas. This velocity difference is caused by a combination of Brownian motion, radial drift, vertical settling, and gas turbulence, and results in the particles moving with respect to each other. Consequently, particles embedded in the gas collide with each other, with different outcomes depending on the properties of the particles and the nature of the collision.

Results from laboratory experiments and theoretical models show that collisions between dust particles generally lead to either sticking, bouncing or fragmentation, with some variations within each category (Blum & Wurm 2008; Güttler et al. 2010). In the collision model of Güttler et al. (2010), they provide the collisional outcome given the mass of the colliding particles and the collision velocity. Furthermore, this model separates between porous and compact particles, as well as similar-sized and different-sized particles (the collision model for porous

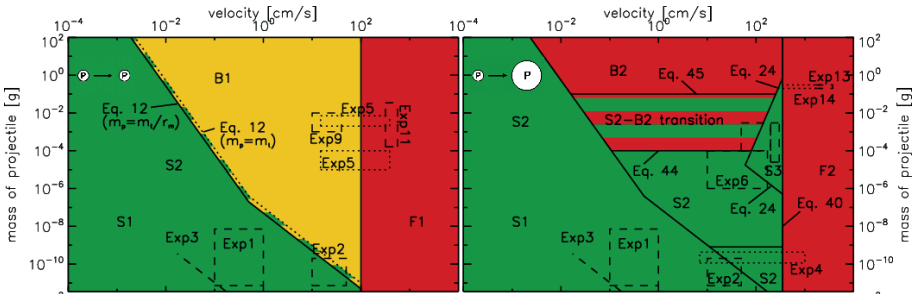

Figure 2.1: The collision model for porous particles from Güttler et al. (2010). Collisions within green regions lead to mass growth (sticking), collisions within yellow regions does not lead to a change in mass, and collisions within red regions lead to mass loss. The model is directly supported by experiments in the regions marked by dashed and dotted boxes (adapted from Güttler et al. 2010). Reproduced with permission © ESO.

particles is shown in Fig. 2.1). In Eriksson et al. (2020), we implemented this collision model into a global model of viscous disk evolution, and found that it typically results in growth up to ∼mm-sizes (see top panel of Fig. 2.2). We further showed that coagulation is faster and leads to larger particle sizes in the inner disk compared to the outer disk.

The collision experiments which the model from Güttler et al. (2010) is based on considers the interacting particles to be dust aggregates consisting of μm-sized silicate particles. If the dust aggregates were to consist of organic or icy material, as is likely the case in the outer disk regions, or oxides and sintered material, as is likely the case in the innermost disk regions, the collisional outcome might change significantly compared to the above model. There are multiple studies on the stickiness of ice-coated dust aggregates, and they typically find enhanced growth compared to the case with bare silica particles; however, this is likely only true within in a narrow temperature range (e.g. Gundlach & Blum 2015; Musiolik & Wurm 2019; Musiolik 2021). Another effect which has been shown to result in enhanced growth is dust charging during collisions (Steinpilz et al. 2020; Jungmann & Wurm 2021; Teiser et al. 2021).

2.2 Radial drift

Gas in the disk experiences a radial pressure support that partially acts against the gravitational pull of the star. Because of this, gas in the disk orbits at a sub-

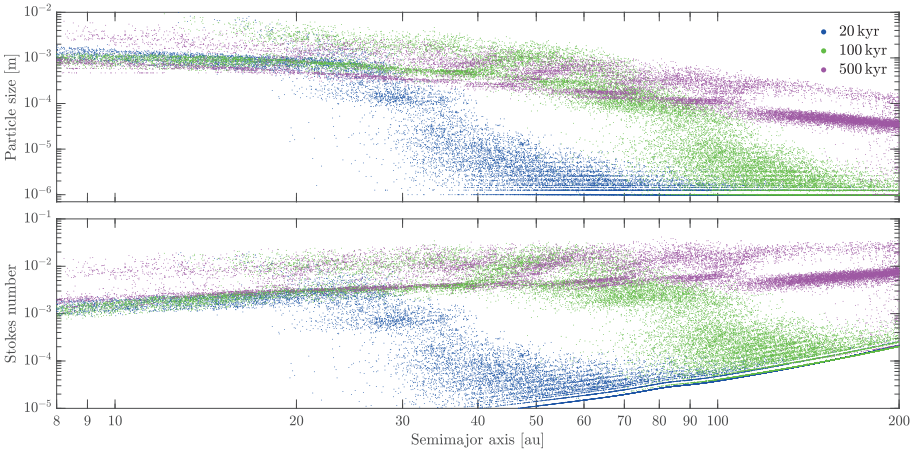

Figure 2.2: *Top*: Evolution of the particle size distribution when both coagulation and radial drift are included. The model contains 100,000 particles with an initial size of 1 μm, and the underlying disk model is that of an evolving viscous accretion disk. *Bottom*: Stokes number versus semimajor axis for the same data as in the top panel. Data from Run #2 ($0.50\,M_{\rm iso}$) of Eriksson et al. (2020).

Keplerian velocity,

$$v_\phi = v_K(1-\eta), \tag{2.1}$$

where $v_K = \sqrt{GM_*/r}$ is the Keplerian orbital velocity and η is the dimensionless pressure gradient parameter, defined as

$$\eta = -\frac{1}{2}\left(\frac{H}{r}\right)^2 \frac{\partial \ln P}{\partial \ln r} \tag{2.2}$$

(Weidenschilling, 1977; Nakagawa et al., 1986). Solid particles, which are not pressure-supported, orbit at the Keplerian velocity, and therefore experience a headwind as they move through the gas. The resulting drag force on the solid particles causes them to lose angular momentum and drift towards the star, which is known as radial drift (see Fig. 2.3 for a sketch of the described process).

The radial drift velocity can be expressed in terms of the Stokes number τ_s, and is given by

$$v_r = -\frac{2\eta v_K}{\tau_s + \tau_s^{-1}}. \tag{2.3}$$

The Stokes number is defined as

$$\tau_s = \frac{\rho_\bullet a}{\rho c_s}\Omega_K, \tag{2.4}$$

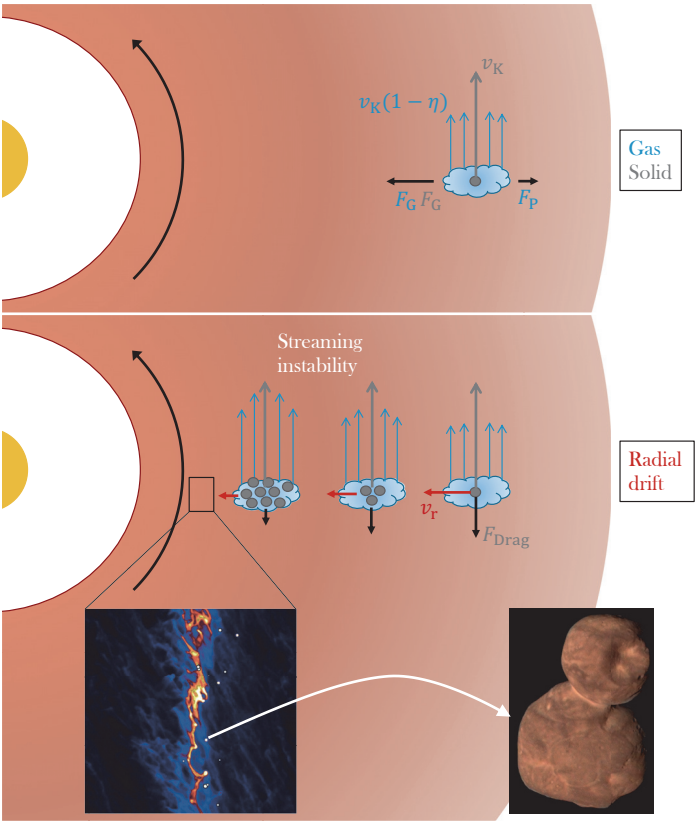

Figure 2.3: Sketch describing the processes of radial drift and the streaming instability (SI, introduced in Sect. 2.4). Gas in the disk is supported by both gravity and pressure and orbits at a sub-Keplerian velocity. Solid particles are not supported by pressure and orbit at the Keplerian velocity. Because solid particles orbit at a velocity faster than the gas, they feel a drag force, lose angular momentum and drift towards the star (radial drift). The particles also push on the gas, resulting in a locally enhanced gas velocity and thus less radial drift. Since larger collections of particles push more on the gas, isolated particles from beyond are able to catch up, resulting in even larger collections of particles, that push even more on the gas, etc... This is a runaway process which results in the formation of dense filaments (plot from simulation of the SI by Johansen et al. 2015, adapted with permission). Planetesimals form via the subsequent gravitational collapse of these particle filaments (image of Arrokoth, credit: NASA/Johns Hopkins University Applied Physics Laboratory/Southwest Research Institute/Roman Tkachenko).

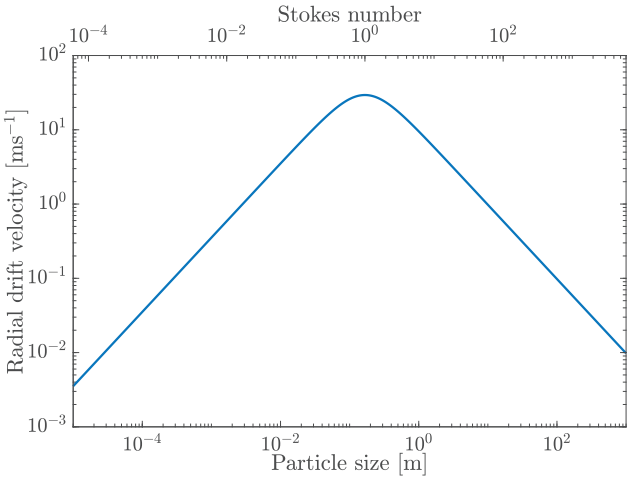

Figure 2.4: Radial drift velocity versus particle size calculated at 10 au in a 1 Myr old disk (calculated using the same disk model and disk parameters as in Fig. 1.9). The corresponding Stokes numbers are shown at the top of the plot. The maximum drift velocity is 30 ms^{-1} and is obtained for a 10 cm-sized particle.

and is a dimensionless measure of the time it takes for a particle of size a and density $\rho_\bullet$ to change its velocity as a result of gas drag. See Fig. 2.4 for a plot of the drift velocity versus particle size and Stokes number. Small particles with $\tau_s \ll 1$ are well-coupled to the gas and mostly move with it, resulting in small drift velocities. Particles with $\tau_s \gg 1$ are large enough not to be very affected by the gas drag and therefore also don't experience a lot of radial drift. Radial drift is most efficient for particles with $\tau_s \sim 1$, which typically corresponds to particles of $\sim$10 cm in size. Such particles obtain very high drift velocities (30 m s^{-1} in Fig. 2.4) and are quickly lost to the star, which is known as the radial drift barrier. In Fig. 2.2 the evolution of the particle size and Stokes number are shown for a model including both coagulation and radial drift (simulation from Eriksson et al. 2020). The quick decrease of the gas density with semimajor axis causes the particle Stokes numbers to increase outwards, even though the particle sizes show the opposite trend.

2.3 Observational constraints on particle sizes

The particle size distribution in disks is an important property to determine, as the size of the particles sets the coupling with the gas and therefore affects mechanisms such as radial drift and planetesimal formation. Primitive meteorites in the Solar System are mostly made up of ∼mm-sized chondrules, which formed during the first 3 Myr of disk evolution (Connelly et al. 2012; Bollard et al. 2017), suggesting that pebbles in the Solar System were roughly mm in size. Constraints on particle sizes can also be obtained from disk observations at mm wavelengths, most commonly from the slope of the SED.

Radiation emitted at mm wavelengths is dominated by dust thermal emission, and in the case where the optical depth is dominated by absorption (negligible scattering) and the disk is optically thin, there exists the following simple relation between the slope of the SED and the slope of the dust absorption coefficient in the Rayleight-Jeans regime:

$$I_\nu \propto \nu^{2+\beta} \Rightarrow 2 + \beta = \frac{\mathrm{d} \ln I_\nu}{\mathrm{d} \ln \nu}. \tag{2.5}$$

In the above expression I_ν is the intensity at frequency ν, and β is the slope of the dust absorption coefficient. The maximum particle size can then be estimated from the relationship between β and the particle size distribution, where lower values of β indicate larger particles (Miyake & Nakagawa 1993; Draine 2006).

Using the above method typically results in maximum particle sizes around mm-cm (e.g. Testi et al. 2014; Long et al. 2020). However, the assumptions of optically thin emission and absorption dominated opacity have recently been challenged, and Carrasco-González et al. (2019) show that they result in an overestimation of the maximum particle size. Recent estimates based on high-resolution multi-wavelength ALMA observations, which further take into account scattering effects, typically result in maximum particle sizes of ∼1 mm (Carrasco-González et al. 2019; Macías et al. 2021, see also Fig. 2.5). Similar size estimates were obtained from a survey of disks in Lupus at intermediate resolution (Tazzari et al. 2021a,b).

Maximum particle sizes can also be determined using polarization observations at mm wavelengths (Kataoka et al., 2015). Polarization observations with ALMA have found a scattering-induced polarization pattern at ∼1 mm in many disks, and since polarization induced by self-scattering is efficient when $\lambda \sim 2\pi a_{\mathrm{max}}$, this suggests a maximum particle size of ∼100 μm (e.g. Hull et al. 2018; Dent et al. 2019). In general, this method typically results in maximum particle sizes

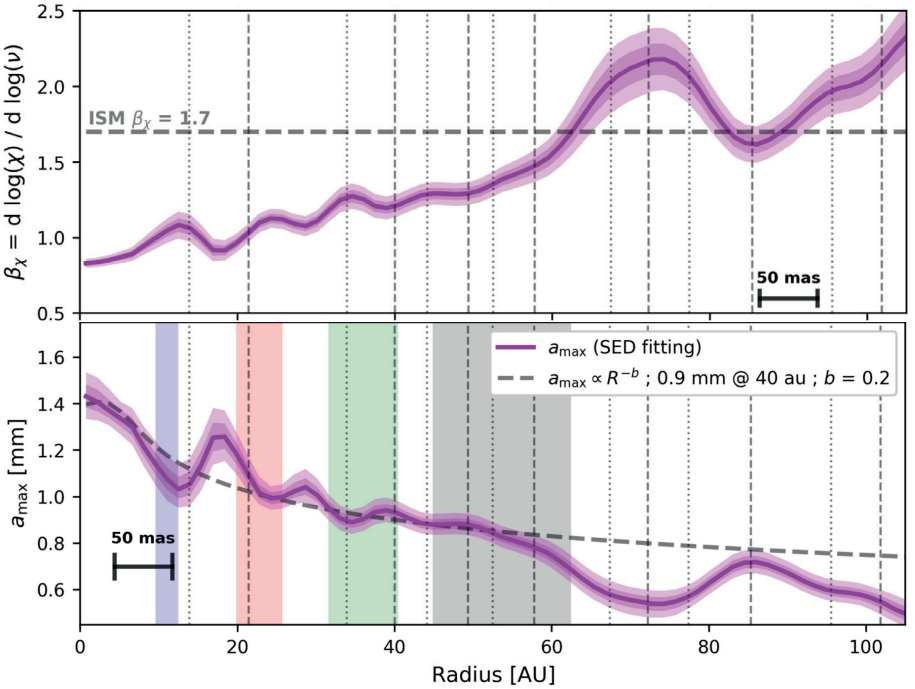

Figure 2.5: Radial profiles of (*top*) the slope of the dust extinction coefficient χ (absorption+scattering) and (*bottom*) the maximum particle size, obtained from radial SED fitting of HL Tau. The horizontal dashed line in the top plot shows the value of β in the interstellar medium. The maximum particle size is estimated to around 1 mm, and decreases outwards (adapted from Carrasco-González et al. 2019). © AAS. Reproduced with permission.

which are ten times smaller than what is obtained from SED fitting and what is expected from coagulation models. Recent studies by Kirchschlager & Bertrang (2020) and Ueda et al. (2021) suggest that this tension could be alleviated if the particles are non-spherical and/or there is significant sedimentation, in which case the polarization observations could be explained by mm particles.

2.4 Planetesimal formation

The direct growth from pebbles to planetesimals via coagulation is hindered by radial drift and bouncing and/or fragmentation. Instead, planetesimals form via the gravitational collapse of particle clumps. There are numerous mechanisms to

concentrate particles in the disk, one being via particle trapping in local pressure maxima. In the equations for radial drift it can be seen that if the radial pressure gradient turns to zero, there is no radial drift. If there is a local pressure maximum somewhere in the disk, then pebbles drifting into this maximum will become trapped, resulting in a locally enhanced particle density. If this pressure maximum is long-lived, then enough particles can become trapped to trigger gravitational collapse into planetesimals (e.g. Carrera et al. 2021). This occurs when the particle density reaches the so called Roche density, which can be defined as

$$\rho_{\mathrm{R}} = \frac{9\Omega_K^2}{4\pi G}. \tag{2.6}$$

Another mechanism for concentrating particles and driving clump formation is the streaming instability (SI, Youdin & Goodman 2005; Johansen & Youdin 2007). The mutual drag between particles and gas in the disk does not only result in radial drift, but the particles also exert a back-reaction on the gas. Given a local particle overdensity, the particles push on the surrounding gas and increase its velocity, resulting in a smaller velocity difference, that leads to a smaller drag force and less radial drift. Inwards-drifting particles from further out in the disk are able to catch up to this particle overdensity, resulting in even larger particle concentrations, that push even more on the gas, (etc.) (see sketch in Fig. 2.3). Once triggered this is a runaway process which leads to the formation of dense filaments, which subsequently gravitationally collapse to form planetesimals.

The SI has been shown to drive clump formation for a broad range of parameters, the most important parameters being the local solid-to-gas ratio (also called the metallicity), the Stokes number of the particles, and the radial gas pressure gradient. Yang et al. (2017) performed high-resolution simulations of particle-gas interactions to map out for which combinations of metallicities and Stokes numbers the SI drives clump formation. They found that the smallest critical metallicity is obtained for a Stokes number of $\sim 10^{-1}$, and is above the 1% solar metallicity. In other words, there still needs to be some concentration mechanism active that produces the initial over-density required to trigger the SI, for example particle trapping in pressure bumps. However, recent simulation by Li & Youdin (2021) find an even wider parameter space, with critical metallicities as low as 0.4% (see Fig. 2.6). It should be noted that these results are obtained in the absence of external turbulence, which if present would act to stir up the particles and lead to higher critical metallicities. Furthermore, the above studies are performed using a singular size particle distribution, whereas in real disks a range of particle sizes are expected to be present. Exactly how the criterion for clump formation is affected

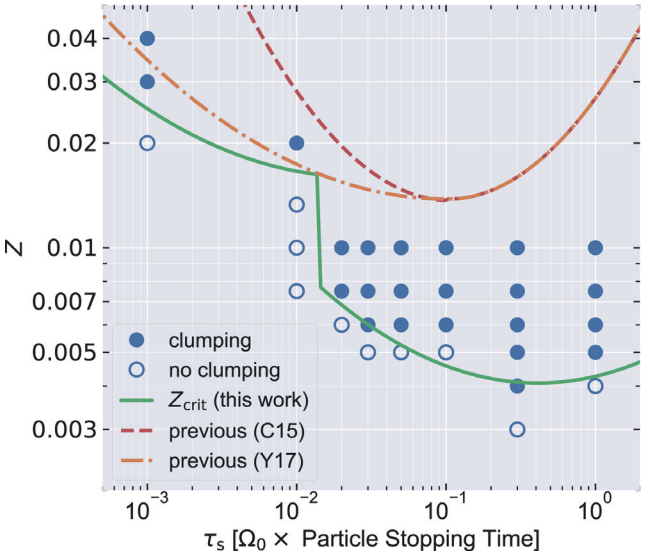

Figure 2.6: Critical curves for particle clumping by the SI for a wide range of Stokes number and metallicities, Z. The green line shows the critical curve obtained by Li & Youdin (2021), which is lower than the curves obtained by Carrera et al. (2015) and Yang et al. (2017) (adapted from Li & Youdin 2021). © AAS. Reproduced with permission.

by the inclusion of multiple particle sizes is still under debate, and studies of the process show conflicting results (e.g. Krapp et al. 2019; Schaffer et al. 2021; Yang & Zhu 2021; Zhu & Yang 2021).

The triggering of the SI further depends strongly on the radial gas pressure gradient, such that the critical metallicity increases with an increasing pressure gradient (Bai & Stone 2010; Auffinger & Laibe 2018; Abod et al. 2019). This makes local pressure bumps, in which the pressure gradient is small, even more favorable locations for planetesimal formation via the SI. This has been confirmed in simulations by Carrera et al. (2021), where they find efficient planetesimal formation via the SI even in the case of small pressure bumps. This result was however obtained for cm-sized particles, and in the case of mm-sized particles they did not find any clumping. In Eriksson et al. (2020), we studied the efficiency of planetesimal formation in the pressure bumps formed at planetary gap edges, and found that this is a very efficient process which is capable of converting a large fraction of the pebble flux into planetesimals. Fig. 2.7 shows how the amount of planetesimal formation at the gap edges varies when the dependence of the critical metallicity

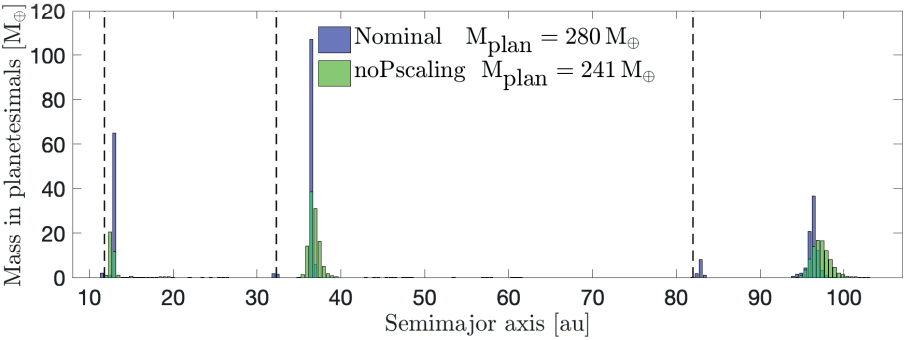

Figure 2.7: Histogram showing the total amount of mass in planetesimals that has formed at different locations in the disk after 1 Myr, for the nominal simulation and the simulation with no pressure scaling from Eriksson et al. (2020). The dashed lines mark the location of the planets semimajor axes. When pressure scaling is included, there is very efficient planetesimal formation at the center of the pressure maxima. When pressure scaling is turned off, planetesimal formation occurs in a wider region around the pressure maxima, and there is slightly less planetesimals forming.

on the pressure gradient is turned on and off. Note that when the pressure gradient is exactly zero, the SI is formally absent. However, other mechanisms, such as the secular gravitational instability, are still present and result in efficient planetesimal formation in this case (see discussion in Eriksson et al. 2020).

High-resolution simulations of the SI have shown that the initial mass distribution of planetesimals formed via the SI is top-heavy (Schäfer et al. 2017; Simon et al. 2017; Li et al. 2019). The mass frequency distribution is however decreasing with the planetesimal size, meaning that even though most mass is contained in the largest planetesimals, they are relatively rare. Simon et al. (2017) find that the initial mass distribution of planetesimals can be fit by a simple power law,

$$\frac{dN}{dM_\mathrm{p}} \propto M_\mathrm{p}^{-p}, \tag{2.7}$$

where M_p is the planetesimal mass and $p = 1.6 \pm 0.1$. Their results indicate that the slope of the initial mass distribution is near-universal, a result which was also obtained in e.g. Schäfer et al. (2017) and Abod et al. (2019). However, recent simulations by Li et al. (2019) performed with higher resolution than the previous studies, find that even though the mass distribution for different setups is always top-heavy and with similar overall shapes, it is not universal. They also

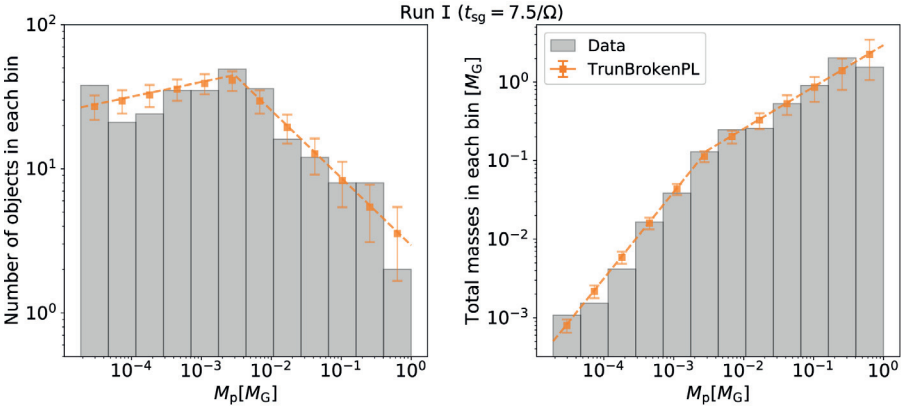

Figure 2.8: *Left*: Number of clumps formed per mass interval (logarithmic) in a high-resolution simulation of the SI. *Right*: Total mass of clumps formed in each mass interval. The mass distribution is top-heavy and features a turn-over towards lower masses (adapted from Li et al. 2019). © AAS. Reproduced with permission.

find the first evidence for a turnover in the mass frequency distribution towards small planetesimals (see Fig. 2.8). Comparison with Solar System observations show that there is a good match between the initial mass distribution of planetesimals formed via the SI, and the initial mass distribution of the cold Kuiper belt (Kavelaars et al., 2021) and the asteroid belt (Johansen et al., 2015).

Modern SI simulations have high enough resolution to identify individual clumps; however, they can not follow the subsequent gravitational collapse into planetesimals. By studying the properties of the formed clumps, Nesvorný et al. (2019) and Nesvorný et al. (2021) found that they possess excess angular momentum, suggesting that the collapse is likely to result in binary planetesimals. These binaries typically have equal-size components and mostly prograde orbits. Since the components are formed from the same clump they also have identical compositions, and thus the same colors in observations. These features of the planetesimal population formed via the SI match the observed properties of trans-Neptunian objects, a large fraction of which are binary, lending much credibility to the SI (e.g. Noll et al. 2008; Grundy et al. 2019; Marsset et al. 2020).

2.5 The effects of gas drag

Planetesimals moving through the disk at a velocity different from the gas velocity experience gas drag, which does not only affect the planetesimals dynamically, but also physically via ablation and erosion. The acceleration $\boldsymbol{a}$ of a planetesimal due to gas drag is calculated as,

$$\boldsymbol{a}_{\text{drag}} = -\frac{1}{t_s}(\boldsymbol{v}_{\text{pl}} - \boldsymbol{v}_{\text{gas}}), \tag{2.8}$$

where $\boldsymbol{v}$ is the velocity vector and t_s is the stopping time (Whipple, 1972). The stopping time is positively correlated with the planetesimal size and the solid density, and negatively correlated with the gas density and the velocity difference between the gas and the planetesimal (e.g. Perets & Murray-Clay 2011). The gas drag onto planetesimals does not lead to radial drift as in the case of pebbles (see Fig. 2.4), but acts mostly as a damper of eccentricity and inclination. Since the stopping time is positively correlated with the planetesimal size, small planetesimals have their orbits damped faster than large planetesimals. In the inner disk where the gas density is high, small planetesimals quickly have their orbits circularized by gas drag.

Ablation occurs when the planetesimal surface becomes heated enough to cause vaporization of the volatile ices, resulting in mass loss (see sketch in Fig. 2.9). The heating of the surface occurs via irradiation from the surrounding gas and frictional heating due to gas drag. The mass ablation rate is highly dependent on the surface temperature and the composition of the planetesimals. The surface temperature of the planetesimals is set by a balance between heating from irradiation and frictional heating, and cooling due to the release of latent heat of vaporization (Ronnet & Johansen, 2020). In other words, the cooling is caused by the energy loss associated with the transition from solid to gas phase. The ablation process is typically efficient for excited planetesimals in the inner regions of the disk (the extent of which is heavily dependent on the gas density and the planetesimal composition), and can often be neglected for planetesimals with large semimajor axes. We confirmed this in Eriksson et al. (2021), when we simulated the dynamical evolution of planetesimals formed at planetary gap edges, taking mass ablation into account. We demonstrated that a large fraction of the planetesimal mass can be ablated in young disks, and that this ablation can result in transport of solids across planetary gaps. Fig. 2.9 shows the ablation rate as a function of semimajor axis for different volatile ices and planetesimal surface temperatures, calculated for a relatively young disk.

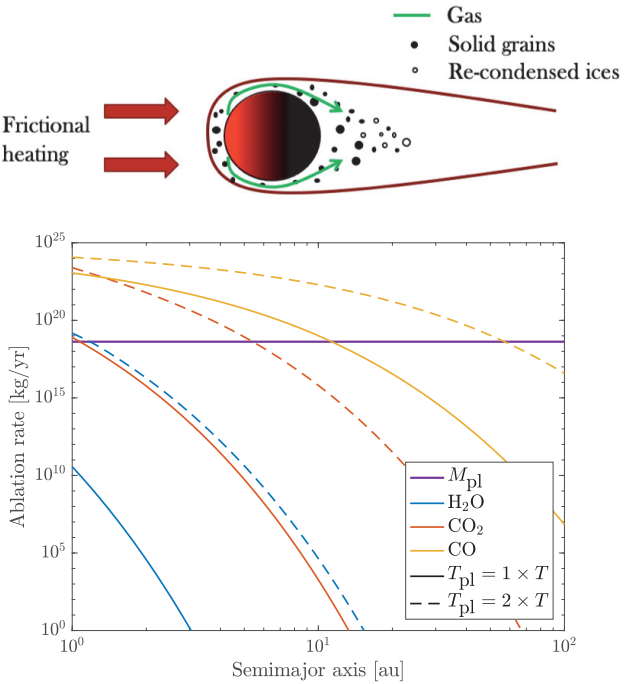

Figure 2.9: A sketch of the ablation process is shown at the *top*. When the ices on the planetesimal surface transition to the gas phase, solid grains embedded within the ice can be released as well. Depending on the temperature of the surrounding disk and the composition of the released gas, some of this gas will eventually re-condense to form solid ice. *Bottom*: Ablation rate versus semimajor axis for three abundant volatile ices, calculated for a surface temperature which is either equal to the disk temperature (solid line) or twice as large (dashed line). The purple line marks the typical mass of a $\sim$100 km-sized planetesimal; above this line such a planetesimal is ablated within one year (adapted from Eriksson et al. 2021). Reproduced with permission © ESO.

Planetesimals can further lose mass via aerodynamical erosion (e.g. Demirci et al. 2019; Schaffer et al. 2020). Whether or not erosion occurs depends on the strength of the gas flow, and the physical properties of the planetesimals. Schaffer et al. (2020) find that erosion is fast and significant for planetesimals on eccentric orbits in the inner $\sim$1 au of the disk. Planetesimals residing further out in the disk are mostly safe from erosion. To the best of my knowledge, there exist no studies that compare the timescale for erosion versus the timescale for ablation in

protoplanetary disks. Both processes should be efficient under similar conditions, although ablation can occur further out in the disk depending on the planetesimal composition.

Chapter 3

Formation of giant planets

The largest planetesimals formed via the SI are roughly 100 km in size. The continued growth up to protoplanets ($\sim$1000 km in size) mainly occurs by accretion of other planetesimals. In the classical core accretion model for the formation of giant planets, growth by planetesimal accretion continues also after this and eventually leads to the formation of planetary cores ($\sim 10\,M_\oplus$, Pollack et al. 1996). However, the timescale for core formation via this mechanism has been proven to be much too long (e.g. Goldreich et al. 2004). This issue can be solved by taking into account the accretion of mm-cm sized pebbles, which have been detected in large amounts in protoplanetary disks (e.g. Testi et al. 2003; Tazzari et al. 2016).

Owning to the dissipation of energy by gas drag as pebbles move past the protoplanet, pebbles are accreted onto the protoplanet much more efficiently than planetesimals (Johansen & Lacerda 2010; Ormel & Klahr 2010). The resulting mass growth rates for pebble accretion are orders of magnitudes higher than planetesimal accretion rates (Lambrechts & Johansen, 2012), making pebble accretion the dominant growth mechanism once a protoplanet has formed (Johansen & Lambrechts, 2017). This growth continues until the so-called pebble isolation mass has been reached ($M_{\rm iso}$, $\sim 10\,M_\oplus$), or it can end earlier if the supply of pebbles is shut off. The pebble isolation mass is reached when the planet opens up a deep enough gap to create a zero pressure gradient at the outer gap edge, thus halting the drift of pebbles (Lambrechts et al., 2014). This marks the end of core formation.

3.1 Planetary gaps

Forming planets excite density waves (spirals) due to gravitational interactions with the surrounding disk that carry angular momentum away from the planet and deposit it on the disk through their damping. The resulting torque exerted on the disk causes gas to be repelled from the planetary orbit, and leads to the opening of a gap (Lin & Papaloizou 1979; Goldreich & Tremaine 1980). Gap-opening is often modeled by applying a torque on the disk; for example, we used the torque density distribution (Λ) derived by D'Angelo & Lubow (2010) to account for planetary gaps in Eriksson et al. (2020). In the common case of a thin viscous accretion disk, the resulting perturbation to the gas surface density profile is taken into account by simply adding a second term to the viscous evolution equation,

$$\frac{\partial \Sigma}{\partial t} = \frac{1}{r}\frac{\partial}{\partial r}\left[3r^{1/2}\frac{\partial}{\partial r}\left(\nu\Sigma r^{1/2}\right) - \frac{2\Lambda\Sigma r^{3/2}}{(GM_*)^{1/2}}\right] \tag{3.1}$$

(Lin & Papaloizou, 1986). In Fig. 3.1, I show the normalized surface density evolution for a disk with three planets, modeled using the above expression (data from the nominal simulation of Eriksson et al. 2020).

In Eriksson et al. (2021) and Eriksson et al. (2022) we choose to use a much simpler approach, where the planetary gaps were modeled using a Gaussian profile. There exist numerous analytic and empirical expressions for the depths and widths of planetary gaps. Kanagawa et al. (2015b) derived the following analytic relation between the gap depth, the planetary mass (M_p), the disk aspect ratio and the disk viscosity:

$$\frac{\Sigma_{\text{min}}}{\Sigma_0} = \frac{1}{1 + 0.04\,K}, \tag{3.2}$$

where

$$K = \left(\frac{M_p}{M_*}\right)^2 \left(\frac{H}{r}\right)^{-5} \alpha^{-1}. \tag{3.3}$$

In Johansen et al. (2019) the gap depth is instead given as a function of the planetary mass and the pebble isolation mass,

$$\frac{\Sigma_{\text{min}}}{\Sigma_0} = \frac{1}{1 + \left(\frac{M_p}{2.3M_{\text{iso}}}\right)^2}. \tag{3.4}$$

It should be noted that these are simple 1D expressions, and it has been demonstrated that gaps in 1D simulations are deeper and narrower than their higher dimensional analogs (Johansen et al. 2019; Eriksson et al. 2020). Empirical formulas

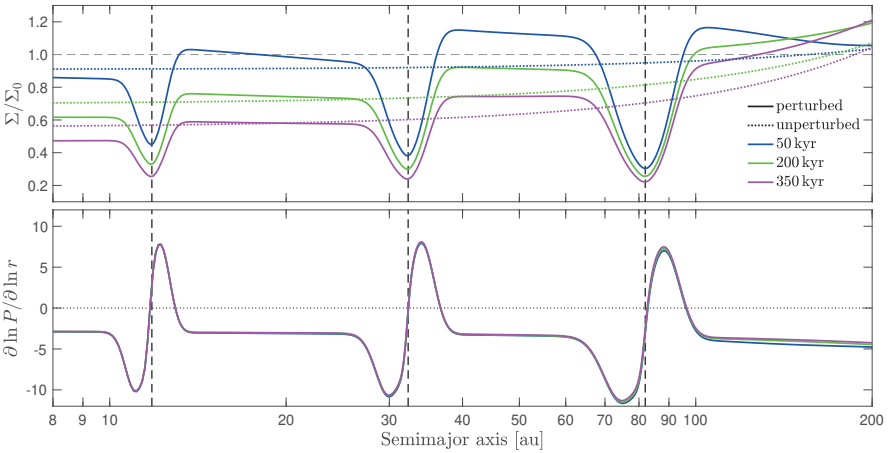

Figure 3.1: *Top*: Evolution of the normalized gas surface density profile for an unperturbed viscous accretion disk (dotted lines), and a viscous accretion disk perturbed by three planets with masses larger than the pebble isolation mass (solid lines). The semimajor axes of the planets are marked with dashed lines. *Bottom*: Evolution of the radial pressure gradient. The radial drift of particles is halted where the pressure gradient is equal to zero. Data from the nominal simulation of Eriksson et al. (2020).

for the shape of planetary gaps, constructed from 2D hydrodynamic simulations, are provided by for example Kanagawa et al. (2017) and Duffell (2020). In Kanagawa et al. (2017), they further give a relationship between the depth and width of planetary gaps, that can be used to determine whether or not a gap is formed by a planet.

In theory, the above 1D expressions can be used to directly constrain the masses of the hidden planets in ringed disks, provided the gas surface density profiles, disk aspect ratios and level of viscosity are well known (see e.g. Kanagawa et al. 2015a). However, most high-resolution observations of ringed disks trace the distribution of solid particles, which does not necessarily follow that of the gas. Zhang et al. (2018) used 2D hydrodynamical simulations including both gas and dust, to derive a relationship between the planetary mass and the shape of the gap in millimeter continuum (simulated dust continuum emission maps from this study are shown in Fig. 1.7). They use this relationship to derive masses for the potential planets in the DSHARP disks, and found a population of wide-orbit giant planets (see Fig. 3.2). In Zhang et al. (2022), the results of these 2D simulations were further used to develop a neural network for predicting planet masses from

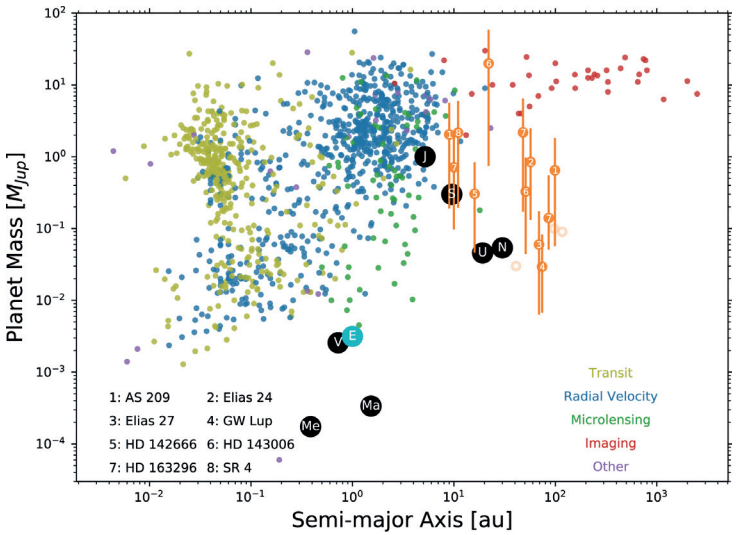

Figure 3.2: Plot of planet mass versus semimajor axis. The plot contains the confirmed exoplanet population as of August 2018 (small colored dots), the Solar System planets (large dots with white text), as well as the inferred potential planet population in the DSHARP disks (orange dots with white numbering). The potential planets in the DSHARP disks have wide orbits and large masses, and represent a population of planets which are not easily observed with traditional exoplanet detection techniques (adapted from Zhang et al. 2018). © AAS. Reproduced with permission.

continuum images. In the future, such networks could be used to infer masses of potential planets from large surveys of disks.

In isothermal disks the radial pressure gradient is given by

$$\frac{\partial \ln P}{\partial \ln r} = \frac{\partial \ln(\Sigma T/H)}{\partial \ln r}, \tag{3.5}$$

and thus a local perturbation to the surface density also results in a local perturbation to the pressure gradient. In the bottom panel of Fig. 3.1, I show how the radial pressure gradient varies as a function of semimajor axis in a disk with three planets. The pebble isolation mass is defined as the planetary mass required to turn the pressure gradient to zero, thus creating a pressure maximum at the outer gap edge. Bitsch et al. (2018) used 3D hydrodynamical simulations to derive the following analytic fitting formula for the pebble isolation mass,

$$M_{\rm iso} = 25\,{\rm M}_\oplus \times f_{\rm fit}, \tag{3.6}$$

and

$$f_{\text{fit}} = \left[\frac{H/r}{0.05}\right]^3 \left[0.34\left(\frac{\log \alpha_3}{\log \alpha}\right)^4 + 0.66\right]\left[1 - \frac{\partial \ln P/\partial \ln r + 2.5}{6}\right] \quad (3.7)$$

where $\alpha_3 = 10^{-3}$.

3.2 Planetary migration

The angular momentum exchange between the planet and the disk due to gravitational interactions does not only result in gap opening, but also leads to orbital migration. For low planetary masses, the angular momentum exchange with the disk due to gravitational interactions is small compared to the viscous transport of angular momentum, resulting in a relatively unperturbed surface density profile. The net torque on the planet in this case is typically calculated by summing up contributions from the inner and outer Lindblad torques, and the corotation torque. This is called Type I migration (Ward, 1997). The Type-I migration rate can be described by the scaling law

$$\dot{r} = -k_{\text{mig}} \frac{M_p}{M_*} \frac{\Sigma r^2}{M_*} \left(\frac{H}{r}\right)^{-2} v_K, \quad (3.8)$$

where the prefactor k_{mig} is a function of the radial gradients of surface density and temperature (a fit to k_{mig} is provided by for example D'Angelo & Lubow 2010). Type I migration is typically directed inwards and results in fast orbital decay. It should be mentioned that other torques can exist as well, with potential effects such as halting or reversing the direction of the migration (see Raymond & Morbidelli 2022 for an overview).

For large planetary masses, the angular momentum exchange with the disk due to gravitational interactions is strong enough to result in gap opening. According to classical migration theory, when this occurs the orbital evolution of the planet becomes coupled to the viscous evolution of the disk, known as Type II migration. However, this is only true if gas is prevented from flowing across the gap, and simulations have shown that this is not the case (Duffell et al. 2014; Dürmann & Kley 2015). Results from more recent 2D simulations by Kanagawa et al. (2018), rather showed that the torque on the planet is well described by the classical Type I torque, multiplied by the relative height of the gap. In this migration model, which we used in Eriksson et al. (2022), the migration rate quickly decreases once the planet grows massive enough to open a deep gap.

The orbital migration of planets is still a hot debate, and there exist more prescriptions than those mentioned above. Furthermore, the described migration prescriptions are valid in the case of viscous driven accretion. As was shown by Kimmig et al. (2020), migration in the case of wind driven accretion can differ strongly compared to the classical migration models.

3.3 Gas accretion

During the core growth phase, the protoplanet begins to attract a gaseous envelope. The heat which is generated as pebbles rain down through the proto-atmosphere prevents the envelope from contracting onto the core. As the pebble isolation mass is reached and the accretion of pebbles is halted, this heating source disappears and the envelope can begin to contract. This is the beginning of gas accretion; however, some small amounts of highly polluted gas can become bound to the protoplanet already during the core growth phase (Bitsch et al. 2015; Valletta & Helled 2020).

The rate of gas accretion onto a protoplanet is highly uncertain, and there exists a plethora of different prescriptions (see discussion in Johansen et al. 2019). The first phase of gas accretion is typically called the contraction phase, or the attached phase. During this phase, which can potentially last very long, the proto-atmosphere grows gradually through cooling by Kelvin-Helmholtz contraction. Prescriptions for the gas accretion rate during this phase are provided by for example Ikoma et al. (2000) and Bitsch et al. (2015), and heavily depend on the mass of the protoplanet and the opacity of the envelope. A lower opacity allows for faster radiative cooling, resulting in a more rapid contraction (Piso & Youdin, 2014). Furthermore, if there is ongoing planetesimal accretion, this has the potential for slowing down or speeding up the contraction rate (see discussion in Eriksson et al. 2022).

As the contraction continues, the proto-atmosphere eventually reaches the crossover mass, which is when the mass of the atmosphere equals that of the core. Around this point gravity begins to dominate the growth, and gas accretion enters a new phase called the runaway phase or the detached phase. When this occurs, the gas accretion rate accelerates and becomes limited by the rate at which gas can enter the Hill sphere (prescriptions are provided by e.g. Tanigawa & Tanaka 2016). Additionally, D'Angelo et al. (2006) found that planets cannot accrete at a rate which is higher than $\sim$80% of the disk accretion rate $\dot{M}$. This is because some gas will always be able to cross the planetary gaps, even in the case of massive planets. In Fig. 3.3 I show growth-tracks for Jupiter and Saturn, generated using the

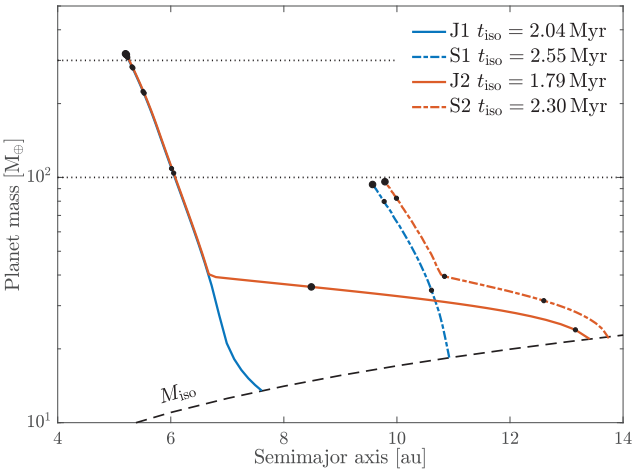

Figure 3.3: Growth tracks for Jupiter (J) and Saturn (S), starting from the moment the protoplanet reaches the pebble isolation mass. Migration is performed using Eq. 3.8 and multiplying with the relative gap height. Gas accretion during the contraction phase is modeled using the prescription by Ikoma et al. (2000) in scheme 1, and the prescription by Bitsch et al. (2015) in scheme 2. Gas accretion during runaway is modeled using the prescription by Tanigawa & Tanaka (2016). Small dots are separated by 0.2 Myr, and large dots indicate a time of 2 and 3 Myr (adapted from Eriksson et al. 2022). Reproduced with permission © ESO.

migration prescription by Kanagawa et al. (2018), and two different prescriptions for gas accretion. Long contraction timescales typically result in long migration distances, such that the protoplanet needs to form far out in the disk, while short contraction timescales result in short migration distances.

Enrichment of heavy elements

In order to get insight into giant planet interiors, such as density distributions and heavy element masses, structure models are used and fitted to observational data. Jupiter structure models that fit data from the Juno spacecraft suggest that the planet has a fuzzy core, potentially extending out to a few tens of percent of Jupiter's radius, and a total heavy element mass of $\sim 20 - 60\ M_\oplus$ (see Helled et al. 2022 and references therein). Recent structure models for Saturn that fit data from the Cassini spacecraft typically infer a total heavy element mass of $\sim 15 - 20\ M_\oplus$ (Militzer et al. 2019; Ni 2020). In the case of exogiants, the inferred heavy

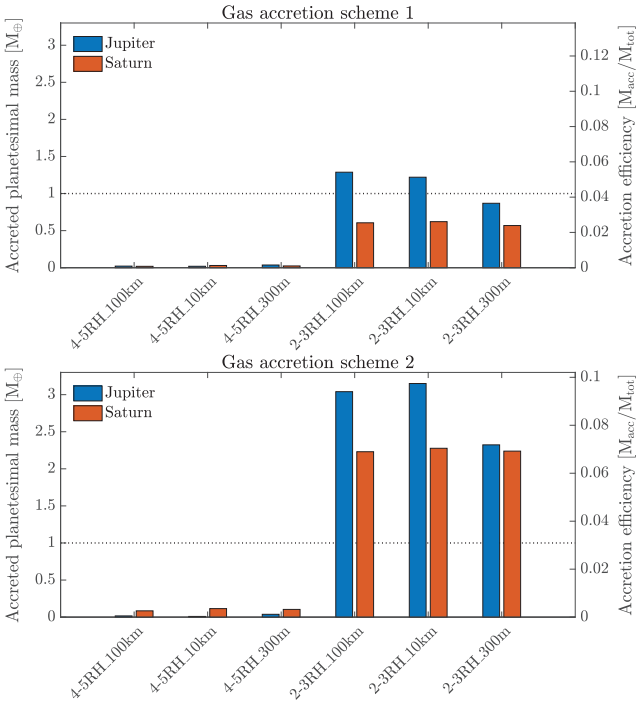

Figure 3.4: Total accreted planetesimal mass, and the corresponding accretion efficiency, onto Jupiter and Saturn. Gas accretion scheme 1 and 2 corresponds to growth track 1 and 2 in Fig. 3.3. The planetesimals are initiated at either $2-3\,\mathrm{R_H}$ or $4-5\,\mathrm{R_H}$ from the planets, and have sizes of either $300\,\mathrm{m}$, $10\,\mathrm{km}$ or $100\,\mathrm{km}$. The accretion efficiency is never higher then 10%, indicating that a very large amount of planetesimals need to form at the gap edges in order to explain the enriched giant planet envelopes (adapted from Eriksson et al. 2022). Reproduced with permission © ESO.

element masses ranges from $\sim 10-100\,\mathrm{M_\oplus}$ (Thorngren et al., 2016). Provided these estimates are correct, it indicates that giant planets typically have enriched envelopes.

In Eriksson et al. (2022), we discuss potential mechanisms for enriching giant planet envelopes. We demonstrate that it is hard to enrich the envelopes via the accretion of planetesimals formed at planetary gap edges, since it requires a very large initial planetesimal mass reservoir (see Fig. 3.4). Enrichment via planetesimal accretion has however been shown to be efficient, if the planet migrates far through a massive wide-spread disk of planetesimals (e.g. Shibata & Helled 2022). Future

studies of this process that compare different initial planetesimal mass reservoirs and include relevant physical processes such as ablation are required in order to fully assess whether or not planetesimal accretion is a viable enrichment mechanism for giant planets. Alternative enrichment mechanisms are giant impacts (e.g. Liu et al. 2019; Ogihara et al. 2021), core erosion (e.g. Madhusudhan et al. 2017) and accretion of enriched gas from evaporating pebbles (e.g. Schneider & Bitsch 2021a,b).

References

Abod, C. P., Simon, J. B., Li, R., et al. 2019, ApJ, 883, 192, doi: 10.3847/1538-4357/ab40a3

Akiyama, E., Hashimoto, J., Liu, H. B., et al. 2016, AJ, 152, 222, doi: 10.3847/1538-3881/152/6/222

Alexander, R., Pascucci, I., Andrews, S., Armitage, P., & Cieza, L. 2014, in Protostars and Planets VI, ed. H. Beuther, R. S. Klessen, C. P. Dullemond, & T. Henning, 475, doi: 10.2458/azu_uapress_9780816531240-ch021

ALMA Partnership, Brogan, C. L., Pérez, L. M., et al. 2015, ApJ, 808, L3, doi: 10.1088/2041-8205/808/1/L3

Andre, P., Ward-Thompson, D., & Barsony, M. 1993, ApJ, 406, 122, doi: 10.1086/172425

Andrews, S. M. 2020, ARA&A, 58, 483, doi: 10.1146/annurev-astro-031220-010302

Andrews, S. M., Huang, J., Pérez, L. M., et al. 2018, ApJ, 869, L41, doi: 10.3847/2041-8213/aaf741

Ansdell, M., Williams, J. P., van der Marel, N., et al. 2016, ApJ, 828, 46, doi: 10.3847/0004-637X/828/1/46

Armitage, P. J. 2015, arXiv e-prints, arXiv:1509.06382. https://arxiv.org/abs/1509.06382

Auffinger, J., & Laibe, G. 2018, MNRAS, 473, 796, doi: 10.1093/mnras/stx2395

Bai, X.-N. 2017, ApJ, 845, 75, doi: 10.3847/1538-4357/aa7dda

Bai, X.-N., & Stone, J. M. 2010, ApJ, 722, L220, doi: 10.1088/2041-8205/722/2/L220

Balbus, S. A., & Hawley, J. F. 1991, ApJ, 376, 214, doi: 10.1086/170270

Béthune, W., Lesur, G., & Ferreira, J. 2017, A&A, 600, A75, doi: 10.1051/0004-6361/201630056

Bitsch, B., Lambrechts, M., & Johansen, A. 2015, A&A, 582, A112, doi: 10.1051/0004-6361/201526463

Bitsch, B., Morbidelli, A., Johansen, A., et al. 2018, A&A, 612, A30, doi: 10.1051/0004-6361/201731931

Blum, J., & Wurm, G. 2008, ARA&A, 46, 21, doi: 10.1146/annurev.astro.46.060407.145152

Bollard, J., Connelly, J. N., Whitehouse, M. J., et al. 2017, Science Advances, 3, e1700407, doi: 10.1126/sciadv.1700407

Boss, A. P. 1998, Annual Review of Earth and Planetary Sciences, 26, 53, doi: 10.1146/annurev.earth.26.1.53

Carrasco-González, C., Sierra, A., Flock, M., et al. 2019, ApJ, 883, 71, doi: 10.3847/1538-4357/ab3d33

Carrera, D., Johansen, A., & Davies, M. B. 2015, A&A, 579, A43, doi: 10.1051/0004-6361/201425120

Carrera, D., Simon, J. B., Li, R., Kretke, K. A., & Klahr, H. 2021, AJ, 161, 96, doi: 10.3847/1538-3881/abd4d9

Casassus, S., & Pérez, S. 2019, ApJL, 883, L41, doi: 10.3847/2041-8213/ab4425

Casassus, S., van der Plas, G. M., Perez, S., et al. 2013, Nature, 493, 191, doi: 10.1038/nature11769

Chiang, E. I., & Goldreich, P. 1997, ApJ, 490, 368, doi: 10.1086/304869

Connelly, J. N., Bizzarro, M., Krot, A. N., et al. 2012, Science, 338, 651, doi: 10.1126/science.1226919

D'Angelo, G., & Lubow, S. H. 2010, ApJ, 724, 730, doi: 10.1088/0004-637X/724/1/730

D'Angelo, G., Lubow, S. H., & Bate, M. R. 2006, ApJ, 652, 1698, doi: 10.1086/508451

Demirci, T., Krause, C., Teiser, J., & Wurm, G. 2019, A&A, 629, A66, doi: 10.1051/0004-6361/201935767

Dent, W. R. F., Pinte, C., Cortes, P. C., et al. 2019, MNRAS, 482, L29, doi: 10.1093/mnrasl/sly181

Dong, R., Liu, S.-y., Eisner, J., et al. 2018, ApJ, 860, 124, doi: 10.3847/1538-4357/aac6cb

Draine, B. T. 2006, ApJ, 636, 1114, doi: 10.1086/498130

Drążkowska, J., & Alibert, Y. 2017, A&A, 608, A92, doi: 10.1051/0004-6361/201731491

Dubrulle, B., Marié, L., Normand, C., et al. 2005, A&A, 429, 1, doi: 10.1051/0004-6361:200400065

Duffell, P. C. 2020, ApJ, 889, 16, doi: 10.3847/1538-4357/ab5b0f

Duffell, P. C., Haiman, Z., MacFadyen, A. I., D'Orazio, D. J., & Farris, B. D. 2014, ApJL, 792, L10, doi: 10.1088/2041-8205/792/1/L10

Dullemond, C. P., Birnstiel, T., Huang, J., et al. 2018, ApJ, 869, L46, doi: 10.3847/2041-8213/aaf742

Dürmann, C., & Kley, W. 2015, A&A, 574, A52, doi: 10.1051/0004-6361/201424837

Eriksson, L. E. J., Johansen, A., & Liu, B. 2020, A&A, 635, A110, doi: 10.1051/0004-6361/201937037

Eriksson, L. E. J., Ronnet, T., & Johansen, A. 2021, A&A, 648, A112, doi: 10.1051/0004-6361/202039889

Eriksson, L. E. J., Ronnet, T., Johansen, A., et al. 2022, arXiv e-prints, arXiv:2202.12723. https://arxiv.org/abs/2202.12723

Favre, C., Fedele, D., Maud, L., et al. 2019, ApJ, 871, 107, doi: 10.3847/1538-4357/aaf80c

Flaherty, K. M., Hughes, A. M., Teague, R., et al. 2018, ApJ, 856, 117, doi: 10.3847/1538-4357/aab615

Flaherty, K. M., Hughes, A. M., Rose, S. C., et al. 2017, ApJ, 843, 150, doi: 10.3847/1538-4357/aa79f9

Ginski, C., Stolker, T., Pinilla, P., et al. 2016, A&A, 595, A112, doi: 10.1051/0004-6361/201629265

Goldreich, P., Lithwick, Y., & Sari, R. 2004, ARA&A, 42, 549, doi: 10.1146/annurev.astro.42.053102.134004

Goldreich, P., & Tremaine, S. 1980, ApJ, 241, 425, doi: 10.1086/158356

Greene, T. P., Wilking, B. A., Andre, P., Young, E. T., & Lada, C. J. 1994, ApJ, 434, 614, doi: 10.1086/174763

Grundy, W., Noll, K., Roe, H., et al. 2019, Icarus, doi: https://doi.org/10.1016/j.icarus.2019.03.035

Gundlach, B., & Blum, J. 2015, ApJ, 798, 34, doi: 10.1088/0004-637X/798/1/34

Güttler, C., Blum, J., Zsom, A., Ormel, C. W., & Dullemond, C. P. 2010, A&A, 513, A56, doi: 10.1051/0004-6361/200912852

Guzmán, V. V., Huang, J., Andrews, S. M., et al. 2018, ApJL, 869, L48, doi: 10.3847/2041-8213/aaedae

Hartmann, L. 2009, Accretion Processes in Star Formation: Second Edition

Hartmann, L., Calvet, N., Gullbring, E., & D'Alessio, P. 1998, ApJ, 495, 385, doi: 10.1086/305277

Hayashi, C. 1981, Progress of Theoretical Physics Supplement, 70, 35, doi: 10.1143/PTPS.70.35

Helled, R., Movshovitz, N., & Nettelmann, N. 2022, arXiv e-prints, arXiv:2202.10046. https://arxiv.org/abs/2202.10046

Huang, J., Andrews, S. M., Pérez, L. M., et al. 2018, ApJL, 869, L43, doi: 10.3847/2041-8213/aaf7a0

Hull, C. L. H., Yang, H., Li, Z.-Y., et al. 2018, ApJ, 860, 82, doi: 10.3847/1538-4357/aabfeb

Ikoma, M., Nakazawa, K., & Emori, H. 2000, ApJ, 537, 1013, doi: 10.1086/309050

Johansen, A., Ida, S., & Brasser, R. 2019, A&A, 622, A202, doi: 10.1051/0004-6361/201834071

Johansen, A., & Lacerda, P. 2010, MNRAS, 404, 475, doi: 10.1111/j.1365-2966.2010.16309.x

Johansen, A., & Lambrechts, M. 2017, Annual Review of Earth and Planetary Sciences, 45, 359, doi: 10.1146/annurev-earth-063016-020226

Johansen, A., Mac Low, M.-M., Lacerda, P., & Bizzarro, M. 2015, Science Advances, 1, 1500109, doi: 10.1126/sciadv.1500109

Johansen, A., & Youdin, A. 2007, ApJ, 662, 627, doi: 10.1086/516730

Johansen, A., Youdin, A., & Klahr, H. 2009, ApJ, 697, 1269, doi: 10.1088/0004-637X/697/2/1269

Jungmann, F., & Wurm, G. 2021, A&A, 650, A77, doi: 10.1051/0004-6361/202039430

Kanagawa, K. D., Muto, T., Tanaka, H., et al. 2015a, ApJL, 806, L15, doi: 10.1088/2041-8205/806/1/L15

Kanagawa, K. D., Tanaka, H., Muto, T., & Tanigawa, T. 2017, PASJ, 69, 97, doi: 10.1093/pasj/psx114

Kanagawa, K. D., Tanaka, H., Muto, T., Tanigawa, T., & Takeuchi, T. 2015b, MNRAS, 448, 994, doi: 10.1093/mnras/stv025

Kanagawa, K. D., Tanaka, H., & Szuszkiewicz, E. 2018, ApJ, 861, 140, doi: 10.3847/1538-4357/aac8d9

Kataoka, A., Muto, T., Momose, M., et al. 2015, ApJ, 809, 78, doi: 10.1088/0004-637X/809/1/78

Kavelaars, J. J., Petit, J.-M., Gladman, B., et al. 2021, ApJL, 920, L28, doi: 10.3847/2041-8213/ac2c72

Kenyon, S. J., & Hartmann, L. 1987, ApJ, 323, 714, doi: 10.1086/165866

Keppler, M., Benisty, M., Müller, A., et al. 2018, A&A, 617, A44, doi: 10.1051/0004-6361/201832957

Kimmig, C. N., Dullemond, C. P., & Kley, W. 2020, A&A, 633, A4, doi: 10.1051/0004-6361/201936412

Kirchschlager, F., & Bertrang, G. H. M. 2020, A&A, 638, A116, doi: 10.1051/0004-6361/202037943

Klahr, H. H., & Bodenheimer, P. 2003, ApJ, 582, 869, doi: 10.1086/344743

Krapp, L., Benítez-Llambay, P., Gressel, O., & Pessah, M. E. 2019, ApJL, 878, L30, doi: 10.3847/2041-8213/ab2596

Kunitomo, M., Ida, S., Takeuchi, T., et al. 2021, ApJ, 909, 109, doi: 10.3847/1538-4357/abdb2a

Lada, C. J. 1987, in Star Forming Regions, ed. M. Peimbert & J. Jugaku, Vol. 115, 1

Lambrechts, M., & Johansen, A. 2012, A&A, 544, A32, doi: 10.1051/0004-6361/201219127

Lambrechts, M., Johansen, A., & Morbidelli, A. 2014, A&A, 572, A35, doi: 10.1051/0004-6361/201423814

Lesur, G. 2020, arXiv e-prints, arXiv:2007.15967. https://arxiv.org/abs/2007.15967

Lesur, G., Ercolano, B., Flock, M., et al. 2022, arXiv e-prints, arXiv:2203.09821. https://arxiv.org/abs/2203.09821

Lesur, G. R. J. 2021, A&A, 650, A35, doi: 10.1051/0004-6361/202040109

Li, R., & Youdin, A. N. 2021, ApJ, 919, 107, doi: 10.3847/1538-4357/ac0e9f

Li, R., Youdin, A. N., & Simon, J. B. 2019, ApJ, 885, 69, doi: 10.3847/1538-4357/ab480d

Lin, D. N. C., & Papaloizou, J. 1979, MNRAS, 186, 799, doi: 10.1093/mnras/186.4.799

—. 1986, ApJ, 309, 846, doi: 10.1086/164653

Liu, B., Ormel, C. W., & Johansen, A. 2019, A&A, 624, A114, doi: 10.1051/0004-6361/201834174

Long, F., Pinilla, P., Herczeg, G. J., et al. 2018, ApJ, 869, 17, doi: 10.3847/1538-4357/aae8e1

Long, F., Herczeg, G. J., Harsono, D., et al. 2019, ApJ, 882, 49, doi: 10.3847/1538-4357/ab2d2d

Long, F., Pinilla, P., Herczeg, G. J., et al. 2020, ApJ, 898, 36, doi: 10.3847/1538-4357/ab9a54

Lynden-Bell, D., & Pringle, J. E. 1974, MNRAS, 168, 603, doi: 10.1093/mnras/168.3.603

Lyra, W., Johansen, A., Zsom, A., Klahr, H., & Piskunov, N. 2009, A&A, 497, 869, doi: 10.1051/0004-6361/200811265

Macías, E., Guerra-Alvarado, O., Carrasco-González, C., et al. 2021, A&A, 648, A33, doi: 10.1051/0004-6361/202039812

Madhusudhan, N., Bitsch, B., Johansen, A., & Eriksson, L. 2017, MNRAS, 469, 4102, doi: 10.1093/mnras/stx1139

Mamajek, E. E. 2009, in American Institute of Physics Conference Series, Vol. 1158, Exoplanets and Disks: Their Formation and Diversity, ed. T. Usuda, M. Tamura, & M. Ishii, 3–10, doi: 10.1063/1.3215910

Manara, C. F. 2014, PhD thesis, LMU Munich, Germany

Marsset, M., Fraser, W. C., Bannister, M. T., et al. 2020, , 1, 16, doi: 10.3847/PSJ/ab8cc0

Michel, A., van der Marel, N., & Matthews, B. C. 2021, ApJ, 921, 72, doi: 10.3847/1538-4357/ac1bbb

Militzer, B., Wahl, S., & Hubbard, W. B. 2019, ApJ, 879, 78, doi: 10.3847/1538-4357/ab23f0

Miyake, K., & Nakagawa, Y. 1993, Icarus, 106, 20, doi: 10.1006/icar.1993.1156

Musiolik, G. 2021, MNRAS, 506, 5153, doi: 10.1093/mnras/stab1963

Musiolik, G., & Wurm, G. 2019, ApJ, 873, 58, doi: 10.3847/1538-4357/ab0428

Muzerolle, J., Hillenbrand, L., Calvet, N., Briceño, C., & Hartmann, L. 2003, ApJ, 592, 266, doi: 10.1086/375704

Nakagawa, Y., Sekiya, M., & Hayashi, C. 1986, Icarus, 67, 375, doi: 10.1016/0019-1035(86)90121-1

Nesvorný, D., Li, R., Simon, J. B., et al. 2021, , 2, 27, doi: 10.3847/PSJ/abd858

Nesvorný, D., Li, R., Youdin, A. N., Simon, J. B., & Grundy, W. M. 2019, Nature Astronomy, 364, doi: 10.1038/s41550-019-0806-z

Ni, D. 2020, A&A, 639, A10, doi: 10.1051/0004-6361/202038267

Noll, K. S., Grundy, W. M., Chiang, E. I., Margot, J. L., & Kern, S. D. 2008, in The Solar System Beyond Neptune, ed. M. A. Barucci, H. Boehnhardt, D. P. Cruikshank, A. Morbidelli, & R. Dotson, 345

Ogihara, M., Hori, Y., Kunitomo, M., & Kurosaki, K. 2021, A&A, 648, L1, doi: 10.1051/0004-6361/202140464

Ormel, C. W., & Klahr, H. H. 2010, A&A, 520, A43, doi: 10.1051/0004-6361/201014903

Papaloizou, J., & Lin, D. N. C. 1984, ApJ, 285, 818, doi: 10.1086/162561

Pascucci, I., Testi, L., Herczeg, G. J., et al. 2016, ApJ, 831, 125, doi: 10.3847/0004-637X/831/2/125

Perets, H. B., & Murray-Clay, R. A. 2011, ApJ, 733, 56, doi: 10.1088/0004-637X/733/1/56

Picogna, G., Ercolano, B., Owen, J. E., & Weber, M. L. 2019, MNRAS, 487, 691, doi: 10.1093/mnras/stz1166

Pinilla, P., Pohl, A., Stammler, S. M., & Birnstiel, T. 2017, ApJ, 845, 68, doi: 10.3847/1538-4357/aa7edb

Pinte, C., Dent, W. R. F., Ménard, F., et al. 2016, ApJ, 816, 25, doi: 10.3847/0004-637X/816/1/25

Pinte, C., van der Plas, G., Ménard, F., et al. 2019, Nature Astronomy, 3, 1109, doi: 10.1038/s41550-019-0852-6

Piso, A.-M. A., & Youdin, A. N. 2014, ApJ, 786, 21, doi: 10.1088/0004-637X/786/1/21

Pollack, J. B., Hubickyj, O., Bodenheimer, P., et al. 1996, Icarus, 124, 62, doi: 10.1006/icar.1996.0190

Pringle, J. E. 1981, Annual Review of Astronomy and Astrophysics, 19, 137, doi: 10.1146/annurev.aa.19.090181.001033

Raymond, S. N., & Morbidelli, A. 2022, in Astrophysics and Space Science Library, Vol. 466, Demographics of Exoplanetary Systems, Lecture Notes of the 3rd Advanced School on Exoplanetary Science, ed. K. Biazzo, V. Bozza, L. Mancini, & A. Sozzetti, 3–82, doi: 10.1007/978-3-030-88124-5_1

Richard, S., Nelson, R. P., & Umurhan, O. M. 2016, MNRAS, 456, 3571, doi: 10.1093/mnras/stv2898

Riols, A., & Lesur, G. 2019, A&A, 625, A108, doi: 10.1051/0004-6361/201834813

Ronnet, T., & Johansen, A. 2020, A&A, 633, A93, doi: 10.1051/0004-6361/201936804

Ros, K., Johansen, A., Riipinen, I., & Schlesinger, D. 2019, A&A, 629, A65, doi: 10.1051/0004-6361/201834331

Schäfer, U., Johansen, A., & Banerjee, R. 2020, A&A, 635, A190, doi: 10.1051/0004-6361/201937371

Schäfer, U., Yang, C.-C., & Johansen, A. 2017, A&A, 597, A69, doi: 10.1051/0004-6361/201629561

Schaffer, N., Johansen, A., Cedenblad, L., Mehling, B., & Mitra, D. 2020, A&A, 639, A39, doi: 10.1051/0004-6361/201935763

Schaffer, N., Johansen, A., & Lambrechts, M. 2021, A&A, 653, A14, doi: 10.1051/0004-6361/202140690

Schneider, A. D., & Bitsch, B. 2021a, A&A, 654, A71, doi: 10.1051/0004-6361/202039640

—. 2021b, A&A, 654, A72, doi: 10.1051/0004-6361/202141096

Segura-Cox, D. M., Looney, L. W., Stephens, I. W., et al. 2015, ApJL, 798, L2, doi: 10.1088/2041-8205/798/1/L2

Segura-Cox, D. M., Schmiedeke, A., Pineda, J. E., et al. 2020, Nature, 586, 228, doi: 10.1038/s41586-020-2779-6

Shakura, N. I., & Sunyaev, R. A. 1973, A&A, 500, 33

Shibata, S., & Helled, R. 2022, ApJL, 926, L37, doi: 10.3847/2041-8213/ac54b1

Simon, J. B., Armitage, P. J., Youdin, A. N., & Li, R. 2017, ApJ, 847, L12, doi: 10.3847/2041-8213/aa8c79

Steinpilz, T., Joeris, K., Jungmann, F., et al. 2020, Nature Physics, 16, 225, doi: 10.1038/s41567-019-0728-9

Stevenson, D. J., & Lunine, J. I. 1988, Icarus, 75, 146, doi: 10.1016/0019-1035(88)90133-9

Takahashi, S. Z., & Inutsuka, S.-i. 2014, The Astrophysical Journal, 794, 55, doi: 10.1088/0004-637X/794/1/55

Tanigawa, T., & Tanaka, H. 2016, ApJ, 823, 48, doi: 10.3847/0004-637X/823/1/48

Tazzari, M., Clarke, C. J., Testi, L., et al. 2021a, MNRAS, 506, 2804, doi: 10.1093/mnras/stab1808

Tazzari, M., Testi, L., Ercolano, B., et al. 2016, A&A, 588, A53, doi: 10.1051/0004-6361/201527423

Tazzari, M., Testi, L., Natta, A., et al. 2021b, MNRAS, 506, 5117, doi: 10.1093/mnras/stab1912

Teague, R., Bae, J., Huang, J., & Bergin, E. A. 2019, ApJL, 884, L56, doi: 10.3847/2041-8213/ab4a83

Teague, R., Hull, C. L. H., Guilloteau, S., et al. 2021, ApJ, 922, 139, doi: 10.3847/1538-4357/ac2503

Teiser, J., Kruss, M., Jungmann, F., & Wurm, G. 2021, ApJL, 908, L22, doi: 10.3847/2041-8213/abddc2

Testi, L., Natta, A., Shepherd, D. S., & Wilner, D. J. 2003, A&A, 403, 323, doi: 10.1051/0004-6361:20030362

Testi, L., Birnstiel, T., Ricci, L., et al. 2014, in Protostars and Planets VI, ed. H. Beuther, R. S. Klessen, C. P. Dullemond, & T. Henning, 339, doi: 10.2458/azu_uapress_9780816531240-ch015

Testi, L., Natta, A., Manara, C. F., et al. 2022, arXiv e-prints, arXiv:2201.04079. https://arxiv.org/abs/2201.04079

Thorngren, D. P., Fortney, J. J., Murray-Clay, R. A., & Lopez, E. D. 2016, ApJ, 831, 64, doi: 10.3847/0004-637X/831/1/64

Toomre, A. 1964, ApJ, 139, 1217, doi: 10.1086/147861

Ueda, T., Kataoka, A., Zhang, S., et al. 2021, ApJ, 913, 117, doi: 10.3847/1538-4357/abf7b8

Valletta, C., & Helled, R. 2020, ApJ, 900, 133, doi: 10.3847/1538-4357/aba904

van der Marel, N., Dong, R., di Francesco, J., Williams, J. P., & Tobin, J. 2019, ApJ, 872, 112, doi: 10.3847/1538-4357/aafd31

van der Marel, N., & Mulders, G. D. 2021, AJ, 162, 28, doi: 10.3847/1538-3881/ac0255

van der Marel, N., van Dishoeck, E. F., Bruderer, S., et al. 2016, A&A, 585, A58, doi: 10.1051/0004-6361/201526988

van der Marel, N., van Dishoeck, E. F., Bruderer, S., Pérez, L., & Isella, A. 2015, A&A, 579, A106, doi: 10.1051/0004-6361/201525658

Villenave, M., Benisty, M., Dent, W. R. F., et al. 2019, A&A, 624, A7, doi: 10.1051/0004-6361/201834800

Vlemmings, W. H. T., Lankhaar, B., Cazzoletti, P., et al. 2019, A&A, 624, L7, doi: 10.1051/0004-6361/201935459

Ward, W. R. 1997, Icarus, 126, 261, doi: 10.1006/icar.1996.5647

Weidenschilling, S. J. 1977, Monthly Notices of the Royal Astronomical Society, 180, 57, doi: 10.1093/mnras/180.1.57

Whipple, F. L. 1972, in From Plasma to Planet, ed. A. Elvius, 211

Wyatt, M. C. 2008, ARA&A, 46, 339, doi: 10.1146/annurev.astro.45.051806.110525

Yang, C. C., Johansen, A., & Carrera, D. 2017, A&A, 606, A80, doi: 10.1051/0004-6361/201630106

Yang, C.-C., & Zhu, Z. 2021, MNRAS, 508, 5538, doi: 10.1093/mnras/stab2959

Yang, H., & Bai, X.-N. 2021, ApJ, 922, 201, doi: 10.3847/1538-4357/ac250a

Youdin, A. N., & Goodman, J. 2005, ApJ, 620, 459, doi: 10.1086/426895

Zhang, K., Blake, G. A., & Bergin, E. A. 2015, ApJL, 806, L7, doi: 10.1088/2041-8205/806/1/L7

Zhang, K., Booth, A. S., Law, C. J., et al. 2021, ApJS, 257, 5, doi: 10.3847/1538-4365/ac1580

Zhang, S., Zhu, Z., & Kang, M. 2022, MNRAS, 510, 4473, doi: 10.1093/mnras/stab3502

Zhang, S., Zhu, Z., Huang, J., et al. 2018, ApJL, 869, L47, doi: 10.3847/2041-8213/aaf744

Zhu, Z., Nelson, R. P., Dong, R., Espaillat, C., & Hartmann, L. 2012, ApJ, 755, 6, doi: 10.1088/0004-637X/755/1/6

Zhu, Z., & Yang, C.-C. 2021, MNRAS, 501, 467, doi: 10.1093/mnras/staa3628

Part II

Scientific publications

Author contributions

A summary of my contribution to each paper included in this thesis.

Paper I

Pebble drift and planetesimal formation in protoplanetary discs with embedded planets

L.E.J. Eriksson, A. Johansen, B. Liu (2020)
Astronomy & Astrophysics, vol. 635, A110 (19 pp.)

The original idea for the project was provided by Anders Johansen (AJ). The development of the project was discussed at weekly meetings together with AJ, Linn Eriksson (LE) and Beibei Liu (BL). The code used for performing the simulations was initially developed by AJ and further built upon by LE. The computer simulations were performed and analyzed by LE. The final paper was written by LE with comments and corrections by AJ and BL.

Paper II

The fate of planetesimals formed at planetary gap edges

L.E.J. Eriksson, T. Ronnet, A. Johansen (2021)
Astronomy & Astrophysics, vol. 648, A112 (22 pp.)

The original idea for the project was provided by all three authors together. The development of the project was discussed at weekly meetings together with AJ, LE and Thomas Ronnet (TR). The computer simulations were set up and performed by LE, with help and advice from TR. LE analyzed the results and wrote the final paper, which was corrected and commented upon by TR and AJ.

Paper III

A low accretion efficiency of planetesimals formed at planetary gap edges

L.E.J. Eriksson, T. Ronnet, A. Johansen, R. Helled, C. Valletta, A.C. Petit (2022)
Astronomy & Astrophysics, in press, 10.1051/0004-6361/202142391 (13 pp.)

The original idea for the project was provided by AJ and Ravit Helled (RH). The computer simulations were set up and performed by LE, with help and advice from TR. The prescription for the capture radius was provided by Claudio Valletta (CV). AJ, TR, Antoine Petit, RH and CV contributed with ideas, comments and corrections to the final paper, which was written by LE.

Paper I

A&A 635, A110 (2020)
https://doi.org/10.1051/0004-6361/201937037

Astronomy & Astrophysics

Pebble drift and planetesimal formation in protoplanetary discs with embedded planets

Linn E. J. Eriksson, Anders Johansen, and Beibei Liu

Lund Observatory, Department of Astronomy and Theoretical Physics, Lund University, Box 43, 221 00 Lund, Sweden
e-mail: linn@astro.lu.se

Received 1 November 2019 / Accepted 29 January 2020

ABSTRACT

Nearly axisymmetric gaps and rings are commonly observed in protoplanetary discs. The leading theory regarding the origin of these patterns is that they are due to dust trapping at the edges of gas gaps induced by the gravitational torques from embedded planets. If the concentration of solids at the gap edges becomes high enough, it could potentially result in planetesimal formation by the streaming instability. We tested this hypothesis by performing global 1D simulations of dust evolution and planetesimal formation in a protoplanetary disc that is perturbed by multiple planets. We explore different combinations of particle sizes, disc parameters, and planetary masses, and we find that planetesimals form in all of these cases. We also compare the spatial distribution of pebbles from our simulations with protoplanetary disc observations. Planets larger than one pebble isolation mass catch drifting pebbles efficiently at the edge of their gas gaps, and depending on the efficiency of planetesimal formation at the gap edges, the protoplanetary disc transforms within a few 100 000 yr to either a transition disc with a large inner hole devoid of dust or to a disc with narrow bright rings. For simulations with planetary masses lower than the pebble isolation mass, the outcome is a disc with a series of weak ring patterns but there is no strong depletion between the rings. By lowering the pebble size artificially to a 100 micrometer-sized "silt", we find that regions between planets get depleted of their pebble mass on a longer time-scale of up to 0.5 million years. These simulations also produce fewer planetesimals than in the nominal model with millimeter-sized particles and always have at least two rings of pebbles that are still visible after 1 Myr.

Key words. planets and satellites: formation – protoplanetary disks – planet-disk interactions

1. Introduction

High spatial resolution dust continuum observations with the Atacama Large Millimeter Array (ALMA) have shown that concentric rings and gaps are common features in protoplanetary discs (see e.g., ALMA Partnership et al. 2015; Andrews et al. 2016; Isella et al. 2016; Pinte et al. 2016). Detections of rings and gaps are common in millimeter continuum emission, which traces the population of millimeter-sized pebbles (e.g., Clarke et al. 2018; Dipierro et al. 2018; Fedele et al. 2018; Long et al. 2018, 2019); however, the same patterns have also been observed in the distribution of micron-sized dust grains via scattered light observations (e.g., Ginski et al. 2016; van Boekel et al. 2017; Avenhaus et al. 2018), and in the gas surface density via observations of molecular emission (e.g., Isella et al. 2016; Fedele et al. 2017; Teague et al. 2017; Favre et al. 2019). Since these features are seen in both the solid and the gas component of the disc, they have been interpreted as a signature of planet-disc interactions (e.g., Pinilla et al. 2012; Dipierro et al. 2015; Favre et al. 2019; Fedele et al. 2018). Numerical simulations have long predicted that massive planets will open gap(s) in the disc, creating local pressure maxima at the gap edges where particles can become trapped (e.g., Papaloizou & Lin 1984; Paardekooper & Mellema 2004; Dong et al. 2015). This idea has gained relevance, as Dullemond et al. (2018) recently found evidence that at least some of the rings seen in observations are due to dust trapping in radial pressure bumps. Since the dust-to-gas ratios in these pressure bumps can become significantly higher than the global value, they are a likely site for planetesimal formation via the streaming instability (Youdin & Goodman 2005; Johansen & Youdin 2007; Bai & Stone 2010a; Yang & Johansen 2014). This is the key process that we investigate in this work.

In this paper, we explore observational consequences of the formation of gaps by embedded planets. Particularly, we investigate whether particle trapping at the edges of planetary gaps is efficient enough to trigger the streaming instability and result in the formation of planetesimals. To this end, we used a dust evolution model including both radial drift, stirring, and coagulation, and we performed first principle calculations in 1D over large spatial scales (1−500 au) and long disc evolution lifetimes (1 Myr). The main points that we want to address can be summarized as follows: (1) do planetesimals form at the edges of planetary gaps; (2) if so, how efficient is this process and how does the efficiency vary with different disc and planet parameters; (3) what does the distribution of dust and pebbles look like for the different simulations; and (4) how do these distributions compare with observations of protoplanetary discs?

We find that planetesimals do indeed form at the edges of planetary gaps. For millimeter-sized pebbles and planetary masses larger than the pebble isolation mass, essentially all pebbles trapped at the pressure bump are turned into planetesimals. In combination with fast radial drift, this results in the depletion of pebbles in the region's interior to the outermost planet, leaving us with something that resembles a transition disc (Andrews et al. 2011). When the particle size is lowered to 100 μm, a larger dust-to-gas ratio is required to trigger the streaming instability. Because of this, the planetesimal formation efficiency drops, and at least one ring of pebbles remains visible in the

otherwise empty inner disc. When the planetary mass is lowered to less than the pebble isolation mass, trapping at the gap edges becomes less efficient. Pebbles are also able to partially drift through the planetary gaps, resulting in a continuous replenishing of pebbles to the inner disc, and the pebble distribution appears as a series of weak gaps and rings at the locations of the planets.

In Sect. 2, we present our models for disc evolution, dust growth, and planetesimal formation. The numerical set up of the simulations is described in Sect. 3. In Sect. 4, we present the results for the nominal model and the parameter study. In the nominal simulation, the maximum pebble size reached by coagulation is around one millimeter; the results from simulations where the maximum grain size was artificially decreased to 100 μm are presented in Sect. 5. In Sect. 6, we compare our results to observations, and in Sect. 7 we discuss the shortcomings of the model. The most important results and findings are summarized in Sect. 8. In Appendix A, we describe the method used to model particle collisions, and in Appendix B we show particle size distributions for some interesting simulations in the parameter study.

2. Theory

In our model, we used a 1D gas disc that is evolving viscously. We applied planetary torques to the disc in order to simulate gap opening by planets. For the evolution of dust particles, we used a model containing both particle growth, stirring, and radial drift. We further included a model for planetesimal formation where the conditions for forming planetesimals were derived from streaming instability simulations.

2.1. Disc model

The initial surface density profile of the disc was chosen to be that of a viscous accretion disc,

$$\Sigma = \frac{\dot{M}_0}{3\pi\nu}\exp\left[-\frac{R}{R_{\rm out}}\right], \tag{1}$$

where Σ is the surface density of the gas, $\dot{M}_0$ is the initial disc accretion rate, ν is the kinematic viscosity of the disc, R is the semimajor axis, and $R_{\rm out}$ is the location of the outer disc edge (e.g., Pringle 1981). The evolution of the surface density was solved using the standard 1D viscous evolution equation from Lin & Papaloizou (1986) for a disc that is being perturbed by a planet,

$$\frac{\partial\Sigma}{\partial t} = \frac{1}{R}\frac{\partial}{\partial R}\left[3R^{1/2}\frac{\partial}{\partial R}(\nu\Sigma R^{1/2}) - \frac{2\Lambda\Sigma R^{3/2}}{(GM_*)^{1/2}}\right]. \tag{2}$$

In the above equation, t is the time, Λ is the torque density distribution, G is the gravitational constant, and M_* is the stellar mass. Equation (2) is essentially the continuity equation in cylindrical coordinates,

$$\frac{\partial\Sigma}{\partial t} = \frac{1}{R}\frac{\partial}{\partial R}\left(\Sigma v_{\rm R} R\right), \tag{3}$$

where the radial velocity $v_{\rm R}$ has two components, which can be obtained from the comparison of the two equations. The kinematic viscosity was approximated using the alpha approach from Shakura & Sunyaev (1973),

$$\nu = \alpha_{\rm visc}\Omega H^2, \tag{4}$$

where $\alpha_{\rm visc}$ is a parameter related to the efficiency of viscous transport, $\Omega = (GM_*/R^3)^{1/2}$ is the Keplerian angular velocity, and H is the scale height of the disc. The scale height was calculated as

$$H = \frac{c_{\rm s}}{\Omega}, \tag{5}$$

where $c_{\rm s}$ is the sound-speed,

$$c_{\rm s} = \left(\frac{k_{\rm B}T}{\mu m_{\rm H}}\right)^{1/2}. \tag{6}$$

In the above equation, $k_{\rm B}$ is the Bolzmann constant, T is the temperature, $m_{\rm H}$ is the mass of the hydrogen atom, and μ is the mean molecular weight, which was set to be 2.34 for a solar-composition mixture of hydrogen and helium (Hayashi 1981). We used a fixed powerlaw structure for the temperature,

$$T = T_{\rm const}\times(R/{\rm AU})^{-\zeta}, \tag{7}$$

with a radial temperature gradient of $\zeta = 3/7$ and a midplane temperature of $T_{\rm const} = 150\,{\rm K}$ at 1 au (Chiang & Goldreich 1997).

2.2. Planetary torque

The effect on the disc due to the planet is governed by the torque density distribution, Λ, which here is defined as the rate of angular momentum transfer from the planet to the disc per unit mass. For modeling of the torque density distribution, we follow D'Angelo & Lubow (2010),

$$\Lambda = -F(x,\beta,\zeta)\Omega_a^2 a^2 q^2\left(\frac{a}{H_a}\right)^4. \tag{8}$$

In the above equation F is a dimensionless function, $x = (R-a)/H_a$, β, and ζ are the negative radial gradients of surface density and temperature, respectively, and q is the planet-to-star mass ratio. The subscript a denotes the location of the planet. The analytic expression used for function F is

$$F(x,\beta,\zeta) = \left\{p_1\exp\left[-\frac{(x+p_2)^2}{p_3^2}\right] + p_4\exp\left[-\frac{(x+p_5)^2}{p_6^2}\right]\right\} \times \tanh(p_7 - p_8 x), \tag{9}$$

where the parameters $(p_1,\ldots,p_8)$ are provided as a fit to actual simulations. Table 1 of D'Angelo & Lubow (2010) gives values for these parameters for a set of discrete values of β and ζ. As mentioned in the previous subsection, we used a fixed radial temperature gradient of $\zeta = 3/7$, and we chose to simplify the problem even further by also using a constant surface density gradient of $\beta = 15/14$. For these values of β and ζ the parameters $(p_1,\ldots,p_8)$ take on the values listed in Table 1.

2.3. Pebble isolation mass

The pebble isolation mass ($M_{\rm iso}$) is defined as the mass when the planet can perturb the local pressure gradient in the midplane enough to make it zero outside the gap, thus creating a pressure bump. Pebbles drifting inward are trapped at the pressure bump, resulting in a locally enhanced solid density just outside the orbit of the planet (e.g., Lambrechts et al. 2014; Pinilla et al. 2016; Weber et al. 2018). The planetary masses used in our simulations are always in units of pebble isolation masses.

Table 1. Values of the parameters p_n in Eq. (9) for $\beta = 15/14$ and $\zeta = 3/7$.

p_n	Value
p_1	0.029355
p_2	1.143998
p_3	0.918121
p_4	0.042707
p_5	0.859193
p_6	1.110171
p_7	−0.152072
p_8	3.632843

Notes. The values were obtained from linear interpolation using Table 1 in D'Angelo & Lubow (2010).

We used an analytical fitting formula for the pebble isolation mass, which was derived by Bitsch et al. (2018) using 3D hydrodynamical simulations of planet-disc interactions,

$$M_{\rm iso} = 25\, M_\oplus \times f_{\rm fit}, \tag{10}$$

and

$$f_{\rm fit} = \left[\frac{H/R}{0.05}\right]^3 \left[0.34\left(\frac{\log(\alpha_3)}{\log(\alpha_{\rm visc})}\right)^4 + 0.66\right]\left[1 - \frac{\frac{\partial \ln P}{\partial \ln R} + 2.5}{6}\right]. \tag{11}$$

In the above equation $\alpha_3 = 0.001$.

The pebble isolation mass is extremely dependent on the gap depth, which is known to vary between 1D and multidimensional simulations (e.g., Lin & Papaloizou 1986; Kanagawa et al. 2015; Hallam & Paardekooper 2017). In general, 1D simulations produce narrower and deeper gaps than their higher dimensional analogs. This means that the mass required to reach a radial pressure gradient of zero is smaller in 1D simulations than in 3D simulations. In other words, the pebble isolation masses derived by Bitsch et al. (2018) are significantly higher than the pebble isolation mass obtained in our simulations using the tabulated torques of D'Angelo & Lubow (2010).

We performed our own 1D simulations to calculate the pebble isolation mass, and found during comparison that the pebble isolation masses obtained in 1D and 3D simulations are related by a scalar factor, which only seems to depend on $\alpha_{\rm visc}$. Approximate values of this scalar, which we denote $k_{\rm 3D/1D}$, can be found in Table 2 for a range of values of $\alpha_{\rm visc}$. As an example: if $\alpha_{\rm visc} = 0.01$, then the pebble isolation mass at 11.8 au is 59.6 $M_\oplus$, according to Eq. (10) and by using the values quoted for $T_{\rm const}$, β, and ζ. The planetary mass required to obtain a zero pressure gradient outside a planet orbiting at the same semimajor axis in our simulations is 59.6/1.5 = 39.7 $M_\oplus$. Figure 3 of Johansen et al. (2019) shows a similar systematic difference between the 1D and the 3D gap depth.

In our simulations, to avoid working with an artificially low pebble isolation mass due to the 1D approach, we modified the magnitude of the torque density distribution in the following way,

$$\Lambda \rightarrow \frac{\Lambda}{k^2_{\rm 3D/1D}}. \tag{12}$$

In other words, for $\alpha = 0.01$ we simply divided Eq. (8) by 1.5^2, and then the pebble isolation masses obtained from Eq. (10) are correct even in 1D. The power of two is there because the torque density is proportional to the planetary mass square (Eq. (8)).

Table 2. Approximate values of the scalar $k_{\rm 3D/1D}$ for discrete values of $\alpha_{\rm visc}$.

$\alpha_{\rm visc}$	$k_{\rm 3D/1D}$
0.01	1.5
0.001	2
0.0005	2.5
0.0001	5

Notes. This scalar tells us that for a specific value of $\alpha_{\rm visc}$, say 0.01, the planetary mass required to obtain a zero pressure gradient in our 1D simulations is 1.5 times lower than the mass obtained using the equation from Bitsch et al. (2018), which was obtained using 3D simulations.

2.4. Dust evolution

We adopted the approach of Lagrangian super-particles for the solid component of the disc. Each super-particle represents multiple identical physical solid particles, and each super-particle i has its own position $\boldsymbol{x}_i$ and velocity $\boldsymbol{v}_i$. The particle velocity was taken as the sum of the drift velocity and the turbulent velocity, the algorithms for which are described below.

2.4.1. Drift velocity

The radial drift velocity of a dust particle in a disc that is accreting gas is

$$v_{\rm D} = -\frac{2\tau_{\rm s}}{1+\tau_{\rm s}^2}\left(\eta v_{\rm kep} - \frac{1}{2\tau_{\rm s}} v_{\rm R}\right), \tag{13}$$

where η is the difference between the azimuthal gas velocity (v_θ) and the Keplerian velocity ($v_{\rm kep}$), $v_{\rm R}$ is the gas velocity in the radial direction, and $\tau_{\rm s}$ is the Stokes number, which is sometimes referred to as the dimensionless stopping time (Nakagawa et al. 1986; Guillot et al. 2014). The η parameter is directly related to the pressure gradient of the disc as

$$\eta = -\frac{1}{2}\left(\frac{H}{R}\right)^2 \frac{\partial \ln P}{\partial \ln R}. \tag{14}$$

The Stokes number for a particle in the Epstein regime is

$$\tau_{\rm s} = \frac{s\rho_\bullet}{H\rho}; \tag{15}$$

it is important to note that the factor $\sqrt{\pi/8}$ in Eq. (6) from Carrera et al. (2015) is not included in this work and would not have changed the results significantly. In the above equation s is the particle radius, ρ is the gas density in the midplane (related to the gas surface density through $\rho = \Sigma/(2\pi H)$), and $\rho_\bullet$ is the solid density. We adopt the value $\rho_\bullet = 1000\,{\rm kg\,m^{-3}}$ throughout this work. This density could approximately represent the density of icy pebbles with a significant porosity.

2.4.2. Turbulent velocity

Solid particles in the protoplanetary disc experience a drag force due to the turbulent motion of gas in the disc. The resultant turbulent diffusion of the particles can be modeled as a damped random walk, which we implemented by using the algorithm from Ros et al. (2019). They calculated the turbulent diffusion coefficient (D) by applying a force acceleration (f) to the particles on a time-scale $\tau_{\rm for}$, and damping the turbulent velocity on

the correlation time-scale $\tau_{\rm cor}$. The forcing time-step $\tau_{\rm for}$ was set to equal the time-step of the simulation, and the correlation time is the approximate time-scale over which a particle maintains a coherent direction, which was calculated as the inverse of the Keplerian angular velocity ($\tau_{\rm cor} = \Omega^{-1}$). As an addition to the algorithm from Ros et al. (2019), the falling of D with Stokes number was implemented here following Eq. (37) in Youdin & Lithwick (2007). We used a value of one for the dimensionless eddy time.

2.4.3. Particle collisions

Our model of particle collisions follows the results of Güttler et al. (2010). They combine laboratory collision experiments and theoretical models to show that collisions among dust particles in the disc lead to either sticking, bouncing, or fragmentation. The outcome is determined by the mass of the projectile (the lightest of the colliding particles) and the collision velocity, which is calculated as the sum of the relative speed from drift, Brownian motion, and turbulent motion. The result of the collision also varies depending on the mass ratio of the projectile to target particle and on whether the particles are porous or compact. In our simulations, we limited ourselves to porous particles, and drew the line between equal-size particles and nonequal-size particles at a mass ratio of 10 (using effectively only the two upper panels of Fig. 11 in Güttler et al. 2010). If the outcome is sticking, then the target mass was either doubled, or multiplied by $(1 + M_{\rm projectile}/M_{\rm target})$ if the total mass in the projectile particle $M_{\rm projectile}$ was smaller than the total mass in the target particle $M_{\rm target}$. For fragmentation, we set all of the target and projectile particles to the mass of the projectile. For a complete description of the collision algorithm, see Appendix A.

2.5. Planetesimal formation

Carrera et al. (2015) performed hydrodynamical simulations of particle-gas interactions to find out under which conditions solid particles in the disc come together in dense filaments that can collapse under self-gravity to form planetesimals. By doing so, they mapped out for which solid concentrations and particle Stokes number filaments emerge. This map was revised by Yang et al. (2017) who expanded on the investigation by using longer simulation times and significantly higher resolutions. The critical curves on the map for when the solid concentration is large enough to trigger particle clumping are given by Yang et al. (2017) as

$$\log Z_{\rm c} = 0.3(\log \tau_{\rm s})^2 + 0.59 \log \tau_{\rm s} - 1.57 \quad (\tau_{\rm s} > 0.1), \tag{16}$$

and

$$\log Z_{\rm c} = 0.1(\log \tau_{\rm s})^2 + 0.20 \log \tau_{\rm s} - 1.76 \quad (\tau_{\rm s} < 0.1), \tag{17}$$

where $Z_{\rm c} = \Sigma_{\rm solid}/\Sigma_{\rm total}$ and the logarithm is with base 10. These equations were derived for a laminar disc model; however, unless the degree of turbulence is very high, they may also be valid for nonlaminar discs (Yang et al. 2018). For example, Yang et al. (2018) find a critical solid-to-gas ratio of 2% when using $\tau_{\rm s} = 0.1$ particles and a vertical turbulence strength of 10^{-3}, driven by density waves excited by the magnetorotational instability in the turbulent surface layers.

2.5.1. Pressure dependence

The map from Yang et al. (2017) determines whether or not the streaming instability forms filaments based on the solid abundance and the Stokes number; however, the degree of clumping is also strongly dependent on the radial pressure gradient (Bai & Stone 2010b; Abod et al. 2019; Auffinger & Laibe 2018). Simulations by Bai & Stone (2010b) show that the critical solid abundance required to trigger particle clumping via the streaming instability monotonically increases with the radial pressure gradient. In other words, planetesimal formation is most likely to occur inside pressure bumps where the pressure gradient is small, a result which has also been obtained from a linear analysis (Auffinger & Laibe 2018). From Bai & Stone (2010b), it appears that the critical solid abundance is roughly linearly dependent on the radial pressure gradient. In order to catch this dependency, we scaled the metallicity threshold from Yang et al. (2017) with the local radial pressure gradient divided by the background pressure gradient. Here we made the assumption that the background pressure gradient in our simulations is the same as in Yang et al. (2017). This is a simplification; however, a comparison of simulations using the different background pressure gradients show that the results are unaffected.

When the pressure gradient is exactly zero, there is no particle drift, meaning that the streaming instability is formally absent. However, there is another planetesimal formation mechanism that is still active, which we have not not included in our simulations, namely secular gravitational instability (e.g., Youdin 2011; Takahashi & Inutsuka 2014). Recently, Abod et al. (2019) performed simulations of planetesimal formation for various pressure gradient conditions (including a zero pressure gradient). They find that many results and conclusions obtained in their study of planetesimal formation via the streaming instability are also valid in the case of a zero pressure gradient. Motivated by this result, we chose to use the same mechanism for planetesimal formation at a pressure gradient of zero as we otherwise did.

2.5.2. Code implementation

We implemented planetesimal formation in the code in the following way: (1) we calculated the solid abundance in each grid cell, excluding the already formed planetesimals; (2) we calculated the local pressure gradient in each grid cell; (3) we scaled the metallicity threshold $Z_{\rm c}$ up and down linearly by the found local pressure gradient divided by the background pressure gradient; (4) we calculated the mean Stokes number in each grid cell; (5) if the criterion for planetesimal formation is reached, then we set the radius of the first super-particle in the grid cell to 100 km; (6) we repeated the process until the criterion was no longer met. We note that the planetesimal size is arbitrary since we do not follow the dynamical evolution of the planetesimals after their formation.

The algorithm described above implies that every time the conditions for the streaming instability are met, planetesimals form. This can be thought of as a limiting maximum case for the planetesimal formation efficiency, and a discussion regarding how accurate this algorithm is can be found in Sect. 7.3.

2.5.3. An alternative model for planetesimal formation

The criterion used in this paper for planetesimal formation via the streaming instability is not the only one that exists. Another commonly used criterion is that the dust-to-gas ratio in the midplane has to be larger than unity. Such a planetesimal formation model is used in Stammler et al. (2019), for example, who conducted a similar study of planetesimal formation in pressure bumps. We implemented this planetesimal formation criterion,

which we refer to as the midplane model, in the code and make a comparison of the two planetesimal formation models in Sect. 4.4. For code implementation, we used the same algorithm as above, except that it was applied to the midplane density ratio rather than to the column density ratio.

3. Numerical set up

The code we used for simulations is called PLANETESYS, and it is a modified version of the Pencil Code (Brandenburg & Dobler 2002), which was designed for highly parallel calculations of the evolution of gas and dust particles in protoplanetary discs. The code was developed under the ERC Consolidator Grant "PLANETESYS" (PI: Anders Johansen) and this paper together with the recent paper by Ros et al. (2019) represent the first publications using this tool.

The evolution of the surface density was solved using a first order finite difference scheme with an adaptive time-step. The disc stretches from 1 to 500 au with $R_{\rm out}$ = 100 au and it was modeled using a linear grid with 4000 grid cells. For the inner boundary condition, we copied the values of the adjacent cells, and for the outer boundary condition we simply set the density to zero at the outer disc edge. This provides the right solution to the viscous disc problem, and fits the analytically derived surface density profile well out to at least 200 au. We used a stellar mass of 1 $M_\odot$ throughout the simulations and an initial disc accretion rate of $\dot{M}_0 = 10^{-7}\,M_\odot\,{\rm yr}^{-1}$. The accretion rate drops to $2\times10^{-8}\,M_\odot\,{\rm yr}^{-1}$ after 1 Myr, as material drains onto the star. Most simulations were run on 40 cores to speed up the calculations. The typical wall time was 90 h.

Three planets of fixed masses and semimajor axes (except in simulation migration) are included in the simulations, and they were inserted at semimajor axes corresponding to the locations of the major gaps in the disc around the young star HL Tau: at 11.8, 32.3, and 82 au (Kanagawa et al. 2016). The solid population of the disc is represented by 100 000 superparticles (approximately 25 per grid cell). The superparticles were initially placed equidistantly throughout the disc with a radius of 1 μm. The mass of each superparticle was set so as to yield a constant solid-to-gas ratio (also referred to as the metallicity) across the disc. Planetesimal formation was initiated after some time $t_{\rm plan}$, which was varied between the simulations depending on how much time it takes for the planets to clear most of their gaps from dust. Furthermore, we only allowed for planetesimal formation interior to 200 au. This is because our numerical surface density profile starts to diverge from the analytically derived one beyond a few hundred astronomical units; however, since we are only interested in the inner ~100 au where the planets are located, this does not affect the results. Finally the system is evolved for 1 Myr. This long running time is a major motivation for simulating in 1D only.

In the nominal model (simulation #1 in Table 3), we used a turbulent viscosity of 10^{-2}, a turbulent diffusion of 10^{-3}, and an initial solid-to-gas ratio of 0.01. We set the planetary masses ($M_{\rm p}$) to two times their respective pebble isolation mass, and we kept the planets at a fixed position ($V_{\rm p}$ = 0). In this simulation, planetesimal formation was initiated after 5000 yr. To explore how the above mentioned parameters affect the planetesimal formation efficiency and the distribution of dust and pebbles, we conducted a parameter study. The parameter values used in the different simulations can be found in Table 3. In simulations #2–#5, we varied the planetary masses; in simulations #6–#8, we lowered the value of the viscosity parameter and turbulent diffusion; in simulation #9, we increased the initial solid-to-gas ratio in the disc; and in simulation #10, we let the planets migrate radially inward with a constant velocity.

Table 3. Model set up for the simulations in the parameter study.

Run	$\alpha_{\rm visc}$	$\alpha_{\rm turb}$	$\Sigma_{\rm solid}/\Sigma$	$M_{\rm P}$ ($M_{\rm iso}$)	$V_{\rm P}$ (au/Myr)
#1 nominal	10^{-2}	10^{-3}	0.01	2	0
#2 0.50 $M_{\rm iso}$	10^{-2}	10^{-3}	0.01	0.5	0
#3 0.75 $M_{\rm iso}$	10^{-2}	10^{-3}	0.01	0.75	0
#4 1 $M_{\rm iso}$	10^{-2}	10^{-3}	0.01	1	0
#5 3 $M_{\rm iso}$	10^{-2}	10^{-3}	0.01	3	0
#6 lowVisc	10^{-3}	10^{-3}	0.01	2	0
#7 lowTurb	10^{-2}	10^{-4}	0.01	2	0
#8 lowViscTurb	10^{-4}	10^{-4}	0.01	2	0
#9 highMetal	10^{-2}	10^{-3}	0.02	2	0
#10 migration	10^{-2}	10^{-3}	0.01	2	6.3

4. Results

Results on the disc structure, particle distribution, and efficiency of planetesimal formation in the nominal model are presented in Sect. 4.1. In Sect. 4.2 we show how these results change when we no longer include the pressure scaling for the streaming instability, and when planetesimal formation is removed completely. In Sect. 4.3, we varied different disc and planet parameters and investigate how it affects the results. Finally, in Sect. 4.4, we make a comparison between our model for planetesimal formation and the midplane model.

4.1. Nominal model

The parameters used in the nominal model are found in simulation #1 of Table 3. The evolution of the normalized gas surface density across the disc is shown in the top panel of Fig. 1, and the evolution of the solid-to-gas surface density ratio is plotted in the bottom panel. The solid component was divided into planetesimals and dust+pebbles. The evolution of the particle size distribution and the Stokes number is shown in Fig. 2.

From Fig. 1, it is clear that the part of the disc that is closer to the star than the outermost planet becomes depleted of dust and pebbles already after a few hundred thousand years. Meanwhile, the region's exterior to the outermost planet maintains a high solid-to-gas ratio for much longer, and at the end of the simulation, it is still at 25% of the initial value. To understand why this is the case, we look at the evolution of the particle sizes in Fig. 2. Considering the inner part of the disc, particle collisions are frequent and quickly result in the formation of millimeter-sized pebbles, which drift toward the star quickly. The same process results in smaller particle sizes and takes more time in the outer part of the disc. Another feature of the particle size distribution is that it is bimodal. The reason for this is that except for very low relative velocities, coagulation is only possible if the projectile is much less massive than the target (compare the two upper panels of Fig. 11 in Güttler et al. 2010). Hence any coherent size distribution evolves to a bimodal distribution as the largest particles grow in mass, while the small are stuck. The bimodal size distribution nevertheless collapses with time to a narrower size distribution as the remaining small particles are finally swept up by the larger pebbles.

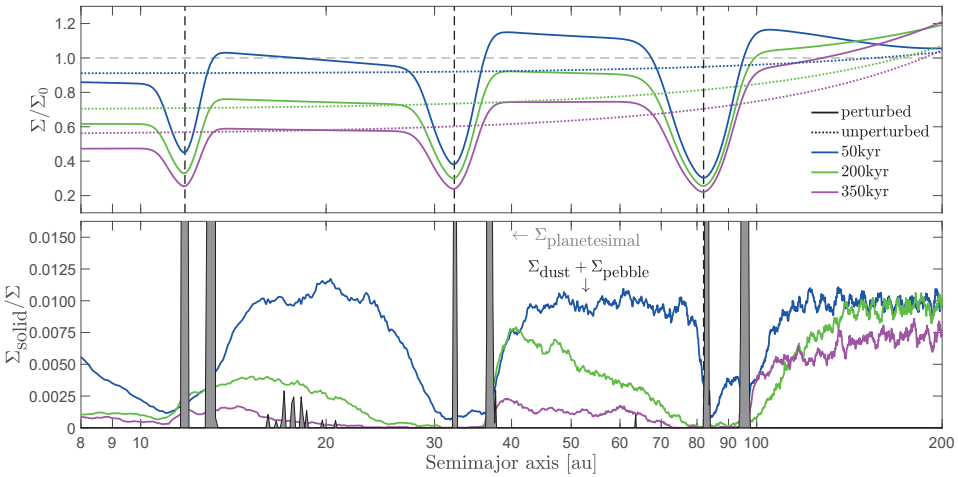

Fig. 1. *Top panel*: evolution of the gas surface density, which is normalized against the initial gas surface density, across the protoplanetary disc for the nominal model with planets (solid lines) and without planets (dotted lines). The vertical dashed lines mark the semimajor axes of the planets, and they coincide with the locations of the three major gaps in the disc around HL Tau (Kanagawa et al. 2016). *Bottom panel*: evolution of the solid-to-gas surface density ratio across the protoplanetary disc for the nominal model. The solid component is divided into planetesimals (marked with gray) and dust+pebbles. Planetesimals form in narrow rings at the location of the gap edges and inside the planetary gaps (the amount of planetesimals formed inside the gaps is negligible). The interplanetary regions are depleted of dust and pebbles within a few hundred thousand years.

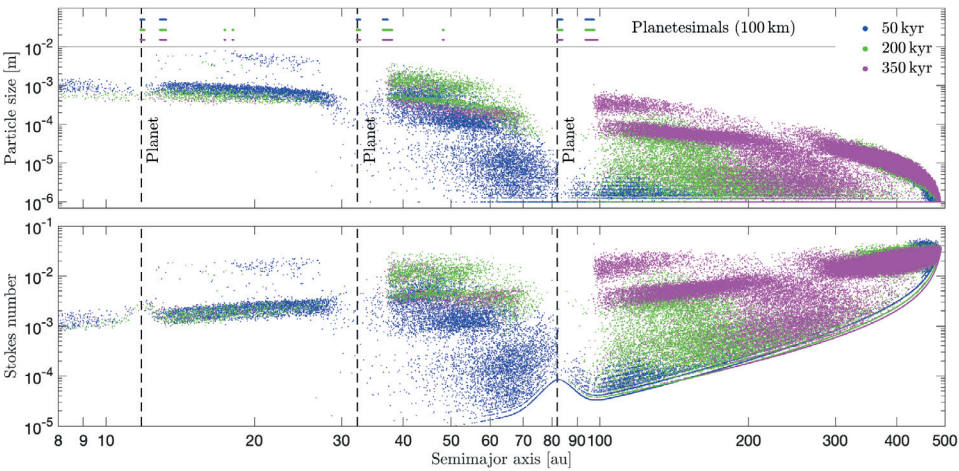

Fig. 2. *Top panel*: size distribution of particles in the protoplanetary disc at different times during disc evolution for our nominal model. The semimajor axes of the formed planetesimals are indicated at the top of the plot. Particles were initialized with an equal spacing all over the disc and with a radius of 1 μm. Efficient coagulation and high drift velocities in the inner disc result in a depletion of the interplanetary regions after only a few 100 000 yr. These processes occur on a longer timescale in the outer disc. *Bottom panel*: particle Stokes number versus semimajor axis for the same data as in the top panel.

The planetary masses used in the nominal simulation lead to relatively deep gaps, which act as hard barriers that stall all particles with a Stokes number that is larger than a certain critical value (see e.g., Pinilla et al. 2012; Bitsch et al. 2018; Weber et al. 2018). The pebbles formed by coagulation beyond the middle planet have Stokes numbers that are well above this critical value, and they are therefore efficiently trapped at the planetary gap edges. Since no particles make it past the gaps, there is no replenishing of the interplanetary disc regions. Combined with fast radial drift, this is the reason why the solid-to-gas ratio in these regions drops to less than 0.001 after only 500 000 yr.

From Figs. 1 and 2, it is evident that planetesimal formation takes place almost exclusively in narrow rings at the location of the gap edges and inside the planetary gaps. These are locations which correspond to places where the pressure gradient is close to zero, that is, places where there is a pressure bump. When the pressure gradient is close to zero the critical density required for the streaming instability to form filaments becomes very low, and because of this essentially everything that enters the pressure bump is turned into planetesimals. So since everything that goes into the pressure bump is turned into planetesimals, and there is no replenishing of the interplanetary regions, the part of the disc that is closer to the star than the outermost planet becomes empty of dust and pebbles. As is seen in Sect. 4.2 Fig. 3, efficient planetesimal formation at the gap edge of the innermost planet is the reason why no pebbles can make it past that gap to the innermost disc region.

The narrowness of the rings in which planetesimals form is also an effect caused by the dependency of the streaming instability on the pressure gradient. The magnitude and steepness of the pressure bump increases with increasing planetary mass, and for a planetary mass of two pebble isolation masses, the pressure gradient is only close to zero in two very narrow regions. In between these regions, the pressure gradient becomes very high, resulting in that very large critical densities are required to form filaments, which is why no planetesimals form in between the location of the gap edges and inside the planetary gaps.

The pressure maxima inside the planetary gaps are unstable equilibrium points due to the fact that tiny displacements from this point are amplified with time due to divergent drift, but we still formed some planetesimals there because we turned on planetesimal formation before the gaps had been entirely cleared of dust and pebbles. Later on during the simulation, all planetesimals form at the gap edges. A histogram showing the total amount of planetesimals that have formed per semimajor axis bin can be viewed in the uppermost panel of Fig. 4. A total of 280 Earth masses of planetesimals have formed at the end of the nominal simulation. The total amount of mass in planetesimals and dust+pebbles at the end of all the simulations is provided in Table 4 for each ring.

4.2. The cases with no pressure scaling and no planetesimal formation

How efficiently pebbles are converted into planetesimals at the gap edges has a major effect on the distribution of dust and pebbles in the disc. In the nominal model, planetesimals form whenever the critical density required for the streaming instability to form filaments has been reached. Together with the linear pressure scaling this can be thought of as a maximum limiting case for planetesimal formation. If the dependency of the streaming instability on the pressure gradient is weakened or removed, the critical density increases, resulting in more dust and pebbles being left in the rings. It would also result in planetesimals forming in wider regions around the pressure bump. The case with no planetesimal formation at all is of course the minimum limiting case for planetesimal formation, and the real efficiency should be somewhere in between the minimum and maximum case.

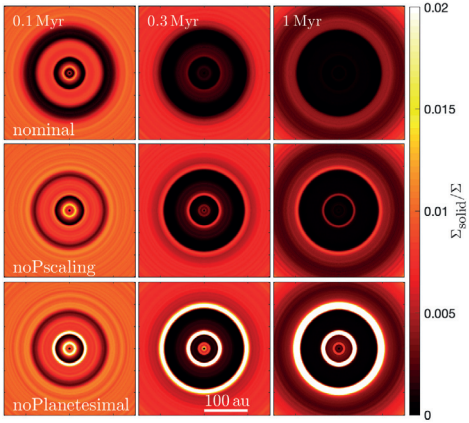

Fig. 3. 2D symmetric disc images of the evolution of the solid-to-gas surface density (excluding the formed planetesimals) for three different versions of the nominal model: the nominal model (*top row*), the nominal model with planetesimal formation but with no dependency on the pressure gradient (*middle row*), and the nominal model without planetesimal formation (*bottom row*). In the nominal model, essentially everything that enters the pressure bump is converted into planetesimals, resulting in a large cavity in the distribution of dust and pebbles. When the pressure dependence is neglected, the critical density required to trigger the streaming instability increases, and we see some rings in the dust and pebble distribution. When planetesimal formation is removed completely, we are left with three rings in which the dust and pebble density is very high.

In Fig. 3, the evolution of the solid-to-gas surface density ratio is shown as 2D surface density plots (here referred to as disc images) for the following: the nominal model; the nominal model with no pressure scaling for planetesimal formation; and the nominal model without planetesimal formation. In the case without planetesimal formation (simulation noPlanetesimal), the disc would be seen to have very bright rings at the positions of the outer gap edges, which is similar to AS 209 (Fedele et al. 2018). The amount of dust and pebbles in each ring is written in Table 4, and it is roughly a hundred Earth masses for the two outermost rings, which corresponds to 3–11 Earth masses per astronomical unit. In contrast, the inner ring only has a few Earth masses of dust and pebbles. Comparing that to the tens of Earth masses of planetesimals that form in the ring in the nominal model, it suggests that millimeter-sized pebbles with low Stokes numbers (i.e., close to the star) can drift past our planetary gaps quite efficiently, but that the efficient planetesimal formation in the nominal model prevents them from doing so.

When planetesimal formation without pressure scaling is included (simulation noPscaling) the solid-to-gas surface density ratio drops drastically in the rings. The two rings, which are still clearly visible, are also much thinner than in the case with no planetesimal formation. The amount of dust and pebbles left

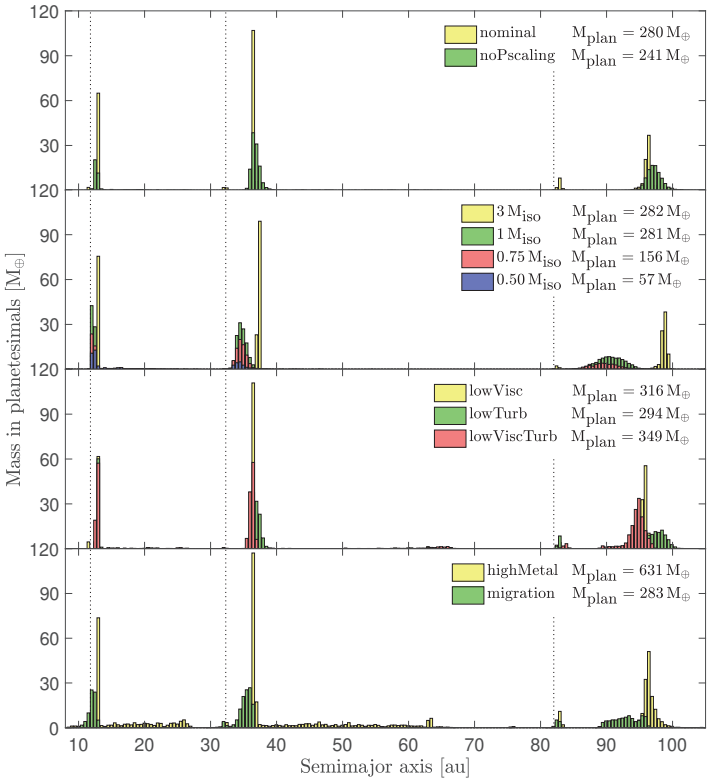

Fig. 4. Histogram showing the total amount of mass in planetesimals that has formed at different locations in the disc after 1 Myr for each simulation in the parameter study. The dotted vertical lines indicate the semimajor axes of the planets. When the pressure scaling is removed (simulation "noPscaling"), the critical density required for forming planetesimals at the gap edge increases, resulting in less planetesimal formation. The amount of planetesimal formation does not vary a lot between the simulations where the planetary mass is larger than the pebble isolation mass since millimeter pebbles cannot drift past the gaps and planetesimal formation is extremely efficient where the pressure gradient is close to zero. For planetary masses that are lower than the pebble isolation mass, the amount of planetesimals that form rapidly decreases with decreasing planetary mass. Lowering the viscosity parameter and the turbulent diffusion results in faster drift velocities in the viscously expanding part of the disc. Because of this, more pebbles reach the outermost gap edge and are turned into planetesimals. Increasing the metallicity (simulation highMetal) results in sporadic planetesimal formation in the interplanetary regions. When a constant migration speed is added to the planets, the location of the gap edges are shifted inward with time, resulting in the region where planetesimals form to shift inward accordingly.

in these rings are now on the order of a few Earth masses, which corresponds to a quarter of an Earth mass per astronomical unit. When pressure scaling is applied (i.e., the nominal model) the amount of early transport through the gaps decreases, resulting in a faster pebble depletion. After 1 Myr, all rings that were previously visible interior to the outermost planet have disappeared, and we are left with a cavity of roughly 100 au in size in the dust and pebble distribution. A comparison between the amount of planetesimals that form, as well as where they form, in simulations with and without the pressure scaling can be seen in the top panel of Fig. 4. The differences between the simulations in Fig. 3 tells us that two discs that are similar in all aspects except for in the efficiency of planetesimal formation could come across as completely different in observations (see discussion in Sect. 7.3 on the efficiency of the streaming instability).

4.3. Parameter study

To explore how different parameters affect the planetesimal formation efficiency and the distribution of dust and pebbles in the disc, we conducted a parameter study. The values of the parameters which we investigate can be found in Table 3. A histogram showing the total amount of mass locked up in planetesimals at different semimajor axes after 1 Myr is presented in Fig. 4 for all simulations in the parameter study. The evolution of the dust and pebble surface density relative to the gas surface

Table 4. Total amount of mass in dust+pebbles and planetesimals in each ring at the end of the simulations.

	Inner ring		Middle ring		Outer ring	
Run	dust+pebbles	planetesimals	dust+pebbles	planetesimals	dust+pebbles	planetesimals
#1 nominal	0.01 $M_\oplus$	68 $M_\oplus$	0.1 $M_\oplus$	116 $M_\oplus$	3.7 $M_\oplus$	94 $M_\oplus$
noPscaling	0.05	34	2.1	110	7.7	90
noPlanetesimal	2.7		95		97	
#2 0.50 $M_{\rm iso}$	1.3	27	2.7	19	8.3	2.1
#3 0.75 $M_{\rm iso}$	1.0	40	2.4	72	6.4	41
#4 1 $M_{\rm iso}$	0.007	71	0.2	116	4.7	92
#5 3 $M_{\rm iso}$	0.1	76	0.1	122	3.5	84
#6 lowVisc	0.5	69	0.1	120	3.7	126
#7 lowTurb	0.02	66	0.07	105	11	96
#8 lowViscTurb	0.6	76	1.8	109	13	151
#9 highMetal	0	83	0.03	152	1.7	169
#10 migration	0	0	0.002	2.0	2.7	94
			Maximum grain size 100 μm			
#1 nominal	0.05	39	1.3	112	5.8	65
noPscaling	1.8	0.02	7.5	55	16	48
noPlanetesimal	4.0		28		61	
#3 0.75 $M_{\rm iso}$	2.2	0.1	6.0	37	15	38
#4 1 $M_{\rm iso}$	0.1	55	1.7	106	12	66
#6 lowVisc	10	0.02	4.6	60	3.2	106
#7 lowTurb	0	40	3.3	95	12	71

Notes. The inner ring edges were chosen to be the semimajor axes of the planets, and the outer ring edges were chosen to be four gas scale heights away from this location. The region where particles pile-up varies with, e.g., the planetary mass and the level of turbulence in the disc, but for simplicity and for the sake of easy comparison purposes, we used the same criteria for the ring widths in all simulations. The gas scale height at the location of the three planets starting at the inner one are as follows: 0.58, 2.12 and 7.03 au. These are the gas scale heights at the initial locations of the planets. In simulation #10, the final semimajor axes of the planets are 5.48, 25.98 and 75.676 au. The corresponding gas scale heights are: 0.22, 1.61, and 6.34 au.

density is presented in Fig. 5 as 2D symmetric disc images for the same simulations. The total amount of mass in planetesimals and dust+pebbles in each ring can be found in Table 4. The evolution of the particle size distribution for a few interesting simulations in the parameter study is shown in Fig. B.1.

4.3.1. Planetary mass

The planetary mass is the main controller of the width and depth of the planetary gap as well as the radial pressure gradient. The width of the gap determines where pebbles are trapped, and thus the location of planetesimal formation. The planetesimal formation efficiency is strongly related to the strength of the pressure maxima, both via the scaling of the streaming instability with the radial pressure gradient and via the efficiency of particle trapping. The distribution of dust and pebbles for simulations with varying planetary masses is shown in Fig. 5 (simulations nominal, 0.50 $M_{\rm iso}$, 0.75 $M_{\rm iso}$, 1 $M_{\rm iso}$ and 3 $M_{\rm iso}$).

For the simulations 0.50 $M_{\rm iso}$ and 0.75 $M_{\rm iso}$, we used a planetary mass that is lower than the pebble isolation mass. In these simulations dust and pebbles are partly transported through the planetary gaps, resulting in a continuous replenishing of the interplanetary regions and the region interior to the innermost planet. There is a small pile-up of pebbles at the gap edges, resulting in a gap-and-ring-like structure. As can be seen in Fig. 4, the amount of planetesimals that form decreases quickly with decreasing planetary mass. By lowering the planetary mass to 25% below the pebble isolation mass, the amount of pebbles that are converted into planetesimals is halved. Since the radial pressure gradient is shallow around the gap edges, planetesimals form in relatively wide regions as opposed to in two narrow rings, such as in the nominal model. A plot of the size distribution of particles for simulation 0.75 $M_{\rm iso}$ can be viewed in Fig. B.1.

In the simulations nominal, 1 $M_{\rm iso}$ and 3 $M_{\rm iso}$, the planetary masses are two, one, and three times the pebble isolation mass. For these cases, the amount of mass converted into planetesimals does not change with increasing planetary mass. This is due to two reasons: (1) the planetary gaps act as hard barriers, which prevent any pebbles from passing through; (2) there are pressure maxima outside all gaps, which efficiently turn most or all pebbles into planetesimals. The locations where planetesimals form nevertheless do change a bit, since the widened gap and the steepened pressure gradient result in planetesimals forming further away from the planet and in narrower regions. In summary, all simulations with planetary masses equal to or above the pebble isolation mass appear as discs with large central cavities, with the only difference being a slight dependence of the width of the cavity and the width of the rings on the planetary mass.

4.3.2. Viscous and turbulent α

The viscosity parameter $\alpha_{\rm visc}$ governs the gas accretion rate onto the central star, and it also enters the particle drift equation via the radial gas velocity $v_{\rm R}$. The turbulent diffusion $\alpha_{\rm turb}$ governs the turbulent speed of particles, which in turn affects the frequency of particle collisions as well as the collision velocities. The values inferred from observations of these parameters vary a lot in the literature. In Pinte et al. (2016), they find a value of

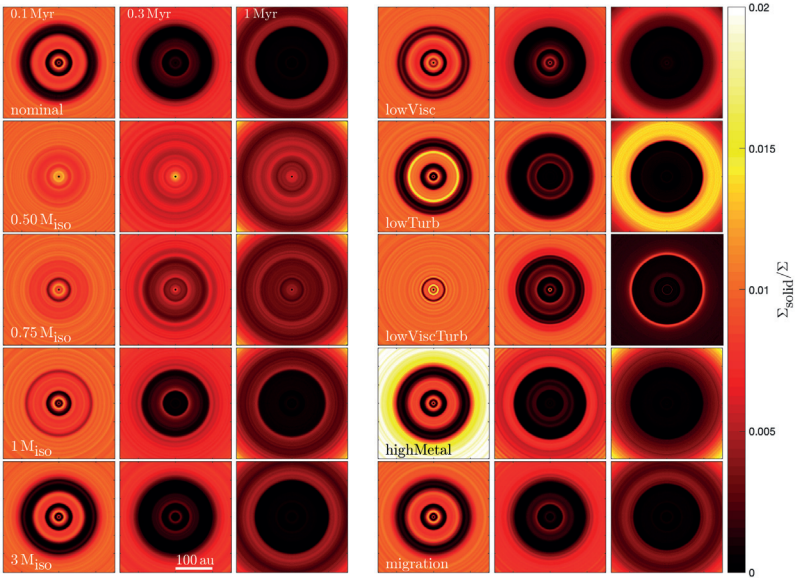

Fig. 5. 2D symmetric disc images of the evolution of the solid-to-gas surface density excluding planetesimals for all simulations in the parameter study. In the nominal simulation where we used a planetary mass of two times the pebble isolation mass fast pebble drift, little or no transport through the planetary gaps and efficient planetesimal formation at the gap edges result in that the part of the disc that is closer to the star than the outermost planet gets depleted of dust and pebbles. In the simulations where the planetary mass is lower than the pebble isolation mass (simulations 0.50 $M_{\rm iso}$ and 0.75 $M_{\rm iso}$), increased transport past the gaps and less planetesimal formation results in a gap-and-ring-like structure. The width of the region where dust and pebbles are trapped depends on the planetary mass. Therefore, when the planetary mass is changed to one or three times the pebble isolation mass (simulations 1 $M_{\rm iso}$ and 3 $M_{\rm iso}$), and we compare to the nominal model, the width of the rings becomes narrower or larger, respectively. Except for this, the results are the same as in the nominal model. In simulation lowVisc, the viscosity parameter is lowered, resulting in a slower clearing of the gaps and interplanetary regions, as well as faster radial drift in the viscously expanding part of the disc. When the turbulent diffusion is lowered (simulation lowTurb), the collisional velocities decrease, resulting in larger particles which drift faster toward the star. This causes the bright ring that can be seen beyond the outermost planet at the end of the simulation. In simulation lowViscTurb, the turbulent diffusion is kept at the same level as in simulation lowTurb, but the viscosity parameter is lowered by an extra order of magnitude compared to simulation lowVisc. The combination results in that essentially all solids in the outer disc reach the outermost planetary gap before the end of the simulation, causing the narrow bright ring seen in the dust-to-gas ratio. In simulation highMetal, the initial solid-to-gas ratio in the disc is increased to 2%, which is a change that does not have a big effect on the appearance of the disc at the end of the simulation. Finally in the last simulation, the planets were given a constant radial velocity directed toward the star (simulation migration), resulting in a smaller radius of the cavity.

a few times 10^{-4} for the turbulent diffusion in the disc around HL Tau. They obtained this value by assuming a standard dust settling model, varying the amount of turbulent diffusion and comparing the resulting millimeter dust scale heights to observations. Pinte et al. (2016) further report an upper limit to the viscosity parameter of 10^{-2} for the HL Tau disc, a value which was calculated by using an estimate of the disc accretion rate from Beck et al. (2010). Other examples are Flaherty et al. (2017) who report an upper limit of 0.003 for the turbulent diffusion in HD 163296 and Flaherty et al. (2018) who report an upper limit of 0.007 for the viscosity parameter in TW Hya.

In the nominal model, we used a value of 10^{-2} for the viscosity parameter and 10^{-3} for the turbulent diffusion. In simulation lowVisc, the viscosity parameter was lowered from 10^{-2} to 10^{-3}. In the simulation lowTurb, the turbulent diffusion was decreased by a factor of 10 from 10^{-3} to 10^{-4}. Finally in simulation lowViscTurb, the viscosity parameter was decreased by another order of magnitude to 10^{-4}, while the turbulent diffusion was kept at the same level as in simulation lowTurb. When lowering the viscosity parameter, the initial disc accretion rate is reduced accordingly, ensuring the same initial disc mass.

Lowering the viscosity parameter in simulation lowVisc results in lower gas accretion rates onto the star, and thus the gas disc evolves on much longer time-scales. Because of this the disc does not expand as much, resulting in a smaller disc size. Another effect on the structure of the gas disc is that there is a more pronounced pile-up of gas at the inner and outer edges of the planetary gaps. Looking at Fig. 5 and comparing simulation lowVisc to the nominal simulation, we see that lowering the viscosity parameter results in a slower clearing of the gaps and interplanetary regions. We also find that pebbles in the viscously expanding part of the disc drift inward more quickly. A smaller viscosity parameter results in the velocity component directed outward becoming lower, making it easier for particles

to drift inward. The faster drift velocities result in more pebbles that reach the outermost planetary gap edge and that are then turned into planetesimals. This is the reason why slightly more planetesimals are formed when using this simulation compared to the nominal one.

In simulation lowTurb, the lowering of the turbulent diffusion results in fewer collisions. Because the particle Stokes numbers in our simulations are low, this also results in lower collisional velocities (if the particle Stokes numbers would have been larger so that the particles start to sediment toward the midplane, this would not have been the case, as the decrease in turbulent velocity would have been compensated for by a decrease in dust scale height). Fewer collisions lead to slower particle growth; however, slower collisional velocities result in a larger maximum pebble size. These larger particles obtain higher drift velocities, resulting in many more pebbles reaching the gap edge of the outermost planet. This is the reason why we see a wide and bright ring in the solid-to-gas surface density at 1 Myr for simulation lowTurb in Fig. 5. The larger particle sizes also require a smaller critical density to trigger the streaming instability, allowing for planetesimals to form further away from the pressure maxima (see Fig. 4).

In simulation lowViscTurb, a fast particle drift toward the star in the outer disc now results in all of the pebbles that still remain at the end of the simulation to be concentrated in a narrow bright ring just beyond the outermost planet. Since more pebbles reach the outermost planetary gap edge, the amount of planetesimal formation at that location has increased compared to the amount in the simulations lowVisc and lowTurb. The gas pile-up at the gap edges is also more pronounced, causing some particles to become trapped at the inner gap edges and leading to some planetesimal formation there (see Fig. B.1 for a plot of the particle size distribution for simulations lowTurb and lowViscTurb).

4.3.3. Metallicity

In simulation highMetal, the initial solid-to-gas ratio was doubled, resulting in an increase in the total amount of formed planetesimals. Since the initial solid abundance is closer to the critical value required for the streaming instability to operate, random local concentrations of pebbles now result in some planetesimal formation in the interplanetary regions. However, since the amplitude of the fluctuations caused by diffusion would be much smaller if a physical number of particles were used, this effect is purely numerical.

4.3.4. Planet migration

In the final simulation of the parameter study (simulation migration) all three planets were given a constant velocity directed toward the star. The migration speed was set to 6.3 AU Myr^{-1}, and thus the semimajor axes of the planets after 1 Myr are 5.48 au, 25.98 au, and 75.676 au. This migration speed is not high enough to significantly perturb the shape of the gap. For faster migrating planets, hydrodynamical studies have shown that the impact on the structure of the disc can be large (see e.g., Li et al. 2009; Meru et al. 2019; Nazari et al. 2019).

Since the migration speed in our simulation is both low enough to preserve the shape of the gap and significantly lower than the particle drift velocity, the amount of planetesimal formation does not change. The location where they form does, however, change. As the pressure maximum moves inward, so does the region of planetesimal formation. For the pebble distribution, the only thing that changes is that the radius of the cavity shrinks with time.

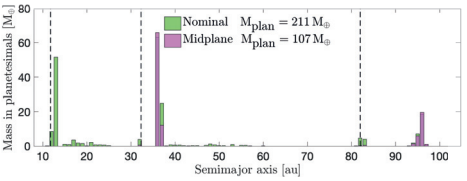

Fig. 6. Histogram showing the total amount of mass in planetesimals that have formed at different locations in the disc after 300 kyr, for the nominal model and the midplane model. The amount of planetesimals formed around the gap edges of the two outermost planets are similar in both models; however, this is not the case at the innermost planetary gap edge. The settling toward the midplane is not efficient enough to counteract the stirring by turbulence in this region, and thus a dust-to-gas density ratio of unity in the midplane is never reached.

4.4. Two planetesimal formation models

The planetesimal formation model used in our simulations was derived from hydrodynamical simulations of particle-gas interactions by Carrera et al. (2015) and Yang et al. (2017). This model tells us whether or not filaments emerge based on the combination of the particle Stokes number and surface density. As mentioned at the end of Sect. 2.5, some authors use a criterion based on the midplane dust-to-gas ratio instead (the midplane model). We compare this criterion with the one used in this paper by performing two simulations that are identical in all aspects except for the planetesimal formation model. We used linear pressure scaling in both simulations. The results of the comparison are presented in Figs. 6 and 7.

The two models produce very similar amounts of planetesimals at the outermost planetary gap-edge, while there are no significant differences in the surface density profiles. Around the second planetary gap-edge, the midplane model produces slightly less planetesimals than the nominal model, resulting in a ring of pebbles that does not exist in the nominal model. At the innermost planetary gap-edge the midplane model fails at producing any planetesimals. This is because the settling toward the midplane is not efficient enough to counteract the stirring by turbulence. Because of this, a large population of dust and pebbles remain at this location. Transport of solids through the planetary gap further results in that the innermost disc region does not get depleted of solids within 300 kyr, which is the case in the nominal model.

In the simulations above, we have taken the dependency of the streaming instability with the pressure gradient into account. If the linear pressure scaling were to be removed, the midplane model does not produce any planetesimals at all. This is because the millimeter-sized pebbles created through coagulation are stirred too much by turbulence, and thus a midplane dust-to-gas ratio of unity is never reached.

5. Lowering the particle size to 100 μm

The dust growth model of Güttler et al. (2010) employed in this work, which is based on a combination of laboratory collision experiments and theoretical models, results in the formation of millimeter-sized pebbles in the inner part of the disc with decreasing grain sizes as the semimajor axis increases. These

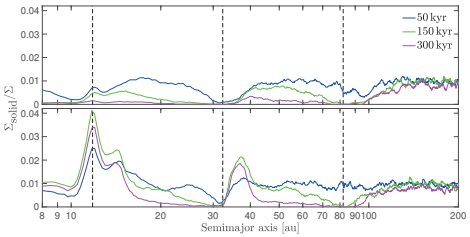

Fig. 7. Evolution of the solid-to-gas surface density ratio across the protoplanetary disc for the nominal model (*top panel*) and the midplane model (*bottom panel*). The solid component includes dust and pebbles, whereas planetesimals are excluded. The two models produce very similar amounts of planetesimals around the outermost planetary gap-edge, resulting in very similar solid-to-gas surface density ratios in this part of the disc. Around the second planetary gap-edge, the midplane model is not quite as efficient at forming planetesimals as the nominal model, and it leaves a ring of dust and pebbles behind that does not exist in the nominal model. At the innermost planetary gap-edge, there is no planetesimal formation at all in the midplane model, and thus the solid-to-gas surface density ratios in the two models are very different.

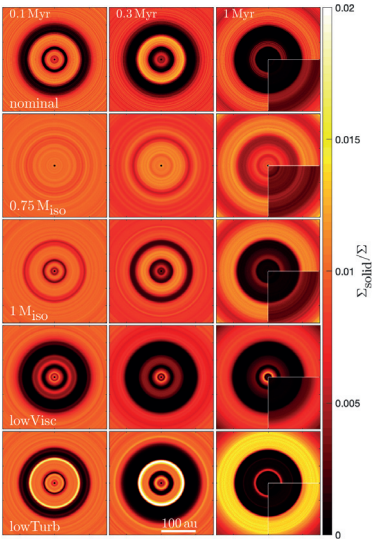

Fig. 8. 2D symmetric disc images for simulations where the maximum particle size was limited to 100 μm. For the sake of easy comparison purposes, images of the same simulations but without the maximum limit on the particle size are added on top of the images at 1 Myr. With smaller particle sizes, it becomes harder to trigger planetesimal formation; the result is that more dust and pebbles remain in the rings at the end of the simulation.

sizes are slightly smaller than the grain size estimates that were obtained from the spectral index of the dust opacity coefficient at millimeter and submillimeter wavelengths, which report maximum grain sizes between 1 millimeter in the outer disc and a few centimeters in the inner disc (e.g., Ricci et al. 2010; Pérez et al. 2012; ALMA Partnership et al. 2015; Tazzari et al. 2016). The estimates based on the spectral index of the dust opacity coefficient nevertheless are not in agreement with the maximum grain sizes that were obtained from observations of polarized emission due to self-scattering, which are consistently around 100 μm, that is, smaller than the pebbles in our simulations (e.g., Kataoka et al. 2017; Hull et al. 2018; Ohashi et al. 2018; Mori et al. 2019).

Even when applied to the same source, the maximum grain sizes obtained from the different methods are inconsistent. As an example, we consider the disc around HL Tau. Carrasco-González et al. (2019) calculated the maximum grain size in HL Tau by fitting the millimeter spectral energy distribution without any assumptions about the optical depth of the emission. By also including the effects of scattering and absorption in the dust opacity, they obtained a maximum grain size of a few millimeters. Kataoka et al. (2017) instead estimated the maximum grain size in HL Tau to be 100 μm from observations of millimeter-wave polarization.

If the maximum grain size was in fact around 100 μm, as suggested by observations of millimeter-wave polarization, it could have a large impact on our results. In the model of Güttler et al. (2010), particle collisions result in the formation of millimeter-sized particles; however, recently Okuzumi & Tazaki (2019) have shown that dust growth models can result in 100 μm-sized particles if the particles are covered by nonsticky CO_2 ice. By incorporating the composition-dependent sticking into a model of dust evolution, they were able to successfully reproduce the polarization pattern seen in the disc around HL Tau.

Decreasing the particle size results in smaller particle Stokes numbers; however, it should be mentioned that this is not the only way to obtain low particle Stokes numbers. If gas discs are in fact much more massive than the minimum mass solar nebula, then millimeter-sized particles would have smaller Stokes numbers than they have in our simulations (Powell et al. 2019). In such a disc, particle drift would be slower and the critical density required for the streaming instability to form filaments would be higher.

5.1. Imposing a maximum particle size of 100 μm in simulations

We study the effect of having a maximum grain size of 100 μm in our simulations by artificially imposing the maximum pebble size to be 100 μm in the coagulation part of our code. In the bottom panel of Fig. B.1, we show the resulting particle size distribution across the disc for the nominal simulation. The solid-to-gas ratios for the following simulations are shown in Fig. 8: nominal, 0.75 M_{iso}, 1 M_{iso}, lowVisc, and lowTurb, with 100 μm particles.

In the nominal simulation, 218 $M_\oplus$ of planetesimals were formed. The amount of dust and pebbles left in the rings is larger compared to the nominal simulation with millimeter-sized particles (see Table 4). Regarding the distribution of pebbles, the Stokes number at the location of the outermost planet is still large enough to prevent most pebbles from drifting across the gap. At the locations of the two innermost planets, this is no longer true. However, because of the linear scaling of the streaming instability with the pressure gradient, pebbles at the gap edges are turned into planetesimals before they have time to drift across the gaps. Therefore, the region interior to the middle planet becomes depleted of dust and pebbles.

When the planetary mass decreases to 0.75 $M_{\rm iso}$, the global solid-to-gas ratio remains at around 1% throughout the simulation (see second row of Fig. 8). There are still some rings and gaps that are visible in the particle distribution, and the amount of planetesimals that formed is now 80 $M_\oplus$. For a planetary mass of 1 $M_{\rm iso}$, it takes more time to clear the interplanetary regions of pebbles than in the nominal simulation, but at the end of the simulation, the solid-to-gas density ratio across the disc looks very similar. The total mass in planetesimals for this simulation is 232 $M_\oplus$.

A lower viscosity (simulation lowVisc) results in faster drift in the viscously expanding part of the disc and more planetesimal formation at the outer gap edge – in total 237 $M_\oplus$ of planetesimals were formed in this simulation. There is no planetesimal formation at the innermost gap edge in this simulation, and instead there are ten Earth masses of pebbles trapped in that ring, corresponding to around five Earth masses per astronomical unit. The amount of pebbles left in the ring outside the middle planet has also increased compared to the nominal model.

When the turbulent diffusion was lowered by an order of magnitude to 10^{-4} (simulation lowTurb), the amount of planetesimals that formed decreased to 192 $M_\oplus$. Lower collisional velocities result in particles growing to 100 μm further out in the disc. These particles obtain higher drift velocities and reach the gap edge of the outermost planet within a million years, causing the wide and bright ring seen in the bottom row of Fig. 8.

5.2. The cases with no pressure scaling and no planetesimal formation

Next we study how the distribution of dust and pebbles change when (1) the dependency of the streaming instability on the pressure gradient is removed, and (2) when planetesimal formation is removed completely (analogous to Sect. 4.2 but for the case with a maximum grain size of 100 μm). The results are presented in Fig. 9.

There is little or no transport through the outermost planetary gap in all simulations; however, the 100 μm sized pebbles do drift past the two innermost gaps in the simulation without planetesimal formation (simulation noPlanetesimal). In the simulation without pressure scaling (simulation noPscaling), some of the pebbles that would otherwise have made it past the gaps are now converted into planetesimals instead, resulting in a quicker depletion of the region interior to the middle planet. Apart from this, simulation noPlanetesimal and simulation noPscaling result in relatively similar images, with the major difference being the brightness and width of the rings. When pressure scaling is added (simulation nominal), the picture changes quite a bit. Efficient planetesimal formation now prevents most pebbles from crossing the middle planetary gap, resulting in that the region interior of this becomes void of pebbles.

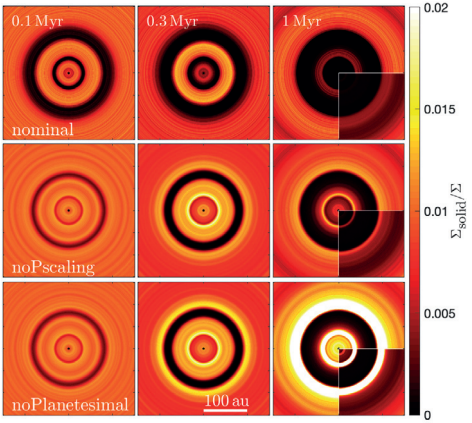

Fig. 9. 2D symmetric disc images of the evolution of the solid-to-gas surface density for three different versions of the nominal model where the maximum grain size was limited to 100 μm: the nominal model (*top row*), the nominal model with planetesimal formation but no dependency on the pressure gradient (*middle row*), and the nominal model without planetesimal formation (*bottom row*). For the sake of easy comparison purposes, images of the same simulations but without the maximum limit on the particle size were added on top of the images at 1 Myr. When the dependency on the pressure gradient is included, efficient planetesimal formation at the gap edges prevents particles from passing through the gaps, resulting in a depletion of the part of the disc that is closer to the star than the middle planet. This does not happen in the other cases, instead several bright rings are seen in the dust-to-gas ratio, and dust is also left in the innermost region of the disc.

6. Comparison to observations

6.1. Dust mass estimates in rings

The amount of dust and pebbles remaining in the rings after 1 Myr varies a lot in our simulations (see Table 4). For example, the amount of dust and pebbles remaining in the outermost ring ranges from 1.7 to 13 Earth masses for simulations in the parameter study. We compare these amounts to dust mass estimates by Dullemond et al. (2018) for rings in the DSHARP survey.

Dullemond et al. (2018) find that the amount of dust stored in each ring is of the order tens of Earth masses. For example, AS 209 was estimated to have around 30 Earth masses of dust trapped in the ring at 69−79 au and 70 Earth masses trapped in the ring at 115−125 au. In general the amount of dust stored in the rings ranges from 1 to 10 Earth masses per astronomical unit (see Table 2 in Dullemond et al. 2018). It should be mentioned that there is much uncertainty as to these estimates, mainly due to the uncertainty in the calculation of the dust opacities.

Comparing with our simulations, the only cases where we have more than ten Earth masses of pebbles remaining in one or several narrow rings after 1 Myr are when we either (1) ignore planetesimal formation completely; (2) ignore the pressure scaling; or (3) use a maximum pebble size of 100 μm (we note that the midplane model is discussed separately below). From Table 4, we find that we have between 2 and 11 Earth masses of dust and pebbles per astronomical unit left in the rings when planetesimal formation is neglected (simulation noPlanetesimal). When the pressure scaling is removed (simulation noPscaling), this value decreases to 0–0.65 Earth masses per astronomical units. Another example is simulation lowVisc for 100 μm-sized particles, where we find that five Earth masses of dust and pebbles per astronomical unit is left in the inner ring, and 0.5 Earth masses per astronomical unit is left in the middle ring.

In order to match the dust mass estimations in the DSHARP rings, we would thus either need a very low planetesimal formation efficiency or some mechanism for destroying the planetesimals and thus replenishing the dust population in the rings (this

is discussed in Sect. 7.2). One mechanism, which would result in a higher dust population and likely lead to less planetesimal formation, is efficient fragmentation in the pressure bumps; see Sect. 7.1 for a discussion on this.

The dust masses quoted in Table 4 are for simulations in which we used the planetesimal formation criteria from Yang et al. (2017). In Sect. 4.4 where we compare this criteria to the midplane model, it is shown that the midplane model produces less planetesimals and results in a larger amount of dust and pebbles remaining in the rings. More precisely, after 300 000 yr, the amount of dust and pebbles remaining in the ring at the innermost planet is roughly $9\,M_\oplus\,\mathrm{au}^{-1}$, and the corresponding amount at the middle planet is $3\,M_\oplus\,\mathrm{au}^{-1}$. For the nominal model after 300 000 yr, the amount of dust and pebbles remaining in the same rings is roughly $0.6{-}0.7\,M_\oplus\,\mathrm{au}^{-1}$. Although the values from the midplane model appear to be a better match to the estimates by Dullemond et al. (2018), the midplane criterion for planetesimal formation has not been confirmed by any hydrodynamical simulation that we know of yet. Since a more detailed comparison of the two planetesimal formation models is beyond the scope of this paper, the rest of the paper is only concerned with the simulations done with our nominal model for planetesimal formation.

6.2. Global dust distribution

Depending on what planet and disc parameters are used, we end up with very different pebble distributions across the disc. For simulations with a maximum grain size of around one millimeter, high drift velocities and little or no dust transportation through the planetary gaps result in the interplanetary regions becoming depleted of pebbles within a few hundred thousand years. This occurs in all simulations except for the ones with planetary masses that are lower than the pebble isolation mass. Combined with efficient planetesimal formation in the pressure bumps, the region interior to the outermost planet becomes devoid of pebbles (see Fig. 5). Such discs with large central cavities resemble transition discs (e.g., Andrews et al. 2011). However, we want to emphasize that we only show the dust-to-gas surface density ratios in this work. We have not looked into how these discs would actually appear in observations of millimeter continuum emission.

If the planetesimal formation efficiency in nature is lower than assumed in our simulations, so that a significant fraction of millimeter-sized pebbles remain in the pressure bumps, then the discs instead evolve a few very narrow and bright rings, which is similar to the structure observed in the protoplanetary disc around AS 209 (Fedele et al. 2018). This can be seen in Figs. 3 and 9 where we present simulations with no planetesimal formation and no dependency on the pressure gradient. Such discs with a high pebble density in the rings could also be created and maintained through cycles of planetesimal formation and planetesimal destruction and/or efficient fragmentation in the rings (see Drazkowska et al. 2019).

Most observed protoplanetary discs with dust rings nevertheless do not appear as AS 209; instead, they have emission coming more evenly from the whole protoplanetary disc (e.g., ALMA Partnership et al. 2015). Such dust distributions could only be obtained in our simulations by using planetary masses that are lower than the pebble isolation mass. Generally, if particles are transported through the planetary gaps efficiently, then the regions between the planets are continuously replenished as long as there is a large enough repository of solids far out in the disc. In our nominal simulation, the outer disc still holds around 100 Earth masses of solids after 1 Myr. If dust transport through the gaps is efficient, it further reduces the solid-to-gas ratios in the pressure bumps, leading to less planetesimal formation. Possible reasons for why dust transport through planetary gaps could be more efficient than in our simulations are discussed in Sects. 7.2–7.4.

Introducing a maximum grain size of $100\,\mu$m results in the interplanetary regions becoming depleted of their pebble mass on a longer time-scale of up to 1 million years. In these simulations, one ring of pebbles remains visible inside the cavity after 1 Myr even for planetary masses that are larger than the pebble isolation mass. As a comparison, the stars in the DSHARP survey have ages between a few hundred thousand to 10 million years (Andrews et al. 2018), so we know that at least some discs must be able to maintain a high pebble density in the rings for a long time.

6.3. Solar System constraints on planetesimal formation

Since the planetesimals in our model form at the edges of planetary gaps, there must have existed an earlier population of planetesimals, which participated in the formation of these gap-opening planets. Those planetesimals should have formed by some other mechanism than the one proposed in our work, for example, through particle pile-ups outside snow lines (Drążkowska & Alibert 2017; Schoonenberg & Ormel 2017). Our planetesimals would thus represent a second generation of planetesimals, which only form once the first gap-opening planet has appeared in the disc, a scenario that fits in well with Solar System observations.

In Kruijer et al. (2017), they used isotope measurements of iron meteorites together with thermal modeling of bodies internally heated by ^{26}Al decay to study the formation of planetesimals in the asteroid belt. From this study, they conclude the following about the parent bodies of noncarbonaceous (NC) and carbonaceous (CC) iron meteorite: (1) they accreted at different times, within 0.4 respective 0.9 Myr after Solar System formation; (2) they accreted at different locations in the disc, with the CC meteorites accreting further out; and (3) they must have remained separated from before 0.9 until 3–4 Myr after Solar System formation. This picture could be neatly explained by the formation of the CC iron meteorite parent bodies at the edge of Jupiter's gap.

The first population of planetesimals form early before 0.4 Myr (the NC iron meteorites). Then at some time before 0.9 Myr, Jupiter reaches the pebble isolation mass and shuts off the flow of pebbles to the inner Solar System. The pressure maximum generated at the edge of Jupiter's gap promotes planetesimal formation and results in a second generation of planetesimals (the CC iron meteorites). Once Jupiter has reached the pebble isolation mass, it continues to grow slowly for a few million years, keeping the NC and CC populations separate. Then at 3–4 Myr after Solar System formation, something occurs that scatters the population of CC iron meteorites toward the inner Solar System and causes them to mix with the NC population. This could be the onset of runaway gas accretion (Kruijer et al. 2017) or interactions with an outer giant planet (Ronnet et al. 2018).

7. Shortcomings of the model

7.1. A proper handle on fragmentation

We used a collision algorithm where target particles are reduced to the mass of the projectiles in the event of a destructive

collision. This is not fully realistic because destructive collisions should result in the formation of multiple fragments, and it prevents us from recovering very small particle sizes. Blum & Münch (1993) showed that when two similar-sized dust particles collide at a velocity higher than the fragmentation threshold, both particles are disrupted into a power-law size distribution. A significant fraction of the mass in such a collision becomes concentrated in the largest particle sizes (Birnstiel et al. 2011; Bukhari Syed et al. 2017). Since most mass is supposed to be tied up in the largest particle sizes, our simplified algorithm is still justified, but it prevents the formation of small dust particles that could make it past the planetary gap. These particles could recoagulate interior to the gap and result in a population of millimeter-sized particles in the interplanetary region.

Drazkowska et al. (2019) used an advanced 2D coagulation model to study the dust evolution in a disc that is being perturbed by a Jupiter-mass planet. They find that fragmentation at the gap edge is indeed important. In their simulations, large grains that are trapped inside the pressure bump fragment and replenish the population of dust, which can then pass through the planetary gaps. This process thus leads to a continuous dust flux through the gaps. Since this process removes solids from the pressure bump, it should also result in less planetesimal formation; however, a comparison between the timescales for drift, fragmentation, and planetesimal formation would be required in order to further assess this.

7.2. Destruction of planetesimals

In our simulations, we only looked at where planetesimals form and how much mass is turned into planetesimals. This means that we did not investigate what happens to the planetesimals once they have formed. The processes which are likely to be important in determining the fate of planetesimals at the edge of planetary gaps are: dynamical interactions with the planet, dynamical interactions with other planetesimals, and sublimation and erosion due to the flow of gas. These processes will be the subject of a follow-up study.

If the planetesimals are not removed from the gap edge directly after formation, then the density of planetesimals in this region should become very high. In such regions planetesimal collisions are likely to be frequent, and as in debris discs such events result in the production of dust (Wyatt 2008). Another process that could result in a replenishing of the dust population in the pressure bumps is planetesimal sublimation due to bow shocks (Tanaka et al. 2013). The heating and sublimation of the planetesimals result in a shrinking of the planetesimal size and the vapor can form dust particles through recondensation. How efficient and relevant these processes are for the production of dust in a pressure bump remains to be studied.

7.3. The streaming instability may not be 100% efficient

We assume in our model that whenever the critical density to trigger the streaming instability is reached, planetesimals form. The planetesimal formation algorithm used in this study results in a maximum efficiency for planetesimal formation. A calculation of the actual formation efficiency would require taking into account the timescale for collapse into planetesimals, the timescale for particles to drift across the gap, turbulence, and many other effects. However, in simulations where there is no transport of pebbles across the gaps, the efficiency should not play a big role. It does not matter if it takes a hundred years or a hundred thousand years to form planetesimals since the particles remain trapped anyways. In simulations where pebbles are able to make it past the gaps, such as in the simulations with 100 micron-sized particles, the efficiency for planetesimal formation becomes much more important.

One mechanism, which would likely result in less planetesimal formation, is efficient fragmentation in the pressure bump, which is discussed in Sect. 7.1. We also stress that the linear scaling with the pressure gradient is an approximation, and if this relation was less steep or leveled out toward a pressure gradient of zero, more pebbles and dust would be left in the pressure bumps. Furthermore, in 1D simulations we do not need to worry about instabilities at the gap edges. However, if the gaps are deep enough in 2D or 3D simulations, the gap edges may become unstable to form vortices (Hallam & Paardekooper 2017). The triggering of vortices could potentially change the efficiency of planetesimal formation; however, planetesimal formation in such an environment is still poorly understood. Finally, the coagulation model from Güttler et al. (2010) results in a bimodal particle size distribution. In Krapp et al. (2019), it is shown that the streaming instability becomes less efficient when multiple particle sizes are involved. However, the difference in the growth rate between single particles and multiple species appears to vanish when the dust-to-gas ratio is above unity. Therefore, we continued to use the mass averaged Stokes number in our planetesimal formation model, and we did not lower the efficiency when the particle size distribution evolved into bimodal.

7.4. Dust filtration through planetary gaps in 1D versus 2D simulations

There could be a systematic difference in the dust filtration by a planet in 2D simulations relative to our 1D simulations. This is shown by Weber et al. (2018) and Haugbølle et al. (2019) who performed detailed studies of dust filtration through planetary gaps. In these works, they used a dust fluid approach in order to track extremely low values of the dust density. They found that dust is more likely to be transported through the gaps in 2D simulations, although the amount on the interior of the planet orbit is diminished greatly by the filtering. In Drazkowska et al. (2019), they instead found the opposite results when comparing dust filtration in 1D and 2D coagulation simulations. One possible reason for this discrepancy could be that the gap profiles in Drazkowska et al. (2019) were the same in both the 1D and 2D simulations, while in Weber et al. (2018) the density profiles varied between the 1D and 2D simulations. Regardless, it seems clear that dust filtration in 1D simulations does differ from the 2D or 3D case; however, exactly how is still not certain.

7.5. The α-disc model

In the classical α-disc model, a macroscopic viscosity is assumed to drive angular momentum transport throughout the disc. However, the actual origin of this viscosity is not known. Alternatively, the angular momentum may be drained from the protoplanetary disc by strong winds. In such models, mass is primarily removed from the disc surface and not from the midplane. The surface density profile of such wind-driven discs vary a lot in the literature, and while some resemble the classical α-disc model, others have positive density gradients in the inner regions of the disc and multiple density maxima spread across the disc (Gressel et al. 2015; Bai et al. 2016; Suzuki et al. 2016; Béthune et al. 2017; Hu et al. 2019). In such discs, particle drift would be very different from what we use in our model, and our results would therefore change. However we still do not know enough about

what drives angular momentum transport in discs, or what the level of turbulent viscosity and wind transport are, to say anything conclusive about which model is correct. Therefore, here, we decided to stick to the well-understood α-model.

8. Conclusions and future studies

In this work we test the hypothesis that dust trapping at the edges of planetary gaps can lead to planetesimal formation via the streaming instability. To study this, we performed 1D global simulations of dust evolution and planetesimal formation in a protoplanetary disc that is being perturbed by multiple planets. We performed a parameter study to investigate how different particle sizes, disc parameters, and planetary masses affect the efficiency of planetesimal formation. We further compare the simulated pebbles' distribution with protoplanetary disc observations.

The answers we have obtained for the questions posed in the introduction can be summarized as follows:

1. Do planetesimals form at the edges of planetary gaps? Planetesimal formation occurs in all of our simulations and is almost exclusively limited to the edges of planetary gaps.
2. How efficient is this process and how does the efficiency vary with different disc and planet parameters? Planets with masses above the pebble isolation mass trap pebbles efficiently, and in the case of millimeter-sized particles essentially all of these trapped pebbles are converted into planetesimals. As long as the pebbles cannot pass through the gaps, the amount of planetesimals that form does not vary between the simulations, although the region in which they form do change a bit. Decreasing the pebble size to 100 micron results in less efficient conversion of pebbles to planetesimals and more transport through the gaps.
3. What does the distribution of dust and pebbles look like for the different simulations? In the case of millimeter-sized pebbles and planetary masses that are larger than the pebble isolation mass, the region's interior to the outermost planet gets depleted of pebbles in a few hundred thousand years. For planetary masses lower than this, transport through the gaps leads to a constant replenishment of the interplanetary region, resulting in a gap-and-ring like pebble distribution. In the case where the particle size was lowered to 100 μm, there is always at least one ring of pebbles remaining inside the cavity. When we lower the efficiency of planetesimal formation, by ignoring the drop in the metallicity threshold for planetesimal formation with decreasing pressure support, the discs instead appear to have narrow and bright rings.
4. How do these distributions compare with observations of protoplanetary discs? Transition discs with large central cavities are known from observations. Similar discs with large cavities are the general outcome of simulations with massive planets, millimeter-sized pebbles, and efficient planetesimal formation. Discs with narrow and bright rings, which are similar to the outer regions of the disc around the young star AS 209, are the outcome of simulations with massive planets but low planetesimal formation efficiency in the rings. A replenishment of the dust population in the rings, through processes such as fragmentation, planetesimal collisions, or planetesimal evaporation and erosion, could result in similar structures and potentially also aid in transporting particles across the gaps (Drazkowska et al. 2019). Setting the maximum grain size to 100 μm results in multiple rings, longer drift time-scales, and a larger variety in disc structures. Generally, the only simulations that could produce images similar to HL Tau, with multiple gap and ring structures but no strong pebble depletion anywhere in the disc, are simulations with planetary masses that are lower than the pebble isolation mass.

In this work, we have focused on studying the efficiency of planetesimal formation and the locations of the formed planetesimal belts, but we have neglected their further evolution after formation. The processes that are likely to be important in determining the fate of planetesimals that formed at the edges of planetary gaps are as follows: dynamical interactions with the gap-forming planets, planetesimal-planetesimal interactions, and erosion and evaporation by the flow of gas. These processes will be the subject of a follow-up study.

Acknowledgements. The authors wish to thank Alexander J. Mustill and the anonymous referee for helpful comments that led to an improved manuscript. The authors further wish to thank Alessandro Morbidelli for inspiring discussions, and Chao-Chin Yang for comments and advice regarding the planetesimal formation model. L.E., A.J. and B.L. are supported by the European Research Council (ERC Consolidator Grant 724 687-PLANETESYS). A.J. further thanks the Knut and Alice Wallenberg Foundation (Wallenberg Academy Fellow Grant 2017.0287) and the Swedish Research Council (Project Grant 2018-04867) for research support. The computations were performed on resources provided by the Swedish Infrastructure for Computing (SNIC) at the LUNARC-Centre in Lund, and are partially funded by the Royal Physiographic Society of Lund through grants.

References

Abod, C. P., Simon, J. B., Li, R., et al. 2019, ApJ, 883, 192
ALMA Partnership (Brogan, C. L., et al.) 2015, ApJ, 808, L3
Andrews, S. M., Wilner, D. J., Espaillat, C., et al. 2011, ApJ, 732, 42
Andrews, S. M., Wilner, D. J., Zhu, Z., et al. 2016, ApJ, 820, L40
Andrews, S. M., Huang, J., Pérez, L. M., et al. 2018, ApJ, 869, L41
Auffinger, J., & Laibe, G. 2018, MNRAS, 473, 796
Avenhaus, H., Quanz, S. P., Garufi, A., et al. 2018, ApJ, 863, 44
Bai, X.-N., & Stone, J. M. 2010a, ApJ, 722, 1437
Bai, X.-N., & Stone, J. M. 2010b, ApJ, 722, L220
Bai, X.-N., Ye, J., Goodman, J., & Yuan, F. 2016, ApJ, 818, 152
Beck, T. L., Bary, J. S., & McGregor, P. J. 2010, ApJ, 722, 1360
Béthune, W., Lesur, G., & Ferreira, J. 2017, A&A, 600, A75
Birnstiel, T., Ormel, C. W., & Dullemond, C. P. 2011, A&A, 525, A11
Bitsch, B., Morbidelli, A., Johansen, A., et al. 2018, A&A, 612, A30
Blum, J., & Münch, M. 1993, Icarus, 106, 151
Brandenburg, A., & Dobler, W. 2002, Comput. Phys. Commun., 147, 471
Brauer, F., Dullemond, C. P., & Henning, T. 2008, A&A, 480, 859
Bukhari Syed, M., Blum, J., Wahlberg Jansson, K., & Johansen, A. 2017, ApJ, 834, 145
Carrasco-González, C., Sierra, A., Flock, M., et al. 2019, ApJ, 883, 71
Carrera, D., Johansen, A., & Davies, M. B. 2015, A&A, 579, A43
Chiang, E. I., & Goldreich, P. 1997, ApJ, 490, 368
Clarke, C. J., Tazzari, M., Juhasz, A., et al. 2018, ApJ, 866, L6
D'Angelo, G., & Lubow, S. H. 2010, ApJ, 724, 730
Dipierro, G., Price, D., Laibe, G., et al. 2015, MNRAS, 453, L73
Dipierro, G., Ricci, L., Pérez, L., et al. 2018, MNRAS, 475, 5296
Dong, R., Zhu, Z., & Whitney, B. 2015, ApJ, 809, 93
Drążkowska, J., & Alibert, Y. 2017, A&A, 608, A92
Drazkowska, J., Li, S., Birnstiel, T., Stammler, S. M., & Li, H. 2019, ApJ, 885, 91
Dullemond, C. P., Birnstiel, T., Huang, J., et al. 2018, ApJ, 869, L46
Favre, C., Fedele, D., Maud, L., et al. 2019, ApJ, 871, 107
Fedele, D., Carney, M., Hogerheijde, M. R., et al. 2017, A&A, 600, A72
Fedele, D., Tazzari, M., Booth, R., et al. 2018, A&A, 610, A24
Flaherty, K. M., Hughes, A. M., Rose, S. C., et al. 2017, ApJ, 843, 150
Flaherty, K. M., Hughes, A. M., Teague, R., et al. 2018, ApJ, 856, 117
Ginski, C., Stolker, T., Pinilla, P., et al. 2016, A&A, 595, A112
Gressel, O., Turner, N. J., Nelson, R. P., & McNally, C. P. 2015, ApJ, 801, 84
Guillot, T., Ida, S., & Ormel, C. W. 2014, A&A, 572, A72
Güttler, C., Blum, J., Zsom, A., Ormel, C. W., & Dullemond, C. P. 2010, A&A, 513, A56
Hallam, P. D., & Paardekooper, S. J. 2017, MNRAS, 469, 3813
Haugbølle, T., Weber, P., Wielandt, D. P., et al. 2019, AJ, 158, 55
Hayashi, C. 1981, Prog. Theor. Phys. Suppl., 70, 35

Hu, X., Zhu, Z., Okuzumi, S., et al. 2019, ApJ, 885, 36
Hull, C. L. H., Yang, H., Li, Z.-Y., et al. 2018, ApJ, 860, 82
Isella, A., Guidi, G., Testi, L., et al. 2016, Phys. Rev. Lett., 117, 251101
Johansen, A., & Youdin, A. 2007, ApJ, 662, 627
Johansen, A., Ida, S., & Brasser, R. 2019, A&A, 622, A202
Kanagawa, K. D., Tanaka, H., Muto, T., Tanigawa, T., & Takeuchi, T. 2015, MNRAS, 448, 994
Kanagawa, K. D., Muto, T., Tanaka, H., et al. 2016, PASJ, 68, 43
Kataoka, A., Tsukagoshi, T., Pohl, A., et al. 2017, ApJ, 844, L5
Krapp, L., Benítez-Llambay, P., Gressel, O., & Pessah, M. E. 2019, ApJ, 878, L30
Kruijer, T. S., Burkhardt, C., Budde, G., & Kleine, T. 2017, Proc. Natl. Acad. Sci., 114, 6712
Lambrechts, M., Johansen, A., & Morbidelli, A. 2014, A&A, 572, A35
Li, H., Lubow, S. H., Li, S., & Lin, D. N. C. 2009, ApJ, 690, L52
Lin, D. N. C., & Papaloizou, J. 1986, ApJ, 309, 846
Long, F., Pinilla, P., Herczeg, G. J., et al. 2018, ApJ, 869, 17
Long, F., Herczeg, G. J., Harsono, D., et al. 2019, ApJ, 882, 49
Meru, F., Rosotti, G. P., Booth, R. A., Nazari, P., & Clarke, C. J. 2019, MNRAS, 482, 3678
Mori, T., Kataoka, A., Ohashi, S., et al. 2019, ApJ, 883, 16
Nakagawa, Y., Sekiya, M., & Hayashi, C. 1986, Icarus, 67, 375
Nazari, P., Booth, R. A., Clarke, C. J., et al. 2019, MNRAS, 485, 5914
Ohashi, S., Kataoka, A., Nagai, H., et al. 2018, ApJ, 864, 81
Okuzumi, S., & Tazaki, R. 2019, ApJ, 878, 132
Ormel, C. W., & Cuzzi, J. N. 2007, A&A, 466, 413
Paardekooper, S. J., & Mellema, G. 2004, A&A, 425, L9
Papaloizou, J., & Lin, D. N. C. 1984, ApJ, 285, 818
Pérez, L. M., Carpenter, J. M., Chand ler, C. J., et al. 2012, ApJ, 760, L17
Pinilla, P., Benisty, M., & Birnstiel, T. 2012, A&A, 545, A81
Pinilla, P., Flock, M., Ovelar, M. d. J., & Birnstiel, T. 2016, A&A, 596, A81
Pinte, C., Dent, W. R. F., Ménard, F., et al. 2016, ApJ, 816, 25
Powell, D., Murray-Clay, R., Pérez, L. M., Schlichting, H. E., & Rosenthal, M. 2019, ApJ, 878, 116
Pringle, J. E. 1981, ARA&A, 19, 137
Ricci, L., Testi, L., Natta, A., et al. 2010, A&A, 512, A15
Ronnet, T., Mousis, O., Vernazza, P., Lunine, J. I., & Crida, A. 2018, AJ, 155, 224
Ros, K., Johansen, A., Riipinen, I., & Schlesinger, D. 2019, A&A, 629, A65
Schoonenberg, D., & Ormel, C. W. 2017, A&A, 602, A21
Shakura, N. I., & Sunyaev, R. A. 1973, A&A, 500, 33
Stammler, S. M., Drazkowska, J., Birnstiel, T., et al. 2019, ApJ, 884, L5
Suzuki, T. K., Ogihara, M., Morbidelli, A. r., Crida, A., & Guillot, T. 2016, A&A, 596, A74
Takahashi, S. Z., & Inutsuka, S.-i. 2014, ApJ, 794, 55
Tanaka, K. K., Yamamoto, T., Tanaka, H., et al. 2013, ApJ, 764, 120
Tazzari, M., Testi, L., Ercolano, B., et al. 2016, A&A, 588, A53
Teague, R., Semenov, D., Gorti, U., et al. 2017, ApJ, 835, 228
van Boekel, R., Henning, T., Menu, J., et al. 2017, ApJ, 837, 132
Weber, P., Benítez-Llambay, P., Gressel, O., Krapp, L., & Pessah, M. E. 2018, ApJ, 854, 153
Wyatt, M. C. 2008, ARA&A, 46, 339
Yang, C.-C., & Johansen, A. 2014, ApJ, 792, 86
Yang, C. C., Johansen, A., & Carrera, D. 2017, A&A, 606, A80
Yang, C.-C., Mac Low, M.-M., & Johansen, A. 2018, ApJ, 868, 27
Youdin, A. N. 2011, ApJ, 731, 99
Youdin, A. N., & Goodman, J. 2005, ApJ, 620, 459
Youdin, A. N., & Lithwick, Y. 2007, Icarus, 192, 588

Appendix A: Particle collisions

Particle collisions were performed through a Monte Carlo method. Each particle swarm was assigned a total mass M_i, an individual particle mass m_i, and a number density $n_i = M_i/m_i$. The total mass M_i is different for different particles, which is useful in order to resolve a wide range of column densities in the disc.

When two particles collide, we define the larger particle as the target and the smaller particle as the projectile. The rate of interaction (defined below) between the target and the projectile is determined as

$$r_{tp} = \sigma_{tp} v_{tp} n_p \frac{m_p}{m_t} \max(M_t/M_p, 1), \tag{A.1}$$

where σ_{tp} and v_{tp} are the collisional cross section and relative speed between the target (t) and the projectile (p). If the total mass in the projectile is larger than or equal to the total mass in the target, then the interaction time-scale is defined as the time for each target particle in a swarm to collide with its own mass in projectiles. If the total mass in target particles is larger than the total mass in projectiles, we multiplied it by M_t/M_p so that the interaction time-scale is instead the time-scale for all projectile particles to have collided with a target particle.

Equation (A.1) can be rewritten as

$$\begin{aligned} r_{tp} &= \sigma_{tp} v_{tp} n_t \frac{M_p}{M_t} \max(M_t/M_p, 1) \\ &= \sigma_{tp} v_{tp} n_t \max(M_p/M_t, 1). \end{aligned} \tag{A.2}$$

Using that the collisional cross section is $\sigma_{tp} = \pi(s_t + s_p)^2$, we obtain the final equation for the mass doubling rate

$$r_{tp} = \pi(s_t + s_p)^2 v_{jk} n_t \max(M_p/M_t, 1), \tag{A.3}$$

where s is particle radius. The relative speed contains contributions from Brownian motion, differential radial and azimuthal drift, differential reaction to the gas accretion speed, and turbulent speed. The turbulent speed is based on the closed-form expressions of Ormel & Cuzzi (2007), all of the other terms are standard in the literature (see e.g., Brauer et al. 2008).

In order to average over the vertical direction, we assume that the two particle species maintain a Gaussian density profile in the vertical direction and that changes to the target particle by coagulation are immediately diffused over the entire column density of the target particle. Here, we follow a similar approach as Brauer et al. (2008), their Appendix B. The coagulation equation written for a given height z over the midplane is

$$r_{tp}(z) = \pi(s_t + s_p)^2 v_{tp} n_p(z). \tag{A.4}$$

The collision rate averaged over $n_t(z)$ is then

$$\overline{r_{tp}} = \frac{\int r_{tp}(z) n_t(z) \mathrm{d}z}{\int n_t(z) \mathrm{d}z}. \tag{A.5}$$

Assuming a Gaussian density distribution with a midplane number density $n_{0,t}$ and scale-heights H_t and H_p, respectively, the integration yields

$$\overline{r_{tp}} = \pi(s_t + s_p)^2 v_{tp} n_{0,t} \times \frac{1}{\sqrt{1 + (H_t/H_p)^2}}. \tag{A.6}$$

In comparing this to Eq. (A.4), we see that the vertical integration of the coagulation equation can be treated as a simple multiplication factor on the rate of collisions in the midplane.

In order to calculate the number density of particles in the midplane, we divided the mass in each superparticle by the area of the annulus where the particle is present ($2\pi r \Delta r$) and then by $1/[\sqrt{2\pi} H_p]$ to obtain the midplane density. The time-step contribution from particle coagulation is based on the interaction rate r_{ij}. The time-step for a particle i is

$$\tau_i = \frac{1}{\sum_j (r_{ij})}. \tag{A.7}$$

The Monte Carlo time-step is then $\min_i(\tau_i)$ times a numerical factor, which was chosen to be 0.2. Once the time-step was calculated, we looped over all of the particles in a grid cell and all their unique partners. For each particle pair, we drew a random number, and if that number was smaller than $\mathrm{d}t \times r_{ij}$, we let the swarms interact. We based the outcome of collisions on experimental results by Güttler et al. (2010), and we assume that the particles are porous. The possible outcomes of a collision are sticking, bouncing, bouncing with mass transfer, and fragmentation. Sticking means that the target either doubles its mass or multiplies its mass by $(1 + M_p/M_t)$, if $M_p < M_t$. For bouncing with mass transfer, we doubled the mass of the projectile particles and subtracted the projectile particle mass from each target particle. For fragmentation, we set all the target and projectile particles to the mass of the projectile. If there are excess target particles, then they retain their original mass.

Appendix B: Particle size distributions

Figure B.1 shows the size distributions of particles at different times during disc evolution for some selected simulations. When a planetary mass is used that is lower than one pebble isolation mass (top panel), the gaps are never completely depleted of dust and pebbles. The pile-up of material at the gap edges is also much less prominent, and since pebbles are now transported through the planetary gaps, the result is a more even distribution of particles throughout the disc. Since there are more particles in the interplanetary regions, we also get more spontaneous concentrations, leading to more planetesimal formation. A comparison with Fig. 4 shows that the amount of planetesimals forming in the interplanetary regions is still negligible compared to the amount that form at the gap edges.

When the turbulent diffusion is lowered by an order of magnitude to 10^{-4} (second panel), the coagulation time-scale increases. Since it takes more time for particles to grow, it also takes more time for the size distribution to become bimodal. The slow particle growth also results in the drift time-scale being longer initially. However, decreasing the amount of turbulence results in lower collisional speeds, which in turn results in larger particle sizes. For such large particles, the time-scale for drift becomes shorter than in the nominal model. The result is that more particles make it from the exponentially tapered outer disc to the inner 100 au where the planets reside. The larger particle sizes also lead to sporadic concentrations becoming more common, which again result in more planetesimal formation in the interplanetary regions.

In the simulation where both the viscous parameter and the turbulence diffusion were decreased to 10^{-4} (second panel), trapping at the inner gap edges results in a significant amount of planetesimals being formed at these locations. A small bump in the gas surface density profile is created at the beginning of all

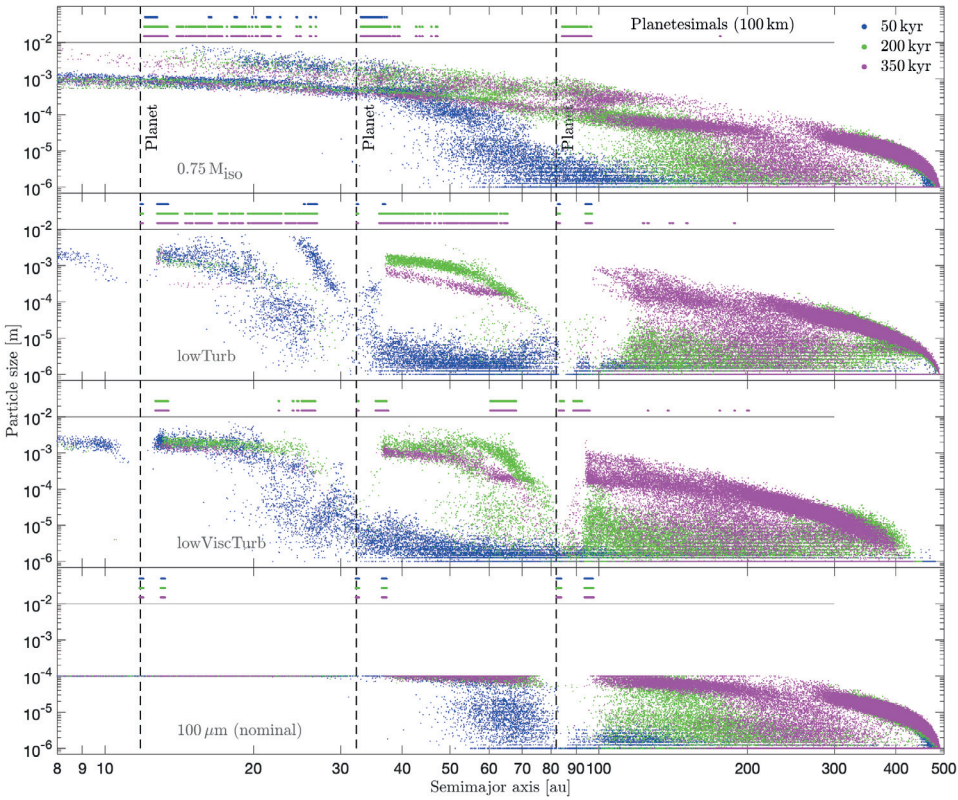

Fig. B.1. Particle size distributions at different times during disc evolution for four different simulations. The semimajor axes of the formed planetesimals are indicated at the top of the plots. *Top panel*: in the simulation with a planetary mass of 0.75 $M_{\rm iso}$, planetesimals form in a wider region around the pressure bump than in the nominal simulation. Less efficient pebble trapping at the pressure bump also results in a more even distribution of dust and pebbles in the disc, with no strong depletion at the location of the planets. *Second panel*: lowering the turbulence diffusion to 10^{-4} results in slower collisional velocities, which results in slower coagulation, but eventually leads to larger particle sizes. *Third panel*: when the viscous parameter is lowered to 10^{-4} as well, we get small bumps in the gas surface density profile at the inner edges of the planetary gaps. Particles become trapped in these bumps, which also result in some planetesimal formation at these locations. *Bottom panel*: this plot shows the implementation of a maximum grain size of 100 μm.

simulations, but when the viscous parameter is high, this bump disappears before planetesimal formation is initiated. For a viscous parameter of 10^{-4}, this pile-up of gas at the inner gap edges is both more prominent and longer lasting than in all other simulations. Since the viscosity is small, the time for gap-clearing is also longer.

In the bottom panel of Fig. B.1, we show the size distribution for particles in the nominal model when a maximum grain size of 100 μm was applied. This constraint does not matter for the particle evolution far out in the disc since particles do not grow that large anyways.

Paper II

A&A 648, A112 (2021)
https://doi.org/10.1051/0004-6361/202039889

Astronomy & Astrophysics

The fate of planetesimals formed at planetary gap edges

Linn E. J. Eriksson[1], Thomas Ronnet[1], and Anders Johansen[1,2]

[1] Lund Observatory, Department of Astronomy and Theoretical Physics, Lund University, Box 43, 221 00 Lund, Sweden
e-mail: linn@astro.lu.se
[2] Center for Star and Planet Formation, GLOBE Institute, University of Copenhagen, Øster Voldgade 5–7, 1350 Copenhagen, Denmark

Received 11 November 2020 / Accepted 4 March 2021

ABSTRACT

The presence of rings and gaps in protoplanetary disks are often ascribed to planet–disk interactions, where dust and pebbles are trapped at the edges of planetary-induced gas gaps. Recent works have shown that these are likely sites for planetesimal formation via the streaming instability. Given the large amount of planetesimals that potentially form at gap edges, we address the question of their fate and their ability to radially transport solids in protoplanetary disks. We performed a series of N-body simulations of planetesimal orbits, taking into account the effect of gas drag and mass loss via ablation. We considered two planetary systems: one that is akin to the young Solar System and another inspired by the structures observed in the protoplanetary disk around HL Tau. In both systems, the proximity to the gap-opening planets results in large orbital excitations, causing the planetesimals to leave their birth locations and spread out across the disk soon after formation. We find that collisions between pairs of planetesimals are rare and should not affect the outcome of our simulations. Collisions with planets occur for ∼1% of the planetesimals in the Solar System and for ∼20% of the planetesimals in the HL Tau system. Planetesimals that end up on eccentric orbits interior of ∼10 au experience efficient ablation and lose all mass before they reach the innermost disk region. In our nominal Solar System simulation, with a stellar gas accretion rate of $\dot{M}_0 = 10^{-7}\,M_\odot\,\mathrm{yr}^{-1}$ and $\alpha = 10^{-2}$, we find that 70% of the initial planetesimal mass has been ablated after 500 kyr. Since the protoplanets are located further away from the star in the HL Tau system, the ablation rate is lower and only 11% of the initial planetesimal mass has been ablated after 1 Myr using the same disk parameters. The ablated material consist of a mixture of solid grains and vaporized ices, where a large fraction of the vaporized ices re-condense to form solid ice. Assuming that the solid grains and ices grow to pebbles in the disk midplane, this results in a pebble flux of $\sim 10-100\,M_\oplus\,\mathrm{Myr}^{-1}$ through the inner disk. This occurred in the Solar System at a time so early in its evolution that there is not likely to be any record of it. Our results demonstrate that scattered planetesimals can carry a significant flux of solids past planetary-induced gaps in young and massive protoplanetary disks.

Key words. planets and satellites: formation – protoplanetary disks – planet–disk interactions

1. Introduction

Concentric rings and gaps in the millimeter continuum emission associated with pebbles are commonly observed features in protoplanetary disks (e.g., ALMA Partnership 2015; Andrews et al. 2018). Recent evidence suggests that at least some of these radial pebble concentrations are due to trapping at pressure bumps (Dullemond et al. 2018). The origin of pressure bumps is often ascribed to planet–disk interactions, where a growing protoplanet carves a gap in the gas disk, leading to the formation of a pressure maximum at the planetary gap edge (e.g., Pinilla et al. 2012; Dipierro et al. 2015; Fedele et al. 2018; Zhang et al. 2018; Favre et al. 2019). The direct observation of protoplanets orbiting within protoplanetary disk gaps support this scenario (Pinte et al. 2019, 2020). Since the ratio of solids-to-gas in these pressure bumps can rise to values significantly higher than the global one, they are favorable spots for planetesimal formation via the streaming instability (SI; Youdin & Goodman 2005; Johansen et al. 2009; Lyra et al. 2009; Bai & Stone 2010; Carrera et al. 2015; Yang et al. 2017).

In Eriksson et al. (2020, hereafter Paper I), we performed global 1D simulations of dust evolution and planetesimal formation via the SI in a protoplanetary disk with multiple gap-opening planets. We found that planetesimals form at the gap edges for a wide range of planetary masses, particle sizes, and disk parameters. A similar study by Stammler et al. (2019) shows that planetesimal formation via the streaming instability can further explain the observed range of optical depths among dust rings in the DSHARP survey. Results from the first 3D simulations of planetesimal formation in a pressure bump were reported in Carrera et al. (2021), who concluded that planetesimal formation in pressure bumps is a robust process in the case of cm-sized particles. They did not, however, find any planetesimal formation in the case of mm-sized particles, but a search based on higher resolution and a broader parameter range is needed to assess this finding.

The above studies assert that planetesimal formation in pressure bumps is likely to be a common process. In this work, we assume that these pressure bumps are formed by growing planets and we consider what the fate of planetesimals formed at these planetary gap edges might be. To answer this question, we performed a suite of N-body simulations, taking into account the effect of gas drag on the planetesimals and mass loss via ablation. We consider two planetary systems: the Solar System with Jupiter and Saturn and an HL Tau inspired system with three planets. The main points we want to address are: (1) the extent to which gravitational interactions with the forming planets eventually redistribute the planetesimals formed at their gap edge; and (2) whether the frictional heating of planetesimals on eccentric orbits drives the production of a significant amount of dust

through surface ablation; and (3) how common collisions are between pairs of planetesimals and between planetesimals and planets.

We find that planetesimals that form at the edges of planetary gaps do not remain at their birth location. Gravitational scattering by the embedded planets causes the planetesimals to spread out across the disk, resulting in high orbital eccentricities. If the planetesimals end up in the inner part of the disk, efficient ablation due to high surface temperatures results in fast mass loss; this prevents any planetesimal from entering the innermost disk region. Collisions between pairs of planetesimals are rare and should not affect the outcome of our simulations, whereas planet–planetesimal collisions do occur, and often more so in the HL Tau system than in the Solar System. In general, the closer proximity to the Sun results in much more ablation in the Solar System than in the HL Tau system. If this ablated material re-condenses to form pebbles in the disk midplane, the result is a significant flux of pebbles both interior and exterior of Jupiter's orbit. Since the ablation efficiency depends strongly on the gas density, this pebble flux should only be present in relatively young and massive disk.

In Sect. 2, we present our disk model, our prescriptions for gas drag and mass ablation, as well as our calculations of condensation temperatures and planetsimal–planetesimal collision timescales. The numerical setup and initial conditions for our simulations are presented in Sect. 3. Results from the Solar System simulations are presented in Sect. 4 and results from the HL Tau simulations are presented in Sect. 5. In Sect. 6, we calculate the pebble flux that derives from planetesimal ablation and discuss how this fits into our understanding of the isotope dichotomy in the Solar System. The effect of planet-planetesimal collisions are discussed in Sect. 7. In Sect. 8, we summarize the key findings of the paper. Further information about the ablation model and some additional figures can be found in Appendix A–F.

2. Theory

We modeled the protoplanetary disk gas using a static 1D accretion disk. We added an acceleration to the equation of motion of the planetesimals in order to account for the friction force they are subject to as they move through the gas. This friction acts to heat up the planetesimals and causes a vaporization of the surface layers. We calculate the rate at which material is ablated from the planetesimals and update their mass at each timestep in the simulation. The temperature and mass loss rate are highly dependent on the composition of the planetesimals, which is set by their formation location relative to the location of the major icelines in the disk. We consider the disk to contain the following volatiles – H_2O, CO_2 and CO – and calculate their respective condensation temperatures. Finally, we estimate the frequency of planetesimal–collisions using an analytic expression.

2.1. Disk model

2.1.1. Surface density Σ

The gas surface density profile was defined to be that of a 1D steady disk,

$$\Sigma = \frac{\dot{M}_0}{3\pi\nu}\exp\left[-\frac{r}{r_{\rm out}}\right], \tag{1}$$

where Σ is the gas surface density, $\dot{M}_0$ is the disk accretion rate, ν is the kinematic viscosity of the disk, r is the semimajor axis, and $r_{\rm out}$ is the position of the outer disk edge (e.g., Pringle 1981). We used the alpha approach from Shakura & Sunyaev (1973) to approximate the kinematic viscosity:

$$\nu = \alpha\Omega H^2, \tag{2}$$

where α is a parameter that determines the efficiency of viscous transport, $\Omega = (GM_*/r^3)^{1/2}$ is the Keplerian angular velocity, and H is the scale height of the gas disk. We calculated the scale height as

$$H = c_{\rm s}/\Omega, \tag{3}$$

where $c_{\rm s}$ is the sound speed,

$$c_{\rm s} = \left(\frac{k_{\rm B}T}{\mu m_{\rm H}}\right)^{1/2}. \tag{4}$$

In the equation above, $k_{\rm B}$ is the Boltzmann constant, T is the temperature, μ is the mean molecular weight, and $m_{\rm H}$ is the mass of the hydrogen atom. The mean molecular weight was set to be 2.34, corresponding to a solar–composition mixture of hydrogen and helium (Hayashi 1981). The midplane temperature of the disk was approximated using a fixed powerlaw structure:

$$T = 150\,{\rm K} \times (r/{\rm AU})^{-3/7}, \tag{5}$$

where 150 K is the temperature at 1 AU (Chiang & Goldreich 1997).

2.1.2. Planetary gaps

Massive planets push away material from the vicinity of their orbits, and as a result opens up a gap in the disk. We modeled these planetary gaps using a simple approach with Gaussian gap profiles. The Gaussian is described by the equation

$$G(r) = \frac{\Sigma_{a,0}}{\Sigma_{a,\rm min}}\exp\left[-\frac{(r-a)^2}{2H_a^2}\right], \tag{6}$$

where $\Sigma_{a,0}$ is the unperturbed surface density at the location of the planet, $\Sigma_{a,\rm min}$ is the surface density at the bottom of the gap, and a is the semimajor axis of the planetary orbit. The depth of the gap is calculated as

$$\frac{\Sigma_{a,\rm min}}{\Sigma_{a,0}} = \frac{1}{1+0.04K}, \tag{7}$$

where K is given by

$$K = q^2\left(\frac{H_a}{a}\right)^{-5}\alpha^{-1}, \tag{8}$$

and q is the planet to star mass ratio (e.g., Kanagawa et al. 2015). Each planet contributes their own Gaussian, and the final surface density profile is then obtained by dividing Eq. (1) by $1 + G(r)_1 + G(r)_2 + ...$, where $G(r)_1$ is the Gaussian of Planet 1 (etc.).

2.1.3. Gas density ρ

We use the following expression to obtain the midplane gas density,

$$\rho(z=0) = \frac{\Sigma}{\sqrt{2\pi}H}. \tag{9}$$

In order to find the gas density at some height, z, away from the midplane, we assume vertical hydrostatic equilibrium for the gas in the disk. We then end up with the equation:

$$\rho(z) = \rho(z=0)\exp\left[\frac{-z^2}{2H^2}\right]. \tag{10}$$

2.2. Drag force

Planetesimals that are moving through the disk at a velocity different from that of the gas either experience a headwind or a tailwind and, as a result, they are decelerated or accelerated towards the value of the gas velocity. This change in velocity occurs on a timescale called the stopping time, t_s. Assuming that the planetesimals are spherical, their stopping time is

$$t_s = \left(\frac{\rho}{\rho_\bullet}\frac{v_{th}}{R_{pl}}\min\left[1, \frac{3}{8}\frac{v_{rel}}{v_{th}}C_D(Re)\right]\right)^{-1}, \quad (11)$$

where $\rho_\bullet$ and R_{pl} are the solid density and radius of the planetesimals, v_{rel} is the relative velocity between the planetesimals and the gas, $v_{th} = \sqrt{8/\pi}c_s$ is the gas thermal velocity, C_D is the dimensionless drag coefficient, and Re is the Reynolds number (e.g., Perets & Murray-Clay 2011; Guillot et al. 2014). The dimensionless drag coefficient is calculated as (Perets & Murray-Clay 2011):

$$C_D = \frac{24}{Re}(1 + 0.27Re)^{0.43} + 0.47\left(1 - \exp\left[-0.04Re^{0.38}\right]\right) \quad (12)$$

and the Reynolds number is

$$Re = \frac{4R_{pl}v_{rel}}{c_s l_g}, \quad (13)$$

where $l_g \sim 5 \times 10^{-6}\,\mathrm{kg\,m^{-3}}/\rho$ is the mean-free path of the gas (Supulver & Lin 2000).

The acceleration of the planetesimal due to gas drag is calculated as

$$\boldsymbol{a}_{drag} = -\frac{1}{t_s}(\boldsymbol{v}_{pl} - \boldsymbol{v}_{gas}), \quad (14)$$

where $\boldsymbol{v}$ is a velocity vector (e.g., Whipple 1972). We assume that the gas velocity in the z-direction is zero and obtain the Cartesian components of the gas velocity by projecting the orbital velocity of the gas,

$$v_{\phi,gas} \approx v_K + \frac{1}{2}\frac{c_s^2}{v_K}\frac{\partial \ln P}{\partial \ln r}, \quad (15)$$

in the x and y plane. In the above equation, $v_K = \sqrt{GM_*/r}$ is the Keplerian orbital velocity and $\partial \ln P/\partial \ln r$ is the radial gas pressure gradient. The radial gas pressure gradient is calculated as $\partial \ln P/\partial \ln r = \partial \ln \Sigma/\partial \ln r + \partial \ln T/\partial \ln r - \partial \ln H/\partial \ln r$, where $\partial \ln \Sigma/\partial \ln r = 15/14$.

2.3. Mass ablation

If a planetesimal becomes sufficiently heated, then the material at its surface can undergo phase transitions, resulting in mass loss. Here it is assumed that the mass loss occurs due to solid material transitioning to gas phase by frictional heating and irradiation from the surrounding gas through a process called ablation. In order to estimate the mass ablation rate from a planetesimal surface, we first need to know its composition. We assume that all planetesimals are non-differentiated and that they consist of a mixture of silicate grains, carbon grains, and volatile ices. In this paper, we consider the three volatiles H_2O, CO_2, and CO, and the volatile content of a planetesimal is set by which volatile ices were present at its formation site. The total ablation rate from a planetesimal surface is then taken to be the sum of the ablation rates for each present volatile ice and since the silicate and carbon grains are well mixed with the ices, we assume them to be released along with the ices (i.e., we assume no crust formation; see Appendices A and B for a discussion of this assumption). For a planetesimal that forms in a region of the disk where H_2O and CO_2 are in solid form, but CO is in gas form, the total ablation rate will thus be calculated as:

$$\dot{m}_{abl} = \dot{m}_{abl,H_2O} + \dot{m}_{abl,CO_2}. \quad (16)$$

We follow Ronnet & Johansen (2020) and use the following expression for the ablation rate of an element X:

$$\dot{m}_{abl,X} = -4\pi R_{pl}^2 P_{sat,X}(T_{pl})\sqrt{\frac{\mu_X}{2\pi R_g T_{pl}}}, \quad (17)$$

where $P_{sat,X}$ is the saturated vapor pressure of element X, T_{pl} is the surface temperature of the planetesimal, μ_X is the molecular weight of element X, and R_g is the ideal gas constant (e.g., D'Angelo & Podolak 2015). Expressions for the saturated vapor pressure as polynomials of the temperature are given in Fray & Schmitt (2009) for all three volatile ices under consideration. These polynomial expressions are only accurate above a certain temperature, which varies depending on the element. We therefore introduce "floor values" to the saturated vapor pressure. A plot of $P_{sat,X}$ versus T_{pl} for all three volatile ices, with the floor values included, is presented in Fig. C.1.

The equilibrium surface temperature of the planetesimals is obtained using the following equation from Ronnet & Johansen (2020):

$$T_{pl}^4 = T^4 + \frac{c_D \rho v_{rel}^3}{32\sigma_{sb}} - \sum_X \frac{P_{sat,X}(T_{pl})}{\sigma_{sb}}\sqrt{\frac{\mu_X}{8\pi R_g T_{pl}}}L_X, \quad (18)$$

where σ_{sb} is the Stefan-Boltzmann constant and L_X is the latent heat of vaporization of element X. We calculated the latent heat of vaporization using the Clausius-Clapeyron relation for low temperatures and pressures, and obtained the following results: $L_{H_2O} = 2.8 \times 10^6\,\mathrm{J\,kg^{-1}}$, $L_{CO_2} = 6.1 \times 10^5\,\mathrm{J\,kg^{-1}}$, and $L_{CO} = 2.8 \times 10^5\,\mathrm{J\,kg^{-1}}$. The second term in Eq. (18) reflects heating due to gas friction and the third term is cooling due to the ablation of volatile ices. Each volatile ice contributes its own cooling term, meaning that the planetesimal temperature will vary depending on what volatile ices it consists of. Since the cooling depends itself on the surface temperature of the planetesimal, the equation has to be solved iteratively. This is done using a bisection method. A plot of the mass ablation rate as a function of the semimajor axis is presented in Fig. D.1 for all three volatile ices and for different surface temperatures of the planetesimals.

2.4. Condensation temperature

We assume an isothermal equation of state for the disk pressure of an element X:

$$P_{d,X} = c_{s,X}^2 \rho_X. \quad (19)$$

The sound speed of X is calculated using Eq. (4), and exchanging the mean molecular weight of the disk with the molecular weight of X. The density of X in the disk midplane is obtained by multiplying the total density in the midplane (Eq. (9)) with the mass fraction of X with respect to the disk. To obtain the relevant mass fractions, we use abundances from Öberg et al. (2011), and

for the calculation, we assume that 25% of the disk mass is in He and the remaining 75% is in H. This results in the following mass fractions: 1.2×10^{-3}, 9.7×10^{-4}, and 3.1×10^{-3} for H_2O, CO_2 and CO. The mass fractions for silicate grains and carbon grains are 3.6×10^{-3} and 5.3×10^{-4}.

The condensation temperature of element X is found by comparing Eq. (19) with the saturated vapor pressure and solving for the temperature. Since the density of the disk depends on $\dot{M}_0$, α and $r_{\rm out}$ and as these are parameters that are varied among the simulations, the condensation temperatures will not be the same in all simulations. This means that a planetesimal which is initiated at the same semimajor axis in two separate simulations can have different compositions.

2.5. Collision timescale

We do not consider planetesimal-planetesimal collisions in our simulations; however, we still want to obtain an estimate of how common they are. If they happen on a timescale that is longer than the actual simulated time, it is a justified choice to neglect them. However, if the opposite is true, we need to consider how they would have affected our results.

Johansen & Bitsch (2019) provide an expression for the collision timescale of planetesimals in the gravitationally unfocused case:

$$t_{\rm coll} = \frac{1}{n_{\rm pl}\sigma_{\rm pl}\delta v} \approx \frac{R_{\rm pl}\rho_\bullet}{\Sigma_{\rm pl}\Omega} = \frac{R_{\rm pl}\rho_\bullet}{2\delta v \rho_{\rm pl}}, \tag{20}$$

where $n_{\rm pl}$ is the number density, $\sigma_{\rm pl}$ is the physical cross section, δv is the relative speed, and $\rho_{\rm pl} = \Sigma_{\rm pl}/(2H_{\rm pl})$ is the volume density of planetesimals. The relative speed between the planetesimals is approximated as (Lissauer & Stewart 1993):

$$\delta v = \left(\frac{5}{4}e^2 + i^2\right)^{1/2} v_{\rm K}. \tag{21}$$

The scale height of the planetesimals is taken to be $H_{\rm pl} = i \times a$, where a is the semimajor axis.

3. Numerical setup

We used the N-body code REBOUND to perform our simulations and modified it to take into account the effect of gas drag and mass ablation (Rein & Liu 2012). The simulations were executed using the hybrid symplectic integrator MERCURIUS and the timestep was set to be one twentieth of the innermost planet's dynamical timescale (Rein et al. 2019). Additional simulations with smaller timesteps were performed as well, in order to check that the outcome was not affected. We added the planets and the central star as active particles, and the planetesimals as semi-active particles with a mass. Semi-active particles only interact gravitationally with active particles. Collisions between active particles and semi-active particles were detected and recorded using a direct search method, and resulted in perfect merging. If a particle were to leave the simulation domain, it is recorded and removed from the simulation.

We considered two planetary systems that would be representative of the young Solar and HL Tau systems. In the Solar System simulations, the protoplanetary disk stretches from 0.1 to 100 au with $R_{\rm out} = 20$ au, and it is modeled using a linear grid with 1000 grid cells. The location of a particle on this grid is found using a binary search algorithm. The simulation box is centered on the sun and stretches 100 au in x and y-direction, and 20 au in z-direction. In the HL Tau simulations, instead we use a disk with 2000 grid cells that stretches from 0.5–200 au and has $R_{\rm out} = 100$ au. The corresponding simulation box is 500 au in x and y-direction and 100 au in z-direction.

We use two planets in the Solar System simulations (Jupiter and Saturn), and three planets in the HL Tau simulations (placed at the locations of the major gaps in the disk). We do not consider planet growth or migration. Jupiter and Saturn are initiated with their current eccentricity and inclination, and we use their current bulk density to calculate the planetary radius, given the masses in Table 1. The three planets in HL Tau are initiated with close to zero eccentricity and inclination, and their radius is calculated using the masses in Table 1 and assuming a constant density of 1000 kg m^{-3}. We use a central star of solar mass and solar luminosity in the HL Tau simulations.

The planetesimals are initiated uniformly between 1 and 2 Hill radii away from the planets, in the direction away from the central star. This is roughly the region in which planetesimals form in Paper I and additional simulations show that small changes to this formation location does not affect the results. A study on how the simulation outcomes are affected by larger changes to the planetesimal formation location is presented in Appendix E. Generally, as long as the planetesimals do not form further away than about 5 Hill radii from the planets, the results do not change significantly. We initiate 50 planetesimals beyond each planetary gap, meaning that each individual Solar System simulation harbors 100 planetesimals and each individual HL Tau simulation harbors 150. In order to provide better statistics, we performed 10 simulations for each set of parameter that we study, so that the total number of planetesimals per parameter set amounts to 1000 and 1500 for the Solar System and HL Tau system simulations, respectively.

The planetesimals are given an initial radius of 100 km, consistent with constraints from Solar System observations (Bottke et al. 2005; Morbidelli et al. 2009) and streaming instability simulations (e.g., Johansen et al. 2015), and have a constant solid density of 1000 kg m^{-3}. We add a property to the planetesimals that is the temperature of the disk at their formation location. This temperature, in relation to the condensation temperatures of the volatile ices, determines the composition of the planetesimals. The effect of gas drag is added as a velocity dependent force and mass ablation is added as a post-timestep modification. We keep track of how much mass is ablated from the planetesimals in each radial bin and at what time during the simulation. If a planetesimal loses more than 99% of its original mass, it is removed from the simulation and its remaining mass is considered to be ablated at the time and location where it was removed. The same procedure is applied if the amount of mass ablated in one timestep is larger than the total remaining mass of the planetesimal.

We performed a parameter study in order to explore how the fate of the planetesimals formed at planetary gap edges is affected by: (1) their composition; (2) the mass of the planets; and (3) the density of the disk (controlled by the disk parameters α and $\dot{M}_0$). The parameter values used in the different simulations can be found in Table 1. In simulation #1, which we will hereafter refer to as the nominal Solar System simulation, the masses of Jupiter and Saturn were set, respectively, to 90 and 30 $M_\oplus$, $\alpha = 10^{-2}$ and $\dot{M}_0 = 10^{-7}\ M_\odot\ {\rm yr}^{-1}$. In such a disk, the CO_2 iceline is located interior to the orbit of Jupiter and the CO iceline is located well beyond the orbit of Saturn, meaning that all planetesimals in this simulation contain H_2O and CO_2 ice. The nominal HL Tau simulation is labeled #7 in Table 1. In this simulation, the planetary masses where set to equal the

Table 1. Parameters for the simulations in the parameter study.

Solar System						
Run	Jupiter M_p	Comp.	Saturn M_p	Comp.	α	$\dot{M}_0$ ($M_\odot$ yr^{-1})
#1 Nominal	90 $M_\oplus$	H_2O, CO_2	30 $M_\oplus$	H_2O, CO_2	10^{-2}	10^{-7}
#2 Nominal (–CO_2)	90	H_2O	30	H_2O	10^{-2}	10^{-7}
#3 $M_p \downarrow$	30	H_2O, CO_2	10	H_2O, CO_2	10^{-2}	10^{-7}
#4 $M_p \uparrow$	150	H_2O, CO_2	50	H_2O, CO_2	10^{-2}	10^{-7}
#5 $\alpha \downarrow$	90	H_2O, CO_2	30	H_2O, CO_2	10^{-3}	10^{-7}
#6 $\dot{M}_0 \downarrow$	90	H_2O	30	H_2, CO_2	10^{-2}	10^{-8}

HL Tau								
Run	Planet 1 M_p	Comp.	Planet 2 M_p	Comp.	Planet 3 M_p	Comp.	α	$\dot{M}_0$ ($M_\odot$ yr^{-1})
#7 Nominal	59.6 $M_\oplus$	H_2O, CO_2	141.2 $M_\oplus$	H_2O, CO_2	313.7 $M_\oplus$	H_2O, CO_2	10^{-2}	10^{-7}
#8 $\alpha \downarrow$	-//-	H_2O, CO_2	-//-	H_2O, CO_2	-//-	H_2O, CO_2, CO	10^{-3}	10^{-7}
#9 $\alpha \downarrow$ (–CO)	-//-	H_2O, CO_2	-//-	H_2O, CO_2	-//-	H_2O, CO_2	10^{-3}	10^{-7}
#10 $\alpha \downarrow$ (–CO, –CO_2)	-//-	H_2O	-//-	H_2O	-//-	H_2O	10^{-3}	10^{-7}
#11 $\dot{M}_0 \downarrow$	-//-	H_2O, CO_2	-//-	H_2O, CO_2	-//-	H_2O, CO_2	10^{-2}	10^{-8}

Notes. Here, M_p denotes planetary mass and "comp." refers to the volatile composition of the planetesimals initiated at the gap edge of the specified planet.

pebble isolation mass, calculated using an analytical fitting formula from Bitsch et al. (2018). As in the nominal Solar System simulation, these planetesimals contain H_2O and CO_2 ice.

4. Simulations of the Solar System

In the Solar System simulations, we include two planets, Jupiter and Saturn, which are placed at their current semimajor axes. The mass ratio between Jupiter and Saturn is 3:1 in all simulations, which is roughly the current value, but the actual masses are varied. Results from the nominal model are presented in Sect. 4.1 and discussed in detail. We examine how varying the parameters affects the results in Sect. 4.2.

4.1. Nominal model

In the nominal model, the mass of Jupiter is set to be 90 $M_\oplus$ and the mass of Saturn is set to be 30 $M_\oplus$. All parameters used in the nominal model, also called simulation #1, can be found in Table 1. The planetesimals are initiated in a narrow region just beyond the orbits of Jupiter and Saturn, as suggested by the streaming instability simulations in Paper I. At these distances from the Sun, and with the disk parameters stated in Table 1, H_2O and CO_2 are in solid form, while CO is in gas phase. We therefore consider these planetesimals to have a volatile content of H_2O and CO_2 and we consider the ablation of both these molecules.

4.1.1. Dynamical evolution

In this section, we address the question of the dynamical redistribution of the planetesimals formed at planetary gap edges. In Figs. 1 and 2, we show the eccentricity and semimajor axis evolution for the 1000 planetesimals in the nominal simulation. The planetesimals are initiated with an eccentricity close to zero, but from Fig. 1, we see that the close proximity to the planets leads to rapid scattering, resulting in eccentricities as high as 0.4 already after 1 kyr of evolution. Most planetesimals that are not immediately scattered interior to the orbit of Jupiter end up in the scattered disk of Jupiter or Saturn. The eccentricities within these scattered disks increases with time, as the planetesimals are continuously scattered at perihelion. Such large eccentricities lead to large velocities at perihelion ($v_{\rm peri}$) relative to the gas,

$$v_{\rm peri} = v_{\rm K} \sqrt{\frac{1+e}{1-e}}, \tag{22}$$

which, in turn, affects the thermodynamic evolution of the planetesimals. The velocity at perihelion is higher within Jupiter's scattered disk than it is within Saturn's for the same orbital eccentricity since the Keplerian velocity decreases with increasing semimajor axis.

In Fig. 2, we separate the planetesimals forming at the gap edge of Jupiter and Saturn into different panels, making the diffusion of the semimajor axes clearly visible. Strong scatterings causes the semimajor axes to diffuse over several au in less than 100 yr. After a few thousand years, planetesimals from both gap edges are spread out across the giant planet region and the ones closest to the star have semimajor axes of ∼3 au. A small number of planetesimals, 13/1000 in this particular simulation, suffer a collision with either Jupiter or Saturn. Most of these collisions are between Jupiter and planetesimals formed at Jupiter's gap edge. Concerning the planetesimals that obtain very large eccentricities and semimajor axes, many of them are eventually scattered outside the simulation domain, and are considered to have been ejected from the system. In this simulation, ∼15% of all planetesimals are eventually ejected.

In summary, planetesimals that form at the edges of planetary gaps do not remain at their initial birth location. The close proximity to the gap-opening planets results in strong scatterings, causing the planetesimals to spread out across the protoplanetary disk. Many planetesimals initially become members of the gap-opening planet's scattered disk, while some are

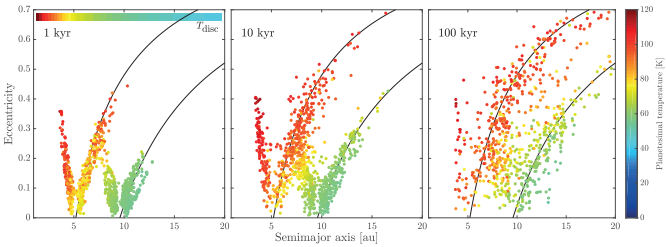

Fig. 1. Eccentricity, semimajor axis, and surface temperature evolution for the 1000 planetesimals in the nominal Solar System simulation. The presented orbital parameters have been averaged over 100 yr and the surface temperatures are the maximum values during the same time period, which roughly corresponds to the surface temperatures at perihelion. The temperature of the surrounding gas ($T_{\rm disk}$) is shown as a colorbar in the *left panel*. The solid black lines mark the orbits with a perihelion corresponding to Jupiter's and Saturn's location. The planetesimals which cluster around these lines are (at least momentarily) members of Jupiter's or Saturn's scattered disk. Planetesimals that are scattered interior of Jupiter's orbit obtain high surface temperatures at perihelion and experience efficient ablation.

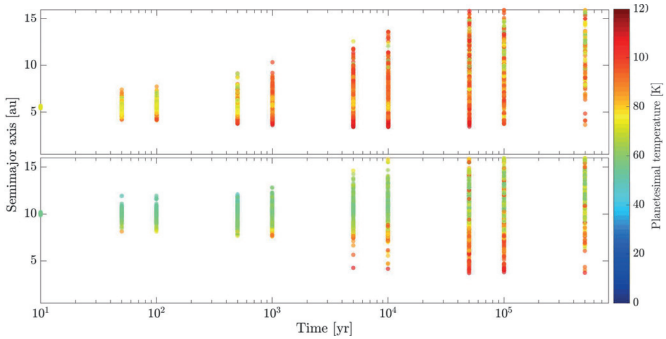

Fig. 2. Semimajor axis and surface temperature evolution for the 1000 planetesimals in the nominal Solar System simulation (same data as in Fig. 1). For simulation times longer than 1 kyr, we average the semimajor axes over 100 yr and show the maximum surface temperatures during the same time period; whereas for shorter simulations times, we show non-averaged values. *Upper panel*: planetesimals formed at the gap edge of Jupiter and *lower panel*: planetesimals formed at the gap edge of Saturn. The close proximity to the giant planets result in continuous scatterings, which causes the fast semimajor axis diffusion that is displayed in the plot.

scattered towards the inner disk region. The resulting high eccentricities lead to a high velocity relative to the gas, which has substantial implications for the mass evolution, as shown in Sect. 4.1.2. In Appendix E, we present simulations where the planetesimals are formed further from the planet. Placing planetesimals further from the planet does not change our results qualitatively, but it does lead to a delayed and slower scattering phase.

4.1.2. Mass evolution

In this section, we look into the mass evolution of planetesimals; that is, the loss of mass due to ablation. The ablation rate depends strongly on the planetesimal surface temperature, which increases towards the central star as the disk temperature and gas density becomes higher. The surface temperature is also highly dependent on the velocity relative to the gas, which increases with increasing orbital eccentricity according to the process described in Sect. 4.1.1. Based on this, the highest surface temperature, and thus the ablation rates, should be obtained at the perihelion passage of eccentric orbits close to the star. This can be seen in Figs. 1 and 2, where we also show the surface temperature evolution of the planetesimals at perihelion. The planetesimals that are scattered interior to Jupiter's orbit obtain surface temperatures around 100 K at perihelion. At these temperatures, CO_2 ablation quickly sublimates the planetesimal, which is why there are no planetesimals in the innermost part of the disk. We note here that the ablation process itself severely decreases the surface temperatures through cooling due to the latent heat of vaporization. A similar simulation without taking into account ablation would result in surface temperatures that are many times higher (see Appendix A). We also note that a planetesimal with the same surface temperature and orbital parameters in a gas-free disk would not experience any ablation due to the lack of frictional heating.

In Fig. 3, we track the mass loss of six selected planetesimals from the nominal simulation, as they are scattered around by the planets. The time evolution of the semimajor axes, perihelia, aphelia, and eccentricity for the same planetesimals can be found in Fig. F.1. The planetesimals that form at Jupiter's gap edge (the first three legend entries) begin to experience mass loss already after 100 yr of evolution. The "red" planetesimal is a

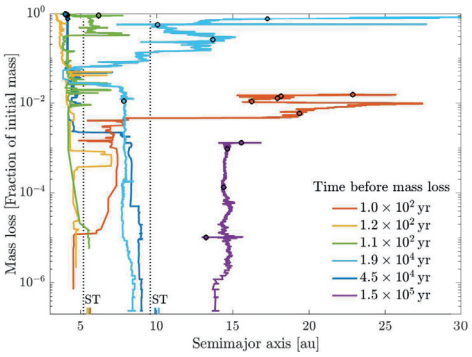

Fig. 3. Mass loss versus semimajor axis for 6 selected planetesimals from the nominal Solar System simulation. The mass loss is calculated as $1 - M(t)/M(t = 0)$. Filled circles mark 100 kyr of evolution and the formation location of the planetesimals (shown at the bottom of the plot) has been marked "ST". The time before the planetesimals first experience mass loss, that is, the time before they appear on the plot, has been included in the legend. The first three legend entries are for planetesimals formed at the gap edge of Jupiter and the following three are for planetesimals formed at the gap edge of Saturn. The dotted lines mark the semimajor axis of Jupiter and Saturn. Planetesimals which are scattered interior of Jupiter's orbit lose mass at a high rate, while those which are scattered exterior of Saturn's orbit experience little mass loss.

member of Jupiter's scattered disk for a few thousand years, until it is kicked towards Saturn's scattered disk, where it remains until the end of the simulation. Since its orbit never enters the inner disk region, ablation is slow and the planetesimal only loses about 2% of its mass. The "yellow" planetesimal obtains multiple kicks by Jupiter during the first few thousand years, after which it ends up interior to Jupiter's orbit with a perihelion of just above 2 au and becomes completely ablated within 10 kyr. The "green" planetesimal is a member of Jupiter's scattered disk for 100 kyr, with a relatively small eccentricity, until a strong planetary encounter leaves it on an orbit interior to Jupiter, where it very quickly becomes ablated.

The planetesimals formed at Saturn's gap edge (the last three legend entries), begin to lose mass much later. The "light-blue" planetesimal sits on a low-eccentric orbit in between Jupiter and Saturn for 150 kyr, after which it obtains a strong kick and becomes a high-eccentric member of Jupiter's scattered disk. Its eccentricity continues to increase until it leaves the simulation domain, having lost 85% of its mass. The "dark-blue" planetesimal is scattered onto a 4 au orbit by Saturn, where it slowly becomes circularized. Once circularized, the relative velocity between the planetesimal and the gas turns to zero, and it remains in the same orbit until the end of the simulation. Finally, the "purple" planetesimal never enters the region interior to Saturn, but remains on a low-eccentric orbit in the outer part of the disk for the entire simulation.

The mass loss tracks presented in Fig. 3 are examples of what can happen to a planetesimal in the simulation. In Fig. 4, we present the mass loss and semimajor axis evolution for all planetesimals in the nominal simulation. The planetesimals formed at Jupiter's gap edge start to lose mass much earlier than those formed at Saturn's gap edge and they generally lose mass at a faster rate. This is very much expected, mostly because the planetesimals form in a warmer part of the disk, but also because the mass of Saturn is lower than that of Jupiter and, therefore, the planetesimals are not scattered as much. Towards the end of the simulation, ~50% of all planetesimals have become completely ablated. In Appendix E we show that placing the planetesimals further from the planet results in a delayed and slower ablation phase.

From the plots presented here, it is evident that mass loss due to ablation plays a major role in the evolution of planetesimals formed at planetary gap edges, at least for the parameters used in the nominal model. In Sect. 4.2, we will investigate exactly how much mass is lost and where and compare that to simulations with varying planetary masses and disk parameters.

4.1.3. Planetesimal–planetesimal collisions

In this section, we use simple calculations to estimate how common planetesimal–planetesimal collisions are. If they occur on the same timescale as dynamical scattering, then they could affect our results. Furthermore, if these collisions are strong enough to disrupt the planetesimals that are involved, it would constitute another mechanism to replenish dust and pebbles in the disk.

We split the disk into multiple semimajor axis rings and find the planetesimals which are located within each ring. We then use the average eccentricity and inclination of those planetesimals to get an estimate of the velocity dispersion (Eq. (21)) and the scale height. To calculate the collision timescale, we further need to know the volume density of planetesimals within each ring. If all solids between the semimajor axis of Jupiter and Saturn are converted into planetesimals at Jupiter's gap edge, then there would be 16 $M_\oplus$ of planetesimals at that location, based on the disk parameters of the nominal model and a dust-to-gas ratio of 1%. We assume that the amount of planetesimals forming at Saturn's gap edge is the same. The total planetesimal mass in a ring is then simply taken to be the sum of the mass of all planetesimals in that ring.

When using a ring-width of 2 au, this resulted in collision timescales above 1 Myr, at all locations in the disk and at all times during the simulation (see Fig. 5). Decreasing the ring-width to 1 au leads to slightly smaller collision timescales. These results indicate that an individual planetesimal suffer a very low risk of colliding with another planetesimal. Since, in reality, there are millions of planetesimals forming at the gap edges, collisions will still be occurring, but not often enough to affect any of our results.

4.2. Parameter study and mass loss profiles

In this section, we vary certain disk and planet parameters in order to find out how the simulation results are affected. The parameters used in each simulation can be found in Table 1. In Fig. 6, we show how the total amount of ablated mass varies across the disk (left panel) and as a function of time (right panel). The mass loss evolution for each simulation is shown in Fig. 7, where the number of planetesimals that have become completely ablated or scattered or that have suffered planetary collisions can be noted and compared as well. The collision timescale for all simulations in the parameter study are very similar to those in the nominal simulation, meaning that planetesimal-planetesimal collisions can be safely ignored as a means of producing dust.

In the nominal simulation, 70% of the initial planetesimal mass has been ablated at the end of the simulation. The majority of this mass is released either just interior of Jupiter's orbit,

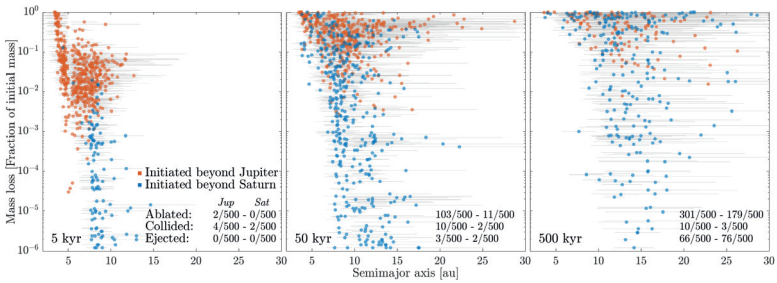

Fig. 4. Mass loss versus semimajor axis evolution for the 1000 planetesimals in the nominal Solar System simulation (same data as in Figs. 1 and 2). The thin grey lines mark the perihelion and aphelion of the planetesimal orbits. The number of planetesimals formed at Jupiter's (red dots) respective Saturn's (blue dots) gap edge which do not appear on the plot, because they have been either: completely ablated; collided with a planet; or ejected beyond the simulations domain, is written in each panel. Planetesimals formed at the gap edge of Jupiter generally experience more ablation than planetesimals formed at the gap edge of Saturn. About 50% of all planetesimals have become completely ablated after 500 kyr.

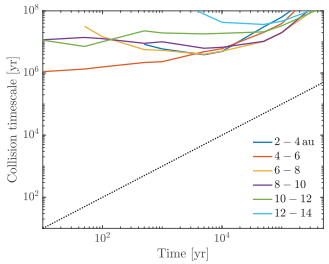

Fig. 5. Time evolution of the timescale for planetesimal-planetesimal collisions for the nominal Solar System simulation. The collision timescale was calculated using Eq. (20) and assuming an initial planetesimal mass of 16 $M_\oplus$ per gap edge. The dotted line marks where the collision timescale equals the time of the simulation. Since the resulting collision timescale for one planetesimal is several orders of magnitude larger than the actual simulated time, planetesimal–planetesimal collisions can be safely ignored in our simulations and will not constitute a significant path to replenishing the dust component in the disk.

between 2 and 5 au, or just outside of it, between 6 and 8 au. The mass loss outside of Jupiter's orbit is possible because of the large orbital eccentricities that result in high surface temperatures. The planetesimals in the nominal simulation all form beyond the CO_2 iceline, and thus both H_2O and CO_2 ablation is considered. In simulation #2 we remove the CO_2 ablation and consider the volatile content of the planetesimals as only made up of H_2O. As a result, the amount of ablated mass at the end of the simulation drops from 70% to 30%. Furthermore, since the ablation rate of H_2O is lower than that of CO_2 for the same temperature (see Fig. D.1), the planetesimals need to be scattered further towards the Sun in order for efficient ablation to occur. This can be seen in the left panel of Fig. 6, where the peak of the ablation curve interior to Jupiter has been shifted closer to the Sun. Additionally, there is no longer any mass released beyond the orbit of Jupiter, telling us that all mass released in this region in the nominal simulation is attributed to the presence of CO_2.

In simulation #3, we decrease the planetary masses by a factor of 3, mimicking an earlier stage of the planet formation process. The mass of Jupiter is now equal to the pebble isolation mass, while the mass of Saturn is only 20% of the pebble isolation mass. In Paper I, the amount of planetesimals that form at the gap edges drops by 80% when the mass is decreased from one pebble isolation mass to half a pebble isolation mass. The amount of planetesimals forming beyond Saturn in this simulation would thus have been very small, if any at all, and so we only include planetesimals at Jupiter's gap edge. The number of planetesimals in the simulation is kept the same as in all other simulations, but since they represent only half the mass, we divide the amount of ablation by a factor of 2, with the results provided in Fig. 6.

Lowering the planetary masses and removing the planetesimals at Saturn's gap edge result in about 40% less mass ablation than in the nominal simulation. The removal of planetesimals at Saturn's gap edge results in fewer planetesimals far out in the disk. Lowering the planetary masses results in weaker planetary scatterings, which, in turn, has several effects: (1) only 1/1000 planetesimals are ejected beyond the simulation domain; (2) the orbits are not as excited, resulting in lower surface temperatures and slower ablation; (3) the planetesimals end up on orbits closer to their birth locations, and thus the mass loss is more concentrated towards Jupiter's location.

In simulation #4, the planetary masses are increased, mimicking a later stage in the planet formation process. The stronger planetary scatterings initially result in higher mass loss rates as the planetesimals orbits quickly become excited. However, the strong planetary scatterings also lead to many more planetesimals being ejected beyond the simulation domain, which leaves fewer planetesimals in the system to be ablated during later times.

In the final two simulations of the parameter study, simulations #5 and #6, the viscosity parameter and disk accretion rate are decreased by a factor of 10. Decreasing the viscosity parameter slightly changes the gap profiles, but mostly it results in a surface density that is ten times larger, thus mimicking an earlier stage of disk evolution. The ice lines are also shifted closer to the Sun, but in this case, that does not change the composition of the planetesimals compared to the nominal model. On the other hand, decreasing the disk accretion rate results in a surface density that is ten times lower, causing the ice lines to move further out in the disk. As a result, the CO_2 ice line ends up beyond the gap edge of Jupiter and, thus, the planetesimals forming there do not contain any CO_2 ice.

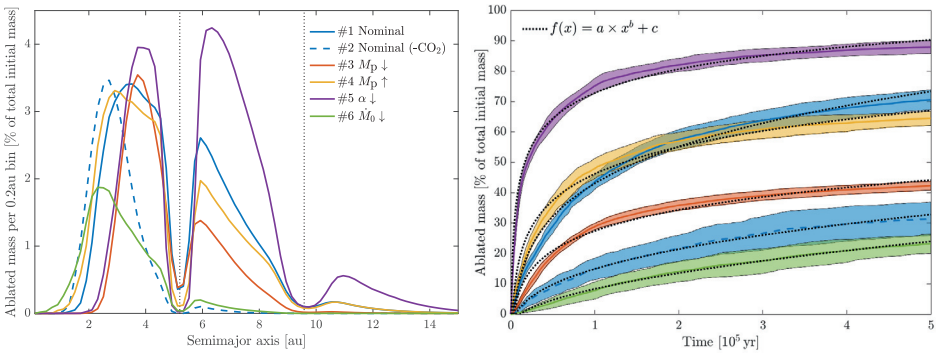

Fig. 6. Distribution of ablated mass as a function of semimajor axis (*left*) and time (*right*) for all Solar System simulations. *Left plot*: Distribution of ablated mass across the disk after 500 kyr. The values on the y-axis represent the amount of mass that has been ablated in a 0.2 au semimajor axis bin. The dotted lines mark the semimajor axes of Jupiter and Saturn. Most mass loss occur in the region just interior to and exterior to Jupiter's orbit. *Right plot*: Total amount of mass that has been ablated as a function of time, for the same data as in the left plot. The colored lines show the average over the ten simulations, and the colored region shows the one standard deviation away from this value. The dotted black lines show the best fit to the curve $f(x)$; and the parameters to the fits can be found in Table 2. The mass ablation rate is highly dependent on the gas surface density, where a high surface density results in a high degree of ablation (#5) and a low surface density results in low degree of ablation (#6).

Table 2. Parameters for the fitted curve $f(x) = a \times x^b + c$, shown in the right panel of Fig. 6.

Run	a	b	c
#1 Nominal	108.1	0.1537	−65.02
#2 Nominal (–CO_2)	23.9	0.3476	−9.02
#3 M_p ↓	117.7	0.0826	−90.24
#4 M_p ↑	572.5	0.0223	−526.30
#5 α ↓	−120.4	−0.0976	193.20
#6 $\dot{M}_0$ ↓	12.29	0.5099	−3.96

Looking at Fig. 6, we see that lowering the viscosity parameter results in more ablation, while lowering the disk accretion rate results in less ablation, just as expected. The higher surface density in simulation #5 results in higher surface temperatures, allowing for planetesimals to lose mass further out in the disk and at a higher rate. This effect in a combination with larger gas friction lead to a result whereby there are almost no planetesimals being ejected from the system. The opposite is the case in simulation #6 and since the planetesimals formed at Jupiter's gap edge do not contain CO_2 ice, there is little mass loss exterior of Jupiter's orbit, just as in simulation #2.

The results from the parameter study show that the surface density of the disk is a key parameter in determining how much mass is ablated from the planetesimals. Since the surface density in disks decreases with time, ablation is expected to be much more efficient in young disks than in old ones. Thus, planetesimals forming at the gap edge late during the disk lifetime might not suffer any significant mass loss due to ablation, but could, for example, be implanted into the asteroid belt or aid in water delivery to Earth (Raymond & Izidoro 2017). The masses of the planets determine how excited the planetesimal orbits become and how far they are scattered within the disk. To some extent, the planetary mass also affects how many planetesimals form at the gap edge (see Paper I). Finally, the composition of the planetesimals plays a major role in determining the efficiency of the ablation process. This is set by the location of formation relative to the location of the major ice lines, which, in a real disk, shifts inwards over time as the temperature of the disk decreases.

5. Simulations of HL Tau

We include three planets in the HL Tau simulations and place them at the locations of the major gaps in the disk, that is, at 11.8, 32.3, and 82 au (Kanagawa et al. 2016). The masses of the planets are set to be 59.6, 141.2, and 313.7 $M_\oplus$, which is exactly equal to the pebble isolation mass using the parameters in simulation #7. For reference, this is the same set-up as in simulation #4 of Paper I. Each simulation contains 150 planetesimals, with 50 formed at each planetary gap edge, and we run ten simulations per parameter set. Results from the nominal simulation are presented in Sect. 5.1, while in Sect. 5.2, we study how these results change when we vary the planetesimal compositions and the disk parameters.

5.1. Nominal model

The three planets in the HL Tau disk are located well beyond the CO_2 iceline, which in the nominal model (simulation #7) is at 4.7 au. The CO iceline sits much further out in the disk at 99.3 au, placing it just beyond the formation location of the outermost planetesimal. Since all planetesimals in the nominal model form in between the CO_2 and CO iceline, we thus consider them to be made up of H_2O and CO_2 ice and we consider the ablation of these two molecules.

The dynamical evolution of the 1500 planetesimals from the nominal simulation is presented in Figs. 8 and 9. Just as in the Solar System simulations, most planetesimals end up in the scattered disks of the planets, with eccentricities increasing over time. The two outermost planets are very massive and deliver strong kicks to the planetesimals formed in their vicinity, causing them to quickly spread out over the entire disk. Many of

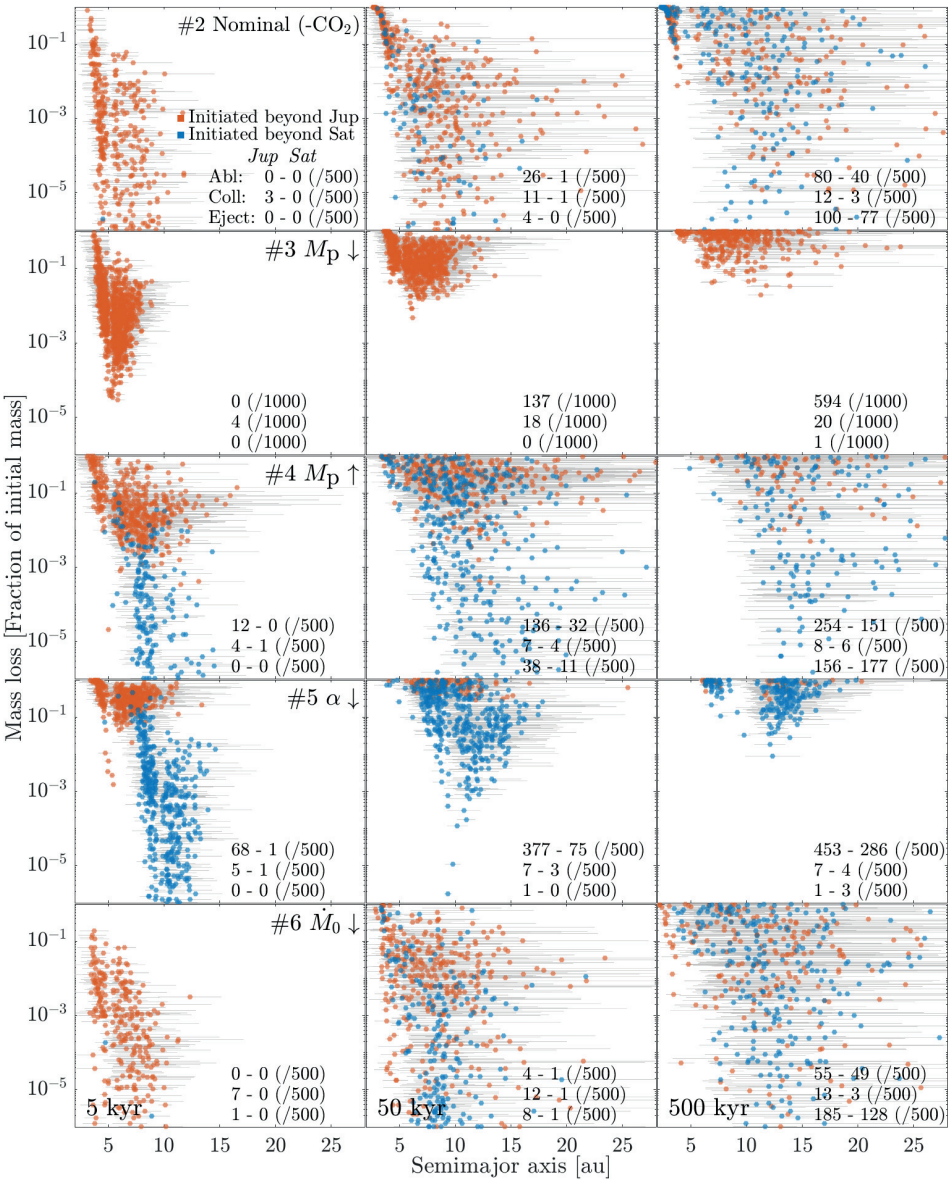

Fig. 7. Mass loss versus semimajor axis evolution for all Solar System simulations. The masses of the planets affect how far the planetesimals are scattered, with more planetesimals leaving the simulation domain when the planetary mass is increased (#4). A large surface density (#5) generally results in efficient ablation and few scatterings beyond the simulation domain since the planetesimals are ablated before they become scattered. The opposite is the case for a low surface density (#6) and ablation also occurs closer to the star.

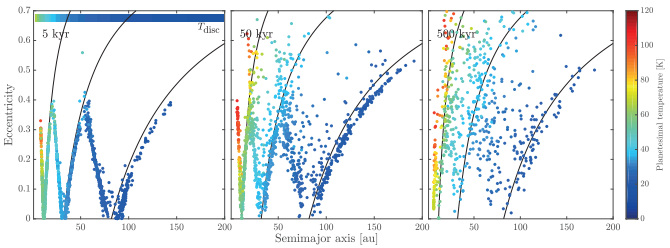

Fig. 8. Eccentricity, semimajor axis, and surface temperature evolution for the 1500 planetesimals in the nominal HL Tau simulation, produced in a similar manner as Fig. 1. The solid black lines mark the perihelia of the planets. Many planetesimals end up in the scattered disks of the planets, where they obtain high eccentricities. Only planetesimals scattered to interior of the innermost planet's orbit obtain perihelion temperatures large enough for ablation to take place.

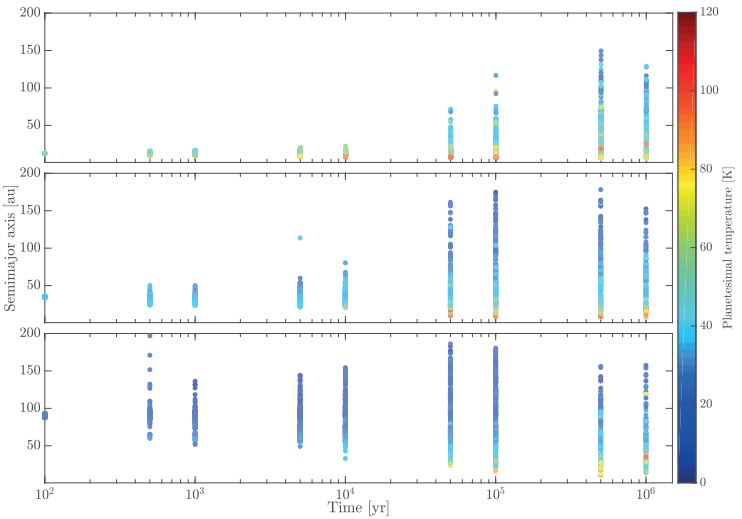

Fig. 9. Semimajor axis and surface temperature evolution for the 1500 planetesimals in the nominal HL Tau simulation, produced in a similar manner as in Fig. 2 (same data as in Fig. 8). Planetesimals formed at the gap edge of the innermost planet is shown in the upper panel. For the middle and outermost planet, these are shown in the *middle and bottom panels*, respectively. Since the planetary masses are set to equal the pebble isolation mass, and the pebble isolation mass increases with semimajor axis, the planetesimals formed at the gap edge of the outermost planet experience stronger scatterings and diffuse faster than those formed at the innermost planet's gap edge.

these planetesimals are eventually ejected beyond the simulation domain. The planetesimals that form at the gap edge of the innermost planet instead suffer weaker kicks and tend to remain in the inner disk region.

The timescale for planetesimal-planetesimal collisions is calculated in the same way as for the Solar System simulations and we use the results from Paper I to infer the total mass of planetesimals formed at each gap edge. In simulation #4 of Paper I, after 1 Myr, 281 $M_\oplus$ of planetesimals have formed. We make the assumption that the amount of planetesimals forming at each gap edge is the same and based on the results of Paper I, this is a reasonable approximation. This yields a collision timescale of $\sim 10^4$ yr in the beginning of the simulation, which then increases roughly linearly with time as the planetesimals spread out across the disk (see Fig. 10). Since the collision timescale remains an order of magnitude larger than the actual simulated time throughout the simulation, for HL Tau we also conclude that planetesimal-planetesimal collisions are not a major source of dust production

The amount of mass that has been ablated as a function of semimajor axis and time for the nominal model is presented in Fig. 11. From the left plot, we learn that all mass loss occurs interior of the innermost planet, with a peak at ~7 au. In total, 11% of the initial planetesimal mass has been ablated after 1 Myr. This is a much smaller number than what we found in the Solar System simulations and the main reason for this is that the planetesimals

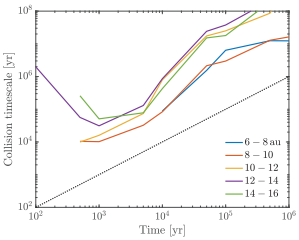

Fig. 10. Time evolution of the timescale for planetesimal–planetesimal collisions for the nominal HL Tau simulation. The collision timescale was calculated using Eq. (20) and using an initial planetesimal mass of 281 $M_\oplus$, following the results from simulation #4 of Paper I. The dotted line marks where the collision timescale equals the time of the simulation. Even though the collision timescale for one planetesimal can be as low as 10^4 yr, it is still roughly an order of magnitude larger than the actual simulated time, meaning that planetesimal-planetesimal collisions can be safely ignored in our simulations as a source of dust production.

form further out in the disk. In order for a planetesimal forming at 90 au to experience efficient ablation, it needs to be scattered inwards by approximately 80 au. Since the planetesimals need to travel a further distance before mass loss can begin to occur, the initial mass loss rate is much lower than in the Solar System simulations, where planetesimals already start to ablate efficiently after a few thousand years. This can also be seen in the top panel of Fig. 12, where the mass loss evolution for all planetesimals in the ten nominal simulations has been plotted. After 10 kyr, the planetesimal with the smallest semimajor axis has still only lost about 30% of its mass.

5.2. Parameter study and mass loss profiles

In this parameter study, we chose to vary the composition of the planetesimals, the α value, and the initial mass accretion rate $\dot{M}_0$. Changing these disk parameters does not result in a significant change to the collision timescale compared to the nominal simulation. As previously explained, lowering α results in an increased surface density, while lowering $\dot{M}_0$ results in a decreased surface density. This change in the surface density also affects the positions of the icelines. Lowering $\dot{M}_0$ by a factor of 10 (simulation #11) does not result in any change of the planetesimal compositions compared to the nominal simulation; however, when α is lowered by a factor of 10, then the planetesimals forming at the gap edge of the outermost planet end up interior of the CO iceline. This gives us an opportunity to study CO ablation since the planetesimals will consist of both H_2O, CO_2, and CO ice.

In order to see the effect of CO ablation, we performed one simulation that includes it (simulation #8) and one simulation without (simulation #9). We note, however, that the only planetesimals which will experience CO ablation in simulation #8 are those that form at the outermost planetary gap edge. Furthermore, we perform one simulation where we only consider the ablation of water ice (simulation #10). The results from these simulations are presented in Fig. 11 and 12.

When only the ablation of water ice is considered, all mass loss occurs interior to the innermost planet. The total amount of mass that has been ablated after 1 Myr is only about 5%. When CO_2 ablation is added, this value increases to 25%, and there is significant mass loss also in the region around the gap edge of the innermost planet. Compared to the nominal simulation, the initial mass loss rate is much higher, which is because of the larger surface density of the disk. Finally, when CO ablation is added, the total amount of ablated mass increases by another few percent. Another key observation is that at this point, a small amount of mass loss is occurring as far out in the disk as 100 au. This is clearly visible in Fig. 12, where planetesimals forming at the outermost planetary gap edge are losing mass at a slow rate all over the disk.

The effect of decreasing $\dot{M}_0$ is very much the same as in the Solar System simulations: the mass loss rate is lower and the mass loss occurs closer to the central star. In such a disk, less than 5% of the planetesimal mass is lost due to ablation. In summary, planetesimals forming at the edges of planetary gaps in the HL Tau system are not as affected by ablation as those forming at the gap edges of Jupiter and Saturn. This is expected since the planets in the HL Tau system are located much further away from the central star. Nevertheless, if the surface density of the disk is large, the amount of mass loss can still be significant. Most of this mass is released closer to the star than the innermost planet, but some small amounts are also released around the gap edge of the innermost planet. If the surface density of the disk is high enough for CO to be in solid phase where some planetesimals form, these planetesimals can ablate at a slow rate far out in the disk.

6. Pebble flux due to ablation

The ablated material consist of a mixture of silicate grains, carbon grains, and vaporized ices. For simplicity, we assume that all of this material lands on the midplane, which is not a bad approximation given that ablation should be most efficient in the dense midplane of the disk. Depending on where in the disk ablation occurs, the vaporized ices will either re-condense to form solid ice, or remain in the gas phase. For example, if the ablation occurs in between the H_2O and CO_2 iceline, then the vaporized H_2O ice will re-condense to form solid ice, but CO_2 and CO will remain in the gas phase. We assume that re-condensation happens instantaneously. We further assume that all solid material (silicate grains, carbon grains, and re-condensed ices) grow to ∼mm-sized pebbles with Stokes number 10^{-3} directly after the ablation occurs. From Paper I, we find that µm-sized grains grow to mm-sizes within ∼10 kyr in the inner region of the disk, so given the timescales under consideration, it is a valid approximation.

The solid material from ablation gives rise to a flux of pebbles, which can be calculated given the initial planetesimal formation rate at the gap edges, the rate at which these planetesimals are ablating (right panel of Fig. 6 and 11), and the distribution of the ablated material (left panel of Fig. 6 and 11). We assume that all planetesimals ablate at the same rate and that their ablated material has the same distribution, which gives the correct behavior for the population as a whole. The planetesimal formation rate is taken directly from Paper I in the case of HL Tau and calculated using some assumptions in the case of the Solar System (description in Sect. 6.1). This information is combined to give the total mass ablation rate (gas + solids) in each semimajor axis bin and at each timestep of the simulation $\dot{M}_{\rm abl}(r, t)$. We then remove the mass fraction from ices that do not re-condense (using abundances from Öberg et al. (2011) and assuming a chemical composition of Mg_2SiO_4 for the silicate grains, and C for the carbon grains), thus, we are left with only the solid (pebble) component.

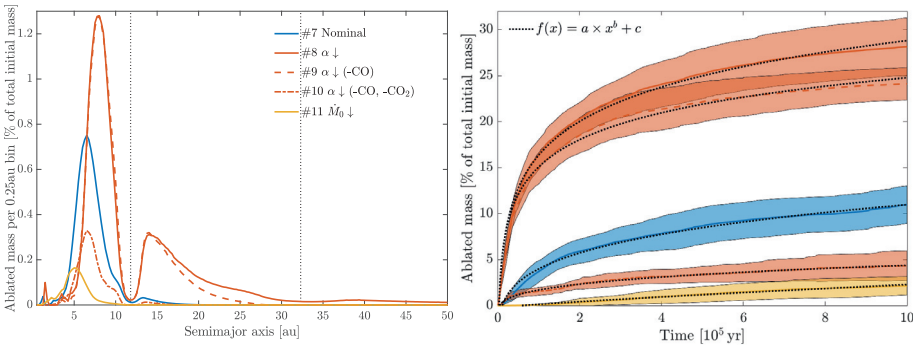

Fig. 11. *Left plot*: distribution of ablated mass across the disk after 1 Myr for all HL Tau simulations. The values on the y-axis represent the amount of mass that has been ablated in a 0.25 au semimajor axis bin. The dotted lines mark the semimajor axes of the two innermost planets. In the nominal simulation, all mass loss occurs just interior of the innermost planet. When the surface density is increased (#8), there is also some mass loss occurring further out in the disk. *Right plot*: total amount of mass that has been ablated as a function of time, for the same data as in the left plot. The colored lines show the average over the 10 simulations and the colored region shows the one standard deviation away from this value. The dotted black lines show the best fit to the curve $f(x)$, and the parameters to the fits can be found in Table 3. Comparison of simulation #8–#10 shows that most mass loss occurs due to the presence of CO_2.

Table 3. Parameters to the fitted curve $f(x) = a \times x^b + c$, shown in the right panel of Fig. 11.

Run	a	b	c
#7 Nominal	10.1	0.2282	−6.14
#8 $\alpha \downarrow$	193.1	0.0272	−176.70
#9 $\alpha \downarrow$ (–CO)	−223.0	−0.0194	238.00
#10 $\alpha \downarrow$ (–CO, –CO_2)	2.89	0.2859	−1.21
#11 $\dot{M}_0 \downarrow$	0.4	0.8262	−0.25

The flux of pebbles in an annulus of with Δr is:

$$F(r,t) = \frac{\dot{M}_{\rm abl}(r,t)}{2\pi r \Delta r}, \tag{23}$$

where F is in units of kg s^{-1} m^{-2}. The total mass flux $F_{\rm tot}(r,t)$ as a function of semimajor axis and time is then obtained by numerically integrating $2\pi r F(r,t)$ from some $r_{\rm in}$ to some $r_{\rm out}$. Here, we make another assumption that the planetary gaps act as hard barriers, which completely block the flow of pebbles past the gaps. In other words: when calculating the total mass flux interior of the innermost planet, we take the integral from the inner disk edge to the semimajor axis of the innermost planet; when calculating the total mass flux in a region between two planets, we take the integral from the inner planet to the outer planet; and when calculating the mass flux exterior to the outermost planet, we take the integral from the outermost planet to the edge of our ablation array (20 au for SS, 100 au for HL Tau). Finally, we calculate the corresponding pebble-to-gas surface density ratio using Eqs. (8)–(13) from Johansen et al. (2019).

6.1. Solar System

In order to calculate how much mass is ablated in the Solar System simulations, we first need an estimate for the initial planetesimal formation rate at Jupiter's and Saturn's gap edges. For Jupiter, we simply assume that all the pebbles initially located between the semimajor axis of Jupiter and Saturn are turned into planetesimals at Jupiter's gap edge (this is the same assumption we used for the collision timescale). Using the parameters of the nominal model and a dust-to-gas ratio of 1%, this gives a result of 16 $M_\oplus$. We calculate that it takes 55 kyr for all these pebbles to reach Jupiter's gap edge, using equations for the pebble drift timescale from Johansen et al. (2019). Assuming a constant drift velocity for all pebbles, this yields an initial planetesimal formation rate of 3×10^{-4} $M_\oplus$ yr^{-1} at Jupiter's gap edge. This is the rate during the first 55 kyr of the simulation, after which it is zero. In order to keep things simple, we assume the exact same formation rate at Saturn's gap edge.

As a first approximation, we neglect any later generations of planetesimals forming at the gap edges from the ablated material. The resulting pebble flux and pebble-to-gas surface density ratio for the nominal model is presented in Fig. 13 as dotted lines. The highest pebble flux is obtained at 50 kyr, after which it decreases with time. The drop in pebble flux at the H_2O iceline is clearly visible. The CO_2 iceline is located in the gap just interior of Jupiter and, therefore, there is no corresponding drop in the pebble flux.

Since we assumed a hard pebble barrier at the planetary gaps, all pebbles flowing into the gap edge will become trapped. If we use the same assumption as for the initial planetesimal formation rate, all these pebbles will collapse into newer generations of planetesimals. We follow the ablation of these planetesimals and even later generations, assuming the same ablation rate and distribution of ablated material as for the initial population. This results in an increased pebble flux and surface density ratio as compared to our first approximation (see solid lines in Fig. 13). In total, about ∼15 $M_\oplus$ of pebbles are delivered to 1 au over the course of the simulation. Inside of the water ice line, this amount drops to ∼12 $M_\oplus$. The presented fluxes are obtained in a young and massive disk, and would not be present in older or low-density disks, thus the formation of transition disks, which are generally old, would not be prevented in such a way.

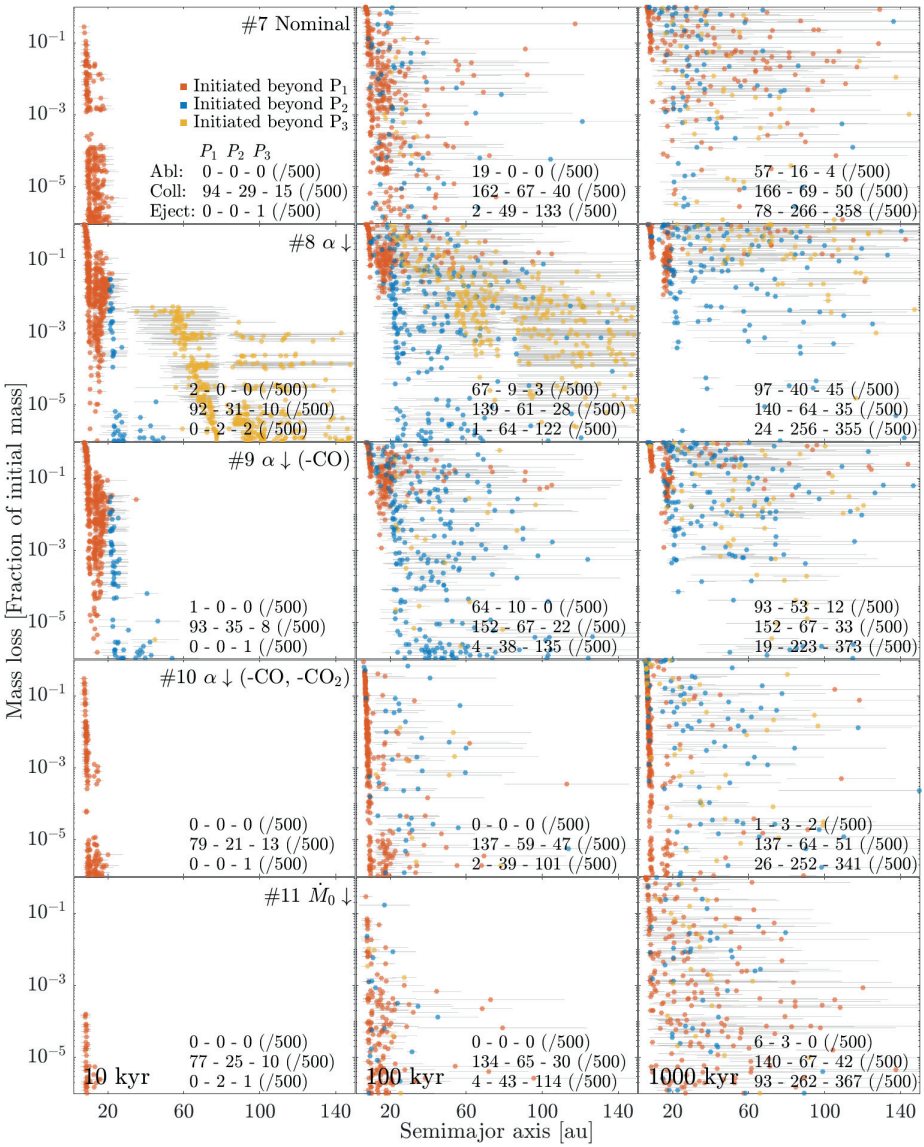

Fig. 12. Mass loss versus semimajor axis evolution for all HL Tau simulations. The red dots are for planetesimals forming at the gap edge of the innermost planet; the blue dots are for planetesimals forming at the gap edge of the middle planet; and the yellow dots are for planetesimals forming at the gap edge of the outermost planet. Ablation is most efficient for planetesimals forming at the gap edge of the innermost planet. Ablation of CO (#8) causes planetesimals to lose mass far out in the disk. The massive planets deliver strong kicks to the planetesimals, which causes many of them to leave the simulation domain.

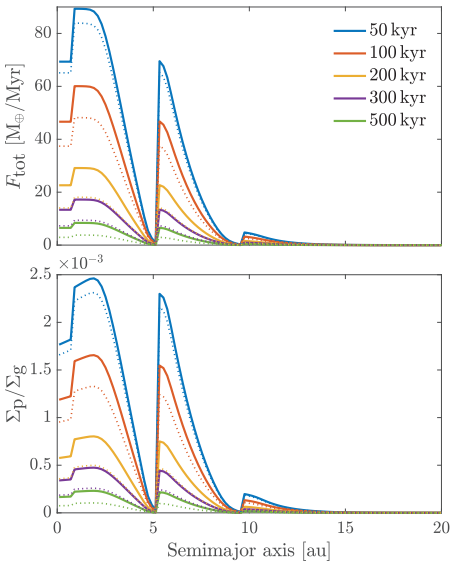

Fig. 13. Material ablated from the planetesimal surfaces re-condense and grows to mm-sized pebbles in the disk's midplane. *Top*: Mass flux of pebbles as a function of time and semimajor axis for the nominal Solar System simulation. The solid lines take into account the formation and ablation of newer generations of planetesimals forming at the gap edges from this flux of pebbles, while the dotted lines do not. *Bottom*: Corresponding pebble-to-gas surface density ratios.

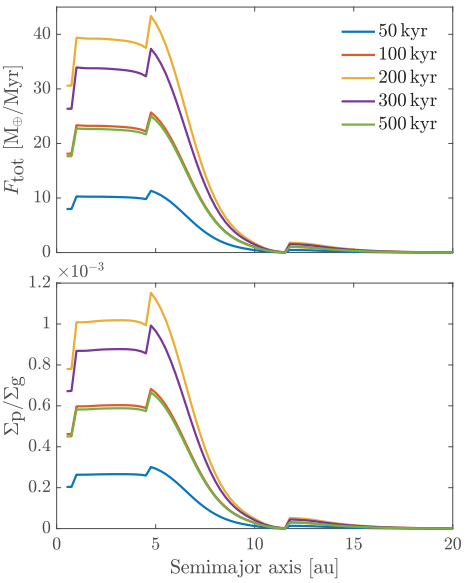

Fig. 14. Flux of pebbles (*top panel*) and pebble-to-gas surface density ratio (*bottom panel*) as a function of semimajor axis and time for the nominal HL Tau simulation (similar to Fig. 13). Since the large majority of mass ablation occurs interior of the innermost planet, we do not consider the formation of newer generations of planetesimals at the planetary gap edges.

6.2. HL Tau

In simulation #4 of Paper I (which has the same parameters as in the nominal simulation) we have 281 $M_\oplus$ of planetesimals forming at the gap edges within 1 Myr. By using the planetesimal formation rate from this simulation and combining it with the ablation rate and distribution of ablated mass from this paper, we obtain the amount of mass which is ablated in each semimajor axis bin and at each timestep. The resulting pebble flux and pebble-to-gas surface density ratio is shown in Fig. 14. Since the amount of ablated material being deposited beyond the innermost planet is very small, we do not consider the formation of newer generation of planetesimals.

Due to the relatively low ablation rate in the nominal simulation (only 11% of the initial planetesimal mass is ablated during 1 Myr), the pebble-to-gas surface density ratio only reaches about 0.1%. The maximum pebble flux is about half that of the Solar System, 40 $M_\oplus\,{\rm Myr}^{-1}$ and the total integrated mass flowing past 1 au is 25 $M_\oplus$. In the Solar System simulations, most ablation occurs within the first 50 kyr, after which the ablation rate drops quickly. In the HL Tau simulations, ablation happens on a longer timescale, and the rate does not drop as quickly after the peak at 200 kyr. Because of this, the flux of pebbles remains high for a much longer time; however, we emphasize that these results are for a non-evolving disk and in an evolving disk, the pebble flux would decrease with time along with the gas surface density.

6.3. Asteroid dichotomy

In this work, we use a simple model of the Solar System with only two planets, Jupiter and Saturn, where neither planet nor disk properties evolve with time. Due to these simplifications, comparisons to Solar System data and observations remain conceptual. We nevertheless comment on how pebble drift due to ablation could fit into our understanding of the accretion history of the inner Solar System, specifically the isotopic dichotomy among the parent bodies of iron meteorites (irons) and chondritic meteorites (chondrites).

Meteorites collected on Earth can be broadly classified as either carbonaceous (CC) or noncarbonaceous (NC) based on their distinct isotope compositions (Warren 2011; Kruijer et al. 2017). This isotopic dichotomy, which could reflect either an infall of material with two compositions (Jacquet et al. 2019) or a temperature-dependent destruction of presolar grains (Trinquier et al. 2009; Schiller et al. 2018) hints towards the formation of meteorite parent bodies from two distinct and spatially separated reservoirs (Kruijer et al. 2017). Since NC chondrites come from dry bodies, whereas CC chondrites show hydration features, it is generally envisioned that the NC population represents inner Solar System bodies while members of the CC group would have formed further out.

Iron meteorites are fragments of cores from melted and differentiated planetesimals that accreted within 1 Myr after the formation of calcium–aluminum-rich inclusions (CAIs;

Kruijer et al. 2017). Chondrites are fragments of non-molten and non-differentiated planetesimals that accreted around 2–4 Myr after CAI formation (Kita & Ushikubo 2012). The parent bodies of NC and CC irons accreted ∼0.4 Myr and ∼0.9 Myr after CAI formation, respectively. Since the two populations have distinct compositions, they must have remained separated even after their formation. Similarly, the NC and CC reservoirs must have been separated at the time of formation of the NC chondrite parent bodies and CC chondrite parent bodies at ∼2 Myr and 3–4 Myr after CAIs, respectively. In the context of pebbles drift, such constraints imply that pebbles bearing a CC isotopic signature either never entered the inner Solar System region where the parent bodies of NC irons and chondrites formed or, if they had, they were not efficiently accreted by the NC population of objects. Below, we discuss these issues in the context of our results.

The formation of Jupiter is likely to have begun early and resulted in gap-opening in less than 1 Myr (Kruijer et al. 2017). At this point, planetesimals should have started to form at its gap edge. As shown in our simulations, a large fraction of these planetesimals would be scattered into the inner Solar System. While the disk is young and massive, a large fraction of these planetesimals become ablated, resulting in a flux of pebbles with (possibly) CC composition both interior and exterior of Jupiter's gap. Given the expected decrease in disk density with time, this process should have stopped being relevant at the time of formation of the NC chondrite parent bodies at ∼2 Myr after CAIs. However, since the NC iron parent bodies formed as early as ∼0.4 Myr after CAIs, they should have been in place at the time Jupiter reached the pebble isolation mass and started to scatter planetesimals inside of its orbit. Thus, there must have been something preventing the NC iron parent bodies from accreting the pebbles produced by the early ablation of planetesimals originating from beyond Jupiter's orbit. This process was likely the early formation of planetary embryos interior of Jupiter's orbit, which caused the inclinations and eccentricities of the planetesimals to be excited, thereby, disconnecting them from the pebbles drifting through the midplane (Schiller et al. 2018). As long as the planetesimals remain excited, they would be unable to efficiently accrete pebbles (e.g., Levison et al. 2015; Liu et al. 2019; Johansen et al. 2015) and should thus have preserved their birth compositions. In general, the described pebble flux was present at a time in the Solar System so early that there is likely no record of it.

7. Planet–planetesimal collisions

In the Solar System simulations, about 1–2% of all planetesimals suffer a collision with a planet. The majority of these collisions are between Jupiter and planetesimals formed at Jupiter's gap edge. Only about 20% of the collisions are between a planet and a planetesimal not formed at that planet's gap edge. Following the assumption made in Sect. 6.1, and assuming that the collisions occur before any mass loss has taken place, the total planetesimal mass colliding with Jupiter is about half an Earth mass. Depending on how high up in the atmosphere this material is deposited, this could be relevant for the composition of Jupiter's atmosphere (e.g., Shibata & Ikoma 2019).

Collisions between planets and planetesimals occur much more frequently in the HL Tau system, where about 15–20% of all planetesimals suffer such a collision. Due to the larger separation between the planetary orbits, nearly all collisions take place between a planet and a planetesimal formed at that planet's gap edge. If a large fraction of the colliding planetesimal mass is accreted high up in the planet's atmospheres, this would certainly be relevant for the atmosphere's compositions.

The collision algorithm employed in this work is rather simple and by making it more advanced, the frequency of collisions could certainly be altered. We use a direct collision search whereby the radius of the planet is determined by assuming a constant density, however, in reality, planets that are accreting gas have an inflated envelope with a significantly larger radius. Thus, the capture radius used in this paper is significantly smaller than it would be in real life, resulting in a smaller number of collisions. The initial formation location of the planetesimals relative to the planet (discussed in Appendix E) could also have an effect on the collision frequency. Another process which has been ignored in this paper but would likely lead to more collisions is planetary migration (Pirani et al. 2019; Carter & Stewart 2020).

8. Conclusions and future studies

In this work, we study the evolution of planetesimals formed at planetary gap edges. To this end, we performed a suite of *N*-body simulations and considered two planetary systems: (1) the Solar System with Jupiter and Saturn and (2) a system inspired by HL Tau with three planets. We then followed the evolution of planetesimals initiated at the gap edges, where the planetesimals are further subjected to gas drag and mass loss via ablation. We assumed that the mass which is ablated from the planetesimals will re-condense to form pebbles in the disk midplane and we calculated the corresponding pebble flux. We reached the following conclusions regarding the main questions posed in the introduction section:

1. With regard to the extent to which gravitational interactions with the forming planets redistribute the planetesimals formed at their gap edge, we find that the close proximity to the gap-opening planets results in large orbital excitations, causing the planetesimals to leave their birth location soon after formation. Within ten orbital periods, the semi-major axes of the planetesimals have diffused over several au and after a few hundred orbital periods, the planetesimals are spread out across the entire disk. If the gap-opening planets are massive, as in the HL Tau system, ∼40% of the planetesimals become ejected from the system within a million years. These planetesimals could potentially be circularized by galactic tides and end up in the Oort cloud (Brasser & Morbidelli 2013). The ejection efficiency generally increases with time as the disk density decreases and the planetary masses increases. If the planetary gaps were to be much wider than assumed in this paper, resulting in formation locations that are further from the planets, the scattering phase would be slower and delayed.
2. Regarding the possibility that frictional heating of planetesimals on eccentric orbits may drive the production of a significant amount of dust through surface ablation, we find that planetesimals on eccentric orbits within ∼10 au experience efficient ablation and because of this there are no planetesimals entering the innermost disk region. In the nominal Solar System simulation with $\dot{M}_0 = 10^{-7}\ M_\odot\ \mathrm{yr}^{-1}$, $\alpha = 10^{-2}$ and Jupiter and Saturn at 30% of their current masses, 70% of the initial planetesimal mass has been ablated after 500 kyr. Planetesimals formed at Jupiter's gap edge lose about two times more mass than planetesimals formed at Saturn's gap edge. The ablation rate is significantly lower in the HL Tau system due to the larger planetary orbits, and only 11% of the initial planetesimal mass has

been ablated after 1 Myr for the same disk parameters. Planetesimals that contain CO_2 ice ablate much more efficiently than planetesimals that contain only H_2O ice, and planetesimals that additionally contain CO ice lose a small amount of mass in the furthest regions of the disk. Given the high dependency on the disk density, ablation is only expected to be important in relatively young and massive disks.

3. Furthermore, we consider how common the occurrence is of collisions between pairs of planetesimals and between planetesimals and planets. We estimated the timescale for planetesimal–planetesimal collisions in our simulations and we found that it is at least an order of magnitude longer than the actual simulated time. In other words, each planetesimal suffers a low risk of colliding with another planetesimal. About 1–2% of all planetesimals in the Solar System simulations will collide with either Jupiter or Saturn, while for the HL Tau system, this value is about ten times higher. Depending on where the material from these planetesimals is deposited in the atmosphere, this could have an impact on the atmospheric compositions.

The material that is ablated from the planetesimal surfaces consists of a mixture of silicate grains, carbon grains, and vaporized ices. A large fraction of these vaporized ices re-condense to form solid ice. The solid material quickly grows to millimeter-sized pebbles in the disk midplane, drift towards the star, and gives rise to a flux of pebbles. In the Solar System, there is a flux of pebbles produced by planetesimal ablation both within and outside of Jupiter's orbit. Beyond Jupiter, this pebble flux could give rise to newer generations of planetesimals. The total integrated mass that reaches 1 au is $\sim$15 $M_\oplus$ in the nominal Solar System simulation and $\sim$25 $M_\oplus$ in the nominal HL Tau simulation. The pebble flux is expected to drop with time as the density in the disk decreases and ablation becomes less important.

In this work (as well as in our previous paper Eriksson et al. 2020), we focus on studying the formation and fate of planetesimals formed at stationary planetary gap edges; however, the reality is that planets migrate. For the formation of planetesimals, this is expected to lead to planetesimals forming in a larger region of the disk (Shibaike & Alibert 2020). The size of this region depends on how far the planet migrates between the onset of planetesimal formation and the halt of migration when the gap becomes very deep. If planetesimals are forming while the migration timescale is smaller than or comparable to the dynamical timescale, it could result in larger excitations of the planetesimal orbits and more planetesimal–planetesimal collisions (Carter & Stewart 2020). The effects of planetary migration will be investigated in a follow-up study.

Acknowledgements. L.E. and A.J. are supported by the Swedish Research Council (Project Grant 2018-04867). T.R. and A.J. are supported by the Knut and Alice Wallenberg Foundation (Wallenberg Academy Fellow Grant 2017.0287). A.J. further thanks the European Research Council (ERC Consolidator Grant 724 687-PLANETESYS), the Göran Gustafsson Foundation for Research in Natural Sciences and Medicine, and the Wallenberg Foundation (Wallenberg Scholar KAW 2019.0442) for research support. The computations were performed on resources provided by the Swedish Infrastructure for Computing (SNIC) at the LUNARC-Centre in Lund, and are partially funded by the Royal Physiographic Society of Lund through grants. Simulations in this paper made use of the REBOUND code which is freely available at `http://github.com/hannorein/rebound`.

References

ALMA Partnership (Brogan, C. L., et al.) 2015, ApJ, 808, L3
Andrews, S. M., Huang, J., Pérez, L. M., et al. 2018, ApJ, 869, L41
Bai, X.-N., & Stone, J. M. 2010, ApJ, 722, 1437
Bitsch, B., Morbidelli, A., Johansen, A., et al. 2018, A&A, 612, A30
Bottke, W. F., Durda, D. D., Nesvorný, D., et al. 2005, Icarus, 179, 63
Brasser, R., & Morbidelli, A. 2013, Icarus, 225, 40
Carrera, D., Johansen, A., & Davies, M. B. 2015, A&A, 579, A43
Carrera, D., Simon, J. B., Li, R., Kretke, K. A., & Klahr, H. 2021, AJ, 161, 96
Carter, P. J., & Stewart, S. T. 2020, Planet. Sci. J., 1, 45
Chiang, E. I., & Goldreich, P. 1997, ApJ, 490, 368
Coradini, A., Capaccioni, F., Capria, M. T., et al. 1997, Icarus, 129, 317
D'Angelo, G., & Podolak, M. 2015, ApJ, 806, 203
Dipierro, G., Price, D., Laibe, G., et al. 2015, MNRAS, 453, L73
Dullemond, C. P., Birnstiel, T., Huang, J., et al. 2018, ApJ, 869, L46
Eriksson, L. E. J., Johansen, A., & Liu, B. 2020, A&A, 635, A110
Favre, C., Fedele, D., Maud, L., et al. 2019, ApJ, 871, 107
Fedele, D., Tazzari, M., Booth, R., et al. 2018, A&A, 610, A24
Fray, N., & Schmitt, B. 2009, Planet. Space Sci., 57, 2053
Guillot, T., Ida, S., & Ormel, C. W. 2014, A&A, 572, A72
Hayashi, C. 1981, Prog. Theor. Phys. Suppl., 70, 35
Jacquet, E., Pignatale, F. C., Chaussidon, M., & Charnoz, S. 2019, ApJ, 884, 32
Johansen, A., & Bitsch, B. 2019, A&A, 631, A70
Johansen, A., Youdin, A., & Mac Low, M.-M. 2009, ApJ, 704, L75
Johansen, A., Mac Low, M.-M., Lacerda, P., & Bizzarro, M. 2015, Sci. Adv., 1, 1500109
Johansen, A., Ida, S., & Brasser, R. 2019, A&A, 622, A202
Kanagawa, K. D., Tanaka, H., Muto, T., Tanigawa, T., & Takeuchi, T. 2015, MNRAS, 448, 994
Kanagawa, K. D., Muto, T., Tanaka, H., et al. 2016, PASJ, 68, 43
Kita, N. T., & Ushikubo, T. 2012, Meteor. Planet. Sci., 47, 1108
Kruijer, T. S., Burkhardt, C., Budde, G., & Kleine, T. 2017, Proc. Natl. Acad. Sci. U.S.A., 114, 6712
Levison, H. F., Kretke, K. A., & Duncan, M. J. 2015, Nature, 524, 322
Lissauer, J. J., & Stewart, G. R. 1993, in Protostars and Planets III, eds. E. H. Levy, & J. I. Lunine, 1061
Liu, B., Ormel, C. W., & Johansen, A. 2019, A&A, 624, A114
Lyra, W., Johansen, A., Klahr, H., & Piskunov, N. 2009, A&A, 493, 1125
Morbidelli, A., Bottke, W. F., Nesvorný, D., & Levison, H. F. 2009, Icarus, 204, 558
Öberg, K. I., Murray-Clay, R., & Bergin, E. A. 2011, ApJ, 743, L16
Orosei, R., Capaccioni, F., Capria, M. T., et al. 1995, A&A, 301, 613
Perets, H. B., & Murray-Clay, R. A. 2011, ApJ, 733, 56
Pinilla, P., Benisty, M., & Birnstiel, T. 2012, A&A, 545, A81
Pinte, C., van der Plas, G., Ménard, F., et al. 2019, Nat. Astron., 3, 1109
Pinte, C., Price, D. J., Ménard, F., et al. 2020, ApJ, 890, L9
Pirani, S., Johansen, A., Bitsch, B., Mustill, A. J., & Turrini, D. 2019, A&A, 623, A169
Prialnik, D. 1997, Earth Moon Planets, 77, 223
Pringle, J. E. 1981, ARA&A, 19, 137
Raymond, S. N., & Izidoro, A. 2017, Icarus, 297, 134
Rein, H., & Liu, S. F. 2012, A&A, 537, A128
Rein, H., Hernandez, D. M., Tamayo, D., et al. 2019, MNRAS, 485, 5490
Ronnet, T., & Johansen, A. 2020, A&A, 633, A93
Schiller, M., Bizzarro, M., & Fernandes, V. A. 2018, Nature, 555, 507
Shakura, N. I., & Sunyaev, R. A. 1973, A&A, 500, 33
Shibaike, Y., & Alibert, Y. 2020, A&A, 644, A81
Shibata, S., & Ikoma, M. 2019, MNRAS, 487, 4510
Stammler, S. M., Drążkowska, J., Birnstiel, T., et al. 2019, ApJ, 884, L5
Supulver, K. D., & Lin, D. N. C. 2000, Icarus, 146, 525
Trinquier, A., Elliott, T., Ulfbeck, D., et al. 2009, Science, 324, 374
Warren, P. H. 2011, Earth Planet. Sci. Lett., 311, 93
Whipple, F. L. 1972, in From Plasma Planet, ed. A. Elvius, 211
Yang, C. C., Johansen, A., & Carrera, D. 2017, A&A, 606, A80
Youdin, A. N., & Goodman, J. 2005, ApJ, 620, 459
Zhang, S., Zhu, Z., Huang, J., et al. 2018, ApJ, 869, L47

Appendix A: No ablation simulation

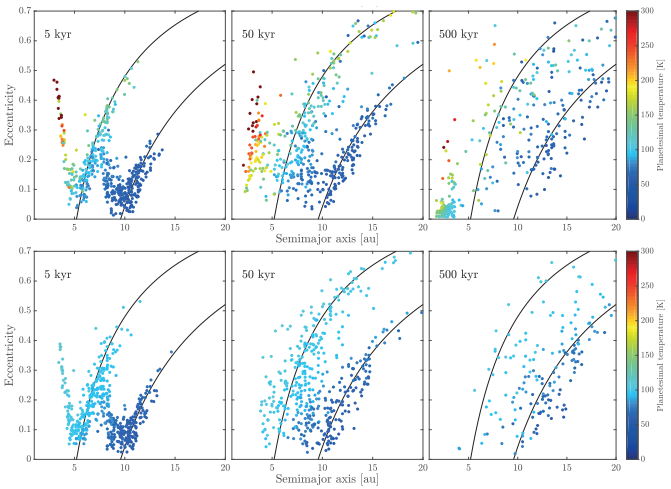

Fig. A.1. Comparison of nominal Solar System simulations without surface ablation (*top panels*), and with surface ablation (*bottom panels*). The temperature range in the plots is set to 0–300 K to allow for easy comparison; the hottest planetesimals in the top panels have surface temperatures of 443 K, 362 K, and 281 K, respectively, *from left to right*. The high temperatures obtained in the non-ablation simulations are due to the lack of cooling due to the release of latent heat of vaporization. The population of planetesimals with low eccentricities and short periods in the non-ablation simulations have been circularized by gas drag, these populations do not exist in the ablation simulations since they are removed by ablation before they become circularized.

In Fig. A.1, we show a comparison of simulations with and without surface ablation. When surface ablation is neglected, there is no cooling due to latent heat of vaporization (last term in Eq. (18)). In regions where surface ablation would still have been inefficient, that is, in regions where the surface temperatures are low, this cooling term is very small and thus there is no significant difference between the surface temperatures in the two simulations. This is the case for planetesimals located in Saturn's scattered disk and beyond. For planetesimals located in Jupiter's scattered disk and closer to the star, the surfaces can reach several hundred degrees higher temperatures than they do in simulations including ablation. If an ablating planetesimal in this region were to suddenly stop ablating for some reason, its surface temperature would rapidly increase.

In runs without ablation, the effect of eccentricity damping by gas drag in the innermost disk becomes visible. Over time, the eccentricities of planetesimals close to the star begin to decrease and after 500 kyr, a population of planetesimals with small and close-to circular orbits emerges. This population does not appear in the ablation simulations since planetesimals become completely ablated before they are circularized.

The disk parameters of the nominal simulation correspond to a young and relatively massive disk. The surface density of disks decreases with time, meaning that both ablation and circularization by gas drag will become less efficient. The difference between the two simulations will thus be less prominent in older disks and, just like ablation, it will occur closer to the star. This means that as the disk evolves with time and ablation becomes inefficient, planetesimals should eventually survive in the asteroid belt region. Finally, we would like to highlight that ablation is a process which occurs in the presence of a major gas component and it could not occur for planetesimals with similar surface temperatures in a system without gas (e.g., comets).

Appendix B: Comments on crust formation

In this work, we assume that solid grains embedded in the ice are released along with the vaporized ices. In a scenario where the outflow of vapor is too small to carry along the solid grains, we might instead expect that a dry dust mantle would build up. Once this mantle has become thick, it would severely limit further mass loss. Here, we present a few arguments for why this should not be the case for the efficiently ablating planetesimals in our simulations.

In Appendix A, we show that if an efficiently ablating planetesimal suddenly stops ablating, then the lack of cooling due to latent heat of vaporization causes the surface temperatures to increase by up to several hundred degrees. In other words, if a dust mantle starts to build up and begins to limit the amount of mass loss via ablation, the surface temperature quickly increases. A similar effect has been studied in the case of comets, although the heating source is different (Orosei et al. 1995; Coradini et al. 1997; Prialnik 1997). The main differences are that: (1) planetesimals can reach much higher surface temperatures than comets if the gas densities are high, which goes against the sustainability of a dust mantle; and (2) the strong headwind around the planetesimals should blow of the dust that is lifted up (whereas dust

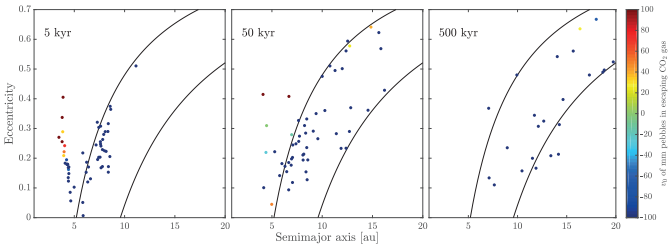

Fig. B.1. Initial vertical velocity for mm-sized pebbles in the outflowing CO_2 gas caused by surface ablation. The calculation is done for planetesimals around perihelion in the nominal Solar System simulation. Pebbles are released along with the gas in the case of high eccentric planetesimals interior of Jupiter's orbit. Lighter gas molecules, smaller pebble sizes, and increased surface temperatures due to a lack of cooling from release of latent heat of vaporization would result in more pebbles being released in this plot.

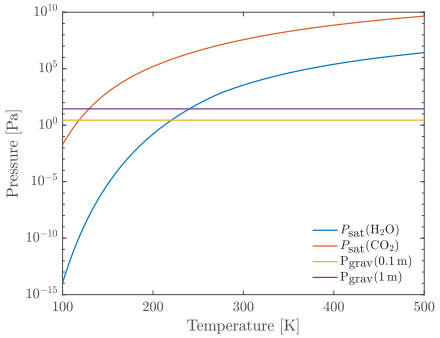

Fig. B.2. Comparison between the saturated vapor pressure and the gravitational pressure at 0.1 m and 1 m below the surface of a 100 km-sized planetesimal at different temperatures and for different molecules. The temperature down to 1 m below the surface is assumed to be the same as on the surface. The temperature needs to be about twice as high when considering H_2O molecules than when considering CO_2 molecules in order for the vapor pressure to win over the gravitational pressure.

can fall back onto comets). The formation of dust mantles in the case of planetesimals is thus more difficult than in the case of comets, and even for comets it is not a process which always occurs (Prialnik 1997).

The process described above relies on the presence of a significant gas component, which is the case for planetesimals on short orbits in young disks. Further away from the star, where the gas density is lower and ablation less efficient, this process is much less dramatic and a dust mantle might be allowed to form; however, since planetesimals in this region do not ablate very efficiently to begin with, the effect should not modify our results significantly. The production of a dust mantle will also get easier with time, as the gas density decreases and ablation becomes less and less efficient.

In order to further validate our method we have performed a calculation to check whether the escaping gas from planetesimals is strong enough to carry mm-sized pebbles along with it. This is assumed to be the case when the drag force exerted on a pebble by the outflowing gas is stronger than the gravitational pull of the planetesimal (we ignore the centrifugal correction on the gravity of the planetesimal). Because of the strong headwind in the disk, any pebble that is lifted up from the surface will be immediately carried away by the headwind. As previously mentioned, this is in contrast with the activity of airless bodies such as comets for which dust grains should fall back if their velocity is smaller than the escape velocity of the body.

The initial vertical velocity of a pebble at the surface is calculated as:

$$v_0 = v_{\rm th} - \frac{GM_{\rm pl} t_{\rm s}}{R_{\rm pl}^2}. \tag{B.1}$$

Here, $v_{\rm th}$ is the outflow speed of the gas molecules and we perform the calculation for CO_2 molecules. The density of the outflowing gas is calculated as:

$$\rho = \frac{\dot{m}_{\rm abl}}{A_{\rm pl} v_{\rm th}}, \tag{B.2}$$

where $A_{\rm pl}$ is the surface area of the planetesimal. The relative velocity between the pebble and the gas, which is required to calculate the stopping time, is then simply

$$v_{\rm rel} = v_0 - v_{\rm th} = \frac{GM_{\rm pl} t_{\rm s}}{R_{\rm pl}^2}. \tag{B.3}$$

Since $t_{\rm s}$ depends also on $v_{\rm rel}$ this equation has to be solved using a bisection method.

The results from this calculation is presented in Fig. B.1 for planetesimals close to perihelion in the nominal Solar System simulation. In this plot, a pebble is being ejected from the planetesimal when its initial vertical velocity is larger than 0. The results show that pebbles are lifted up by the escaping gas in the case of the most efficiently ablating planetesimals. As explained earlier, ablating planetesimals that start to build up a dust mantle would obtain significantly increased surface temperatures. The corresponding initial vertical velocity of pebbles on those planetesimals would then increase, leading to many more pebbles released than what is suggested by the plot. The above calculation is performed for CO_2 molecules. Using H_2O or CO molecules instead results in higher pebble velocities, provided the ablation rate is the same. The pebble size also affects the calculation, with larger pebbles being more difficult to achieve lift off the surface (e.g., Orosei et al. 1995).

Finally, we ask whether a potential crust would have survived the pressure from the vapor sublimated underneath its surface. To answer this, we performed a simple calculation where we compare the saturated vapor pressure with the gravitational pressure at 0.1 m and 1 m below the surface of a 100 km-sized planetesimal, assuming constant density, hydrostatic equilibrium and that the temperature down to 1 m below the surface is the same as on the surface. The result of this calculation is presented in Fig. B.2. When considering CO_2 vapor, a temperature of about 120–130 K is required to blow off the crust, for H_2O a temperature of 220–240 K is required. Comparison with the top panel of Fig. A.1 shows that these temperatures are obtained for planetesimals sitting inside and interior of Jupiter's scattered disk in the case of CO_2 vapor, and for highly eccentric planetesimals interior of Jupiter's orbit in the case of H_2O vapor. Any crust that forms in these regions of the disk is thus likely to be blown off. If a crust were to form further out in the disk on the other hand, it would likely remain and limit any further ablation from the planetesimal surface. However, we note that the formed crust is likely to be porous with a density smaller than what is assumed for this calculation, so the temperatures required to blow off the crust would be lower than what is suggested in Fig. B.2.

Appendix C: Saturated vapor pressure

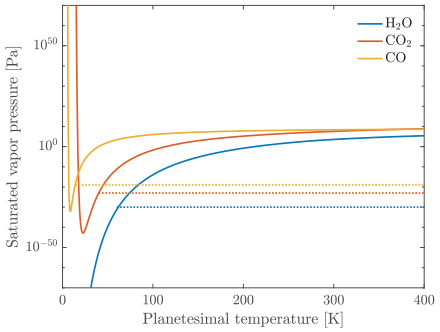

Fig. C.1. Saturated vapor pressure as a function of planetesimal surface temperature for H_2O, CO_2 and CO ice. The dotted lines mark our floor values, which are used for numerical reasons.

Figure C.1 shows the saturated vapor pressure as a function of the planetesimal surface temperature. The saturated vapor pressure is calculated using polynomial expressions from Fray & Schmitt (2009). These expressions are valid in the following temperature range: 0–273.16 K, 40–216.58 K, and 14–68.1 K for H_2O, CO_2, and CO ice, respectively. Looking at Fig. C.1, there is a smooth extrapolation to temperatures above the stated temperature range for all ices. This is not the case below the temperature range. For CO_2 and CO ice the polynomial turns upwards at low temperatures; therefore, we introduce floor-values at 40 K and 14 K, respectively. For H_2O the polynomial heads to minus infinity as the temperature decreases; therefore, we introduce a floor-value at 60 K to prevent numerical issues. Additional tests show that lowering this floor-value does not affect the results. Since there are no issues at the upper temperature range, we do not introduce any similar constraints there.

Appendix D: Mass ablation rate

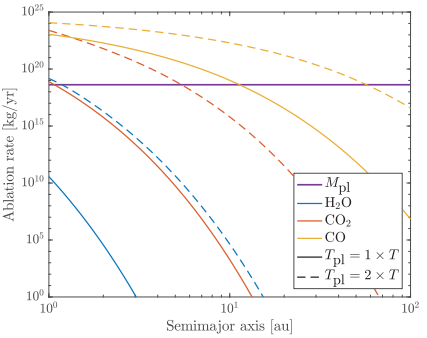

Fig. D.1. Mass ablation rate as a function of semimajor axis for H_2O, CO_2, and CO ice. The planetesimal surface temperature is set to equal integer multiples of the disk temperature. The mass of one planetesimal is marked as a purple line on the plot; above this line, a planetesimal becomes completely ablated within one year.

Figure D.1 shows the mass ablation rate as a function of the semimajor axis for H_2O, CO_2, and CO ice (calculated using Eq. (17)). The ablation of H_2O ice is only efficient in the very innermost part of the disk and does not generate very high ablation rates. The ablation rates for CO ice are on the contrary high enough to completely sublimate a planetesimal on a ∼10 au circular orbit within a year. Planetesimals formed beyond the CO iceline should thus lose mass much further out in the disk than planetesimals formed interior of the CO iceline. The ablation rates for CO_2 ice lie in between the ablation rates for H_2O and CO ice.

Appendix E: Varying the gap width and the planetesimal formation location

The planetesimals in our simulations are initiated between 1–2 Hill radii away from the planets, which is roughly the region in which planetesimals form in Paper I. The formation location in Paper I is strongly affected by (1) the width and depth of the planetary gap; and (2) our assumption that the planetesimals form at the location where the SI is triggered. Regarding (1): There are numerous gap prescriptions in the literature and they often disagree on the resultant gap shape. Wider gaps result in planetesimal formation further from the planet and deeper gaps result in planetesimals forming in a narrower region. Furthermore, 1D simulations generally produce deeper and narrower gaps than their 2D or 3D analogs. Regarding (2), Carrera et al. (2021) performed 3D simulations of the streaming instability in the presence of a pressure bump and found that the planetesimals form inward of the pressure bump that initiated their growth, so not at the exact location where the SI is triggered. Taken together, this means that we do not know exactly where the planetesimals form relative to the planet location. The formation location might be both closer or further away from the planet than it is in our simulations.

In order to study how different formation locations affect our results, we performed three nominal Solar System simulations

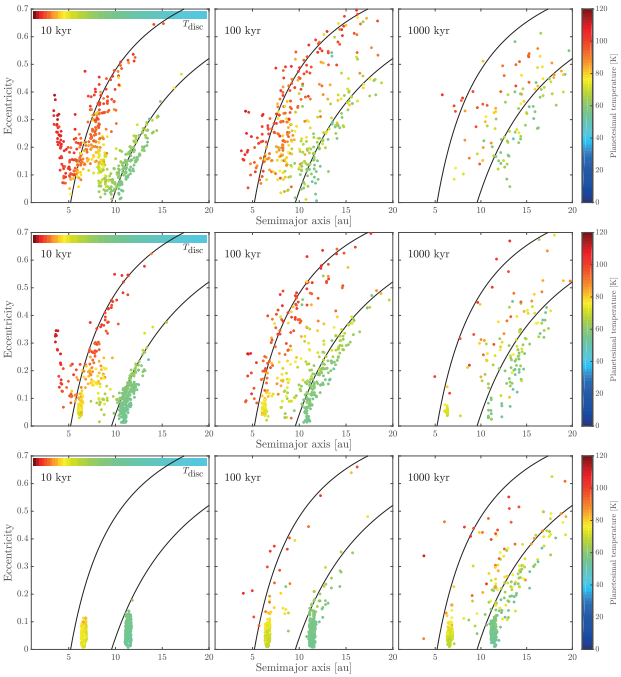

Fig. E.1. Eccentricity, semimajor axis, and surface temperature evolution for three nominal Solar System simulations with 500 planetesimals per simulation and varying planetesimal formation locations. In the *top panel*, the planetesimals are initiated between 1 and 3 Hill radii away from the planets, in the *middle panel* between 3 and 5 Hill radii, and in the *bottom panel* between 5 and 7 Hill radii. The solid black lines mark the perihelia of the planets. Eccentricity excitation occurs much earlier and at a much faster speed for planetesimals initiated close to the planets. When the planetesimals are initiated between 5 and 7 Hill radii away from the planets, a population of planetesimals still remain around their birth location at the end of the simulation.

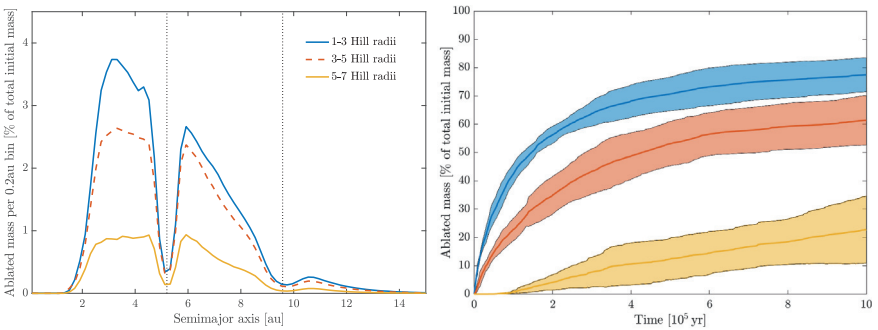

Fig. E.2. Distribution of ablated mass as a function of semimajor axis (*left*) and time (*right*) for the same three simulations as in Fig. E.1. *Left*: Distribution of ablated mass across the disk after 1 Myr. The values on the y-axis represent the amount of mass that has been ablated in a 0.2 au semimajor axis bin. The dotted lines mark the semimajor axes of the planets. The distribution of ablated mass is very similar in all three simulations, with the majority of mass being lost either just within or just outside of Jupiter's orbit. *Right*: Total amount of mass that has been ablated as a function of time for the same data as in the left plot. The colored lines show the average over the five simulations and the colored region shows the one standard deviation away from this value. The ablation rate decreases as the planetesimal formation location with regard to the planet increases; however, the ablation continues for a longer period of time.

where we placed the planetesimals at either 1–3, 3–5, or 5–7 Hill radii away from the planets and extended the simulation time to 1 Myr. The gas surface density profile was kept unchanged. The results of these simulations are presented in Figs. E.1 and E.2. Generally, the excitation of the orbital eccentricities is slower when the planetesimals are formed further away from the planets. Because of this, some planetesimals are still located close to their birth locations at the end of the simulation. The slower orbital excitation also results in lower ablation rates, especially in the beginning of the simulation; however, the ablation continues for a much longer period of time. This would result in the flux of pebbles through the midplane being lower, but persisting for a longer time. The presented results indicate that ablation is important also for planetesimals forming further away from the planets, but it happens on a longer timescale.

In the above simulations, we only varied the formation location of the planetesimals, not the shape of the planetary gas-gap. Narrower gaps will result in mass loss closer to the planet location, and shallower gaps will result in that more mass is lost around the planet location. We confirmed this by performing a simulation with half the gap-width and a much shallower gap. We found that the total amount of mass loss did not change, only the distribution of the ablated material around the location of the planets did, in fact, change.

Appendix F: Dynamical evolution of six planetesimals

Figure F.1 shows the dynamical evolution for the same 6 planetesimals as in Fig. 3. The "red" planetesimal forms at the gap edge of Jupiter, and is a member of Jupiter's scattered disk until it obtains a strong kick and becomes a member of Saturn's scattered disk, where it remains until the end of the simulation. The "yellow" planetesimal is a member of Jupiter's scattered disk for a few thousand years, until a kick by Jupiter places it on an orbit interior of the scattered disk, where it quickly becomes ablated. The "green" planetesimal is a member of Jupiter's scattered disk during most of its lifetime until it is kicked towards the sun and becomes ablated.

The "light-blue" planetesimal forms at the gap edge of Saturn, and sits on an orbit just within Saturn's scattered disk for about 150 kyr, when it is then scattered towards Jupiter's scattered disk and obtains a large eccentricity, which increases with time until the planetesimal leaves the simulation domain. The "dark-blue" planetesimal is a member of Saturn's scattered disk for 50 kyr, until a strong encounter with Saturn places it on an orbit interior of Jupiter, where it becomes circularized. The "purple" planetesimal is a member of Saturn's scattered disk for most of its lifetime, except during a brief period where it has an orbit that is slightly outside the scattered disk.

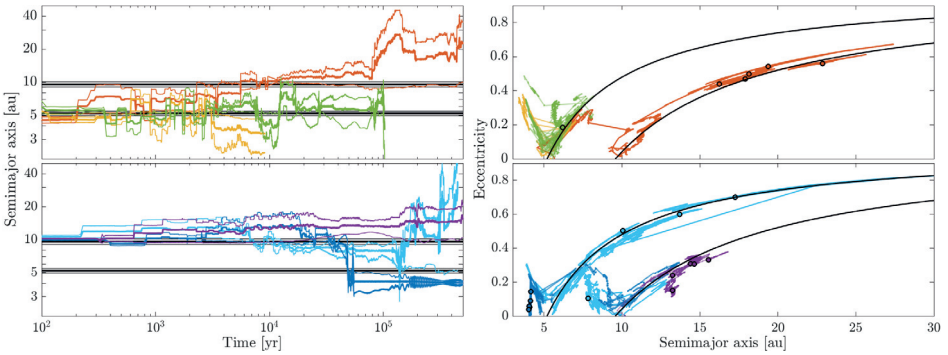

Fig. F.1. Semimajor axis and eccentricity evolution for the same data as in Fig. 3, with the same color-coding. Planetesimals formed at Jupiter's gap edge are plotted in the *top panels*, and planetesimals formed at Saturn's gap edge are plotted in the *bottom panels*. *Left*: evolution of the planetesimals semimajor axis (thick colored lines), perihelion, and aphelion (thin colored lines). The semimajor axes, perihelia and aphelia of Jupiter and Saturn (thick and thin black lines) are included as well. *Right*: eccentricity and semimajor axis tracks, with dots to mark 100 kyr of evolution. The black lines mark the perihelia of Jupiter and Saturn.

Paper III

Astronomy & Astrophysics manuscript no. 42391corr
March 14, 2022

A low accretion efficiency of planetesimals formed at planetary gap edges

Linn E.J. Eriksson[1] , Thomas Ronnet[1] , Anders Johansen[1,2] , Ravit Helled[3] , Claudio Valletta[3] , Antoine C. Petit[2]

[1] Lund Observatory, Department of Astronomy and Theoretical Physics, Lund University, Box 43, 221 00 Lund, Sweden
[2] Center for Star and Planet Formation, GLOBE Institute, University of Copenhagen, Øster Voldgade 5-7, 1350 Copenhagen, Denmark
[3] Institute for Computational Science, University of Zurich, Winterthurerstr. 190, CH-8057 Zurich, Switzerland
e-mail: linn@astro.lu.se

Received X; accepted X

ABSTRACT

Observations and models of giant planets indicate that such objects are enriched in heavy elements compared to solar abundances. The prevailing view is that giant planets accreted multiple Earth masses of heavy elements after the end of core formation. Such late solid enrichment is commonly explained by the accretion of planetesimals. Planetesimals are expected to form at the edges of planetary gaps, and here we address the question of whether these planetesimals can be accreted in large enough amounts to explain the inferred high heavy element contents of giant planets. We performed a series of N-body simulations of the dynamics of planetesimals and planets during the planetary growth phase, taking gas drag into account as well as the enhanced collision cross section caused by the extended envelopes. We considered the growth of Jupiter and Saturn via gas accretion after reaching the pebble isolation mass and we included their migration in an evolving disk. We find that the accretion efficiency of planetesimals formed at planetary gap edges is very low: less than 10% of the formed planetesimals are accreted even in the most favorable cases, which in our model corresponds to a few Earth masses. When planetesimals are assumed to form beyond the feeding zone of the planets, extending to a few Hill radii from a planet, accretion becomes negligible. Furthermore, we find that the accretion efficiency increases when the planetary migration distance is increased and that the efficiency does not increase when the planetesimal radii are decreased. Based on these results, we conclude that it is difficult to explain the large heavy element content of giant planets with planetesimal accretion during the gas accretion phase. Alternative processes most likely are required, such as accretion of vapor deposited by drifting pebbles.

Key words. Planets and satellites: formation — Protoplanetary discs — Planet-disc interactions

1. Introduction

Matching interior structure models of Jupiter and Saturn to their measured gravity fields requires that the planets have a minimum heavy-element content of $\sim$20 $M_\oplus$, with upper bounds that are much higher and depend heavily on what model assumptions are used (e.g., Helled & Guillot 2013; Wahl et al. 2017; Helled 2018). Similarly, results from structure models of transiting planets show that extrasolar giants typically are enhanced in heavy elements, with estimated heavy element masses ranging from $\sim 10 - 100\,M_\oplus$ (Guillot et al. 2006; Miller & Fortney 2011; Thorngren et al. 2016). Such large masses suggest that there are significant amounts of heavy elements in the H/He envelopes, indicating that giant planets typically have enriched atmospheres. Provided that envelope enrichment does not occur via erosion of the initial core alone (Stevenson 1982), this implies that multiple Earth masses of heavy elements must have been accreted after the end of core formation.

Late heavy-element enrichment is often explained by the accretion of planetesimals (e.g., Alibert et al. 2018). In order to match the estimated heavy-element contents of giant planets, a massive wide-stretched disk of planetesimals typically has to be assumed for studies of this process (e.g., Venturini & Helled 2020; Shibata et al. 2020). However, simulations of planetesimal formation via the streaming instability (SI), which is one of the favored mechanisms for forming planetesimals (Nesvorný et al. 2019), suggests that planetesimals form in regions with locally enhanced solid-to-gas ratios (Youdin & Goodman 2005; Johansen et al. 2009; Lyra et al. 2009; Bai & Stone 2010; Carrera et al. 2015; Yang et al. 2017). One such naturally occurring region is in the pressure bump generated at the edges of planetary gaps, where inward drifting pebbles are trapped (Stammler et al. 2019; Eriksson et al. 2020; Carrera et al. 2021).

In Eriksson et al. (2021), we studied the dynamical evolution of planetesimals formed at planetary gap edges, keeping the planet masses and locations fixed. We found that planetesimals are strongly scattered and that they leave their birthplace shortly after formation. In this study, we determine the amount of planetesimals that eventually collide with a planet, considering both planet migration and growth, and we investigate whether the delivered mass is high enough to explain the large heavy element masses in giant planets. We therefore performed a suite of *N*-body simulations, including the effect of gas drag on the planetesimals and the enhanced collision cross section caused by the extended planetary envelope. We focus on the formation of the Solar System's two gas-giant planets, Jupiter and Saturn, as both are massive enough to open up deep gaps in the disk, and thus they likely had planetesimals forming at their gap edges. We consider two different formation pathways for the planets, where one leads to a large-scale planetary migration, while the second one leads to a migration over a few au only. We continuously formed planetesimals at the gap edges from the moment

gas accretion initiated, that is to say when the pebble isolation mass was reached ($M_{\rm iso}$, Lambrechts et al. 2014; Bitsch et al. 2018), until the time of disk dissipation. By further varying the planetesimal size and the formation location of the planetesimals relative to the planet, we explored the sensitivity of the accretion efficiency to these parameters.

In Sect. 2, we present our models for disk evolution and planet formation, as well as the setup of our simulations. We present the results of our simulations in Sect. 3, where we show that the accretion efficiency of planetesimals formed at planetary gap edges is low, leading to the accretion of only a few Earth masses of planetesimals in the most favorable cases. In Sect. 4 we compare our results to the estimated heavy-element content of giant planets, and we reach the conclusion that alternative processes most likely are required in order to explain the high heavy element masses inferred from observations. The key findings of the paper are summarized in Sect. 5. Further information about our model and some additional figures can be found in Appendix A-C.

2. Model

In this section we describe the ingredients and parameters of our simulations. We start by introducing our model for the structure and evolution of the protoplanetary disk. Planetesimals that move through the disk experience a drag force, which we account for following the method outlined in Eriksson et al. (2021). Our model for planetary evolution contains planet migration, gas accretion, and gap opening. Collisions between planets and planetesimals are detected using a direct search method, which requires the capture radius of the planet being known. We used the approximation from Valletta & Helled (2021) for planets that have attained a gaseous envelope (planets with masses above the pebble isolation mass), and assumed that the capture radius is equal to the core radius for lower planetary masses. Finally we describe the numerical setup and initialization of our N-body simulations.

2.1. Disk model

The evolution of the unperturbed surface density $\Sigma_{\rm unp}$ was modeled using a standard alpha-disk model, which is dependent on the disk accretion rate $\dot{M}_g$ and the scaling radius $r_{\rm out}$ (Lynden-Bell & Pringle 1974). The kinematic viscosity was approximated as

$$\nu = \alpha \Omega H^2, \tag{1}$$

where α is the viscosity parameter, Ω is the Keplerian angular velocity, and H is the scale height of the gaseous disk (Shakura & Sunyaev 1973). We considered the scale height to be $H = c_{\rm s}/\Omega$, where $c_{\rm s}$ is the sound speed. The disk's midplane temperature was approximated using a fixed power-law structure for a passively irradiated disk (Chiang & Goldreich 1997). The disk accretion rate is given by the standard viscous accretion rate minus the rate at which gas was removed by photoevaporation $\dot{M}_{\rm pe}$, which we considered to be a constant in time (see Appendix A for details on our disk model).

Massive planets perturb their birth disks by pushing material away from the vicinity of their orbits, leading to gap opening. We used a simple approach with Gaussian gap profiles to model these gaps. The height of the Gaussian was determined by the depth of the gap (see Section 2.4), and the width was considered to be one gas scale height at the planet location. Finally, in order to obtain the gas density at some height, z, over the midplane, we assumed vertical hydrostatic equilibrium for the gas in the disk.

2.2. Migration

For the migration of planets we followed Kanagawa et al. (2018), who found that embedded planets experience a torque which is equal to the classical type-I torque multiplied by the relative gap height, resulting in the following migration rate:

$$\dot{r} = \dot{r}_{\rm I} \times \frac{\Sigma_{\rm gap}}{\Sigma_{\rm unp}} \tag{2}$$

(see Eq. 3-4 in Johansen et al. (2019) for the classical type-I migration rate). This results in little or no migration before the planet reaches a few Earth masses, fast migration during the last stages of pebble accretion and the first stages of gas accretion, and slow migration during runaway gas accretion when the gap has become deep. For the implementation of migration into the N-body code we followed Cresswell & Nelson (2008), who provide the timescales for radial migration as well as the associated eccentricity and inclination damping. The corresponding accelerations were then directly applied to the planets at fixed time intervals.

2.3. Gas accretion

Protoplanets can accrete gaseous envelopes already during the early phases of core formation. During this stage the heating of the envelope from the flux of pebbles prevents it from contracting onto the planet. At a later stage, when the protoplanet reaches the pebble isolation mass and the flux of pebbles stops, the envelope contracts. This is the first stage of significant gas accretion; however, even before this stage, some small amounts of highly polluted gas can become bound to the protoplanet inside its Hill sphere (Bitsch et al. 2015). We followed the assumption of Bitsch et al. (2015) that 10% of the material accreted by the planet prior to the pebble isolation mass is in gas, so that the final mass of the core is $0.9 \times M_{\rm iso}$. We note that this is a simplification, and in reality the gas fraction is expected to increase as the core grows more massive (Valletta & Helled 2020).

The gas accretion rate of a protoplanet during the contraction phase (also known as the attached phase) is highly uncertain and there are several prescriptions to describe this stage, many of which are vastly different. In this work we use the following two different prescriptions: scheme 1 results in a short contraction phase, while scheme 2 leads to a relatively long contraction timescale. In scheme 1 we followed the gas accretion model outlined in Johansen et al. (2019) (Eq. 38-40). The envelope's contraction occurs on the Kelvin-Helmholtz timescale, which depends on the planetary mass M_p and the envelope's opacity κ (Ikoma et al. 2000). For large planetary masses, this accretion rate becomes higher than what the disk can supply. At this point the planet enters the runaway gas accretion phase (also known as the detached phase), and the growth becomes limited by the rate at which gas can enter the Hill sphere (Tanigawa & Tanaka 2016). As an additional constraint, the planet cannot accrete at a rate which is higher than the global disk accretion rate $\dot{M}_g$. Furthermore, Lubow & D'Angelo (2006) found that even high mass planets cannot block all gas from passing the gaps, and that the protoplanets do not accrete at a rate higher than 75-90% of the disk's accretion rate. Therefore, we limited the maximum gas accretion rate to 80% of the disk's accretion rate. The gas accretion rate onto the planet in scheme 1 was then considered to be the minimum of the three aforementioned rates.

In scheme 2 we roughly followed the gas accretion model which was used in Bitsch et al. (2015). During the contraction phase, which is defined as $M_{\rm env} < M_{\rm core}$ here, the envelope contracts on a long timescale while accreting some gas. The accretion rate during this phase depends on the envelope opacity, the core density $\rho_{\rm core}$, the mass of the core and envelope, and the disk temperature (see Eq. 17 in Bitsch et al. (2015), originally derived in Piso & Youdin (2014)). Runaway gas accretion initiates when $M_{\rm env} > M_{\rm core}$, and for this phase we used the gas accretion rate from Tanigawa & Tanaka (2016), which is the same as in scheme 1. Furthermore, we also limited gas accretion to 80% of the disk accretion rate throughout the entire process. The dependence of all of the aforementioned gas accretion rates on the planetary mass is plotted in Fig. B.1.

2.4. Gap depth

For the relative depth of the planetary gaps, we followed Johansen et al. (2019), who show that the gap depth scales with the pebble isolation mass as follows:

$$\frac{\Sigma_{\rm gap}}{\Sigma_{\rm unp}} = \frac{1}{1 + \left(\frac{M_p}{2.3 M_{\rm iso}}\right)^2}. \quad (3)$$

We used the fit from Bitsch et al. (2018) to calculate the pebble isolation mass, which depends on the turbulent viscosity α_t and the unperturbed radial pressure gradient of the disk $\partial \ln P / \partial \ln r$. We used an unperturbed surface density gradient of $-15/14$, which results in a radial pressure gradient of -2.7857.

2.5. Numerical setup and initialization

Table 1 lists the parameter values used in our simulations. The simulations were performed with the N-body code REBOUND and executed using the hybrid symplectic integrator MERCURIUS (Rein & Liu 2012; Rein et al. 2019). The WHFAST time step was set to be one twentieth of Jupiter's current dynamical timescale, and we only performed disk evolution, migration, and gas accretion on this time step. The planets and the central star were added as active particles, and the planetesimals were added as test particles. We used a central star of solar mass and solar luminosity. Collisions were detected using a direct search algorithm and resulted in perfect merging. Particles that left the simulation domain, which is centered on the sun and stretches 100 au in the x and y direction and 20 au in the z direction, were recorded and removed from the simulation.

The protoplanetary disk was modeled using a linear grid with 1000 grid cells, stretching from 0.1 to 100 au. We used standard values of 75 au for the scaling radius and 10^{-2} for the viscosity parameter. The initial disk accretion rate was set to $10^{-7}\ M_\odot\ {\rm yr}^{-1}$, and we chose the photoevaporation rate such that the disk obtained a lifetime of 3 Myr. We continued the orbital integration for an additional 7 Myr after disk dispersal.

We modeled Jupiter's formation starting at the pebble isolation mass, and for Saturn we also included a prescription for the growth of the core. The reason is that in our model, Jupiter reaches the pebble isolation mass and begins to form planetesimals at the gap edge earlier than Saturn, and while we assume that there is no planetesimal formation at Saturn's gap edge during core formation, the formation of its core could still dynamically effect the planetesimals formed at Jupiter's gap edge. The initial semimajor axis and formation time of the planets are determined in Section 3.1. The initial orbital eccentricity and inclination were set to 10^{-3}, and we used a constant opacity of $5 \times 10^{-2}\ {\rm m}^2\ {\rm kg}^{-1}$ for the gaseous envelope.

Table 1. Parameters used throughout the simulations. The parameters which were varied are marked with an asterisk (∗).

Parameter	Value	
	Planet	
e_0	10^{-3}	initial eccentricity
i_0	10^{-3}	initial inclination
$\rho_{\rm core}$	$5.5 \times 10^3\ {\rm kg\ m}^{-3}$	density of core
κ	$5 \times 10^{-2}\ {\rm m}^2\ {\rm kg}^{-1}$	opacity of envelope
	Planetesimal	
$N_{\rm pl}$	10^4	number of planetesimals
$R_{\rm pl}$	$10^5, 10^4, 300$ m	radius*
$\rho_{\rm pl}$	$10^3\ {\rm kg\ m}^{-3}$	density
$a_{\rm pl}$	$2-3, 4-5\ R_H$	initial location rel planet*
$e_{\rm pl,0}$	$\sim 5 \times 10^{-3}$	initial eccentricity
$i_{\rm pl,0}$	$\sim 5 \times 10^{-3}$	initial inclination
	Disk	
$r_{\rm out}$	75 au	scaling radius
$\dot{M}_g(t=0)$	$10^{-7}\ M_\odot\ {\rm yr}^{-1}$	initial disk accretion rate
$\dot{M}_{\rm photo}$	$5.9 \times 10^{-9}\ M_\odot\ {\rm yr}^{-1}$	rate of photo evaporation
$t_{\rm evap}$	3 Myr	disk lifetime
α	10^{-2}	viscosity parameter
$\alpha_{\rm t}$	10^{-4}	turbulent parameter
ϵ	1%	solid-to-gas ratio
	Grid	
$N_{\rm grid}$	1000	number of gridcells
r_1	0.1 au	innermost grid point
r_{1000}	100 au	outermost grid point
	Simulation	
dt	0.6 yr	WHFAST time step
$t_{\rm max}$	10 Myr	simulation time

Each simulation contained a total of 10,000 planetesimals, which were injected at the gap edges ten at a time from the beginning of the simulation until disk dissipation. Given the formation times provided in Table 2, this means that we injected ten planetesimals into the simulation roughly every 1,000 year. The planetesimal radii were varied in between the simulations and set to either 300 m, 10 km, or 100 km (Bottke et al. 2005; Morbidelli et al. 2009; Johansen et al. 2015). The exact formation location of planetesimals at gap edges is unknown (Carrera et al. 2021). Here we tried two different formation locations: in the first setup, we initiated the planetesimals uniformly between 2 and 3 Hill radii from the planets (thus interior of the single planet feeding zone at $2\sqrt{3}R_H$); and in the second setup, we did so between 4 and 5 Hill radii from the planets (thus exterior of the feeding zone). The feeding zone is defined as the region where the Jacobi energy of the planetesimals is positive (Shiraishi & Ida 2008). Finally, in order to provide better statistics, we performed three simulations per parameter set.

3. Result

3.1. Planet growth tracks

Given our models for migration and gas accretion (introduced in Section 2.2 and 2.3), we searched for growth tracks that resulted in Jupiter and Saturn having their current mass and semimajor axis at the time of disk dissipation. The resulting time and semimajor axis at which the planets began to migrate and accrete gas,

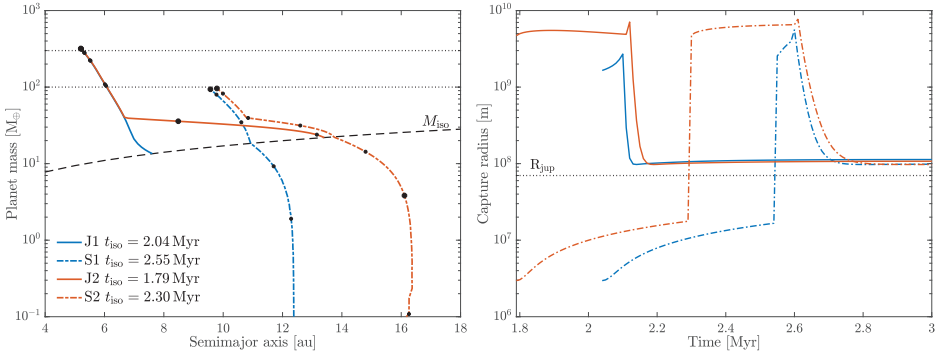

Fig. 1. Planetary growth tracks and evolution of the capture radii. *Left*: Planet mass versus semimajor axis evolution for Jupiter (J) and Saturn (S) in gas accretion scheme 1 and 2. Large dots indicate a time of 2 and 3 Myr, and small dots are separated by 0.2 Myr. We started the simulation at the time when Jupiter reached the pebble isolation mass (t_{iso}), and further included the growth and migration of Saturn's core. In scheme 1 the contraction of the envelope occurs on a short timescale, resulting in fast gap opening and little migration. In scheme 2 this phase is significantly longer, and thus the planets migrate a further distance before coming to a halt due to gap opening. *Right*: Capture radius versus time for the growth tracks presented in the left panel, calculated using a planetesimal radius of 100 km. The approximation for the capture radius has three regimes: before gas accretion is initiated, the capture radius is equal to the core radius; during the first phase of gas accretion, the envelope is enhanced, resulting in a large capture radius; and after the onset of runaway gas accretion, the capture radius decreases by roughly two orders of magnitude, and it takes on a value of about 1.5 times the current Jupiter radius.

Table 2. Parameters for the planet growth tracks. We note that t_{iso} and a_{iso} are the time and semimajor axis at which the planet reaches the pebble isolation mass M_{iso}. Furthermore, a_{core} is the semimajor axis at which Saturn's core has to be initiated in order for it to reach a_{iso} at time t_{iso}.

Run	t_{iso}	a_{iso}	M_{iso}	a_{core}
J1	2.04 Myr	7.61 au	13.50 $M_\oplus$	
S1	2.55	10.94	18.42	12.38 au
J2	1.79	13.41	21.93	
S2	2.30	13.52	22.09	16.17

as well as the corresponding pebble isolation mass, can be found in Table 2. According to these results, Saturn reaches the pebble isolation mass much later than Jupiter. We began our simulations at the time when Jupiter reached the pebble isolation mass, and although we assumed that planetesimals do not form at Saturn's gap edge during core formation, the formation of Saturn's core could still dynamically affect the planetesimals that formed at Jupiter's gap edge. Therefore we also included the growth and migration of Saturn's core in our simulations.

Rather than calculating the actual pebble accretion rate at each iteration, we used a simple approach for Saturn's core growth. We initiated the core at 0.1 $M_\oplus$ at the beginning of the simulation, and grew it up to M_{iso} following a reasonable growth rate, which we chose to be $M_{core} \propto t^2$. This growth rate is slightly shallower than the growth rate suggested by pebble accretion ($M_{core} \propto t^3$ in the 3D regime, see e.g., Morbidelli et al. 2015); however, the effect on the simulation's outcome should be negligible (as is shown in Section 3, accretion onto Jupiter happens before the planetesimals have any chance to dynamically interact with Saturn's core). We note that during this phase, 10% of the accretion is assumed to be in the form of gas, so that the actual core mass is 90% of the above mass (see Section 2.3). Finally we also considered the migration of the core, which was performed using our normal migration prescription. The semimajor axis where the core needs to be initiated in order for Saturn to reach the pebble isolation mass at the right location is listed in the last column of Table 2.

The resulting growth tracks are presented in the left panel of Fig. 1, where 1 and 2 denote gas accretion scheme 1 and gas accretion scheme 2, respectively. In scheme 1 the envelope's contraction occurs on a relatively short timescale, leading to quick gap opening and little migration. In scheme 2 the contraction phase is significantly longer, and as a result the planet migrates much farther before runaway gas accretion is initiated. Gravitational perturbations from Jupiter cause some variations in the growth track of Saturn's core, but these are too small to have any impact on the simulation's outcome. The corresponding time evolution of the capture radius for these growth tracks is presented in the right panel of Fig. 1. The capture radius during gas accretion was calculated using the approximation from Valletta & Helled (2021), which has two regimes depending on whether the planet is in the attached phase ($M_{env} < M_{core}$) or the detached phase ($M_{env} > M_{core}$). For the detached phase, we used the fit obtained at 10^7 yr. During the attached phase the envelope is enhanced, resulting in a large capture radius. This phase ends once runaway gas accretion initiates, and the capture radius decreases to about 1.5 times the current Jupiter radius.

3.2. Dynamical evolution of planetesimals

Planetesimals were continuously injected into the simulation until the time of disk dissipation, following the procedure outlined in Section 2.5. We make two important assumptions regarding planetesimal formation: (1) there is no planetesimal formation at the gap edges before the pebble isolation mass has been reached; and (2) all pebbles that reach the gap edges are trapped and immediately converted into planetesimals. Taken together, this means that when Saturn reaches the pebble isolation mass, the drift of pebbles toward Jupiter is terminated. The time it takes

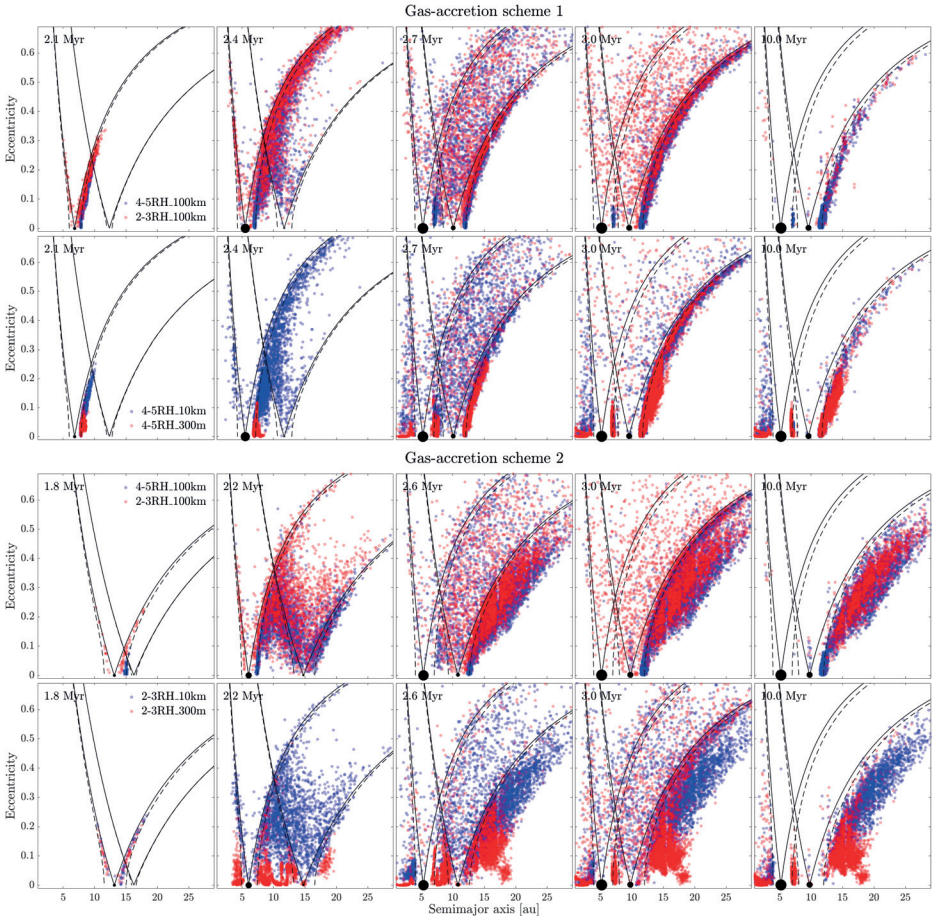

Fig. 2. Eccentricity and semimajor axis evolution for the planetesimals in some selected simulations. Each simulation has a total of 10,000 planetesimals being injected continuously until the time of disk dissipation. The black dots indicate the current mass and location of Jupiter and Saturn. The black lines are lines of equal Tisserand parameter going through the planet location (solid line) and the planet location offset by 5 Hill radii (dashed line). Planetesimals initiated inside the feeding zone of the planet (labeled $2-3\,R_{\rm H}$) suffer from stronger and faster scattering than those initiated outside the feeding zone (labeled $4-5\,R_{\rm H}$). Decreasing the planetesimal size leads to more gas drag and lower eccentricities, and it results in a population of circularized planetesimals interior of Jupiter.

for the remaining pebbles to reach Jupiter's gap edge after this is relatively short, only $10^3 - 10^4$ yr, and therefore we assume that planetesimals cease to form at Jupiter's gap edge when Saturn reaches the pebble isolation mass. Fig. 2 shows the time evolution of the eccentricities and semimajor axes of the planetesimal orbits, and how they vary with the following: 1) the initial formation location relative to the planet; 2) the planetesimal size; and 3) the different gas accretion schemes. Lines of equal Tisserand parameter for coplanar orbits are included in the figure and can be used to understand the planet scattering.

The effect of varying the initial formation location of the planetesimals is shown in row 1 and 3 of Fig. 2. Initiating the planetesimals inside the feeding zone of the planet results in faster and stronger scattering compared to the case when they are initiated outside of the feeding zone. The number of planetesimals scattered into the inner Solar System is also significantly higher in the former case (see also Fig. C.2). The amount of planetesimals which are scattered beyond the simulation domain does, however, not vary with the formation location, which can be seen in Fig. 3. Regardless of the formation location, most

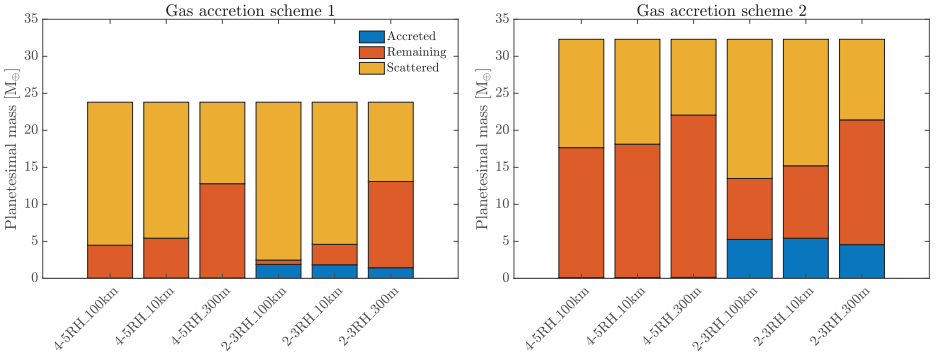

Fig. 3. Histogram showing the total planetesimal mass that has either been accreted onto the planets, that remains in the system at the end of the simulation, or that has been scattered beyond the simulation domain for all simulations in gas accretion scheme 1 (*left*) and gas accretion scheme 2 (*right*). Small planetesimals experience more efficient gas drag than large planetesimals, and they are retained in the system at a higher rate.

planetesimals that remain in the system past disk dispersal are located in a disk beyond Saturn.

In row 2 and 4 of Fig. 2, we show how the dynamical evolution changes when we decreased the planetesimal size. Smaller planetesimals are more affected by gas drag than larger planetesimals, and therefore their eccentricities are more damped. Interior of Jupiter the gas density is high enough to circularize small planetesimals, resulting in a stable population of planetesimals that remain until the end of the simulation. This population has low eccentricities in the case of 300 m-sized planetesimals; it has eccentricities up to around 0.4 in the case of 10 km-sized planetesimals; and it does not exist at all in the case of 100 km-sized planetesimals. Furthermore, there is a small population of planetesimals located around the outer 3:2 resonance with Jupiter, which appears early on and remains until 10 Myr. As expected, the number of planetesimals that are left in the system at the end of the simulation increases with decreasing planetesimal size, which is because of the stronger gas drag (see Fig. 3).

Finally, the effect of changing the gas accretion scheme can be seen by comparing the two upper rows with the two lower rows in Fig. 2. Since the planets migrate larger distances in scheme 2, planetesimals form in a wider region of the disk. A significant amount of the planetesimals formed at Saturn's gap edge become detached from the scattering region due to planet migration (recognized by being located beyond and below the equal Tisserand parameter lines), resulting in a broader planetesimal disk in scheme 2. Toward the end of the simulation, there are more planetesimals remaining in the system with gas accretion scheme 2 (see Fig. 3).

3.3. Planetesimal accretion

In order to calculate the mass represented by each super-particle, we assumed that the pebbles follow the viscous evolution of the disk (Johansen et al. 2019), and that all pebbles which reach the gap edge are converted into planetesimals. The planetesimal formation rate is then simply 1% of the disk accretion rate (photoevaporation is not considered in this calculation as it only affects the gas component of the disk), and the total planetesimal mass that forms in the simulation was calculated by integrating $0.01\times\dot{M}_{\rm g}$ from $t_{\rm iso,jup}$ to $t_{\rm evap}$. With these assumptions, we formed 23.8 $M_\oplus$ of planetesimals in scheme 1 and 32.3 $M_\oplus$ in scheme 2. The total planetesimal mass that formed at each individual gap edge is 14.1 $M_\oplus$ for Jupiter in scheme 1, 9.7 $M_\oplus$ for Saturn in scheme 1, 16.2 $M_\oplus$ for Jupiter in scheme 2, and 16.1 $M_\oplus$ for Saturn in scheme 2. Since the disk accretion rate decreases with time, the super-particles that formed in the beginning of the simulation are much more massive than those that formed toward the end. Given the assumed solid-to-gas ratio, disk model, and formation time of Jupiter, the above masses represent an upper limit on the formed planetesimal mass.

In Fig. 3 we show, for each simulation, how much of the total planetesimal mass that has either been accreted onto the planets, remains in the system, or has been scattered beyond the simulation domain at the end of the simulation. Fig. 4 shows how much of the planetesimal mass has been accreted onto Jupiter and Saturn, along with the corresponding accretion efficiency. The first thing to be noticed is that the maximum accretion efficiency in any simulation and for any planet is $< 10\%$, and the highest amount of solid material accreted onto Jupiter and Saturn is 3.2 $M_\oplus$ and 2.3 $M_\oplus$, respectively. This shows that planetesimal accretion during the gas accretion phase of giant planet formation is a very inefficient process.

A comparison of the simulation results shows that initializing the planetesimals inside the feeding zone of the planet results in a lot more collisions than placing them outside of the feeding zone. This is partly because a fraction of the planetesimals that formed within the feeding zone were captured immediately after formation due to the enhanced envelope (see Fig. 1 and C.3). The planetesimals that formed beyond the feeding zone are too far away from the planet to be affected by the enhanced envelope, and they only suffer from strongly unfocused collisions later on during the evolution.

As mentioned above, decreasing the planetesimal size results in more gas drag. Furthermore, it also results in an increased capture radius of the planets during the enhanced envelope phase (Valletta & Helled 2021), as smaller planetesimals can be captured further up in the atmosphere. The combined effect on the accretion efficiency of planetesimals, however, turns out to be small. In the case of Jupiter, we found that 300 m-sized planetesimals are accreted at a 30% lower rate than 10 and 100 km-sized planetesimals when formed inside the feeding zone. This is be-

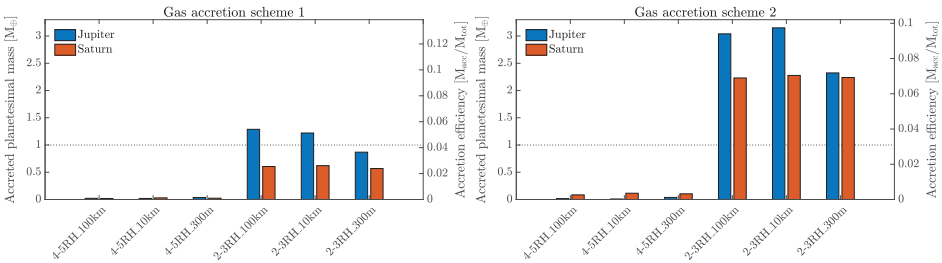

Fig. 4. Total accreted planetesimal mass onto Jupiter and Saturn, and the corresponding accretion efficiency for all simulations in gas accretion scheme 1 (*left*) and gas accretion scheme 2 (*right*). The accretion efficiency is much higher for planetesimals that formed inside the feeding zone, and it does not change significantly with planetesimal size. The maximum accretion efficiency obtained for any planet is < 10%, which corresponds to a mass of ∼3 $M_\oplus$.

cause if the planetesimals are not accreted immediately, they are scattered and eccentricity damping through gas drag quickly puts them out of the feeding zone, resulting in fewer planetesimals crossing Jupiter's orbit. In the case of Saturn, we found no difference between using small and large planetesimals. Some authors have suggested that using small planetesimals might solve the problem of the low planetesimal accretion efficiency (e.g., Alibert et al. 2018), but our results show that this is not the case for planetesimal accretion during the gas accretion phase.

When comparing the accretion efficiencies in scheme 1 and 2, we found that it is generally higher in scheme 2. This is because the enhanced envelope phase lasts longer in scheme 2, allowing for more planetesimals to be captured just after formation (see Fig. 1). Finally, in most of our simulations, Jupiter accreted a higher planetesimal mass than Saturn. In Fig. C.1 we show how the cumulative accreted planetesimal mass evolves with time.

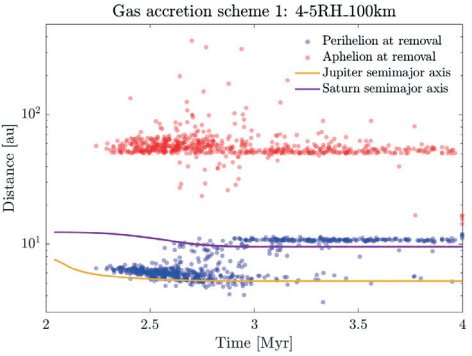

Fig. 5. Plot showing the perihelion and aphelion of 1000 planetesimal orbits at the last time step before they were scattered beyond the simulation domain and thus removed from the simulation, for one of the simulations in gas accretion scheme 1. The time evolution of the planet semimajor axes is included on the plot. The majority of the scattered planetesimals have an aphelion of ∼50 au and a perihelion located ∼1 au exterior of the planets, suggesting that they are not strongly scattered but rather are part of a scattered disk where eccentricities and aphelia increase gently with time.

4. Discussion

4.1. The fate of removed planetesimals

When a planetesimal is scattered beyond the simulation domain, it is removed from the simulation. In order to get an idea of how the planetesimal would have evolved given a larger simulation domain, we studied how the planetesimal orbits looked just before they were removed. The perihelion and aphelion for 1000 planetesimal orbits at the last time step before removal is showed in Fig. 5. Since most planetesimals have aphelion around 50 au and perihelion located ∼1 au exterior of the planets, this indicates that they still belong to the planetary scattered disks at the time of removal. In other words, they do not suffer from strong planetary encounters and should not have been ejected from the system. It is therefore likely that these planetesimals would have also remained in or around the scattered disk at 10 Myr had the simulation domain been larger. If this is the case, then the amount of planetesimal mass deposited in the region exterior of Saturn is at least 10 − 20 $M_\oplus$.

4.2. Implications for Solar System formation

The estimated total heavy element mass in Jupiter and Saturn is $\gtrsim$ 20 $M_\oplus$, with upper bounds that are much higher (e.g., Helled & Guillot 2013; Wahl et al. 2017; Helled 2018). When initiating the planetesimals inside the feeding zone of the planets, we reached a total heavy element mass of 14.8 and 25.1 $M_\oplus$ for Jupiter in scheme 1 and 2, respectively. The same numbers for Saturn were 19.0 and 24.4 $M_\oplus$; however, we note that most of the solid mass comes from pebble accretion (the contribution from planetesimal accretion to these numbers was very small, maximally 12%). Considering scheme 2, we nearly reached the lower end of the predicted heavy element mass; however, we note that this is under the assumption that all planetesimals formed within the feeding zone of the planet, and that the entire pebble flux was converted into planetesimals. When the planetesimals were initiated beyond the feeding zone of the planets, the amount of planetesimal accretion became negligible and the total heavy element mass was almost identical to the pebble isolation mass.

Based on the above discussion, it is difficult to explain the large heavy-element contents of Jupiter and Saturn with planetesimal accretion during the gas accretion phase. In the following we discuss potential ways to increase the accreted planetesimal mass compared to our model.

– If the protoplanetary disk mass was increased, more solids would be available, assuming the same solid-to-gas ratio. However, migration and gas accretion are accelerated in massive disks, meaning that the planets need to form later during disk evolution. As a consequence, planetesimal formation at the gap edges initiates later, and the total mass of planetesimals formed at gap edges would not necessarily be larger than in the case with a lower disk mass.

– Increasing the solid-to-gas ratio above the standard 1% would result in a more available planetesimal mass. However, in our models, we end up with more than $10\,M_\oplus$ of planetesimals in a disk beyond Saturn (see Sect. 4.1). When the smallest planetesimal sizes were considered, we also injected $3 - 9\,M_\oplus$ of planetesimals into the inner Solar System (see Fig. C.2, we note that this is not the case for 100 km-sized planetesimals). If the formed planetesimal mass is increased by a factor of 10, for example, this means that we would en up with several hundred $M_\oplus$ of planetesimals beyond Saturn, which might not be consistent with constraints on the masses of the Solar System's scattered disk and the Oort cloud (Brasser 2008). We nevertheless caution that inferring the original planetesimal mass from the current Oort cloud population is challenging and requires a number of assumptions to be made about the size distribution of the small comets that enter the inner Solar System (see Brasser 2008 for a discussion).

– Planetesimals formed at planetary gap edges represent a later generation of planetesimals, which did not contribute to the formation of the giant planet cores. Some of the planetesimals which must have formed earlier during disk evolution, as well as planetesimals forming at other locations in the disk, could also exist in the system. Our results show that planetesimal accretion is very inefficient when the planetesimals form beyond the feeding zone of the planet; however, in Shibata et al. (2020), Shibata et al. (2021), and Shibata & Helled (2022), they show that accretion can be significant if the planets are migrating far and shepherding the planetesimals in front of them. Taking into account the formation of planetesimals via other mechanisms interior of the planets might thus result in more accretion, although additional effects such as ablation need to be considered when icy planetesimals enter the inner Solar System (Eriksson et al. 2021).

– The accretion of solids onto the planetary envelope could have an effect on the timescale for gas accretion, which would result in the planetary growth tracks changing compared to our model. If the rate of solid accretion during the attached phase is high, then runaway gas accretion can be delayed, resulting in a longer enhanced envelope phase and more planetesimal accretion (Alibert et al. 2018; Valletta & Helled 2020). The dependence of gas accretion on enrichment is discussed in Sect. 4.5.2.

– If the planetary cores formed much earlier than in our model, regardless of whether this occurred via pebble accretion or via some other scenario (e.g., Kobayashi & Tanaka 2021), more solids would remain in the disk and thus the total mass of planetesimals forming at the gap edges would be larger. Our models for gas accretion and migration do not manage to produce Jupiter and Saturn in this scenario, as the planets would become far too massive. The accreted planetesimal mass would likely increase if the cores formed earlier.

4.3. Implications for exoplanets

The estimated heavy element mass for hot Jupiters ranges from $\sim 10 - 100\,M_\oplus$, with many planets containing more than $50\,M_\oplus$ (Guillot et al. 2006; Miller & Fortney 2011; Thorngren et al. 2016). Although our work focuses on the formation of the cold Solar System giants, it is clear from our results that such large heavy element masses are difficult to explain by the accretion of planetesimals. Despite the fact that all planetesimals were initiated inside the feeding zone of the planet, and that we used a 100% pebble-to-planetesimal conversion efficiency at the gap edges, the maximum accretion efficiency obtained in our simulations was < 10%. In order to accrete $\sim 50\,M_\oplus$ of planetesimals, there would thus need to be more than $500\,M_\oplus$ of planetesimals forming at the gap edges.

Based on the discussion in Sect. 4.2, the most promising way of increasing the planetesimal accretion efficiency is to have a prolonged attached phase. One way to achieve this is if the bombardment of planetesimals onto the planetary envelope is high enough to delay runaway gas accretion itself (Alibert et al. 2018; Venturini & Helled 2020). Having a longer attached phase also implies a longer migration distance, such that the planet would start accreting gas further out in the disk. This is in line with the results by Shibata et al. (2020), who found that a Jupiter mass planet can accrete enough planetesimals to explain the observed metallicities, provided that the planet starts migrating at a few tens of au in a massive planetesimal disk ($\sim 100\,M_\oplus$). Efficient planetesimal accretion might thus not be impossible, but it requires extreme conditions. In other cases, alternative processes are required to explain the high metal content of extrasolar giants (see Section 4.4).

4.4. Alternative models for envelope enrichment

There are multiple alternative processes that can lead to envelope enrichment, such as accretion of enriched gas, erosion of the initial core, or giant impacts. The accretion of enriched gas is a natural outcome of planet formation models, where drifting pebbles sublimate at snow lines and subsequently enrich the gas that is closer to the star (Booth et al. 2017; Schneider & Bitsch 2021a,b). Giant planets forming within the snow lines accrete this metal-rich gas and automatically obtain enriched envelopes. In Schneider & Bitsch (2021a,b), they show that this process can result in heavy element contents that match the ones predicted by Thorngren et al. (2016) for hot Jupiter systems, provided that the solid-to-gas ratio in the disk is ∼2%.

Erosion of the initially compact core and subsequent mixing of the heavy elements within the envelope would also result in an enhanced envelope metallicity (e.g., Madhusudhan et al. 2017). However, the efficiency of this mechanism is uncertain (Guillot et al. 2004) and it depends both on material properties and the mixing efficiency within the envelope (Wilson & Militzer 2012; Soubiran & Militzer 2016). Furthermore, in order to match the estimated heavy element content of exogiants, the initial core mass would have to be very large. On the positive side, if feasible, the resulting interior profile of the planet could be one with an extended diluted core, which is typically favored by internal structure models (e.g., Wahl et al. 2017).

Finally, studies by Li et al. (2010) and Liu et al. (2019) show that energetic head-on collisions between proto-Jupiter and large planetary embryos (several $M_\oplus$) could result in shattering and erosion of Jupiter's core. The subsequent mixing of heavy elements into the proto-envelope lead to an enhanced envelope metallicity, and this could produce a diluted core profile. How-

ever, the question remains whether the frequency of giant impacts is high enough.

4.5. Shortcomings of the model

4.5.1. The effect of gas accretion on disk evolution

In our model for gas accretion, we did not consider the effect of gas accretion on disk evolution, other than the opening of a gap. This is a common simplification in planet formation studies; however, in reality the gas which is accreted onto the planet should be removed from the disk accretion rate onto the star. Consequently, if the disk contains multiple planets that are accreting gas simultaneously, then the amount of gas which is available to the inner planet depends on how much gas has been accreted by the outer one. In our model, gas accretion onto Jupiter and Saturn are treated independently, which could in practice result in the sum of the gas accretion rates onto both planets being larger than the disk accretion rate.

Taking the above effects into consideration would result in less gas drag on the planetesimals that are scattered interior of the planetary orbits. This could, for example, effect the population of circularized planetesimals interior of Jupiter that can be seen in panel 2 and 4 of Fig. 2. In the case of Jupiter's formation, when Saturn reaches runaway gas accretion, the mass available for Jupiter to accrete would decrease compared to the current model. Therefore, Jupiter would have to reach the pebble isolation mass earlier during disk evolution. This would not result in a prolonged enhanced envelope phase (gas accretion is independent of the disk mass during the attached phase); however, given that the pebble flux is larger early on during disk evolution, the accreted planetesimal mass would likely increase a bit.

4.5.2. The dependence of gas accretion on enrichment

The accretion of solids onto the planetary envelope affects the efficiency of gas accretion in mainly two ways: (1) the envelope obtains thermal support from the dissipation of kinetic energy from infalling solids, which counteracts the gravity of the core and thus slows down envelope contraction (Alibert et al. 2018); and (2) the enriched envelope obtains a higher molecular weight, which has been shown to result in faster gas accretion and shorter formation timescales (e.g., Stevenson 1982; Venturini et al. 2016; Valletta & Helled 2020). If the first effect dominates, the onset of runaway gas accretion is delayed, resulting in a longer migration distance as well as a longer enhanced envelope phase. This would likely lead to a higher accretion efficiency of planetesimals. In Alibert et al. (2018), they find that a constant accretion rate of at least $10^{-6}\,M_\odot\,yr^{-1}$ is required in order to stall runaway gas accretion for 2 Myr. In principle, the solutions we find with a high planetesimal accretion rate could delay runaway gas accretion and be more consistent with these results.

If the second effect dominates, gas accretion occurs on a shorter timescale, meaning that the planets in our model would need to reach the pebble isolation mass later during disk evolution. This would likely result in a smaller accreted planetesimal mass. The question of how gas accretion is affected by solid enrichment is an important problem, which should be solved in a more self-consistent manner, with detailed calculations and a proper handling of thermal dynamics

5. Conclusion

In this work, we study collisions between gap-opening planets and planetesimals forming at their gap edges, with the aim to determine whether the delivered mass is high enough to explain the large heavy element contents of giant planets. To this end, we used a suite of *N*-body simulations. We considered the formation of Jupiter and Saturn, taking into account the enhanced collision cross section caused by their extended envelopes. Two formation pathways were examined, where one leads to large-scale planet migration, and the other to migration over a few au only. We further varied the formation location of the planetesimals relative to the planets, and the planetesimal sizes. We find that:

- The close proximity to the gap-opening planets causes the planetesimals to leave their birth location soon after formation. Most planetesimals that do not experience ejection or accretion eventually become members of Saturn's scattered disk. In the case of small planetesimal radii, there is also a population of circularized planetesimals in the innermost disk region.
- Planetesimal accretion during the gas accretion phase of giant planet formation is a very inefficient process. The maximum obtained accretion efficiency onto Jupiter or Saturn is less than 10%, corresponding to a mass of $\sim 3\,M_\oplus$ and $\sim 2\,M_\oplus$, respectively. Since these numbers were obtained assuming that all planetesimals form within the feeding zone of the planets, and that all pebbles reaching the gap-edges are turned into planetesimals, they represent an upper limit on the accreted planetesimal mass.
- When planetesimal formation occurs beyond the feeding zone of the planets, accretion becomes negligible. This is a good indication that planetesimal accretion during the gas-accretion phase is inefficient also if the planetesimals form via other processes and in other regions of the disk.
- Decreasing the planetesimal radii does not lead to more efficient accretion. In the literature it is often mentioned that having smaller planetesimals leads to more accretion (e.g., Alibert et al. 2018), but our results demonstrate that this is not the case for planetesimal accretion during the gas accretion stage.
- The accretion efficiency is higher when we considered the formation pathway with a long migration distance. This is in line with the results by Shibata et al. (2020), who found that efficient accretion can occur if a massive planet starts migrating at a few tens of au in a massive planetesimal disk ($\sim 100\,M_\oplus$).

Based on our results, we conclude that it is difficult to explain the large heavy element contents of giant planets with planetesimal accretion during the gas accretion phase, provided they do not migrate very far in a very massive planetesimal disk (Shibata et al. 2020). Hence, alternative processes of envelope enrichment are most likely required in order to explain the high heavy element content inferred for Jupiter and Saturn, as well as that of transiting planets. The accretion of vapor deposited by drifting pebbles is one such promising mechanism (Schneider & Bitsch 2021a,b).

Acknowledgements. L.E. and A.J. are supported by the Swedish Research Council (Project Grant 2018-04867). T.R. and A.J. are supported by the Knut and Alice Wallenberg Foundation (Wallenberg Academy Fellow Grant 2017.0287). A.J. further thanks the European Research Council (ERC Consolidator Grant 724 687-PLANETESYS), the Göran Gustafsson Foundation for Research in Natural Sciences and Medicine, and the Wallenberg Foundation (Wallenberg Scholar KAW 2019.0442) for research support. R.H. and C.V. acknowledge support from the Swiss National Science Foundation (SNSF) under grant 200020_188460.

Simulations in this paper made use of the REBOUND code which is freely available at http://github.com/hannorein/rebound. The computations were performed on resources funded by the Royal Physiographic Society of Lund.

References

Alibert, Y., Venturini, J., Helled, R., et al. 2018, Nature Astronomy, 2, 873
Bai, X.-N. & Stone, J. M. 2010, ApJ, 722, 1437
Bitsch, B., Lambrechts, M., & Johansen, A. 2015, A&A, 582, A112
Bitsch, B., Morbidelli, A., Johansen, A., et al. 2018, A&A, 612, A30
Booth, R. A., Clarke, C. J., Madhusudhan, N., & Ilee, J. D. 2017, MNRAS, 469, 3994
Bottke, W. F., Durda, D. D., Nesvorný, D., et al. 2005, Icarus, 179, 63
Brasser, R. 2008, A&A, 492, 251
Carrera, D., Johansen, A., & Davies, M. B. 2015, A&A, 579, A43
Carrera, D., Simon, J. B., Li, R., Kretke, K. A., & Klahr, H. 2021, AJ, 161, 96
Chiang, E. I. & Goldreich, P. 1997, ApJ, 490, 368
Cresswell, P. & Nelson, R. P. 2008, A&A, 482, 677
Eriksson, L. E. J., Johansen, A., & Liu, B. 2020, A&A, 635, A110
Eriksson, L. E. J., Ronnet, T., & Johansen, A. 2021, A&A, 648, A112
Guillot, T., Santos, N. C., Pont, F., et al. 2006, A&A, 453, L21
Guillot, T., Stevenson, D. J., Hubbard, W. B., & Saumon, D. 2004, The interior of Jupiter, ed. F. Bagenal, T. E. Dowling, & W. B. McKinnon, Vol. 1, 35–57
Hayashi, C. 1981, Progress of Theoretical Physics Supplement, 70, 35
Helled, R. 2018, The Interiors of Jupiter and Saturn, 175
Helled, R. & Guillot, T. 2013, ApJ, 767, 113
Ikoma, M., Nakazawa, K., & Emori, H. 2000, ApJ, 537, 1013
Johansen, A., Ida, S., & Brasser, R. 2019, A&A, 622, A202
Johansen, A., Mac Low, M.-M., Lacerda, P., & Bizzarro, M. 2015, Science Advances, 1, 1500109
Johansen, A., Youdin, A., & Mac Low, M.-M. 2009, ApJ, 704, L75
Kanagawa, K. D., Tanaka, H., & Szuszkiewicz, E. 2018, ApJ, 861, 140
Kobayashi, H. & Tanaka, H. 2021, ApJ, 922, 16
Lambrechts, M., Johansen, A., & Morbidelli, A. 2014, A&A, 572, A35
Li, S. L., Agnor, C. B., & Lin, D. N. C. 2010, ApJ, 720, 1161
Liu, S.-F., Hori, Y., Müller, S., et al. 2019, Nature, 572, 355
Lubow, S. H. & D'Angelo, G. 2006, ApJ, 641, 526
Lynden-Bell, D. & Pringle, J. E. 1974, MNRAS, 168, 603
Lyra, W., Johansen, A., Klahr, H., & Piskunov, N. 2009, A&A, 493, 1125
Madhusudhan, N., Bitsch, B., Johansen, A., & Eriksson, L. 2017, MNRAS, 469, 4102
Miller, N. & Fortney, J. J. 2011, ApJ, 736, L29
Morbidelli, A., Bottke, W. F., Nesvorný, D., & Levison, H. F. 2009, Icarus, 204, 558
Morbidelli, A., Lambrechts, M., Jacobson, S., & Bitsch, B. 2015, Icarus, 258, 418
Nesvorný, D., Li, R., Youdin, A. N., Simon, J. B., & Grundy, W. M. 2019, Nature Astronomy, 364
Piso, A.-M. A. & Youdin, A. N. 2014, ApJ, 786, 21
Rein, H., Hernandez, D. M., Tamayo, D., et al. 2019, MNRAS, 485, 5490
Rein, H. & Liu, S. F. 2012, A&A, 537, A128
Schneider, A. D. & Bitsch, B. 2021a, A&A, 654, A71
Schneider, A. D. & Bitsch, B. 2021b, A&A, 654, A72
Shakura, N. I. & Sunyaev, R. A. 1973, A&A, 500, 33
Shibata, S. & Helled, R. 2022, arXiv e-prints, arXiv:2202.06847
Shibata, S., Helled, R., & Ikoma, M. 2020, A&A, 633, A33
Shibata, S., Helled, R., & Ikoma, M. 2021, arXiv e-prints, arXiv:2112.12623
Shiraishi, M. & Ida, S. 2008, ApJ, 684, 1416
Soubiran, F. & Militzer, B. 2016, ApJ, 829, 14
Stammler, S. M., Drążkowska, J., Birnstiel, T., et al. 2019, ApJ, 884, L5
Stevenson, D. J. 1982, Planet. Space Sci., 30, 755
Tanigawa, T. & Tanaka, H. 2016, ApJ, 823, 48
Thorngren, D. P., Fortney, J. J., Murray-Clay, R. A., & Lopez, E. D. 2016, ApJ, 831, 64
Valletta, C. & Helled, R. 2020, ApJ, 900, 133
Valletta, C. & Helled, R. 2021, MNRAS, 507, L62
Venturini, J., Alibert, Y., & Benz, W. 2016, A&A, 596, A90
Venturini, J. & Helled, R. 2020, A&A, 634, A31
Wahl, S. M., Hubbard, W. B., Militzer, B., et al. 2017, Geophys. Res. Lett., 44, 4649
Wilson, H. F. & Militzer, B. 2012, ApJ, 745, 54
Yang, C. C., Johansen, A., & Carrera, D. 2017, A&A, 606, A80
Youdin, A. N. & Goodman, J. 2005, ApJ, 620, 459

Appendix A: Details of the disk model

We used the analytic solution for the surface density evolution of an unperturbed thin accretion disk from Lynden-Bell & Pringle (1974):

$$\Sigma_{\rm unp}(t) = \frac{\dot{M}_g(t)}{3\pi\nu_{\rm out}(r/r_{\rm out})^{\gamma}} \exp\left[-\frac{(r/r_{\rm out})^{(2-\gamma)}}{T_{\rm out}}\right], \quad (A.1)$$

where

$$T_{\rm out} = \frac{t}{t_s} + 1, \quad (A.2)$$

and

$$t_s = \frac{1}{3(2-\gamma)^2}\frac{r_{\rm out}^2}{\nu_{\rm out}}. \quad (A.3)$$

In the equations above, $\dot{M}_g(t)$ is the disk accretion rate at time t, r is the semimajor axis, $r_{\rm out}$ is the scaling radius, $\nu_{\rm out} \equiv \nu(r_{\rm out})$ where ν is the kinematic viscosity, and γ is the radial gradient of ν. The evolution of the disk accretion rate is given by

$$\dot{M}_g(t) = \dot{M}_g(t=0)\left[\frac{t}{t_s}+1\right]^{-(\frac{5}{2}-\gamma)/(2-\gamma)} - \dot{M}_{\rm pe}, \quad (A.4)$$

where $\dot{M}_{\rm pe}$ is the rate at which material is removed by photoevaporation, which we consider to be constant in time.

The sound speed in the disk was calculated as

$$c_{\rm s} = \left(\frac{k_{\rm B}T}{\mu m_{\rm H}}\right)^{1/2}, \quad (A.5)$$

where $k_{\rm B}$ is the Bolzmann constant, T is the temperature, μ is the mean molecular weight, and $m_{\rm H}$ is the mass of the hydrogen atom. We used a value of 2.34 for the mean molecular weight (Hayashi 1981). The midplane temperature of the disk was approximated using a fixed power-law structure:

$$T = 150\,{\rm K} \times (r/{\rm au})^{-3/7} \quad (A.6)$$

(Chiang & Goldreich 1997).

We used Gaussian gap profiles to model the planetary gaps, where the Gaussian is described by the equation

$$G(r) = \left(1 - \frac{\Sigma_{\rm gap}}{\Sigma_{\rm unp}}\right)\exp\left[-\frac{(r-a)^2}{2H_a^2}\right], \quad (A.7)$$

where a is the semimajor axis of the planetary orbit and H_a is the corresponding gas scale height. The perturbed surface density profile could then be obtained by using the following expression:

$$\Sigma = \frac{\Sigma_{\rm unp}}{1 + G_1 + G_2 + ...}, \quad (A.8)$$

where each planet contributes their own Gaussian. Finally, the gas density at some height, z, away from the midplane was obtained by using the equation

$$\rho(z) = \frac{\Sigma}{\sqrt{2\pi}H}\exp\left[\frac{-z^2}{2H^2}\right], \quad (A.9)$$

where we assumed vertical hydrostatic equilibrium for the gas in the disk.

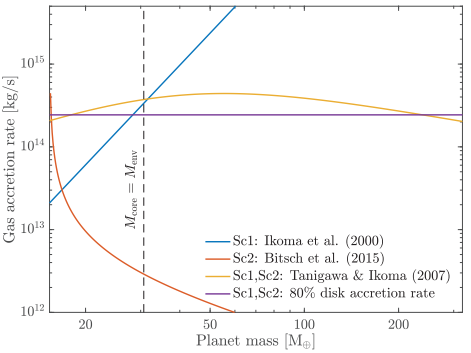

Fig. B.1. Gas accretion rate as a function of planetary mass for a planet located at 10 au in a 2 Myr old protoplanetary disk. The labels Sc1 and Sc2 indicate in which gas accretion scheme the current model is being used.

Appendix B: Gas accretion rate

In Fig. B.1 we have plotted the dependence on planetary mass for all the different gas accretion rates which were used in our models. The rates were calculated using a semimajor axis of 10 au and a disk time of 2 Myr. In scheme 1 the gas accretion rate during envelop contraction increases with increasing planetary mass, and runaway gas accretion initiates when this rate becomes higher than what the disk can supply. In scheme 2 the gas accretion rate during envelop contraction instead decreases with increasing planetary mass, and runaway gas accretion initiates when the core mass equals the envelope mass. At the chosen time and semimajor axis, gas accretion is limited by disk accretion for most of the runaway phase.

Appendix C: Additional plots

In Fig. C.1 we show the amount of planetesimal mass that has been accreted onto Jupiter and Saturn as a function of time for all simulations, along with the corresponding accretion efficiency. This is the same data that are presented in Fig. 4. The "knee" on the accretion curves for planetesimals that formed within the feeding zone coincides with the location where $M_{\rm env} = M_{\rm core}$, which is when runaway gas accretion initiates and the approximation for the capture radius becomes significantly smaller (see right panel of Fig. 1 for a plot of the capture radius versus time). Up until this point, a fraction of the planetesimals were captured immediately after formation due to the enhanced envelope. This trend is not seen in the accretion curves for planetesimals that formed beyond the feeding zone, since they were initiated too far away from the planet to be affected by the enhanced envelope.

In Fig. C.2 the total planetesimal mass residing in the inner Solar System is shown as a function of time (we consider a planetesimal to be in the inner Solar System if its aphelion is less than 4 au). In the case of 100 km-sized planetesimals, the amount of mass injection into the inner Solar System is negligible. Considering 10 km-sized planetesimals, we injected between 0.3 – 2 $M_\oplus$ of the planetesimals into the inner Solar System, which also remains after the dispersal of the gas disk. When using planetesimals of 300 m in size, we scattered and subsequently trapped

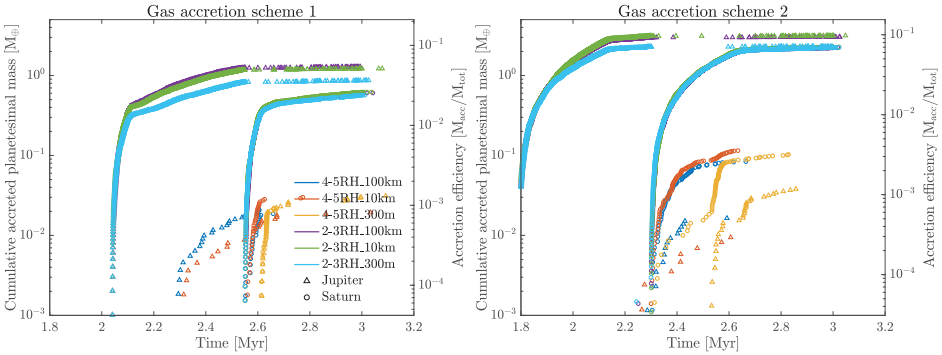

Fig. C.1. Cumulative accreted planetesimal mass as a function of time for all simulations in scheme 1 (*left*) and in scheme 2 (*right*). The corresponding accretion efficiency was calculated by dividing with the total planetesimal mass that formed in the system at the time of disk dissipation. Each scatter point in the plot is one collision event; however, since we performed three simulations per parameter set and show the combined results, the number of collisions in one simulation should be three times smaller than in this plot. The maximum obtained accretion efficiency onto any planet in scheme 1 is 5%, which corresponds to ~1 $M_\oplus$. The accretion efficiency is much higher for planetesimals that formed inside the feeding zone, and it does not change significantly with planetesimal size. The maximum accretion efficiency obtained for any planet in scheme 2 is 10%, which corresponds to a mass of ~3 $M_\oplus$.

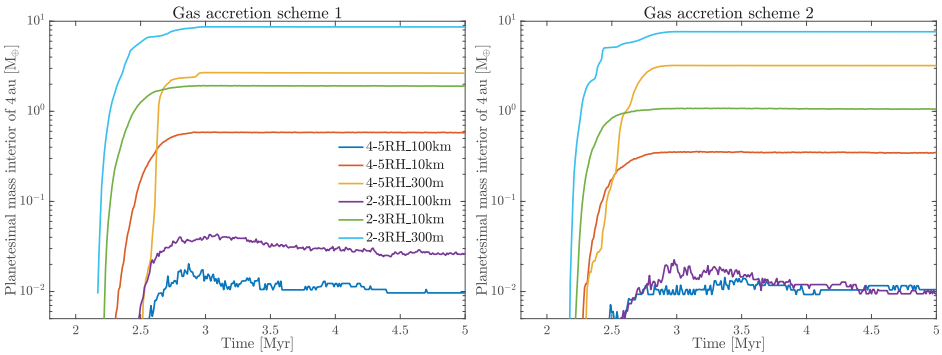

Fig. C.2. Total planetesimal mass residing in the inner Solar System (planetesimals with aphelion less than 4 au) plotted as a function of time for all simulations in scheme 1 (*left*) and in scheme 2 (*right*). The chance of making it into the inner Solar System increases with decreasing planetesimal size and decreasing formation distance relative to the planet.

3 – 9 $M_\oplus$ of the planetesimals in the inner Solar System. We find that planetesimals forming inside the feeding zone of the planet have a higher chance of making it into the inner Solar System, which is because of the more efficient planetary scattering. If the amount of planetesimal formation at the gap edges were to drastically increase, the amount of mass entering the inner Solar System would do so as well.

In Fig. C.3 the median time before collision is presented as a function of the initial separation relative to the planet. Planetesimals that are initiated between $2-2.4\,R_H$ typically collide within 20 orbital periods. This suggests that a significant fraction of the accretion efficiency comes from immediate accretion (a lifetime of ten orbital periods corresponds to roughly two to three close encounters). We do not know whether or not it is realistic for planetesimals to form in regions with immediate accretion, and to our knowledge this has not been studied.

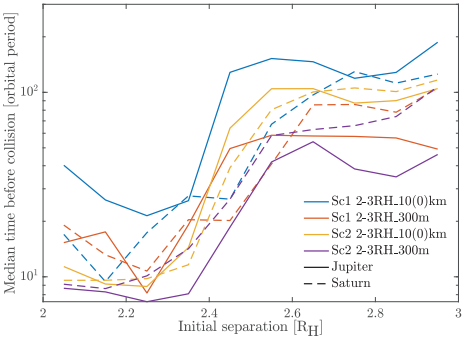

Fig. C.3. Median time before collision versus the initial separation for all simulations with planetesimals initiated inside the feeding zone of the planets. The time is given in units of the orbital period of the planets at the time the planetesimals were formed. Planetesimals initiated between $2 - 2.4\,R_H$ typically collide within 20 orbital periods.

Printed by Media-Tryck, Lund 2022 NORDIC SWAN ECOLABEL 3041 0903

Department of Astronomy
and Theoretical Physics
Faculty of Science

ISBN 978-91-8039-196-2